Easy as XYZ: Exploring non-commuting coherent interactions in trapped ions

Oana Băzăvan

Brasenose College

University of Oxford

A thesis submitted for the degree of

Doctor of Philosophy

Trinity 2024

Acknowledgements

It takes a village, or perhaps a basement, to raise a D.Phil. student. While it's impossible to include everyone who has contributed to this work in one form or another, I will strive to mention as many as I can, for without them, this journey would not have been possible.

I am very grateful to my supervisor, David Lucas, for inviting me to join his group and providing numerous chances to learn, travel, and engage with fascinating, cutting-edge scientific endeavours. David's support took many forms—encouraging me to get involved in non-PhD activities, always generous in ways that kept everything running smoothly, and turning up in the lab or office with words of wisdom and anecdotes. His feedback also had a creative flair—once, he illustrated an ion 'sitting' in a standing wave.

Over the years, I have been part of the Blade/Fast Gates[1]/Fast Blades subgroup, which also blended with the Lab1 crew at times. I need to thank Vera Schaefer for introducing me to the Blade setup and ion trapping and for teaching me how to run calibration experiments from home during the first COVID lockdown. This challenging experience was also a great learning opportunity in remote experiment debugging.

With Amy Hughes, we once changed the memory card of the KC705. I often recall this event because Amy was under significant stress at the end of her PhD, dealing with the first COVID lockdown, finishing her final data collection, and enduring two power cuts in one week, all while this device decided to misbehave. Despite this, she calmly explained the issue and how to solve it. Her level of composure left a lasting impression on me; I don't think I ever managed to replicate it. Amy has also provided invaluable words of wisdom and support to me and the other PhD student working on Blade.

To be honest, I have no idea how 'Fast' got added to 'Blades'. I remember starting to join the subgroup meetings set up by Chris Ballance, which I feel were a turning point in my learning experience. To Chris, I am deeply grateful for the various lessons: 'What's the worst that can happen? Let's derisk it!', 'What is the minimum working case?', 'Always good to have a rubber duck', and his general excitement about trap RF and DC control.

[1]Which are not that fast.

Kaitlin, whom I will introduce later, once talked with me about when we first became confident in discussing, explaining, and enquiring about Physics in a group setting. For both of us, it happened during our PhDs. For me, it started when I began working with Sebastian Saner on Blade. Initially, his inquisitiveness felt like a test, and I found it extremely annoying. However, his questions came without judgment, driven by pure curiosity and a desire to bounce ideas. Over time, Sebastian became a comprehensive lab partner and less annoying, engaging in countless blackboard discussions, teaching me simulations, battling the 674 nm laser, and sharing both great ideas and not-so-great ones. Our collaboration involved long walks, offering each other support, much laughter, and an invaluable friendship. It has been a great pleasure and fun to share the experiment with you, Sebastian. I am proud of what we achieved and learned together.

Gabriel Araneda and Raghu Srinivas, though officially working on HOA2, have been great mentors. In the early days of Fast Blades, they would often share their knowledge and patiently answer our countless questions. From them, I learned to read the arXiv (almost) every day, take and share notes at conferences, present our results effectively, and constructively spy on other lab books within the group.

Gabriel, always inquisitive with his 'Can you explain this?', 'What are you measuring?', and 'Can you do this?' questions, instilled the same curiosity in us. His support with the 674 nm laser was invaluable, from elegantly doing alignments in five minutes to sending his highly effective Gabriel-style emails. Gabriel's arrival in the group also coincided with us becoming more social and eating more cake.

Raghu closely guided us through writing our first paper in one of the lovely Beecroft rooms facing the park, with snacks and late evenings. He seized every opportunity to tell us that lasers suck (he's calmed down since then) while showing immense commitment and enthusiasm for presenting our results in the best way possible. I still think that this paper, the CANZZ (carrier anti-nulled ZZ gate) [1], is my favourite. Raghu's elegant ideas have profoundly shaped this thesis and my PhD.

To finish with the Lab1 people, it has been an amazing learning opportunity and great fun to share the lab with HOA2. Peter Drmota set up the gateware for the phase stabilisation feedback loop used for most of the results in this thesis. Together with Dougal, who contributed to the autolocking process for the 674 nm, they have been great lab partners to Sebastian and me during our final data-taking late evenings. David Nadlinger provided endless ARTIQ support, wrote the code for randomized benchmarking used in this thesis, and taught me how to do S11 measurements while I was frustratingly crying over breaking an AOM in my first year. Beth Nichol, Ellis Ainley, and Ayush Agrawal tirelessly set up the last iteration of the 674 nm and the new 729 in cosy and isolating boxes.

Maybe the ones I learned the most from working with are the freshest DPhil student in our subgroup, Donovan Webb, and our summer students, Mykolas

Sveistrys, Sophie Howarth, Iver Øvergaard (our first master's student), and Lavender Foo. Donovan has been a great addition to our Physics discussions, providing insightful ideas and great humour, and is masterfully advancing the 'Fast' part of the experiment in 'Fast Blades'.
Alejandro Bermudez has been a great collaborator, teaching us about lattice gauge theories, offering mental support during thesis writing, and putting so much trust in us. This trust gave Sebastian and me great confidence in ourselves and helped us not feel guilty about stealing the theorists' coffee.
Kaitlin Gili (the theory group) has been a breath of fresh air in the Beecroft office. She has always been there to listen and support and has become a very good friend. Through her thoughtful messages and conversations, Kaitlin made me reflect more on the scientific process and why we ask the questions that we do. She instilled in me greater awareness and taught me how to better show appreciation for the people around me and how to invest in these relationships.
I would also like to thank the Lab 3 crew/Comet team, including Ryan Hanley, Clemens Löschnauer, and Marius Weber, who answered many questions and helped set up the control system in the early days of Fast Blades. Mario Gili, Aaron Leu, and Molly Smith have always been stylish, artistic, and willing to share their knowledge on various topics.
The Abaqus team, Fabian Pokorny, Ana Sotirova, Jamie Leppard, Andres Vasquez Brennan, and Sophie Decoppet, provided great lunch conversations, assistance with ARTIQ and optical systems, and many laughs in the Beecroft office.
The Cavities group, Joe Goodwin, Jake Blackmore, Thomas Doherty, Will Hughes, Lorenzo Versini, Katie Challoner, Tom Hinde, and Tenzan Araki, also shared their knowledge on various topics and contributed to enjoyable lunch conversations.
I have had the privilege of learning from many excellent teachers and mentors throughout my life. Lothar Maisenbacher and Vitaly Wirthl, in particular, have steered me away from precision measurement and towards the more 'practical' field of quantum computing with trapped ions.
I am grateful to the friends from various parts of the world who enriched my soul and kept me grounded: Mălina, Diana, Elena, Ioana, Rares, Soumya, Jack, Lucas, Naj, Laura, and Danny.
As a kid, I often heard my parents, especially my father, say, 'Oana just needs to gain critical mass, and things will roll from there.' As a 'fluffy' child, I didn't appreciate this statement and didn't understand it. Later, I heard it in the context of my brother as well. Now, I think I get it, this parenting technique, which I wonder where my physicist father came up with, meant that they would pour learning opportunities into me until things clicked and I started finding them for myself. Thank you so much to my parents for their endless support at every step—late

nights solving maths questions on the living room floor, giving me lifts to English classes, friends' parties, and anywhere I needed to go, supporting me through university, and late-night calls on the way back from the lab. Thank you to my brother Andrei for being such an inspiration.

I would like to thank Sebastian Saner, Raghavendra Srinivas, Gabriel Araneda, Amy Hughes, Donovan Webb, and David Lucas for their close reading of this thesis. Their feedback has been invaluable, and future readers will surely benefit from their contributions.

Abstract

Developing coherent control operations to precisely achieve desired unitary evolutions is central to various fields of quantum science. For example, these operations are crucial for creating multi-qubit entangling operations and designing tailored, tunable Hamiltonians for analogue quantum simulations. This challenge is compounded by the fact that the systems in question are neither ideal nor isolated, and they frequently suffer from unavoidable spurious interactions.

A common source of errors in coherent operations typically stems from incoherent processes, where the system interacts with the environment. However, as interaction durations decrease, these become negligible and coherent errors begin to dominate the behaviour of the system. Among these, the most challenging to deal with are errors that do not commute with the main interaction. We investigate such errors within the spin-oscillator system of a trapped ion. For example, in the Mølmer-Sørensen entangling gate operation, the travelling wave fields that generate the essential spin-motion coupling also induce an off-resonant non-commuting carrier term. This term introduces errors in the entanglement operation. To address this, we introduce control over the optical phase of the laser field by using a standing wave, whose position we stabilise to $\lambda/100$ with respect to the ion. This allows us to gain control over the phase degree of freedom of the laser-ion interaction, enabling us to circumvent the non-commutativity and suppress the strength of the problematic carrier term by a factor of 18.

Conversely, non-commuting interactions can also be advantageous, enabling the creation of novel, effective interactions when the appropriate control is employed. By combining two spin-dependent forces that do not commute, we demonstrate a method to generate nonlinear interactions in the motion of an ion with favourable scaling. Unlike conventional methods that rely on higher orders of the Lamb-Dicke parameter expansion, our approach achieves linear scaling with the increase in interaction order. Specifically, we focus on generalised squeezing interactions and experimentally demonstrate squeezing (second order), trisqueezing (third order), and quadsqueezing (fourth order). The quadsqueezing achieved is over 100 times stronger than that possible with conventional methods and, to the best of our knowledge, represents the first implementation of fourth-order generalised squeezing across any platform. Our method does not impose a fundamental limit on the interaction order and is universally applicable to any platform that supports spin-dependent linear interactions.

Contents

1 Introduction

Understanding how to tailor quantum dynamics for the desired evolution of a quantum state is a fundamental challenge across the various fields of quantum science. Typically, quantum dynamics are envisioned as an ideal and isolated process, yet they are often disrupted by unavoidable spurious interactions. These interactions can significantly alter the intended evolution, making it necessary to develop methods that counteract or mitigate these disturbances and preserve the fidelity of quantum operations.

One important aspect of this challenge involves identifying the necessary time-dependent control fields to achieve precise unitary evolution with high accuracy. This task, far from trivial, demands complex mathematical formulations and precise experimental implementations [2]. Despite these complexities, mastering coherent control in quantum systems is essential. It not only underpins the development of robust quantum devices capable of solving problems intractable for classical computers but also enhances our understanding of the underlying physics driving these interactions.

1.1 The time evolution of a quantum state

If the quantum dynamics are described by a time-independent Hamiltonian $\hat{H}$, the time evolution of the state can be simply described as follows

$$|\psi(t)\rangle = \hat{U}(t)\,|\psi(0)\rangle = e^{-\frac{i}{\hbar}\hat{H}t}\,|\psi(0)\rangle\,,$$

where $\hat{U}(t)$ is the time evolution operator or propagator, and $|\psi(0)\rangle$ is the state at time $t = 0$.

However, interactions are often described by time-dependent Hamiltonians. In such cases, computing the propagator becomes non-trivial [3]:

$$\hat{U}(t) = \mathcal{T}\left(e^{-\frac{i}{\hbar}\int_0^t \hat{H}(t')dt'}\right),$$

where $\mathcal{T}$ indicates a time-ordered exponential, whose use is crucial when the Hamiltonian does not commute with itself at different times

$$[\hat{H}(t_1), \hat{H}(t_2)] = \hat{H}(t_1)\hat{H}(t_2) - \hat{H}(t_2)\hat{H}(t_1) \neq 0.$$

Using the Dyson series, the propagator can be expressed as:

$$\hat{U}(t) = \hat{\mathbb{I}} + \sum_{n=1}^{\infty} \hat{U}^{(n)}(t), \tag{1.1}$$

where $\hat{\mathbb{I}}$ is the identity and each term in the sum is defined as:

$$\hat{U}^{(n)}(t) = \left(-\frac{i}{\hbar}\right)^n \int_0^t dt_1 \int_0^{t_1} dt_2 \cdots \int_0^{t_{n-1}} dt_n \hat{H}(t_1)\hat{H}(t_2)\cdots\hat{H}(t_n).$$

Including all the terms in Eq. (1.1) provides a unitary operator. However, we often truncate the series in practice, thus losing unitarity. An alternative approach is the Magnus expansion [4, 5], where the propagator is represented as an infinite series of nested commutators:

$$\hat{U}(t) = \exp\left(\sum_{n=1}^{\infty} \Omega_n(t)\right), \tag{1.2}$$

with the first two terms given by:

$$\Omega_1(t) = -\frac{i}{\hbar}\int_0^t \hat{H}(t_1)dt_1,$$

$$\Omega_2(t) = -\frac{1}{2\hbar^2}\int_0^t dt_1 \int_0^{t_1} [\hat{H}(t_1), \hat{H}(t_2)]dt_2.$$

The advantage of the Magnus expansion is that it maintains the unitarity of the evolution operator at every order, facilitating a clearer understanding of the effects of dynamics. Depending on the structure of the Hamiltonian, the series of nested commutators might terminate at a particular order or continue indefinitely. In the latter case, one can imagine the "soup of interactions" that must be managed. Solving the dynamics with the Magnus expansion provides insights into the effects of spurious terms and informs strategies for managing them [2]. Furthermore, using appropriate control tools, isolating effective interactions within the series described in Eq. (1.2) is possible. A significant part of this thesis investigates this aspect for interactions that couple a spin to a harmonic oscillator. The control tools that we employ are amplitude shaping and phase control techniques, as shown in Fig. 1.1.

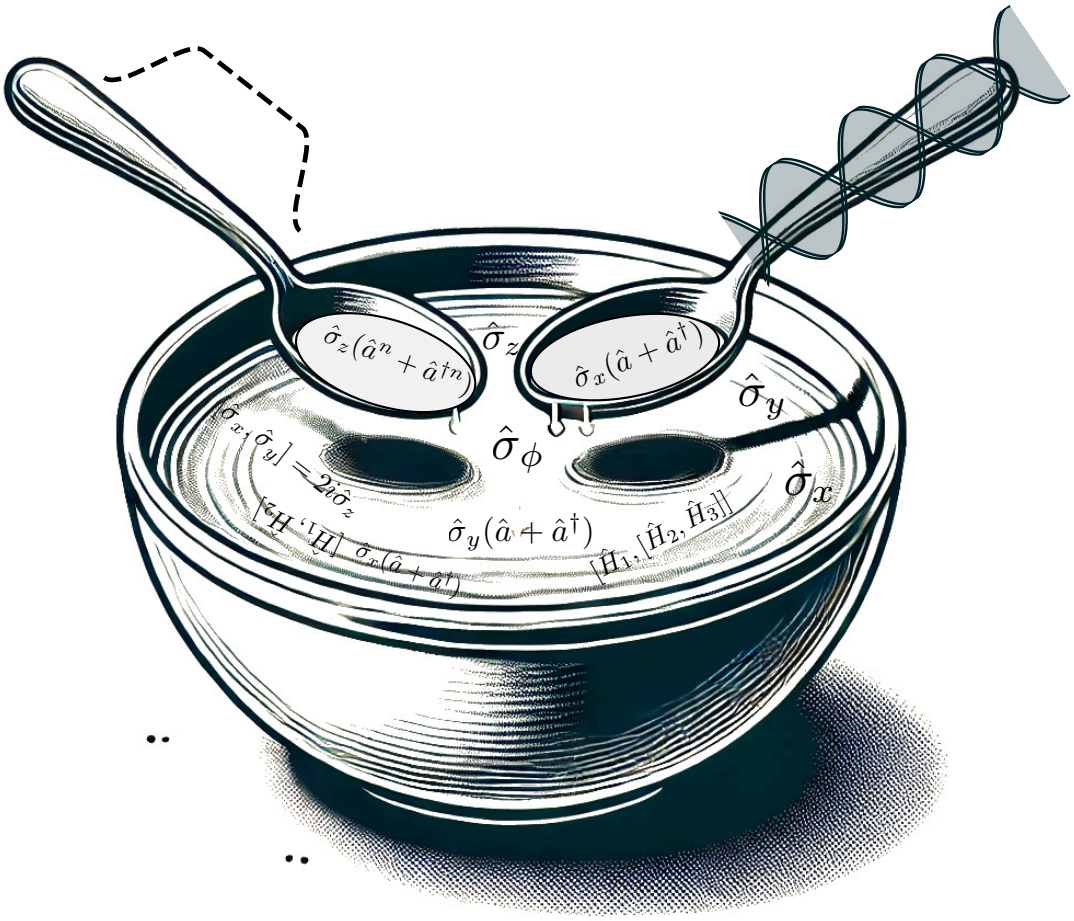

Figure 1.1: Quantum operator soup.

1.2 A spin-oscillator hybrid system

The spin-oscillator hybrid system consists of a two-level system coupled to the infinite-dimensional Hilbert space of a quantum harmonic oscillator. These systems are prevalent across various platforms, including trapped ions [6], atoms [7], superconducting qubits [8], and diamond colour centres [9]. Typically, the main quantum object in which the information is encoded is coupled to an auxiliary component that mediates the otherwise weak interactions between the primary quantum objects. Additionally, hybrid systems provide natural mappings for simulating certain quantum systems, such as quantum field theories [10, 11] or quantum chemistry problems [12–16]. Furthermore, they can potentially enable more resource-efficient error correction [17]. The ability to generate interactions that couple the spin to the oscillator is essential for exploiting the full potential of these systems.

In this thesis, the coupling between spin and oscillator plays a pivotal role in exploring both boson-mediated spin-spin interactions and spin-mediated nonlinear bosonic couplings, where bosons are understood as excitations of the quantum harmonic oscillator. We use a trapped ion as our hybrid system, where the spin corresponds to two internal electronic levels of the ion, and the oscillator is the motion of the ion in an external trapping potential.

1.3 Boson-mediated spin-spin interactions

In trapped ions, direct spin-spin interactions are intrinsically weak due to the Coulomb repulsion, which gives rise to significant spatial separation between the ions. Typically, we rely on the shared motion of the ions to implement indirect spin-spin interactions by temporarily entangling the spin state with the motion [18, 19], which effectively couples the spins. Such boson-mediated spin-spin interactions are extensively used in quantum information processing with trapped ions. For example, we can use them to create spin-spin entangled states [20], such as $|\psi\rangle = \frac{1}{\sqrt{2}}(|\downarrow\downarrow\rangle + |\uparrow\uparrow\rangle)$, where $|\downarrow\rangle$ and $|\uparrow\rangle$ represent the two spin states. Entangled states

have been used to verify fundamental aspects of quantum theory [21] and enhance the sensitivity of metrology experiments [22]. Furthermore, spin-spin interactions can be used to implement two-qubit quantum logic gates, which are essential for quantum computing. When integrated with single-qubit rotations, these gates are essential for building a universal quantum computer [23, 24]—a device designed to execute arbitrary unitary operations across a register of quantum bits.

The ultimate goal of such technology is to achieve fault tolerance [25], enabling it to perform calculations with extremely low error rates. Attaining this level of precision involves overcoming several challenges, including the execution of high-fidelity quantum operations. Boson-mediated spin-spin entanglement has facilitated the achievement of two-qubit gates with record-high fidelities [26–29] when compared to other quantum computing platforms [30].

In this thesis, we explore the challenges of speeding up two-qubit entangling gates in the presence of spurious, non-commuting terms. Speeding up the operations of the entangling gate helps reduce incoherent errors such as motional decoherence and heating, which impact the gate during the transitory coupling of the spin state to the motion [31]. Additionally, faster two-qubit gates facilitate increased circuit depths. However, as the duration of these gates decreases, coherent errors, such as the presence of terms that do not commute with the primary spin-coupling interaction, become more prevalent [32]. This thesis investigates methods of lifting the non-commutativity using phase control techniques, specifically by coherently cancelling spurious terms using two counter-propagating waves (that form a standing wave).

1.4 Harnessing non-commutativity to generate spin-mediated nonlinear bosonic interactions

However, the presence of non-commuting terms can also be used to one's advantage. In Sec. 1.1, we mention how terms in the infinite Magnus expansion can be isolated to drive the desired interaction while using the proper set of tools. In this thesis, we investigate how combining two linear spin-motion couplings with non-commuting spin conditioning gives rise to such an infinite expansion. The emergent terms from

this series manifest as nonlinear bosonic interactions in the motion of a trapped ion, effectively mediated by the spin. Furthermore, the linear spin-motion couplings that we refer to are the very same ones used for implementing the two-qubit gates. Including trapped ions and beyond, the capability to introduce n-th order nonlinear interactions in the quantum harmonic oscillator leads to complex behaviour. For instance, squeezed states generated by second-order bosonic processes reduce uncertainty in one observable while increasing it in its conjugate [33]. This attribute is particularly valuable in applications that require enhanced sensitivity, such as gravitational wave detectors [34], microscopy [35], and electric field measurements [36]. Additionally, higher-order interactions give rise to non-Gaussian states, which are marked by fundamental quantum mechanical properties like Wigner negativity [37–39], underscoring their nonclassical nature.

In the quantum information processing realm, using quantum harmonic oscillators to encode quantum information has garnered significant attention [40]. This interest largely stems from the substantial challenges associated with managing the resource overhead required for fault-tolerant quantum computing. As a potential solution, more efficient use of resources can be achieved by encoding information in larger Hilbert spaces. The paradigm discussed in Section 1.3 employs discrete variables. However, one strategy for enhancing physical resource efficiency involves continuing to use discrete variables but in systems possessing more than two energy levels, known as qudits [41, 42]. Alternatively, employing oscillators with unbounded Hilbert spaces [43, 44] represents another viable approach, falling under the umbrella of continuous-variable quantum computing [45, 46].

Building universal quantum computing with continuous variables necessitates not only Gaussian operations, such as displacement and squeezing, but also at least a non-Gaussian operation, such as third-order bosonic interactions [45–47]. Table 1.1 details the Hamiltonians describing these essential interactions.

Furthermore, unlike for Gaussian operations [48], higher-order interactions introduce computational challenges for classical simulation [49]. These interactions are valuable for real-time quantum simulation of many-body models [50–52] or molecular

gate	Unitary operation	Gaussian?
displacement	$\exp(\alpha\hat{a}^\dagger - \alpha^*\hat{a})$	yes
squeezing	$\exp(z^*\hat{a}^2 - z(\hat{a}^\dagger)^2)$	yes
beamsplitter	$\exp(\theta(e^{i\phi}\hat{a}^\dagger\hat{b} - e^{-i\phi}\hat{a}^\dagger\hat{b})$	yes
Cubic phase gate	$\exp(ic(\hat{a}^\dagger + \hat{a})^3)$	no

Table 1.1: List of some common Gaussian and non-Gaussian operations with $\hat{a}(\hat{b})$ and $\hat{a}^\dagger(\hat{b}^\dagger)$, the annihilation and creation operators, respectively and $\alpha, z, \theta, \phi, c$ constants.

quantum effects [14], with potential advantages over classical hardware in the noisy intermediate-scale quantum (NISQ) era.

Experimental realisations of nonlinear interactions faster than decoherence mechanisms are challenging, especially as interaction strength diminishes with increasing order. Generating such interactions typically requires specific hardware designs, such as tailored ion trap geometries [53] or superconducting microwave circuits [54, 55]. For example, while second-order interactions such as squeezing [56–58] and beamsplitter [59–61] have been demonstrated in various systems, third-order interactions such as trisqueezing have only recently been shown in superconducting microwave circuits [62, 63], and higher-order interactions remain an outstanding challenge. With our method, which relies on the spin mediating the bosonic interaction, we achieve better scaling, enabling quadsqueezing interactions at rates over 100 times faster than those achieved with conventional methods [57] using equivalent parameters. To our knowledge, this is the first demonstration of fourth-order generalised squeezing across any platform.

1.5 Thesis Outline

The structure of this thesis is as follows:

Chapter 2 provides an overview of the theoretical aspects of atom-light interactions in trapped ions relevant to this thesis. It discusses the implications of having non-commuting spin terms (e.g., $\hat{\sigma}_x$, $\hat{\sigma}_y$) in the Hamiltonian, which lead to an infinite series of interactions that can be resonantly driven. This chapter also explores how the interaction dynamics change when the light field is a standing wave.

Chapter 3 offers a brief overview of the experimental apparatus and phase stabilisation techniques employed to tailor quantum dynamics in our system.
Chapter 4 presents an experimental characterisation of the spin-oscillator system used in this work, along with the spin-dependent forces that serve as our linear spin-motion couplings for realising spin-spin entanglement and nonlinear bosonic interactions.
Chapter 5 details experimental results on how a phase-stabilised standing wave can be utilised to implement a universal gate set in the realm of discrete variables, aiming to overcome the effects of spurious non-commuting terms to enable faster entangling gates.
Chapter 6 presents experimental results on using phase stabilisation and amplitude pulse shaping techniques to utilise non-commuting terms for creating the desired effective nonlinear interactions in the motion of the ions.
Chapter 7 discusses potential future experiments leveraging the interactions investigated in this thesis and outlines technical upgrades.
The research presented in this thesis was conducted in close collaboration with Sebastian Saner, particularly the findings in *Chapter 5* and portions of *Chapter 4*, which are published in Ref. [64] and Ref. [1], respectively. Sebastian Saner's thesis, to be published later, will elaborate further on the topics discussed here.

2 Theory

Contents

In this chapter, we introduce the spin-oscillator system, Fig. 2.1, provided by a trapped ion. The ion's internal states constitute the spin states, and its motion represents the oscillator. We discuss how we couple the spin states to the motional oscillator using laser fields, which serves as the foundation of the work presented in this thesis. Moreover, we describe how the interactions between the laser field and the ion change when we use a travelling wave field versus a standing wave field.

2.1 A spin-motional oscillator system

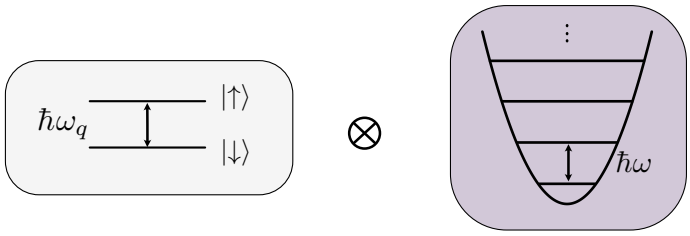

Figure 2.1: Spin-oscillator system.

Spin

When we encode quantum information using the internal electronic states of the ion, very often, we think of a two-level system, which we might also refer to as a spin or a qubit. This two-level system has an energy splitting of $\hbar\omega_q$, with energy eigenstates(eigenvalues) $|\downarrow\rangle$ $(-\hbar\omega_q/2)$ and $|\uparrow\rangle$ $(+\hbar\omega_q/2)$. The system is equivalent to a spin-1/2 in a static magnetic field, defining the quantisation axis. We can describe its free evolution using the Hamiltonian

$$\hat{H}_q = \frac{\hbar\omega_q}{2}\hat{\sigma}_z, \tag{2.1}$$

where $\hat{\sigma}_z$ is a Pauli operator with eigenstates $|\downarrow\rangle, |\uparrow\rangle$ [65].

Quantum harmonic oscillator

To a very good approximation, each mode of vibration of a trapped ion can be described as a quantum harmonic oscillator (QHO) with position operator $\hat{x}_r$ and momentum operator $\hat{p}_r$ using Hamiltonian:

$$\hat{H}_{\text{osc}} = \frac{\hat{p}_r^2}{2M} + \frac{1}{2}M\omega^2\hat{x}_r^2, \tag{2.2}$$

where ω is the angular frequency of the QHO, and M is the mass of a trapped ion[1] [31]. We express Eq. (2.2) in terms of the creation $\hat{a}^\dagger$ and annihilation $\hat{a}$ operators by first defining the dimensionless position $\hat{x}$ and momentum operators $\hat{p}$ [67]:

$$\hat{x} \equiv \sqrt{\frac{M\omega}{\hbar}}\hat{x}_r = \frac{1}{\sqrt{2}}(\hat{a}^\dagger + \hat{a}) \qquad \hat{p} \equiv \sqrt{\frac{1}{M\omega\hbar}}\hat{p}_r = \frac{i}{\sqrt{2}}(\hat{a}^\dagger - \hat{a}) \tag{2.3}$$

[1] In Ref. [66], it is discussed in detail how Eq. (2.2) is modified to account for multiple modes of vibration and multiple ions.

which results in:

$$\hat{H}_{\text{osc}} = \hbar\omega\hat{a}^\dagger\hat{a} = \hbar\omega\hat{n}, \tag{2.4}$$

where $\hat{n}$ is the number operator and we omitted the constant term $\hbar\omega/2$ representing the vacuum fluctuation energy.

Fock state ladder

The eigenstates of $\hat{n}$ are also the eigenstates of $\hat{H}_{\text{osc}}$ and are called Fock states $|n\rangle$, where $n \in \mathbb{N}_0$, hence the Hilbert space provided by the quantum harmonic oscillator is infinite. Moving up and down the ladder of states is done via:

$$\hat{a}^\dagger |n\rangle = \sqrt{n+1}\,|n+1\rangle \qquad \hat{a}\,|n\rangle = \sqrt{n}\,|n-1\rangle \qquad \hat{a}\,|0\rangle = 0. \tag{2.5}$$

Wigner function representation

Due to the commutation relationship $[\hat{x}, \hat{p}] = i$, we cannot define a genuine phase space distribution, as is possible in classical mechanics, to describe the state of the quantum harmonic oscillator. However, we can instead use a Wigner function $W(x, p)$, which depends on the eigenstates of $\hat{x}$ and $\hat{p}$, x and p, respectively [68–70]:

$$W(x,p) = \frac{1}{2\pi\hbar}\int_{-\infty}^{\infty} \langle x + \frac{1}{2}\zeta|\,\hat{\rho}\,|x - \frac{1}{2}\zeta\rangle\, e^{ip\zeta/\hbar} d\zeta, \tag{2.6}$$

where $|x \pm \frac{1}{2}\zeta\rangle$ are position eigenstates. The Wigner function provides a full description of the quantum state represented by the density operator $\hat{\rho}$. Some properties of $W(x, p)$ include that it is real-valued, and by integrating it over the variable p or the variable x, we can compute the probability distribution of position or momentum, respectively (marginals). However, unlike a probability distribution, $W(x, p)$ can take negative values and is thus referred to as a quasiprobability distribution. Wigner negative values can be observed, for example, in the case of Fock states, some of which are plotted in Fig. 2.2, with the Wigner function given by [65]:

$$W_n(\gamma) = \frac{2}{\pi}(-1)^n \mathcal{L}_n(4|\gamma|^2) e^{-2|\gamma|^2}, \tag{2.7}$$

where $\mathcal{L}_n$ is the Laguerre polynomial of degree n, and $\gamma = x/\sqrt{2} + ip/\sqrt{2}$.

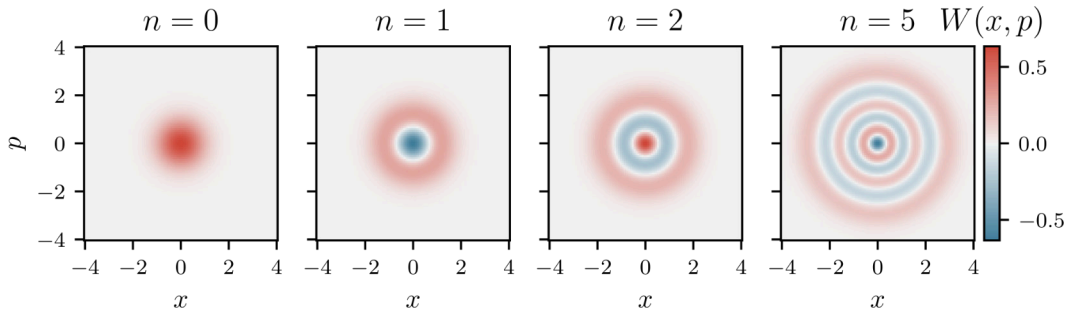

Figure 2.2: Wigner functions $W(x, p)$ of a few Fock states; x, p are the position and momentum variables associated with the dimensionless position and momentum operators $\hat{x}, \hat{p}$, respectively (see Eq. (2.3)).

A useful definition of the Wigner function, that we extensively use in Chapter 6 [71], is that it is given by the Fourier transform of the characteristic function $\chi(\beta)$

$$W(\gamma) = \frac{1}{\pi^2} \int \chi(\beta) e^{\gamma\beta^* - \gamma^*\beta} d^2\beta, \tag{2.8}$$

where $\chi(\beta) = \langle \psi_{\text{osc}} | \hat{\mathcal{D}}(\beta) | \psi_{\text{osc}} \rangle$ is the expectation value of the displacement operator $\hat{\mathcal{D}}(\alpha) = e^{\alpha\hat{a}^\dagger - \alpha^*\hat{a}}$. The effect of the displacement operator is discussed in detail in Sec. 2.3. The characteristic function also provides full information about the oscillator state and is complex-valued [72].

In an ion trap system, there are $3N$ motional modes in total, where N is the number of ions. This thesis focuses on coherent control involving the motional mode along the trap axis (z) with angular frequency ω_z. For most interactions studied, it is a fair assumption that the other motional modes are far off resonant. By combining the spin and the quantum harmonic oscillator, the Hamiltonian of the system is expressed as

$$\hat{H}_0 = \hat{H}_q + \hat{H}_{\text{osc}} = \frac{\hbar\omega_q}{2}\hat{\sigma}_z + \hbar\omega_z \hat{a}^\dagger \hat{a}.$$

2.2 Coherent laser-ion interactions

A motional mode and the internal state can be coupled via a travelling wave[2] electromagnetic field. The Hamiltonian describing the interaction is given as [31]:

$$\hat{H}_{\mathrm{TW}} = \frac{\hbar\Omega}{2}\hat{\sigma}_{+}e^{i\eta(\hat{a}+\hat{a}^{\dagger})}e^{i(-\delta t+\phi_l)} + \mathrm{h.c.}, \quad (\delta \equiv \omega - \omega_q), \tag{2.9}$$

where we have adopted the interaction picture with respect to the internal state Hamiltonian $\hat{H}_q$ and applied the rotating wave approximation as the terms oscillating at $2\omega_q$ are fast, and their effect averages out over the experiment timescales considered in this thesis. The phase ϕ_l is the phase of the laser at the position of the ion, $\hat{\sigma}_+$ is the raising operator, Ω is the Rabi frequency, and η is the Lamb-Dicke parameter, defined in the next to sections.

2.2.1 Rabi frequency

The Rabi frequency Ω hides the specifics of the interaction between the electromagnetic field and the ion's charge distribution. In the experiments presented in this work, we mainly drive an electric quadrupole (EQ) transition or a magnetic dipole (MD) transition for coherent operations. For the quadrupole transition, the Rabi frequency is defined as [66, 73]

$$\Omega_{\mathrm{EQ}} = \sum_{i,j} \langle\uparrow| Q_{i,j} |\downarrow\rangle \left(\frac{\partial E_j}{\partial x_i}\right)_{\mathbf{r_n}} = \langle\uparrow| (e\mathbf{r_e}\cdot\hat{\mathbf{e}})(\mathbf{k_l}\cdot\mathbf{r_e}) |\downarrow\rangle E(\mathbf{r_n})/2\hbar, \tag{2.10}$$

where E the amplitude of the laser field, with polarisation $\hat{\mathbf{e}}$ and wave vector $\mathbf{k_l}$, evaluated at the position of the nucleus $\mathbf{r_n}$, e is the fundamental charge unit and $\mathbf{r_e}$ is the position of the single valence electron relative to the nucleus of the ion. We see that the induced electric-quadrupolar moment with tensor elements Q_{ij} couples to the gradient of the electric field E evaluated at the position of the nucleus $\mathbf{r_n}$. The Rabi frequency for a magnetic dipole transition is defined as [74]

$$\Omega_{\mathrm{MD}} = -\langle\uparrow| \mu\cdot\hat{\mathbf{b}} |\downarrow\rangle B(\mathbf{r_e})/\hbar, \tag{2.11}$$

[2] We will return to this in Sec. 2.4 and Chapter 5.

where μ the magnetic dipole moment interacts directly with the magnetic field with amplitude B and polarisation $\hat{\mathbf{b}}$.

Given that we will draw a comparison between electric quadrupole and electric dipole transitions in Sec. 2.4, we also introduce the Rabi frequency for an electric dipole transition [74]

$$\Omega_{\mathrm{ED}} = \frac{\langle\uparrow| e\mathbf{r_e}\cdot\hat{\mathbf{e}}\,|\downarrow\rangle\, E(\mathbf{r_e})}{\hbar}, \tag{2.12}$$

which interacts directly with the electric field.

2.2.2 Lamb-Dicke parameter

The Lamb-Dicke parameter is defined as $\eta = |\mathbf{k_l}|z_0\cos(\theta)$, where $\mathbf{k_l}$ is the wave vector of the laser beam, θ is the angle between the direction of oscillation of the ion and $\mathbf{k_l}$, and $z_0 = \sqrt{\hbar/2M\omega_z}$ the extension of the oscillator's ground state wavefunction, with M the mass of the ion. In our experiment, we work with $^{88}Sr^{+}$ ions, a laser beam with $\lambda_l = 674\,\mathrm{nm}$, $\theta \approx 45$ deg and $\omega_z/2\pi = 1.17\,\mathrm{MHz}$, which yields $z_0 \approx 7\,\mathrm{nm}$ and $\eta \approx 0.05$. The Lamb-Dicke parameter is a measure of the impact of a single photon emission or absorption on the motion of the ion. If $\eta \neq 0$, we are able to couple the spin to the motion of the ion.

Going back to Eq. (2.9), in the resolved-sideband limit, $\Omega \ll \omega_z$, we can drive coherent transitions between specific energy levels of the oscillator $|\downarrow\rangle|n\rangle \leftrightarrow |\uparrow\rangle|n'\rangle$ by tuning $\delta = (n'-n)\omega_z + \Delta$ and ensuring that $\Delta \ll \omega_z$ so that the influence of other motional states can be neglected, to first-order approximation. The coupling strength of such an interaction is given analytically as:

$$\begin{aligned} \Omega_{n,n'} &= |\langle n'|\, e^{i\eta(\hat{a}+\hat{a}^\dagger)}\,|n\rangle\,|\Omega \\ |\langle n'|\, e^{i\eta(\hat{a}+\hat{a}^\dagger)}\,|n\rangle\,| &= e^{-\eta^2/2}\sqrt{\frac{\min(n,n')!}{\max(n,n')!}}\eta^{|n'-n|}L^{|n'-n|}_{\min(n,n')}(\eta^2) \end{aligned} \tag{2.13}$$

where L^p_n is the generalised Laguerre polynomial [31].

For the majority of the work presented in this thesis, we limit the discussion to working in the Lamb-Dicke regime $\langle\psi_{\mathrm{osc}}|\,\eta^2(\hat{a}+\hat{a}^\dagger)\,|\psi_{\mathrm{osc}}\rangle^{1/2} \ll 1$, which means that the spread of the oscillator wavepacket is small compared to the wavelength of

the driving field. This is a more stringent condition than assuming $\eta \ll 1$ since η only accounts for the ground state, while the Lamb-Dicke regime also considers the oscillator's energy occupation. Working in the Lamb-Dicke regime allows us to neglect the higher orders in η when expanding the exponential in Eq. (2.9):

$$\hat{H}_{\mathrm{TW}} = \frac{\hbar\Omega}{2}\hat{\sigma}_+(1 + i\eta(\hat{a} + \hat{a}^\dagger) + \mathcal{O}(\eta^2))e^{i(-\delta t+\phi_l)} + \mathrm{h.c.}, \tag{2.14}$$

which means that we can drive the following three interactions:

- carrier $n' = n, \delta = \Delta$

$$\hat{H}_{\mathrm{c}} = \frac{\hbar\Omega_{n,n}}{2}(\hat{\sigma}_+ e^{-i(\Delta t-\phi_l)} + \hat{\sigma}_- e^{i(\Delta t-\phi_l)}) \tag{2.15}$$

- first red sideband $n' = n - 1, \delta = -\omega_z + \Delta$

$$\hat{H}_{\mathrm{rsb}} = \frac{i\hbar\Omega_{n,n-1}}{2}(\hat{\sigma}_+ \hat{a} e^{-i(\Delta t-\phi_l)} - \hat{\sigma}_- \hat{a}^\dagger e^{i(\Delta t-\phi_l)}) \tag{2.16}$$

- first blue sideband $n' = n + 1, \delta = \omega_z + \Delta$

$$\hat{H}_{\mathrm{bsb}} = \frac{i\hbar\Omega_{n,n+1}}{2}(\hat{\sigma}_+ \hat{a}^\dagger e^{-i(\Delta t-\phi_l)} - \hat{\sigma}_- \hat{a} e^{i(\Delta t-\phi_l)}), \tag{2.17}$$

with

$$\Omega_{n,n} = \Omega \qquad \Omega_{n,n-1} = \Omega\eta\sqrt{n} \qquad \Omega_{n,n+1} = \Omega\eta\sqrt{n+1}. \tag{2.18}$$

Eq. (2.15), (2.16) and (2.17) were obtained by going into the interaction picture with respect to $\hat{H}_{\mathrm{osc}}$ and neglecting the terms oscillating at $2\omega_z$ under the RWA. The first-order red sideband Hamiltonian is also called the Jaynes-Cummings Hamiltonian, and the first-order blue sideband Hamiltonian is the anti-Jaynes-Cummings Hamiltonian.

2.2.3 Rotations

The propagator describing the coherent transitions between $|\downarrow\rangle|n\rangle \leftrightarrow |\uparrow\rangle|n'\rangle$ is given by [31]:

$$\hat{U}(t) = \begin{pmatrix} e^{\frac{-i\Delta t}{2}}\left[\cos\left(\frac{W_{n,n't}}{2}\right) + \frac{i\Delta}{W_{n,n'}}\sin\left(\frac{W_{n,n't}}{2}\right)\right] & -i\frac{\Omega_{n,n'}}{W_{n,n'}}e^{i(\frac{\Delta}{2}t-\phi_l-\frac{\pi}{2}|n'-n|)}\sin\left(\frac{W_{n,n't}}{2}\right) \\ -i\frac{\Omega_{n,n'}}{W_{n,n'}}e^{-i(\frac{\Delta}{2}t-\phi_l-\frac{\pi}{2}|n'-n|)}\sin\left(\frac{W_{n,n't}}{2}\right) & e^{\frac{-i\Delta t}{2}}\left[\cos\left(\frac{W_{n,n't}}{2}\right) - \frac{i\Delta}{W_{n,n'}}\sin\left(\frac{W_{n,n't}}{2}\right)\right] \end{pmatrix}, \tag{2.19}$$

where $W_{n,n'} = \sqrt{\Omega_{n,n'}^2 + \Delta^2}$ is the effective Rabi frequency. The propagator gives rise to Rabi oscillations that get faster with the increase in Δ but also prevent the complete, coherent population transfer between the two levels. We are often interested in the case in which the transition is driven on resonance, i.e., $\Delta = 0$. Eq. (2.19) simplifies to

$$\begin{aligned}\hat{U}(t) = \hat{R}(\theta', \phi') &= \begin{pmatrix} \cos(\theta'/2) & -ie^{i\phi'}\sin(\theta'/2) \\ -ie^{-i\phi'}\sin(\theta'/2) & \cos(\theta'/2) \end{pmatrix} \\ &= \cos(\theta'/2)\hat{\mathbb{I}}_2 - i\sin(\theta'/2)(\hat{\sigma}_x\cos\phi' + \hat{\sigma}_y\sin\phi')\end{aligned} \tag{2.20}$$

with $\theta' = \Omega_{n,n'}t$, $\phi' = \phi_l$, $\hat{\sigma}_{x,y}$ Pauli operators and $\hat{\mathbb{I}}_2$ identity. In this case, the population can be fully transferred between the two states, allowing us to implement arbitrary rotations on the Bloch sphere [74]. Some common rotations are a $\pi/2$-pulse or π-pulse, which can be achieved by setting θ' to $\pi/2$ and π, respectively. By adjusting the laser phase ϕ', we can decide the axis of rotation.

2.2.4 ac Stark shift or light shift

Looking at Eq. (2.20), we can easily see how we can implement rotations about axes in the equatorial plane of the Bloch sphere ($\hat{\sigma}_x\cos\phi' + \hat{\sigma}_y\sin\phi'$). Implementing rotations about $\hat{\sigma}_z$ axis can be done by using a composite pulse comprising $\hat{R}(\theta', \phi')$ rotations [75] or by driving the two-level system with a far off-resonant beam, i.e., if $\Delta \gg \Omega$. Then, Eq. (2.19) becomes:

$$\hat{U}(t) = \begin{pmatrix} e^{\frac{iW_{n,n'}t}{2}} & 0 \\ 0 & e^{-\frac{iW_{n,n'}t}{2}} \end{pmatrix}, \tag{2.21}$$

where we dropped the global phase term. This results in no Rabi oscillations as the probability of population transfer between the two levels goes to zero. The corresponding Hamiltonian for this propagator is then:

$$\hat{H}_{\mathrm{LS}} = -\frac{\hbar W_{n,n'}}{2}\hat{\sigma}_z \approx -\left(\frac{\hbar\Delta}{2} + \frac{\hbar\Omega^2}{4\Delta}\right)\hat{\sigma}_z \tag{2.22}$$

where the states are shifted from their unperturbed eigenenergies ($\pm\hbar\Delta/2$) by the light shift or ac Stark shift $\pm\Omega^2/4\Delta$.

In defining our two-level system, we must not forget about the rest of the (not so silent) spectator electronic energy levels. An electric field resonant with our qubit will also off-resonantly couple to other transitions. Hence, the ac Stark shift of one level will be a cumulative effect of many transitions.

Inducing a controlled ac Stark shift can be a useful experimental technique; examples include lifting degeneracies to spectrally isolate the desired qubit [1, 76, 77] or directly introducing a $\hat{\sigma}_z$ interaction for analogue quantum simulations [78]. However, in this work, light shifts give rise to errors as they do not commute with the primary interaction in most cases. More on how we address its effects will be discussed in Sec. 4.2.2.

2.2.5 Motional state analysis

We can use the Rabi frequency dependence on the phonon number to obtain information about the ion's motional state. If the spin-oscillator system is prepared in $|\downarrow\rangle|\psi_{\text{osc}}\rangle$, we can apply the blue sideband interaction[3] (Eq. (2.17)) for variable durations t. If we then measure the probability of finding the spin state in $|\downarrow\rangle$, $p_{|\downarrow\rangle}$, we find, using Eq. (2.20), that

$$p_{|\downarrow\rangle}(t) = \sum_{n=0}^{\infty} p_{|n\rangle} \cos^2\left(\frac{\sqrt{n+1}\eta\Omega t}{2}\right), \tag{2.23}$$

where $p_{|n\rangle} = |\langle n|\psi_{\text{osc}}\rangle|^2$ the probability of finding the harmonic oscillator in Fock state $|n\rangle$ before applying the blue sideband interaction.

We can modify Eq. (2.23) to include imperfections due to decoherence effects by including decay phenomenological constants γ_n [36, 57, 79]:

$$p_{|\downarrow\rangle}(t) = \frac{1}{2}\left(1 + \sum_{n=0}^{\infty} p_{|n\rangle} e^{-\gamma_n t} \cos\left(\sqrt{n+1}\eta\Omega t\right)\right), \tag{2.24}$$

where we also used trigonometric identities to simplify the equation. By fitting Eq. (2.24) to measured spin populations, we can extract the Fock state occupation probabilities, $p_{|n\rangle}$. However, using this method, it is impossible to obtain a complete description of the oscillator state, as it does not provide any information about the coherences of the state.

[3] If it is prepared in $|\uparrow\rangle|\psi_{\text{osc}}\rangle$, we apply the red sideband interaction, instead.

2.3 Spin-dependent forces

Another common method of coupling the spin to the motional state of the ion is by using spin-dependent forces (SDFs). These still classify as coherent laser-ion interactions; however, as they serve as the main workhorse in this work, they deserve their own section. In trapped ions, spin-dependent forces are the primary means of generating high-fidelity spin-spin entanglement, mediated by the motion of the ions [19, 80, 81] (see Sec. 5.3.1). This method effectively overcomes the intrinsically weak direct spin-spin interactions[4].

2.3.1 Dynamics

The interaction of a spin coupled to a motional mode, with frequency ω_z, via a spin-dependent force with driving frequency ω_d and phase ϕ, and no spatial dependence is described by the Hamiltonian [83]:

$$\begin{aligned}
\hat{H}_{\mathrm{SDF}} &= -\hat{\sigma}_\alpha \hat{z} F(t) \\
&= -z_0 F_0 \hat{\sigma}_\alpha (\hat{a} e^{-i\omega_z t} + \hat{a}^\dagger e^{i\omega_z t}) \cos(\omega_d t - \phi) \qquad (2.25) \\
&= -\frac{z_0 F_0}{2} \hat{\sigma}_\alpha [\hat{a}(e^{i[(\omega_d-\omega_z)t-\phi]} + e^{-i[(\omega_d+\omega_z)t-\phi]}) + \hat{a}^\dagger (e^{i[(\omega_d+\omega_z)t-\phi]} + e^{-i[(\omega_d-\omega_z)t-\phi]})] \\
&\approx -\frac{z_0 F_0}{2} \hat{\sigma}_\alpha (\hat{a} e^{i(\Delta t-\phi)} + \hat{a}^\dagger e^{-i(\Delta t-\phi)}), \qquad (2.26)
\end{aligned}$$

where $\hat{\sigma}_\alpha$ is a Hermitian operator and a linear combination of the Pauli operators $\hat{\sigma}_{x,y,z}$, $\hat{z}$ the position operator of the QHO, z_0 the extension of the QHO's ground state wavefunction and F_0 the amplitude of the driving force. Hamiltonian in Eq. (2.25) is in the interaction picture with respect to the bare Hamiltonian $\hat{H}_0$. To transition from Eq. (2.25) to Eq. (2.26), we defined $\Delta \equiv \omega_d - \omega_z$ the detuning of the driving force away from the motional mode frequency. We also dropped the counter-rotating terms oscillating at $\omega_z + \omega_d$ (RWA).

We want to compute the time evolution operator to understand the effect of applying the SDF. The Hamiltonian in Eq. (2.26) often serves as an example of applying the

[4] This is a consequence of the Coulomb repulsion, which leads to a considerable spatial separation between the ions [82].

Magnus expansion (see Sec. 1.1) to compute the propagator, as the Hamiltonian does not commute with itself at different times [4, 5].

Magnus expansion
Using Magnus expansion, the propagator is represented by an infinite series of nested commutators

$$\hat{U}(t) = \mathcal{T}\left(e^{\frac{-i}{\hbar}\int_0^t \hat{H}(t')dt'}\right) = \exp\left(\sum_{n=1}^{\infty}\Omega_n(t)\right) \tag{2.27}$$

$$\simeq \exp\Big(-\frac{i}{\hbar}\int_0^t dt_1\hat{H}_1 \tag{2.28}$$

$$-\frac{1}{2\hbar^2}\int_0^t\int_0^{t_1} dt_1dt_2[\hat{H}_1,\hat{H}_2] \tag{2.29}$$

$$+\frac{i}{6\hbar^3}\int_0^t\int_0^{t_1}\int_0^{t_2} dt_1dt_2dt_3\left(\left[\hat{H}_1,\left[\hat{H}_2,\hat{H}_3\right]\right]+\left[\left[\hat{H}_1,\hat{H}_2\right],\hat{H}_3\right]\right) \tag{2.30}$$

$$+\frac{1}{12\hbar^4}\int_0^t\int_0^{t_1}\int_0^{t_2}\int_0^{t_3} dt_1dt_2dt_3dt_4$$
$$\Big(\left[\left[\left[\hat{H}_1,\hat{H}_2\right],\hat{H}_3\right],\hat{H}_4\right]+\left[\hat{H}_1,\left[\left[\hat{H}_2,\hat{H}_3\right],\hat{H}_4\right]\right]$$
$$+\left[\hat{H}_1,\left[\hat{H}_2,\left[\hat{H}_3,\hat{H}_4\right]\right]\right]+\left[\hat{H}_2,\left[\hat{H}_3,\left[\hat{H}_4,\hat{H}_1\right]\right]\right]\Big)\Big), \tag{2.31}$$

where $\mathcal{T}$ denotes the time-ordering operator and $\hat{H}_k \equiv \hat{H}(t_k)$ is the Hamiltonian describing the system at time t_k. We truncate the expression at the fourth order.

To evaluate the second-order term in the expansion (Eq. (2.29)), we compute:

$$[\hat{H}_{\mathrm{SDF}}(t_1),\hat{H}_{\mathrm{SDF}}(t_2)] = i\frac{(z_0F_0)^2}{2}\hat{\sigma}_\alpha^2\sin\left(\Delta(t_1-t_2)\right) \tag{2.32}$$

and to evaluate the third-order term (Eq. (2.30)),

$$\begin{aligned}[[\hat{H}_{\mathrm{SDF}}(t_1),\hat{H}_{\mathrm{SDF}}(t_2)],\hat{H}_{\mathrm{SDF}}(t_3)] = 0,\\ [\hat{H}_{\mathrm{SDF}}(t_1),[\hat{H}_{\mathrm{SDF}}(t_2),\hat{H}_{\mathrm{SDF}}(t_3)]] = 0.\end{aligned} \tag{2.33}$$

As the nested commutators for the third-order term vanish, all the following terms in the Magnus expansion will vanish as well. The propagator is then given by

$$\begin{aligned}\hat{U}_{\mathrm{SDF}}(t) &= \exp\left(i\frac{z_0F_0}{\hbar}\frac{1}{\Delta}\hat{\sigma}_\alpha\sin\left(\frac{\Delta\, t}{2}\right)[\hat{a}e^{i(\Delta\, t/2-\phi)}+\hat{a}^\dagger e^{-i(\Delta\, t/2-\phi)}]\right)\\ &\times\exp\left(-i\left(\frac{z_0F_0}{\hbar}\right)^2\frac{1}{4\Delta^2}\hat{\sigma}_\alpha^2[\Delta\, t-\sin\left(\Delta\, t\right)]\right)\\ &= \hat{\mathcal{D}}(\alpha(t)\hat{\sigma}_\alpha)e^{-i\Phi(t)\hat{\sigma}_\alpha^2},\end{aligned} \tag{2.34}$$

where $\hat{\mathcal{D}}(\cdot)$[5] is the displacement operator, defined as $\hat{\mathcal{D}}(\alpha) = e^{\alpha\hat{a}^\dagger - \alpha^*\hat{a}}$ and with the complex displacement variable

$$\alpha(t) = i\frac{z_0 F_0}{\hbar}\frac{1}{\Delta}\sin\left(\frac{\Delta t}{2}\right)e^{-i(\Delta t/2-\phi)}. \tag{2.35}$$

Assuming that the eigenstates and eigenvalues of $\hat{\sigma}_\alpha$ are $|\lambda_\alpha\rangle$ and λ_α respectively, we can expand the last line in Eq. (2.34) as:

$$\hat{U}_{\mathrm{SDF}}(t) = \sum_{\lambda_\alpha}\hat{\mathcal{D}}(\alpha(t)\lambda_\alpha)e^{-i\Phi(t)\lambda_\alpha^2}\left|\lambda_\alpha\right\rangle\left\langle\lambda_\alpha\right|. \tag{2.36}$$

The effect of the SDF is that it displaces the oscillator wavepacket in phase space based on the eigenstates of the spin basis $\hat{\sigma}_\alpha$. Also, each of the eigenstates gains a geometric phase $\Phi(t)\lambda_\alpha^2$, where

$$\Phi(t) = \left(\frac{z_0 F_0}{\hbar}\right)^2\frac{1}{4\Delta^2}[\Delta t - \sin(\Delta t)] \tag{2.37}$$

and $\lambda_\alpha^2 = 1$.

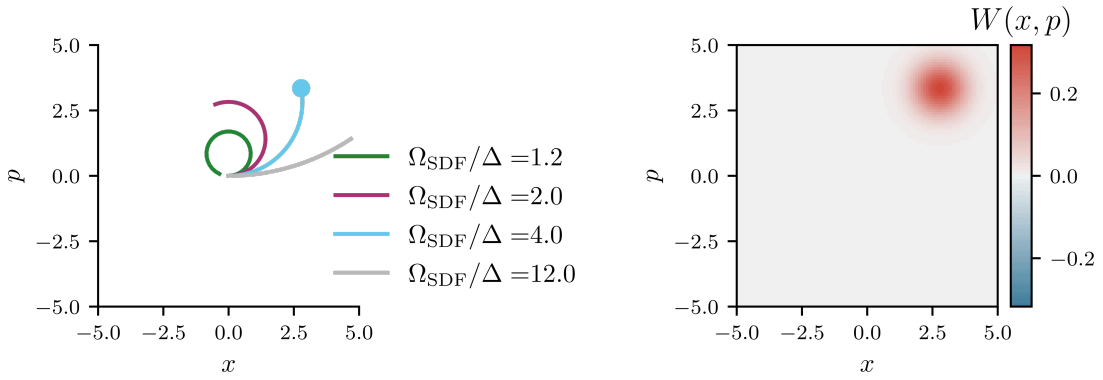

Figure 2.3: Phase space trajectories of the quantum harmonic oscillator state under the effect of an off-resonant SDF, where the initial spin state is an eigenstate of the SDF spin basis. The representations are in the interaction frame rotating at ω_z. The strength of the SDF is kept constant $\Omega_{\mathrm{SDF}} = z_0 F_0/\hbar$, and the duration for which the SDF is applied is scanned such that $\Omega_{\mathrm{SDF}} t/2\pi = [0., 1.2]$ and we consider various values for $\Omega_{\mathrm{SDF}}/\Delta$. On the right-hand side, we show the Wigner function $W(x, p)$ of the oscillator (after we trace over the spin component) at an instant in time for parameters corresponding to the circle indicated in the plot on the left; x, p are the position and momentum variables associated with the dimensionless position and momentum operators $\hat{x}, \hat{p}$, respectively (see Eq. (2.3)).

[5]The α in $\hat{\sigma}_\alpha$ and $\alpha(t)$ do not have anything in common.

In experiments, we usually apply the SDF interaction and then read out the spin state to evaluate its effect. Irrespective of the spin-conditioning $\hat{\sigma}_\alpha$ of the SDF, the resulting spin dynamics is broadly the same [84]. Hence, without loss of generality, we evaluate an SDF conditioned on $\hat{\sigma}_\alpha = \hat{\sigma}_x$, with eigenstates $|\pm\rangle$. In the forthcoming chapters, SDFs conditioned on $\hat{\sigma}_x$ are used extensively for measuring the strength of the SDF (Chapters 4 and 5) and creating and probing motional states (Chapter 6). If the spin-oscillator system is initialised in $|+\rangle|0\rangle$ and we apply an SDF conditioned on $\hat{\sigma}_x$, then the state of the system at time t is given as:

$$|\psi(t)\rangle = e^{-i\Phi(t)}|+\rangle|\alpha(t)\rangle, \tag{2.38}$$

where $|\alpha\rangle = \hat{\mathcal{D}}(\alpha)|0\rangle$ is a coherent state. The effect of the SDF is that the oscillator state is displaced in circles/loops in phase space, with a diameter dependent on $\Omega_{\mathrm{SDF}}/\Delta$, where $\Omega_{\mathrm{SDF}} = z_0 F_0/\hbar$, see Fig. 2.3. In doing so, the state also accumulates a geometric phase $\Phi(t)$, which depends on the area enclosed by the motional path. The loops close, i.e., the oscillator state returns to its origin $\alpha(t) = 0$, for integer multiples of $2\pi/\Delta$.

If, instead, we initialise the system in state $|\downarrow\rangle|0\rangle$, where $|\downarrow\rangle = (|+\rangle - |-\rangle)/\sqrt{2}$, applying the SDF gives rise to:

$$|\psi(t)\rangle = \frac{1}{\sqrt{2}}(e^{-i\Phi(t)}|+\rangle|\alpha(t)\rangle - e^{-i\Phi(t)}|-\rangle|-\alpha(t)\rangle), \tag{2.39}$$

which is a superposition of spatially separated oscillator wave packets and entangled with the spin state, often referred to as a Schrödinger-cat state [6, 85, 86]. The two wave packets are displaced in phase space in circular trajectories with the same characteristics mentioned before; see Fig. 2.4. We observe that in both cases, Eq. (2.38) and (2.39), the geometric phase is just a global phase.

If we make a measurement of the spin state (Eq. (2.39)), the probability of finding the system in $|\downarrow\rangle$ is given by:

$$p_{|\downarrow\rangle} = \frac{1}{4}\Big(2 + 2\langle\alpha| - \alpha\rangle\Big) = \frac{1}{2}\Big(1 + e^{-2|\alpha(t)|^2}\Big), \tag{2.40}$$

where we used $\langle\alpha|\beta\rangle = \exp(\alpha^*\beta - |\alpha|^2/2 - |\beta|^2/2)$. This means that by measuring $p_{|\downarrow\rangle}$, we can infer the overlap between the two displaced motional states $\langle\alpha| - \alpha\rangle$.

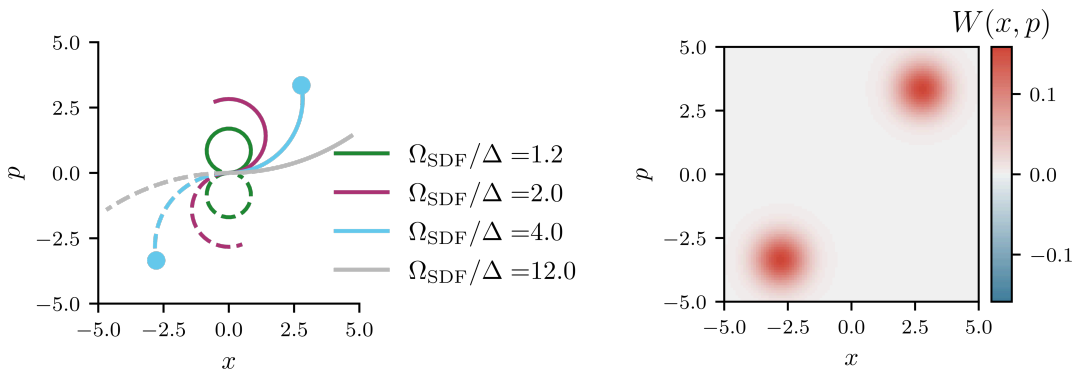

Figure 2.4: Phase space trajectories of the quantum harmonic oscillator state under the effect of an off-resonant SDF, where the initial spin state is not an eigenstate of the SDF spin basis. More specifically, we consider the case of an equal superposition of eigenstates. The representations are in the interaction frame rotating at ω_z. The strength of the SDF is kept constant Ω_{SDF}, and the duration for which the SDF is applied is scanned such that $\Omega_{\mathrm{SDF}}t/2\pi = [0., 1.2]$ and we consider various values for $\Omega_{\mathrm{SDF}}/\Delta$, where $\Omega_{\mathrm{SDF}} = z_0 F_0/\hbar$. On the right-hand side, we show the Wigner function $W(x,p)$ of the oscillator state (after we trace over the spin component) at an instant in time for parameters corresponding to the circle indicated in the plot on the left; x, p are the position and momentum variables associated with the dimensionless position and momentum operators $\hat{x}, \hat{p}$, respectively (see Eq. (2.3))

More often than not, in the experiment, we are not able to initialise in Fock state $|0\rangle$, but rather in a thermal state [65] with average phonon state occupation of $\bar{n}_{\mathrm{osc}}$ close to 0, then Eq. (2.40) is modified to

$$p_{|\downarrow\rangle} = \frac{1}{2}\left(1 + e^{-|2\alpha(t)|^2(\bar{n}_{\mathrm{osc}}+\frac{1}{2})}\right). \tag{2.41}$$

2.3.2 SDF via a bichromatic field driving

A common way to implement SDFs in trapped ions is by using a Mølmer-Sørensen (MS) scheme [80, 87]. This involves applying a bichromatic field composed of two tones symmetrically detuned from the qubit frequency ω_q by $\pm\delta$. The blue-detuned tone ($\delta_b = \delta$) has a coupling strength Ω_b, while the red-detuned tone ($\delta_r = -\delta$) has a coupling strength Ω_r. Using Eq. (2.9), the Hamiltonian describing the bichromatic field interaction is given by:

$$\hat{H}_{\mathrm{bi}} = \sum_{i=b,r} \frac{\hbar\Omega_i}{2}\hat{\sigma}_+ e^{i\eta(\hat{a}+\hat{a}^\dagger)} e^{i(-\delta_i t+\phi_i)} + \mathrm{h.c.}, \tag{2.42}$$

where ϕ_b and ϕ_r are the phases of the blue and red detuned tones at the position of the ion, respectively. Using that $\eta \ll 1$, we Taylor expand the exponential

$$\hat{H}_{\mathrm{bi}} = \sum_{i=b,r} \frac{\hbar\Omega_i}{2}\hat{\sigma}_+(1 + i\eta(\hat{a} + \hat{a}^\dagger) + \mathcal{O}(\eta^2))e^{i(-\delta_i t+\phi_i)} + \mathrm{h.c.}. \tag{2.43}$$

Assuming that $\Omega_b = \Omega_r = \Omega$ and neglecting the higher order terms $\mathcal{O}(\eta^2)$ under the Lamb-Dicke regime[6], after some regrouping[7] and moving into the interaction picture with respect to the oscillator Hamiltonian $\hat{H}_{\mathrm{osc}}$, the expression can be simplified to:

$$\hat{H}_{\mathrm{bi}} = -\hbar\Omega\eta\hat{\sigma}_{\phi_s}\cos(\delta t - \phi_d)(\hat{a}e^{-i\omega_z t} + \hat{a}^\dagger e^{i\omega_z t}) + \hbar\Omega\hat{\sigma}_{\phi_s-\pi/2}\cos(\delta t - \phi_d), \tag{2.44}$$

where $\phi_s = \pi/2 - (\phi_b + \phi_r)/2$ is the phase associated with the spin, $\phi_d = (\phi_b - \phi_r)/2$ is the difference phase associated with the motion and $\hat{\sigma}_\phi = \cos(\phi)\hat{\sigma}_x + \sin(\phi)\hat{\sigma}_y$. The first term is the sought-after spin-dependent force with $\Omega_{\mathrm{SDF}} = z_0 F_0/\hbar = \eta\Omega$ in Eq. (2.25). The second term drives spin flips off-resonantly but does not couple to the motional mode; hence, it is referred to as the carrier term. The carrier term is commonly disregarded, which is a reasonable assumption in the $\Omega \ll \delta$ regime. However, as Ω increases by, e.g., increasing the amplitude of the driving fields, it becomes necessary to consider its effects more closely. Crucially, the spin-dependent force and the carrier term do not commute. Therefore, spin-echo techniques cannot be utilised [88, 89]. Amplitude pulse shaping is frequently employed instead [90]. While amplitude shaping would reduce any off-resonant excitation of the carrier transition by reducing the extent of the pulse in frequency space, the effects on the non-commuting term are slightly more subtle and will be discussed in the following section.

Thus far, the exact value of δ, which is the amount of detuning away from the qubit frequency ω_q of the two tones, has intentionally been omitted. This choice becomes obvious in the following subsection, where we explore the effect of the non-commuting carrier on the spin-dependent force in detail. The section is based on the article published in Ref. [1].

[6] This corresponds to assuming that the force $F(t)$ in Eq. (2.25) has no spatial dependence.
[7] We used $\hat{\sigma}_+ = \hat{\sigma}_x + i\hat{\sigma}_y$ and $\hat{\sigma}_- = \hat{\sigma}_x - i\hat{\sigma}_y$.

2.3.3 SDFs in $\hat{\sigma}_\phi$ and $\hat{\sigma}_z$ basis

We can gain a better understanding of the interplay between the carrier and the spin-dependent force by moving into the bichromatic interaction picture, i.e., the interaction picture with respect to the carrier term $\hbar\Omega\hat{\sigma}_{\phi_s-\pi/2}\cos(\delta t-\phi_d)$. To do this, we make use of the formalism developed in Refs. [90, 91] and obtain

$$\begin{aligned}\hat{H}_I = & -\hbar\eta\Omega\cos\left(\delta t-\phi_d\right)(\hat{a}e^{-i\omega_z t}+\hat{a}^\dagger e^{i\omega_z t})\times \\ & \Big[\hat{\sigma}_\phi\Big(J_0(2\Omega/\delta)+2\sum_{n=1}^{\infty}J_{2n}(2\Omega/\delta)\cos\left(2n(\delta t-\phi_d)\right)\Big) \\ & -2\hat{\sigma}_z\sum_{n=1}^{\infty}J_{2n-1}(2\Omega/\delta)\sin\left((2n-1)(\delta t-\phi_d)\right)\Big],\end{aligned} \tag{2.45}$$

where we use $[\hat{\sigma}_{\phi-\pi/2},\hat{\sigma}_\phi]=i2\hat{\sigma}_z$ and J_n are the Bessel functions of the first kind. This is the main result from Ref. [91]. The derivation steps for reaching this result are nicely presented in Ref. [92]. In contrast to Ref. [91], where laser-free interactions are considered, here both the carrier and the spin-dependent force term oscillate at the same frequency δ as they originate from the same source, the laser (see Eq. (2.44)). Hence, Eq. (2.45) can be simplified by distributing the $\cos(\delta t-\phi_d)$ to the terms inside the parentheses and rearranging

$$\begin{aligned}\hat{H}_I = & -\hbar\eta\Omega(\hat{a}e^{-i\omega_z t}+\hat{a}^\dagger e^{i\omega_z t})\times \\ & \Big[\hat{\sigma}_\phi\sum_{n=0}^{\infty}\Big(J_{2n}(2\Omega/\delta)+J_{2n+2}(2\Omega/\delta)\Big)\cos\left((2n+1)(\delta t-\phi_d)\right) \\ & -\hat{\sigma}_z\sum_{n=1}^{\infty}\Big(J_{2n-1}(2\Omega/\delta)+J_{2n+1}(2\Omega/\delta)\Big)\sin\left(2n(\delta t-\phi_d)\right)\Big].\end{aligned} \tag{2.46}$$

Equation (2.46) reveals an infinite series of resonances that can be selectively driven by the choice of δ. When $\delta\approx\omega_z/(2n+1)$ we drive SDFs conditioned on $\hat{\sigma}_\phi$ basis, while $\delta\approx\omega_z/(2n)$ corresponds to SDFs conditioned on $\hat{\sigma}_z$.

For $\delta\approx\omega_z$, which corresponds to the conventional Mølmer-Sørensen scheme [80, 87, 93], the near-resonant term is:

$$\begin{aligned}\hat{H}_\phi = & -\hbar\eta\Omega[J_0(2\Omega/\delta)+J_2(2\Omega/\delta)]\times \\ & \cos\left(\delta t-\phi_d\right)\hat{\sigma}_\phi(\hat{a}e^{-i\omega_z t}+\hat{a}^\dagger e^{i\omega_z t}),\end{aligned} \tag{2.47}$$

where we notice that the coupling strength is modulated by J_0+J_2 and the spin-dependent force is in the $\hat{\sigma}_\phi$ basis. To visualise the effect of this modulation better,

in Fig. 2.5, we plot $|J_0(2\Omega/\delta) + J_2(2\Omega/\delta)|$ and $\Omega_{\mathrm{SDF}} = \eta\Omega|J_0(2\Omega/\delta) + J_2(2\Omega/\delta)|$ by setting $\delta/2\pi = \omega_z/2\pi \approx 1.17\,\mathrm{MHz}$ and varying Ω.

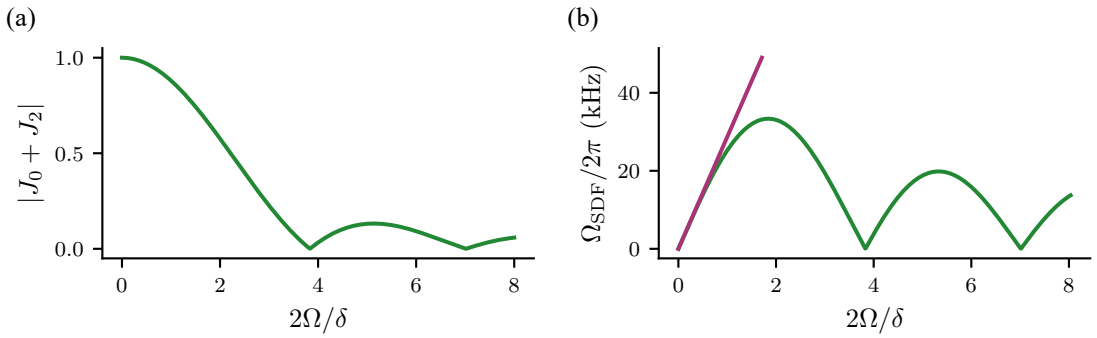

Figure 2.5: Effect of the non-commuting carrier on the magnitude of the spin-dependent force for $\delta = \omega_z$. (a) The magnitude is modulated by the sum of the Bessel functions of the first kind $|J_0(2\Omega/\delta) + J_2(2\Omega/\delta)|$. (b) Spin-dependent force magnitude versus $2\Omega/\delta$ if the non-commuting carrier term is included in the dynamics (green) and if it is excluded (magenta).

In Fig. 2.5(b), we also plot the strength without the modulation, i.e., $\Omega_{\mathrm{SDF}} = \eta\Omega$. For $\Omega \ll \delta$, the two strengths nearly coincide, as $|J_0 + J_2| \approx 1$. Therefore, as mentioned earlier, disregarding the effect of the carrier term is a reasonable assumption. As Ω increases, we encounter the first peak in the modulated coupling strength, representing a global maximum and thus limiting the achievable SDF strength. By choosing $\delta \approx \omega_z/2$ [90, 94, 95], the near-resonant term

$$\begin{aligned}\hat{H}_z =& \hbar\eta\Omega(J_1(2\Omega/\delta) + J_3(2\Omega/\delta))\times \\ & \sin\left(2(\delta t - \phi_d)\right)\hat{\sigma}_z(\hat{a}e^{-i\omega_z t} + \hat{a}^\dagger e^{i\omega_z t}),\end{aligned} \tag{2.48}$$

drives a $\hat{\sigma}_z$ interaction with a coupling strength modulated by $J_1 + J_3$. The effective coupling strength is then $\Omega_{\mathrm{SDF}} = \eta\Omega(J_1(2\Omega/\delta) + J_3(2\Omega/\delta))$. In Fig. 2.6, we plot $|J_1 + J_3|$ and Ω_{SDF} for fixed $\delta/2\pi = \omega_z/2/2\pi \approx 1.17/2$ MHz and by varying Ω. This interaction occurs because the spin bases of the two terms in Eq. (2.44) do not commute, $[\hat{\sigma}_{\phi-\pi/2}, \hat{\sigma}_\phi] \neq 0$. In this case, the carrier term is not a bug but a feature of our interaction[8]. We can observe that for small values of Ω, where the off-resonant carrier term is negligible, the strength of the effective $\hat{\sigma}_z$ interaction is

[8]Sebastian or Raghu came up with 'not a bug, but a feature' on a late Friday wintery evening in the lab

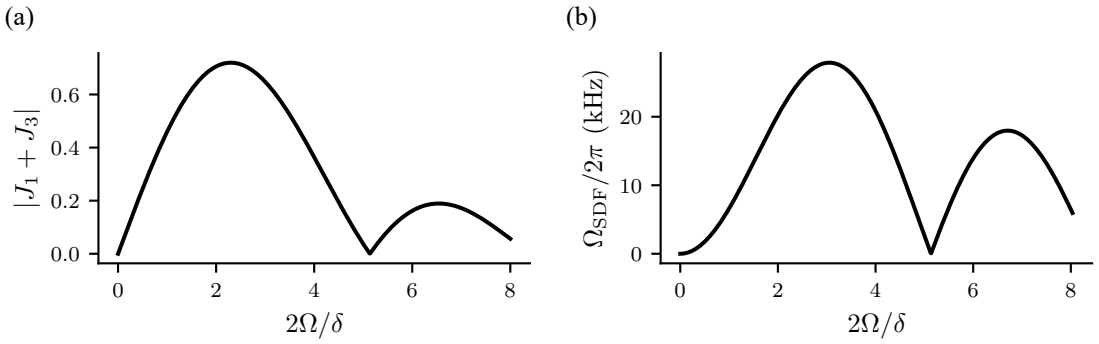

Figure 2.6: Effect of the non-commuting carrier on the magnitude of the spin-dependent force for $\delta = \omega_z/2$. (a) The magnitude is modulated by the sum of the Bessel functions of the first kind $|J_1(2\Omega/\delta) + J_3(2\Omega/\delta)|$. (b) Spin-dependent force magnitude versus $2\Omega/\delta$.

close to zero. However, it increases with the rise in Ω. As in the case of the $\hat{\sigma}_\phi$ SDF, the coupling strength of the effective $\hat{\sigma}_z$ SDF also saturates with the increase in Ω.

2.3.4 Amplitude pulse shaping

We have expressed the Hamiltonian in the bichromatic interaction picture, which reveals the governing dynamics in an easily interpretable manner and provides greater insight into the effect of the carrier term. This interpretation is only possible if the two tones in the laser bichromatic field are adiabatically switched on and off. This allows us to move smoothly in and out of the bichromatic interaction picture, such that the dynamics in the interaction picture with respect to the qubit and the motion are identical to the dynamics in the bichromatic interaction picture. In this section, we aim to clarify the concept of 'adiabatic' within this context, i.e., over which duration t_{ramp} we need to slowly switch on and off the laser fields slowly.
Going back to the Hamiltonian in the interaction picture with respect to the qubit and the motion, see Eq. (2.44), the Hamiltonian in the bichromatic interaction picture is calculated as

$$\hat{H}_I(t) = \hat{U}_c^\dagger(t)\hat{H}_m(t)\hat{U}_c(t), \tag{2.49}$$

where

$$\hat{U}_c(t) = \exp\Big(-\frac{i}{\hbar}\int_0^t dt' \hat{H}_c(t') \Big) \tag{2.50}$$

is the propagator of $\hat{H}_c(t) = \hbar\Omega\hat{\sigma}_{\phi_s-\pi/2}\cos(\delta t - \phi_d)$ which commutes with itself at all times. If the Hamiltonian in the interaction picture with respect to the qubit and the motion acts on state $|\psi(t)\rangle$, then, in the bichromatic interaction picture, we introduce the state

$$|\psi_I(t)\rangle = \hat{U}_c^\dagger |\psi(t)\rangle . \tag{2.51}$$

The time evolution of $|\psi_I(t)\rangle$ is governed by

$$i\hbar\dot{|\psi_I(t)\rangle} = \hat{H}_I(t)\,|\psi_I(t)\rangle , \tag{2.52}$$

which can be solved to obtain the propagator $\hat{T}_I$ such that

$$|\psi_I(t)\rangle = \hat{T}_I(t)\,|\psi_I(0)\rangle . \tag{2.53}$$

Using Eq. (2.51) and (2.53), the final state in the interaction picture with respect to the ion and the motion is given as

$$|\psi(t_f)\rangle = \hat{U}_c\,|\psi_I(t_f)\rangle = \hat{U}_c(t_f)\hat{T}_I(t_f)\,|\psi_I(0)\rangle = \hat{U}_c(t_f)\hat{T}_I(t_f)\hat{U}_c^\dagger(0)\,|\psi_I(0)\rangle . \tag{2.54}$$

If $\hat{U}_c(t_f) \to \hat{\mathbb{I}}$ and given that $\hat{U}_c^\dagger(0) = \hat{\mathbb{I}}$, then

$$|\psi(t_f)\rangle = \hat{T}_I(t_f)\,|\psi_I(0)\rangle , \tag{2.55}$$

which means that the propagators in the two interaction pictures are equal. We can achieve $\hat{U}_c(t_f) \to \hat{\mathbb{I}}$ by switching on and off slowly our laser pulses over a duration t_{ramp}. Introducing the time dependence $\hat{H}_c(t) = \hbar\Omega g(t)\hat{\sigma}_{\phi_s-\pi/2}\cos(\delta t - \phi_d)$ and imposing the boundary conditions on $g(t)$

$$\begin{aligned} g(0) = g(t_f) = 0, \\ g(t_{\text{ramp}} \le t \le t_f - t_{\text{ramp}}) = 1, \end{aligned} \tag{2.56}$$

which means that the laser tones are off at the start and end of the interaction, and between the ramps, they have constant amplitude. We evaluate $\hat{U}_c(t_f)$

$$\begin{aligned} \hat{U}_c(t_f) &= \exp\Big(-i\int_0^{t_f} dt\Omega g(t)\cos(\delta t - \phi_d)\hat{\sigma}_{\phi_s-\pi/2}\Big) \\ &= \exp\Big(\frac{i\Omega}{\delta}\Big(\int_0^{t_{\text{ramp}}} dt\dot{g(t)}\sin(\delta t - \phi_d) \\ &+ \int_{t_f-t_{\text{ramp}}}^{t_f} dt\dot{g(t)}\sin(\delta t - \phi_d)\Big)\hat{\sigma}_{\phi_s-\pi/2}\Big), \end{aligned} \tag{2.57}$$

where we integrated by parts and made use of the boundary conditions on $g(t)$. If $\dot{g(t)}$ changes slowly compared to $\sin(\delta t)$, then the longer t_{ramp} is relative to $2\pi/\delta$, the smaller the integral values become. Therefore, if $2\pi/\delta \ll t_{\text{ramp}}$, $\hat{U}_c(t_f) \to \hat{\mathbb{I}}$ holds true. This effect is independent of the specific shape of the pulse envelope as long as it varies slowly.

In the experiments, we amplitude shape our pulses in the following way

$$g(t) = \begin{cases} \sin^2(\frac{\pi t}{2t_{\text{ramp}}}), \ t < t_{\text{ramp}} \\ 1, \ t_{\text{ramp}} \leq t \leq t_f - t_{\text{ramp}} \\ \sin^2(\frac{\pi(t_f - t)}{2t_{\text{ramp}}}), \ t_f - t_{\text{ramp}} < t < t_f. \end{cases} \tag{2.58}$$

We integrate $\hat{H}_c(t)$ with the amplitude shaping included and investigate the conditions on t_{ramp} to ensure that $\hat{U}_c(t_f) \to \hat{\mathbb{I}}$, as shown in Fig. 2.7. The spin state is initialised in $|\downarrow\rangle$, and we measure the probability of remaining in this state, $p_{|\downarrow\rangle}$. The Hamiltonian induces oscillations in $p_{|\downarrow\rangle}$ with periodicity determined by δ (Fig. 2.7(a)) and constant amplitude determined by the ratio Ω/δ and t_{ramp} (Fig. 2.7(b)).

For the two plots in Fig. 2.7(a), we used the same parameters, $\Omega/\delta = 0.5$ and $t_{\text{ramp}} = 2\pi/\delta$, resulting in the same oscillation amplitude for both cases. The interaction duration t_{int} is defined as the full width at half-maximum of the pulse. In Fig. 2.7(b), we plot the amplitude of the oscillations for different values of Ω/δ and t_{ramp}. The ramp durations are expressed as multiples of $2\pi/\delta$. We observe that as the ramp duration increases, the oscillation amplitude is strongly suppressed, indicating that $\hat{U}_c(t_f) \to \hat{\mathbb{I}}$.

2.4 Standing-wave-ion interactions

2.4.1 Dealing with non-commuting terms

In Sec. 2.3.3, we examined the effects of the non-commuting off-resonant carrier term alongside a spin-dependent force. We demonstrated that the presence of this term enables the creation of forces conditioned both on the $\hat{\sigma}_\phi$ basis and the $\hat{\sigma}_z$ basis. The latter results from the commutator of the carrier term with the spin conditioning of the SDF, i.e., $[\hat{\sigma}_{\phi-\pi/2}, \hat{\sigma}_\phi] = 2i\hat{\sigma}_z$. However, we also observed that

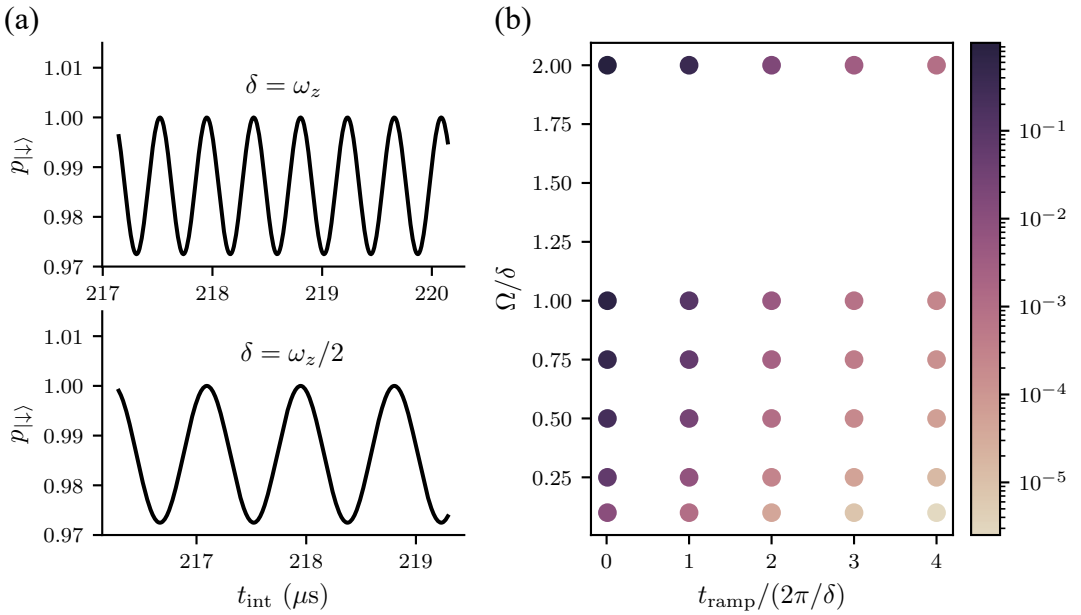

Figure 2.7: Understanding $\hat{U}_c(t_f) \to \hat{\mathbb{I}}$ as a function of t_{ramp}. (a) Plot of the oscillations induced by the carrier term for $\delta = \omega_z$ and $\delta = \omega_z/2$ and with $\Omega/\delta = 0.5$ and $t_{\text{ramp}} = 2\pi/\delta$ for both cases. (b) Plot of the amplitude of these oscillations for different values of Ω/δ and t_{ramp}.

the strength of this effective interaction saturates as the Rabi frequency, Ω, increases. Given that SDFs are integral to generating other interactions, notably spin-spin entanglement in trapped ions (see Sec. 5.3.1), the saturation of SDF magnitude effectively imposes a speed limit on these quantum operations.

To address the issue of the carrier non-commuting term, it is helpful to understand its origins. Utilising a travelling wave (TW) allows us to drive both carrier and spin-motional transitions simultaneously, although not both resonantly (see Sec. 2.2.2). Moreover, the relative coupling strength between these interactions is fixed; for example, the ratio between the strength of the first sideband and the carrier is given by η, the Lamb-Dicke parameter. The type of interaction we can drive depends on how the electric field interacts with the free electron. In the context of a quadrupole transition, which is utilised in this work, the carrier coupling is proportional to the spatial gradient of the electric field (Eq. (2.10)), while the coupling to motion depends on the spatial derivative of the carrier coupling along the motional direction [96]. Considering an electric field in one dimension, this

means that the carrier coupling is maximised where the spatial gradient is highest, coinciding with points where the amplitude of the electric field is zero. Consequently, driving sideband transitions is not possible at these points. Conversely, the coupling to the sideband is maximised at the peak amplitude of the electric field, where the coupling to the carrier goes to zero[9]. Thus, controlling the phase of the field at the ion's position enables us to select which interaction to drive and, hence, allows us to eliminate the non-commuting carrier term. This can be achieved by using a standing wave (SW) instead of a travelling wave. The following sections explore how the light-ion interactions, discussed previously, change when interacting with a standing wave.

2.4.2 Monochromatic standing-wave

Starting from Eq. (2.9), to understand the interaction with a standing wave, we want to combine two counterpropagating travelling waves with the following characteristics. For the first travelling wave, the phase of the laser at the position of the ion is ϕ_1 (i.e., $\phi_l = \phi_1$ in Eq. (2.9)), the Rabi frequency $\Omega_1 = \Omega$ and the Lamb-Dicke parameter $\eta_1 = \mathbf{k_l}\hat{\mathbf{z}} = \eta$. For the second travelling wave, counterpropagating with respect to the first one, the laser phase is ϕ_2, Rabi frequency $\Omega_2 \propto \partial E_{2,j}/\partial x_i = -\partial E_{1,j}/\partial x_j \propto -\Omega$ and Lamb-Dicke parameter $\eta_2 = \mathbf{k_2}\hat{\mathbf{z}} = -\mathbf{k_l}\hat{\mathbf{z}} = -\eta$. The SW-ion interaction is then given as

$$\begin{aligned}\hat{H}_{\mathrm{SW}} &= \hat{H}^1_{\mathrm{TW}} + \hat{H}^2_{\mathrm{TW}} \\ &= \frac{\hbar\Omega}{2}\hat{\sigma}_+ e^{i\eta(\hat{a}+\hat{a}^\dagger)} e^{i(-\delta t+\phi_1)} - \frac{\hbar\Omega}{2}\hat{\sigma}_+ e^{-i\eta(\hat{a}+\hat{a}^\dagger)} e^{i(-\delta t+\phi_2)} + \mathrm{h.c.} \\ &= i\hbar\Omega\, e^{i\left(\frac{\phi_1+\phi_2}{2}-\delta t\right)} \sin\left(\eta(\hat{a}+\hat{a}^\dagger) + \frac{\phi_1-\phi_2}{2}\right)\hat{\sigma}_+ + \mathrm{h.c.}\end{aligned} \tag{2.59}$$

Using $\sin(x+y) = \cos(x)\sin(y) + \sin(x)\cos(y)$, we write the equation as

$$\begin{aligned}\hat{H}_{\mathrm{SW}} = {} & e^{-i\delta t}\hbar\Omega\, e^{i\tilde{\phi}}\hat{\sigma}_+ \sin\left(\eta(\hat{a}+\hat{a}^\dagger)\right)\cos\left(\frac{\phi_1-\phi_2}{2}\right) \\ & + e^{-i\delta t}\hbar\Omega\, e^{i\tilde{\phi}}\hat{\sigma}_+ \cos\left(\eta(\hat{a}+\hat{a}^\dagger)\right)\sin\left(\frac{\phi_1-\phi_2}{2}\right) \\ & + \mathrm{h.c.},\end{aligned} \tag{2.60}$$

[9]This is in contrast to a dipole transition, where the carrier coupling is maximised when the amplitude of the electric field is at its peak (Eq. (2.12)) and the coupling to the motion is strongest at the point of maximum spatial gradient.

where we absorb the factor of i in the mean phase $\tilde{\phi} = (\phi_1 + \phi_2 + \pi)/2$. Using the Lamb-Dicke expansion with $\eta \ll \pi$, we obtain

$$\begin{aligned}\hat{H}_{\mathrm{SW}} = & e^{-i\delta t}\hbar\Omega\ e^{i\tilde{\phi}}\hat{\sigma}_+ \sin\left(\frac{\phi_1-\phi_2}{2}\right) \\ & + e^{-i\delta t}\hbar\eta\Omega\ e^{i\tilde{\phi}}\hat{\sigma}_+(\hat{a}+\hat{a}^\dagger)\cos\left(\frac{\phi_1-\phi_2}{2}\right) \\ & + \sin\left(\frac{\phi_1-\phi_2}{2}\right)\mathcal{O}\left(\eta^{2j}\right) + \cos\left(\frac{\phi_1-\phi_2}{2}\right)\mathcal{O}\left(\eta^{2j+1}\right) + \mathrm{h.c.},\end{aligned} \tag{2.61}$$

where $\mathcal{O}(\eta^{2j})$ and $\mathcal{O}(\eta^{2j+1})$ represent higher-order terms in the Lamb-Dicke expansion, with j being a positive integer ($j \geq 1$). As discussed for the travelling wave in Sec. 2.2.2, by setting $\delta = 0$ or $\delta = \pm\omega_z$, we can bring the carrier (first term in Eq. (2.61)) or the first-order sidebands (second term in Eq. (2.61)) into resonance, respectively. Higher orders in the Lamb-Dicke expansion can be resonantly driven by setting $\delta = \pm j\omega_z$ for even orders and $\delta = \pm(2j+1)\omega_z$ for odd orders. However, compared to the TW, the SW offers an additional degree of control through $\phi_1 - \phi_2$: by setting $\phi_1 - \phi_2 = 0$ (ion at the anti-node of the SW), we can drive the first order sidebands[10], while suppressing all even orders in the Lamb-Dicke expansion, including the carrier term. Conversely, setting $\phi_1 - \phi_2 = \pi$ (ion at the node of the SW) enables us to drive the carrier coupling[11] while suppressing all odd terms, including the first sidebands.

Now that we have identified how the strength of SW-ion interactions depends on the ion's position within the SW, we can apply any dynamics from Sec. 2.2 to the SW context. For instance, to drive carrier Rabi flops, we set $\delta = 0$ in Eq. (2.61) and use Eq. (2.20) to analyse a spin state initialised in $|\downarrow\rangle$. The probability of finding the state still in $|\downarrow\rangle$ after interacting with the SW for a duration t is given by:

$$p_{|\downarrow\rangle} = \cos^2\left(\frac{\Omega_{\mathrm{eff}}t}{2}\right) = \cos^2\left(\frac{2\Omega t\sin\left(\frac{\phi_1-\phi_2}{2}\right)}{2}\right), \tag{2.62}$$

where Ω is the Rabi frequency of the individual beams forming the SW.

[10] We can also drive the other odd orders in the Lamb-Dicke expansion.
[11] We can also drive the other even orders in the Lamb-Dicke expansion.

2.4.3 SDFs using a bichromatic standing-wave

Understanding the interaction between an ion and a monochromatic SW sets the foundation for exploring how a bichromatic standing wave can be used to eliminate the non-commuting carrier term, which gives rise to the SDF magnitude suppression. To achieve this, we combine a blue-detuned SW with detuning $\delta_b = \delta$ and Rabi frequency $\Omega_b = \Omega$, and a red-detuned SW with $\delta_r = -\delta$ and $\Omega_r = \Omega$

$$\begin{aligned}\hat{H}_{\text{bi-SW}} = \sum_{i=b,r} \Bigg(& e^{-i\delta_i t}\hbar\Omega_i \; e^{i\tilde{\phi}_i}\hat{\sigma}_+ \sin\left(\frac{\phi_{1,i}-\phi_{2,i}}{2}\right) \\ & + e^{-i\delta_i t}\hbar\eta\Omega \; e^{i\tilde{\phi}_i}\hat{\sigma}_+(\hat{a}+\hat{a}^\dagger)\cos\left(\frac{\phi_{1,i}-\phi_{2,i}}{2}\right) + \text{h.c.}\Bigg)\end{aligned} \tag{2.63}$$

where we used Eq. (2.61) and kept only the first two terms in the Lamb-Dicke expansion. This can be simplified further by assuming that the blue and the red-detuned SWs are in phase at the position of the ion, i.e. $\phi_{1,b} - \phi_{2,b} = \phi_{1,r} - \phi_{2,r} = \phi_1 - \phi_2$ to

$$\begin{aligned}\hat{H}_{\text{bi-SW}} = {} & 2\hbar\eta\Omega\hat{\sigma}_{\tilde{\phi}_s}\cos\left(\delta t - \tilde{\phi}_d\right)(\hat{a}e^{-i\omega_z t} + \hat{a}^\dagger e^{i\omega_z t})\cos\left(\frac{\phi_1-\phi_2}{2}\right) \\ & + 2\hbar\Omega\hat{\sigma}_{\tilde{\phi}_s}\cos\left(\delta t - \tilde{\phi}_d\right)\sin\left(\frac{\phi_1-\phi_2}{2}\right),\end{aligned} \tag{2.64}$$

by following the same steps as in the case of the travelling wave in Sec. 2.3.2. The spin phase is defined as $\tilde{\phi}_s = -(\tilde{\phi}_b + \tilde{\phi}_r)/2 = -(\phi_{1,b} + \phi_{2,b} + \phi_{1,r} + \phi_{2,r} + 2\pi)/4$ and the motional phase as $\tilde{\phi}_d = (\tilde{\phi}_b - \tilde{\phi}_r)/2 = (\phi_{1,b} + \phi_{2,b} - (\phi_{1,r} + \phi_{2,r}))/4$. To eliminate the carrier we could simply adjust $\phi_1 - \phi_2$. This may be useful, but a more significant outcome is that the spin-basis of the SDF and the carrier term now commute[12] (whether or not the latter is suppressed). This means that the effects of SDF magnitude saturation are no longer a concern. While dealing with a term that commutes with the main interaction (in this case, the SDF) is simpler, one might question the relevance of tuning the SW phase to cancel the carrier term. However, placing the ion at the maximum electric field amplitude, where the two counterpropagating beams constructively interfere, not only simplifies the system by suppressing the carrier but also allows for more efficient use of laser power, see

[12]To understand the origin of this change, note that in comparison to Eq. (2.43), there is a factor of i missing in front of the term that couples to the motion.

the factor of 2 increase in Eq. (2.64) compared to Eq. (2.44).

Now, let's head to the lab to see how we navigate this complex soup of interactions and phase relationships.

3

Experimental setup and techniques

Contents

This chapter briefly outlines the experimental setup used for the experiments involving the spin-oscillator system presented in the following chapters. The spin-oscillator system in this work consists of a trapped $^{88}Sr^{+}$ ion. An in-depth description of the setup can be found in Refs. [97–99]. I also detail the experimental extensions developed during my D.Phil., together with another D.Phil. student,

Sebastian Saner, which enabled us to perform phase-stable coherent operations with two bichromatic fields.

3.1 Trap and motional harmonic oscillator

The $^{88}Sr^{+}$ ions are trapped in a linear Paul blade trap [100], designed by Sarah Woodrow [101] and built by Keshav Thirumalai [98]. The trap consists of four 'blade'-shaped electrodes, with one pair driven by rf and the other pair grounded, along with two cylindrical endcap electrodes to which DC is applied. This setup is housed in a vacuum system operated at room temperature. Details of the trap characterisation can be found in Ref. [97]. In this setup, the trapping potentials can be well approximated by a three-dimensional harmonic potential. Thus, the motion of a single trapped $^{88}Sr^{+}$ ion can be described by three independent modes of oscillation: the motion along the trap axis with $\omega_z/2\pi = 1.17\,\mathrm{MHz}$, which forms the harmonic oscillator used in this work, and radial modes with $\omega_x/2\pi = 1.55\,\mathrm{MHz}$ and $\omega_y/2\pi = 1.67\,\mathrm{MHz}$.

3.2 Internal states and control laser systems

The experimental setup is designed for quantum information processing using both $^{88}Sr^{+}$ and $^{43}Ca^{+}$ ions. Using mixed species gives access to powerful tools such as sympathetic cooling [102, 103], individually addressing without focusing beams onto single ions, quantum non-demolition measurement [104], and using an ion better suited for a specific task [105]. $^{43}Ca^{+}$ has a nuclear spin $I = 7/2$, which allows for hyperfine atomic clock transitions [106]. Using a clock transition as a qubit is advantageous because these transitions are first-order insensitive to magnetic field fluctuations, a major source of decoherence in trapped ions. The system is operated at $B_0 = 146\,\mathrm{G}$ as such a transition occurs in the $4S_{1/2}$ ground level of $^{43}Ca^{+}$ for this magnetic field value [106]. However, for the experiments presented in this thesis, we use $^{88}Sr^{+}$ ($I = 0$), where the transitions are first-order dependent on the strength of the field, which poses limitations in some cases. The advantages of

ions with $I = 0$ include the simplicity of their electronic structure, which facilitates a more straightforward cooling process.

The relevant electronic levels of $^{88}Sr^+$ and the transitions addressed by lasers or rf fields are shown in Fig. 3.1(a), while Fig. 3.1(b) indicates the beam directions and polarisations with respect to the trap axis and magnetic field direction.

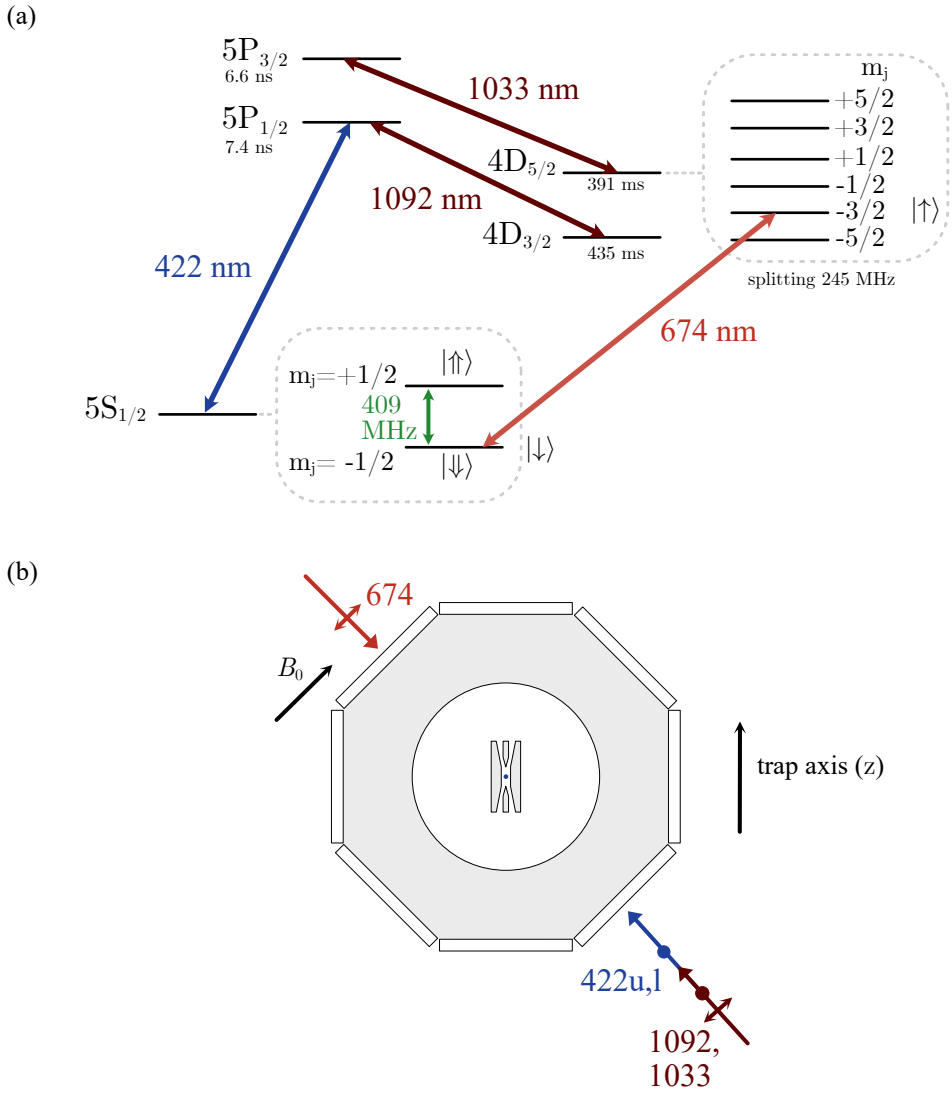

Figure 3.1: Internal states and control laser systems. (a) Relevant atomic level structure of $^{88}Sr^+$ at magnetic field $B_0 = 146\,\mathrm{G}$. Arrows indicate the lasers and rf fields employed in the experiments. We show the lifetimes of the excited states [107–110]. Experiments use the ground state qubit $|\Downarrow\rangle \leftrightarrow |\Uparrow\rangle$ or the optical qubit $|\downarrow\rangle \leftrightarrow |\uparrow\rangle$. (b) Beam geometry at the trap. We indicate the trap axis and the magnetic field direction. Ion not to scale.

3.2.1 Qubits

We use the ground-state qubit with states $|\Downarrow\rangle \equiv |5S_{1/2}, m_j = -1/2\rangle$ and $|\Uparrow\rangle \equiv |5S_{1/2}, m_j = 1/2\rangle$ and an optical qubit with states $|\downarrow\rangle \equiv |5S_{1/2}, m_j = -1/2\rangle$ and $|\uparrow\rangle \equiv |4D_{5/2}, m_j = -3/2\rangle$.

The ground state qubit is driven using an antenna mounted inside the vacuum system, which allows us to reach π times $\approx 3\,\mu s$. The magnetic field sensitivity of this qubit is 2.8 MHz/G.

With the current beam geometry and polarisation choice, using Eq. (2.10), we only have non-zero coupling for transitions with $\Delta m_j = \pm 1$ between $5S_{1/2}$ and $4D_{5/2}$. With $|\downarrow\rangle = |5S_{1/2}, m_j = -1/2\rangle$, choosing $|\uparrow\rangle = |4D_{5/2}, m_j = -3/2\rangle$ gives access to the higher coupling strength and the lower magnetic field sensitivity (1.12 MHz/G) compared to $|\uparrow\rangle = |4D_{5/2}, m_j = 1/2\rangle$.

3.2.2 Lasers for incoherent/dissipative operations

To load $^{88}Sr^+$ in our trap, atoms originating from a resistively heated stainless steal tube are photoionised (PI) through a two-step process [111]. The PI lasers are at 461 nm and 378 nm.

The motion of the ions is cooled down in the first step by using the $5S_{1/2} \leftrightarrow 5P_{1/2} \leftrightarrow 4D_{3/2}$ Doppler cooling cycle, which is addressed using the 422 nm and 1092 nm beams. The 422 nm contains two different frequencies close to the resonances of $422u$: $5S_{1/2}, m_j = -1/2 \leftrightarrow 5P_{1/2}, m_j = 1/2$ and $422l$: $5S_{1/2}, m_j = 1/2 \leftrightarrow 5P_{1/2}, m_j = -1/2$ such that we can address populations in both ground state levels and implement frequency-selective state preparation. The spin state $|5S_{1/2}, m_j = -1/2\rangle$ is initialised through optical pumping by only applying one of the 422 nm frequencies ($422l$) together with 1092 nm.

The Doppler cooling beams are also used for state detection. If the population has been coherently transferred to the $4D_{5/2}$ state, which is outside the Doppler-cooling cycle, using the 674 nm laser (see Sec. 3.2.3), it appears as 'dark'. Otherwise, it fluoresces ('bright'). When the qubit is encoded in the two $5S_{1/2}$ Zeeman levels, the readout step is always preceded by a 'shelving' 674 nm π-pulse. The Doppler cooling

beams are, then, applied for 200 µs, and for a single strontium ion we measure a count rate of 220 kHz above the 80 kHz background. A 1033 nm laser dissipatively returns the $4D_{5/2}$ population to the Doppler-cooling cycle.

All the lasers mentioned in this section, except the 378 nm, which is a free-running diode[1], are external cavity diode lasers[2]. The 422 nm and 1092 nm are frequency stabilised to reference cavities[3], while the 461 nm and 1033 nm are digitally stabilised using a Fizeau-interferometer-based wavemeter[4]. We use acousto-optical modulators (AOMs) to shift the frequency and pulse the laser beams. Once delivered to the trap via optical fibres, the laser beams are polarisation cleaned, and their power is stabilised by using photodiodes to measure a small portion of the light and adjusting the amplitude of the rf signal driving the AOM accordingly, using a Sample and Hold servo loop [32]. This is not the case for the PI lasers, where the switching is performed using mechanical shutters.

3.2.3 674 nm laser for coherent operations

To drive the optical qubit and, hence, to implement almost all coherent operations in this work, we use a 674 nm laser. This is a CW Ti:Sapphire laser[5] with an output of ~ 1.4 W[6], pumped by a ~ 15 W of 532 nm diode-pumped solid-state laser[7]. The wavelength of the laser is locked to a high-finesse cavity to obtain a narrow line (~ 1 Hz). The laser itself is located in a separate room from the ion trap experiment, and the light is delivered to the trap table via a 15 m single-mode optical fibre for which we use an active phase noise cancellation (FNC) system[8]. A more detailed description can be found in Ref. [98].

On the trap table, the beam passes through a double-pass (DP) AOM, which is used for intensity stabilisation and 'carving' the pulses (Sec. 3.3.3), and a second

[1]Toptica iBeam smart.
[2]Toptica Photonics DL Pro with DLC Pro controllers.
[3]National Physical Laboratory (NPL) Low Drift Etalon.
[4]HighFinesse WS7.
[5]M Squared SolsTiS
[6]at the time of writing
[7]M Squared Equinox for the majority of the D.Phil., until December 2022, and changed to Coherent Verdi starting with April 2023.
[8]Cavity and lock and FNC electronics provided by Stable Laser Systems.

single-pass (SP) AOM used for driving the bichromatic field (Sec. 3.3.2) and phase stabilisation (Sec. 3.4, 3.5). The light is then coupled into a single-mode fibre, which brings it close to the trap. On the trap side, there are polarisation cleaning optics, a non-polarising beam splitter picking up a small percentage of light used for intensity stabilisation, and a servo-controlled mirror used for carefully positioning the beam on the ion and focusing optics used to achieve a beam waist radius of $\approx 20\,\mu m$ at the position of the ion. The 674 nm beam enters the vacuum system as indicated in Fig. 3.1(b) and has a projection on all motional modes.

3.3 Experimental control system

The experimental setup is managed using ARTIQ[9] (Advanced Real-Time Infrastructure for Quantum Physics), an open-source control system. The core of this system is the ARTIQ process, which operates on a host computer and performs various tasks, which include submitting experiments, prioritising scheduling, compiling kernels, handling asynchronous remote procedure calls (RPCs), as well as collecting, broadcasting, analysing, and saving data.

The kernels are programs executed on the core device field-programmable gate array (FPGA), known as Kasli, instead of the host computer. This allows for real-time event execution with 1 ns precision on hardware from the open-source Sinara family [112], which includes modules with specialised functionality such as:

- digital input/output (DIO) card; used for monitoring PMT fluorescence counts for readout, switching power profiles and rf drives for specific AOMs on and off, and opening and closing mechanical shutters.
- direct digital synthesis (DDS) card (Urukul); primarily used for coherent operations (see Sec. 3.3.1)
- arbitrary wave generator (AWG) card, (Phaser) used for coherent operations and amplitude pulse shaping of pulses (see Sec. 3.3.3)

[9] M-Labs, Advanced Real-Time Infrastructure for Quantum Physics, version 7.0; https://m-labs.hk/experiment-control/sinara-core/

- analogue to digital converter (ADC) card (Sampler); used to monitor photodiode output. We combine a Sampler and a Urukul board with a custom gateware core[10] for the FPGA, enabling phase-coherent phase stabilisation (see Sec. 3.4.1).

3.3.1 Coherent control

In Sec. 3.2.2, we mentioned using AOMs to switch laser beams and shift their frequency. By having control over the rf signal driving of the AOM, we can not only control the intensity and frequency of the laser beam but also its phase. Coherent experiments often require multiple rf channels. For instance, generating two tones for a bichromatic field involves using two rf channels, where the phase relationship between these tones impacts the resulting interaction, as described in Eq. (2.44). Therefore, precise control over distributed rf channels is required. To achieve this control, we utilise the AD9910 variant of the Urukul card, which supports multi-chip synchronisation. This capability allows for precise update timing when adjusting phase or frequency values.

Furthermore, within a single pulse sequence, a single rf channel may handle multiple interactions, such as the following sequence: qubit rotation→red sideband rotation→qubit rotation (see Sec. 4.1.2). Maintaining a consistent phase reference during temporary frequency switches is important, especially for preserving the relative phase between different interactions. Using the AD9910 variant of the Urukul board enables us to operate in phase tracking/coherent mode, ensuring that when a channel temporarily switches frequencies and returns, the phase offset remains consistent as if the channel had never switched at all.

We primarily discussed these aspects of coherent control in the context of driving AOMs with rf signals. However, the same principles apply to driving the ground state qubit using the antenna, where the rf source is also a Urukul rf channel.

[10] Kindly implemented by Peter Drmota.

3.3.2 Bichromatic field implementation

We generate the 674 nm bichromatic field by simultaneously applying two rf signals to the SP AOM (see Sec. 3.2.3). Each one of the rf signals (tones) is provided by one of the channels of the Urukul board.

For single qubit rotations, the SP AOM is driven at the central frequency $f_{c,\mathrm{SP}}$, and the DP AOM at frequency $f_{c,\mathrm{DP}} + f_{o,\mathrm{DP}}$, using a single rf signal in both cases; $f_{c,\mathrm{DP}}$ is the central frequency of the DP AOM and $f_{o,\mathrm{DP}}$ an offset frequency applied to the DP AOM. For interactions requiring a bichromatic field, the drive for the DP AOM remains unchanged, while the two tones applied to the SP AOM are at $f_{c,\mathrm{SP}} \pm f_{o,\mathrm{SP}}$, where the frequency offset is $f_{o,\mathrm{SP}} \approx \omega_z/2\pi$ or $\omega_z/4\pi$, depending on the interaction type (see Sec. 2.3.2).

The same rf channel is used to drive the SP AOM for single qubit rotations ($f_{c,\mathrm{SP}}$) or the blue-detuned tone ($f_{c,\mathrm{SP}} + f_{o,\mathrm{SP}}$). The rf signal from this channel is combined with another using an rf splitter in reverse to implement the bichromatic field. Therefore, to ensure that the same power reaches the AOM for all configurations, the amplitude of the rf field is set to 1 for single qubit rotations and to 0.7 for each tone of the bichromatic field.

3.3.3 Amplitude shaping of the pulses

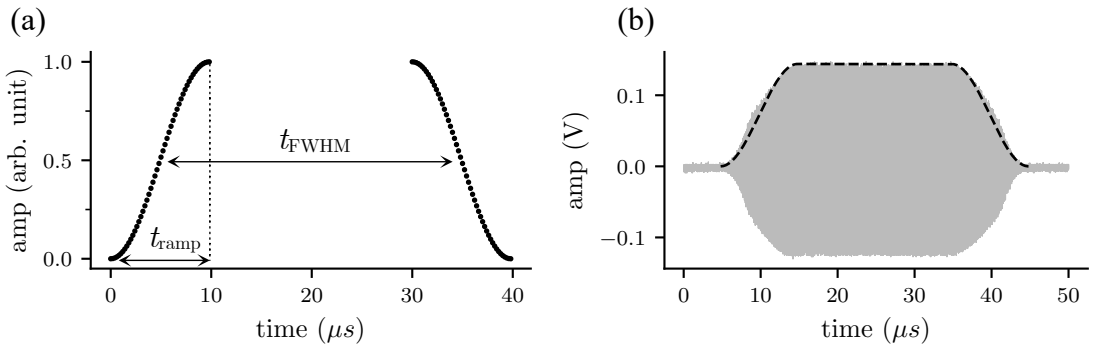

Figure 3.2: Amplitude pulse shaping. (a) Programming the shape of the pulse envelope. To program a $\sin(\pi t/(2t_{\mathrm{ramp}}))^2$ shape for the pulses, we send a series of amplitudes to the Phaser with low time resolution ($t_{\mathrm{res}} = 0.2\,\mu\mathrm{s}$, black circles). These amplitudes follow the $\sin(\pi t/(2t_{\mathrm{ramp}}))^2$ function with $t_{\mathrm{ramp}} = 10\,\mu\mathrm{s}$ for a pulse with $t_{\mathrm{FWHM}} = 30\,\mu\mathrm{s}$. (b) The resulting waveform (grey) was measured from the Phaser, where we fit the $\sin^2$ dependence (dashed line).

In the case of the 674 nm coherent operations, we use the DP AOM to 'carve' the pulses (Sec. 2.3.4). During the experimental sequence, the drive for the SP AOM is switched on first, followed by the DP AOM. The DP AOM is driven by an rf signal generated by a Phaser board, which features two I/Q mixers. In its default gateware configuration, the Phaser board functions as a precision rf synthesiser capable of producing up to five tones per channel. Additionally, it can act as a short-time Fourier transform (STFT) pulse generator, which we use to generate amplitude-shaped pulses [113]. We apply a $\sin(\pi t/(2t_{\mathrm{ramp}}))^2$ envelope to adiabatically ramp the rf signal on and off over a duration t_{ramp}. An example of this can be seen in Fig. 3.2[11]. In the following chapters, when we use an amplitude-shaped pulse, we will specify t_{ramp} and the full-width half-maximum duration t_{FWHM}, unless stated otherwise.

3.4 Two counter-propagating 674 nm beam setup

In Sec. 2.4, we discussed how using standing waves (SWs) enables us to deal with the effect of the non-commuting off-resonant carrier term. In this section, we describe how we create the standing wave(s) in the laboratory and how we control the phase of the SW field at the position of the ion. The counter-propagating 674 nm beam setup presented in this section is used in Chapter 5.

We introduce a counter-propagating beam to create the standing wave, as shown in Fig. 3.3(a). We refer to the two 674 nm beams as branch 1 (b1) and branch 2 (b2). Branch 2 is only activated for coherent operations using the standing wave. For other operations, such as sideband cooling or employing a travelling wave spin-dependent force with a bichromatic field, we use branch 1.

In Fig. 3.3(b), we present a simplified schematic of the 674 nm beam path on the trap table. For b2, we replicate the majority of the b1 setup; this includes the SP AOM, fibre, pico-motor mirror, polarisation cleaning, and focusing optics (the latter

[11] The best resolution achievable is $t_{\mathrm{res}} = 0.04\,\mu\mathrm{s}$. However, each amplitude update counts as a real-time event, and there is a limited number of real-time events that can be included in an experimental sequence. Therefore, we need to balance the smoothness of the pulse with the number of events that can be executed. Ideally, the interpolation functionality should address this issue, reducing the need for numerous real-time events to achieve a smooth ramp shape. Unfortunately, we have not been able to get this to work.

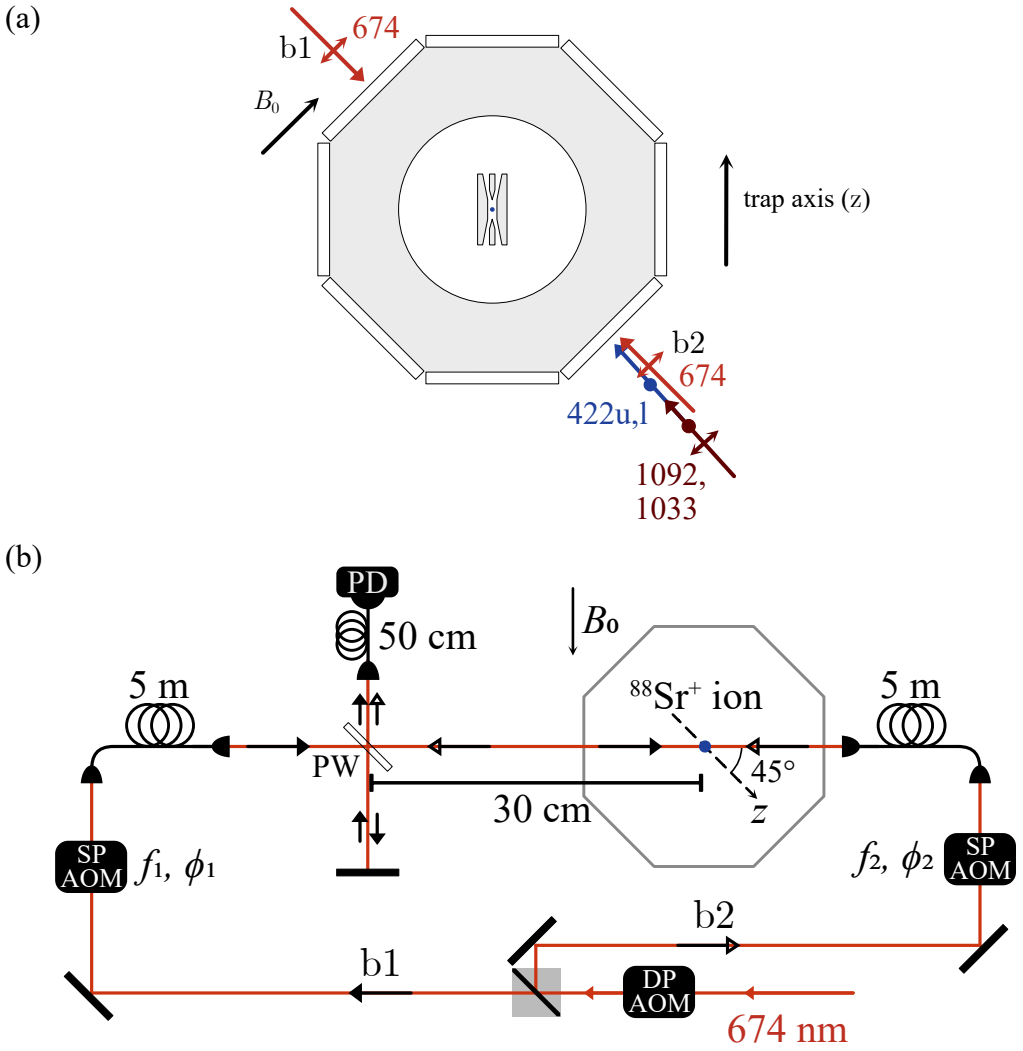

Figure 3.3: Two counter-propagating 674 nm beam setup. (a) Beam geometry at the trap. We indicate the two 674 nm branches (b1, b2), the trap axis and the direction of the magnetic field. The two 674 nm beams have polarisation parallel to the magnetic field B_0. (b) Simplified schematic of the 674 nm beam path on the trap table. The entire beam path is located on an enclosed optical table. The incoming 674 nm beam is split into two beams (b1, b2) of equal intensity at the ion(s). The acousto-optic modulators (AOMs) are used to control the frequencies (f_1, f_2) and phases (ϕ_1, ϕ_2) of the two counter-propagating beams. We close the resulting interferometer with a pick-off window (PW) ≈ 30 cm away from the ion(s). For the fast feedback step (see text), we stabilise the interference fringe intensity on a photodiode (PD) by adjusting the phase of the rf signal driving the single pass (SP) AOM in b1. The intensity stabilisation and beam-focusing optics are omitted.

three are not included in the schematic). The DP AOM is a shared component between the two branches. This design choice ensures minimal latency in switching on both beams simultaneously at the ion's position; any delays only occur from the optical path difference between the two branches. Additionally, adding an extra

DP AOM would result in a power loss. One potential drawback of our current beam path setup is that the intensity stabilisation is performed by adjusting the rf signal driving the double pass AOM. This means that we can only stabilise the intensity of one of the branches, which, in this case, is b1. If the intensity fluctuations are primarily due to fluctuations that occur before the PBS (that splits the beam into the two branches), then stabilising b1 also improves the intensity stability in b2. In the experiments considered in this work (Chapter 5 and 6), we have not found this to be a limiting factor.

Other experimental implementations of standing waves involve using reflection from a mirror or even from the surface of a trap chip [114–116]. We chose to use a separate counter-propagating beam as it enables us to quickly switch between the standing wave (SW) and travelling wave (TW) configurations. Additionally, having two separate beams provides more flexibility in matching their intensities at the ion's position and allows for individual phase control. To optimise the overlap between b1 and b2, we cross-couple them in the respective fibre, i.e., b1 in the fibre of b2 and b2 in the fibre of b1, using the two-mirror setups on the trap side.

For our experiments, we need to be able to control the phase of the standing wave with respect to the ion. Rather than moving the ions themselves [117, 118], we adjust the phase of the rf field driving the SP AOM in b1 to shift the standing wave relative to the ions.

The two counter-propagating branches form an interferometer. Around one-fourth of the physical length of the interferometer is in free space, while the rest is in optical fibres. Changes in the relative optical path lengths of the branches cause drifts in their phase difference at the position of the ion. These drifts are detrimental to the experiments since, for example, the antinode of the standing wave drifts away from the position of the ions. The main sources of drift arise from vibrations in the optical setup, temperature, humidity, and air currents in the laboratory. To mitigate these issues, we actively stabilise the relative phase between the two branches at the ion's position. This involves a two-stage feedback process: initially stabilising the phase using a photodiode (PD) to address fast drifts (discussed in

Section 3.4.1) and subsequently using the ion itself as a sensor to manage slower drifts (detailed in Sec. 3.4.2 and 3.4.4). The closest point where we could set up a lock point for the PD feedback was $\approx 30\,\mathrm{cm}$ away from the ion position. In section 3.4.3, we discuss improvements in the passive stability over this distance. To avoid any confusion, it is important to note that both feedback stages are conducted using a monochromatic field for each branch. In Sec. 3.4.5, we address how the phase corrections are introduced when employing the two bichromatic fields.

3.4.1 Photodiode feedback

For observing the interference fringes using the photodiode, we pick off a small fraction of light ($\approx 6\%$) from each one of the branches using a glass window[12]. Then, the two branches are coupled into a single-mode optical fibre, which acts as a mode filter, and sent to the photodiode. Using the fibre ensures a high degree of mode matching between the two branches, which enables a high-contrast interference signal at the photodiode (PD), as the beam parts that do not interfere are rejected. To lock the phase of the interferometer, we consider two schemes: homodyne and heterodyne measurements. In the homodyne measurement, the frequencies in b1 (f_1) and b2 (f_2) are equal. In the heterodyne measurement, $f_1 \neq f_2$. For the main experimental sequence, where we study the interaction between the standing wave and the ion, we need $f_1 = f_2$. However, due to gateware constraints[13], a signal oscillating around zero is required for efficient hardware implementation of the stabilisation. Thus, we use a heterodyne scheme[14] for phase stabilisation. To characterise the stability of our signal, we employ both heterodyne

[12]Thorlabs WG41010; we choose this to keep the amount of light picked off from each one of the branches roughly the same

[13]We usually use the Sampler (ADC board) and the Urukul (DDS board) in tandem for amplitude stabilisation mode. In phase stabilisation mode, the offset parameter—originally used as the target for the amplitude stabilisation loop—is repurposed as the output amplitude to align with the existing memory layout. As a result, we need to hard-code the target for the phase stabilisation loop, setting it to an amplitude of zero for simplicity.

[14]If we were to use the homodyne setup instead, the amplitude target would be given by $(V_{\max} + V_{\min})/2$ (see below), which depends on the maximum and minimum intensity of the interference signal. This value would require frequent calibration, hence frequent updates of the hardcoded value in the gateware.

and homodyne measurements, with the homodyne measurement resembling the frequency configuration used for implementing the standing wave.

In the case of the homodyne measurement ($f_1 = f_2$), the signal measured at the PD is:

$$V_{\text{homodyne}} = \frac{V_{\max} - V_{\min}}{2}(\cos\phi + 1) + V_{\min}, \tag{3.1}$$

where the maximum value of the voltage, $V_{\max}$ and the minimum value of the voltage, $V_{\min}$ correspond to the constructive and destructive interference points at the position of the PD, respectively, and ϕ is the relative phase between the two branches at the PD. The half-fringe point, where $\phi = \pi/2$ and the voltage is $(V_{\max} + V_{\min})/2$, exhibits maximum phase sensitivity and would be the lock point for the interferometer if we used this method. However, it is important to note that the lock point is sensitive to intensity fluctuations in the two branches and would require regular calibration.

For the heterodyne measurement, we set $f_1 \neq f_2$. A diagram of the electronic setup used for this measurement is shown in Fig. 3.4. The signal from the photodiode[15] is mixed down with a local oscillator (LO) at $f_{\text{LO}} = f_1 - f_2$, the beatnote frequency of the two branches. After the mixer, we introduce a low pass filter[16] to reduce any high-frequency signals that cannot be compensated with our feedback setup and higher harmonics of the beatnote frequency. The signal used for locking the phase is then given by:

$$V_{\text{heterodyne}} = \frac{V_{\max} - V_{\min}}{2}\sin(\phi - \theta_{\text{LO}}), \tag{3.2}$$

as mentioned before, ϕ is the relative phase between the two branches as measured at the photodiode and θ_{LO}, the phase of the LO signal. We expect the maximum and the minimum values of the signal to be equal, i.e., $|V_{\max}| = |V_{\min}|$; however, imperfections in the mixer can introduce a DC offset. A low-noise amplifier[17] (AMP) is introduced to make this DC offset negligible compared to the amplitude of the signal itself. Hence, the voltage at the half-fringe point, $\phi - \theta_{\text{LO}} = 0$, is ≈ 0 and

[15] Thorlabs, PDA36A2
[16] Minicircuits SLP-1.9+
[17] Minicircuits ZFL-500LN+

does not depend on the amplitudes of the branches or the LO, which is an advantage of the heterodyne configuration over the homodyne one.

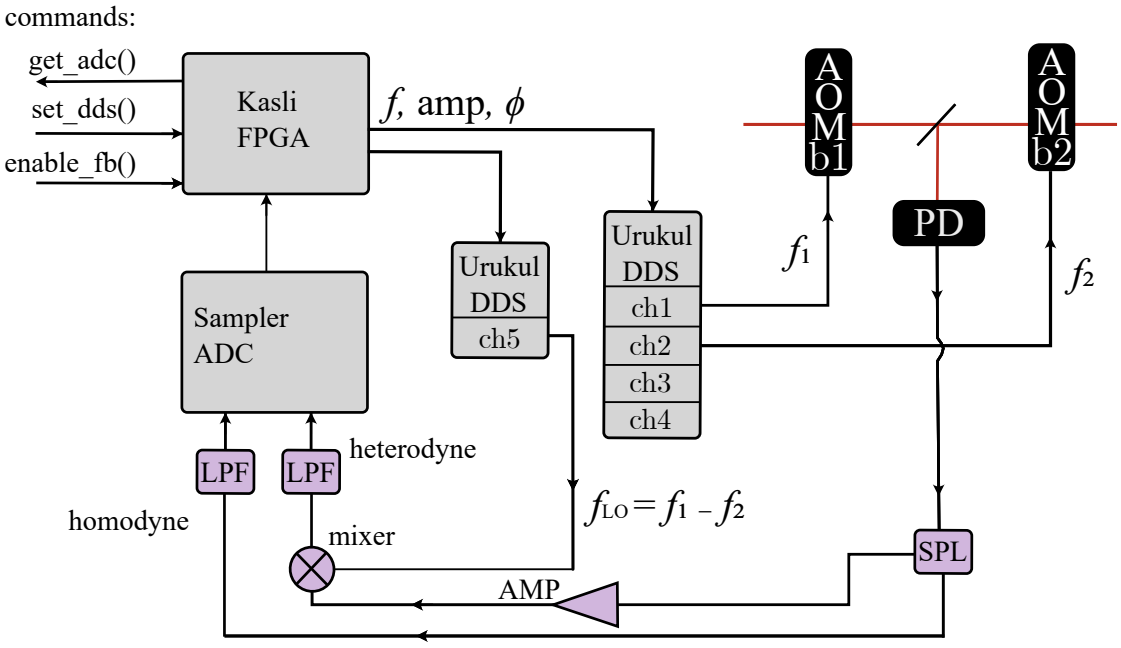

Figure 3.4: Simplified schematic of the phase stabilisation and characterisation setup. The signal from the PD is split into two parts using a splitter (SPL). The arm containing the mixer is used for stabilisation and characterisation in the heterodyne configuration, while the other arm is used for characterisation only in the homodyne configuration. Examples of commands sent to the FPGA that are used the most are: set_dds() is used for setting the frequencies for the heterodyne or homodyne setup, get_adc() is used for reading the voltages at the channels of the ADC, and enable_fb() is used for enabling the phase stabilisation. Once enabled, the feedback process runs continuously at a rate of $\approx 435\,\text{kHz}$ and only writes the phase corrections to ch1, which controls the AOM in b1. The low-pass filters (LPF) for the heterodyne and homodyne configurations are the same. Kasli, Sampler, and Urukul are the names of the FPGA, ADC, and DDS boards, respectively, in the ARTIQ Sinara family.

The interferometric signal, $V_{\text{heterodyne}}$, is acquired using an analog-to-digital converter (ADC) card. The 16-bit input channels have a sampling rate of up to 700 kHz and are combined with the FPGA, which is used for implementing the phase-locking control loop algorithm. After comparing to zero, the error signal goes to a proportional-integral (PI) gain circuit. The inferred correction for the phase is then written to the direct digital synthesis (DDS) board channel that feeds the AOM in the b1 rf signal. This process is done at a rate of $\approx 435\,\text{kHz}$ and sets the limit on the speed of the feedback loop.

We use the experimental sequence shown in Fig. 3.5 to characterise the quality of the interferometer stability. For each shot of the experimental sequence, we apply the feedback loop with the PD for 50 µs, then cool down the motion of the ions close to the ground state, prepare them in the desired spin state, conduct an ion-light interaction experiment, and perform state readout. Including the ion state preparation operations allows us to calibrate and characterise the PD feedback with the duty cycle required for any SW-ion experiment implementation.

The stability measurement using the heterodyne method is conducted immediately after the phase stabilisation, while the homodyne measurement is performed after the ion state preparation operations, which take around 18 ms per shot. We show the recorded photodiode signals for both free-drifting and locked interferometer states in Fig. 3.6(a.i) and 3.6(b.i), respectively, for heterodyne and homodyne stability characterisation measurements.

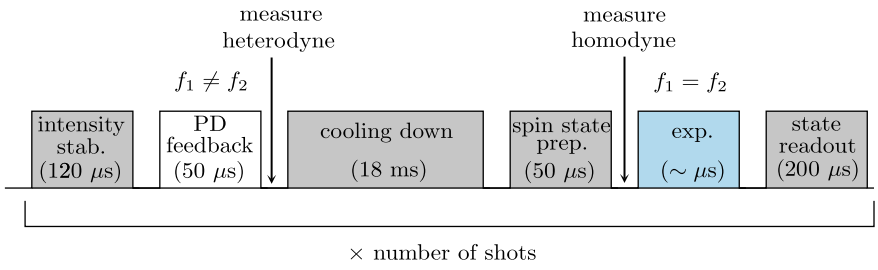

Figure 3.5: Experimental sequence used for characterising the phase stability at the photodiode. During the intensity stabilisation, we ensure that the 674 nm is always at the same power for every shot. The arrows indicate where the phase stability measurements are performed in the heterodyne and homodyne configurations. We indicate that during the PD feedback (white box), the two branches are at different frequencies ($f_1 - f_2 = 2$ MHz), while in the experiment concerned with the SW-ion interaction (blue box), they are at the same frequency.

One figure of merit for the interferometer stability quality is the ratio between the standard deviation of the stabilised signal and the total extent of a standing wave fringe. For the heterodyne configuration, we measure residual fluctuations in voltage of 1% and, in the homodyne case, of 2%. At first, we thought the homodyne case was worse because we allowed the system to free drift for some time before recording the measurement. However, performing the homodyne measurement

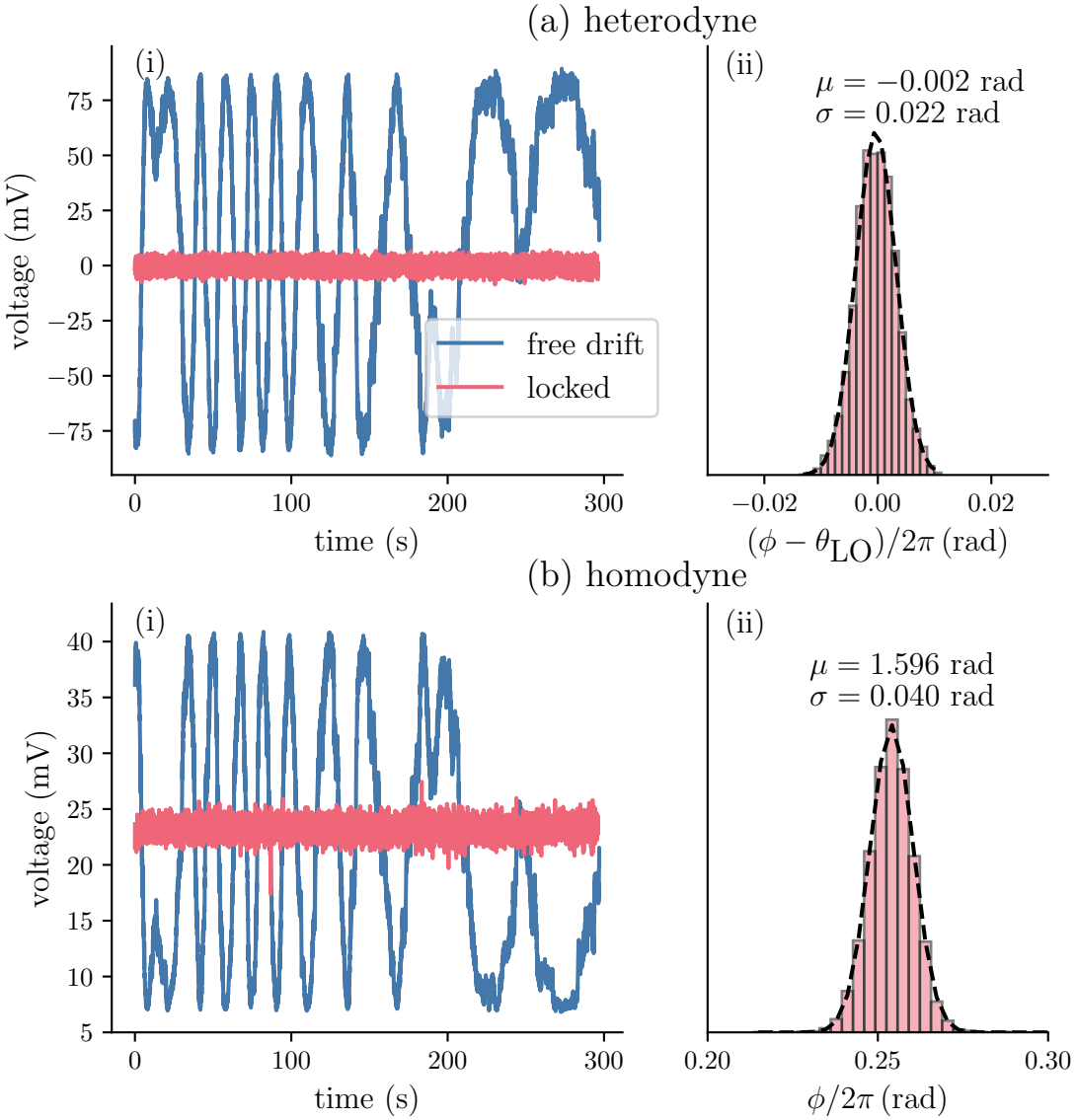

Figure 3.6: Photodiode signal measured in heterodyne, (a) and homodyne, (b) configuration. (i) Time traces of the photodiode signal when free drifting (blue) and when the feedback is enabled (pink). (ii) Histogram of the phase stabilised PD signal. Black dashed line shows a Gaussian fit with μ, σ mentioned in the text box. The blue curves in (a.i) and (b.i) were taken within the same experimental run and separated by only a few ms (see text). The same applies to the pink curves.

immediately after the PD feedback did not result in any improvements. As of now, this issue still requires further investigation.

It is useful to convert the measured voltage to residual phase fluctuations, σ using Eq. (3.2) and (3.1) for the heterodyne and homodyne signals, respectively. We plot the histogram of the obtained residual phase fluctuations for the heterodyne

measurement $\phi - \theta_{\mathrm{LO}}$ in Fig. 3.6(a.ii) and for the homodyne case, ϕ in 3.6(b.ii). The residual phase fluctuations are given by one standard deviation $\sigma = 0.022\,\mathrm{rad}$ for the heterodyne configuration and $\sigma = 0.040\,\mathrm{rad}$ for the homodyne configuration. For the heterodyne case, the distribution is centred around 0 rad, which is to be expected as $V_{\mathrm{heterodyne}} = 0\,\mathrm{V}$ at the lock point. In the homodyne case, only used for characterisation, the distribution is centred around a value that can be controlled by changing θ_{LO}; this is set such that the stabilised signal is close to half-fringe for maximum sensitivity, i.e., $\phi \approx \pi/2$.

The gain values for the PI circuit are optimised by minimising σ in the heterodyne measurement, which is equivalent to minimising σ in the homodyne measurement.

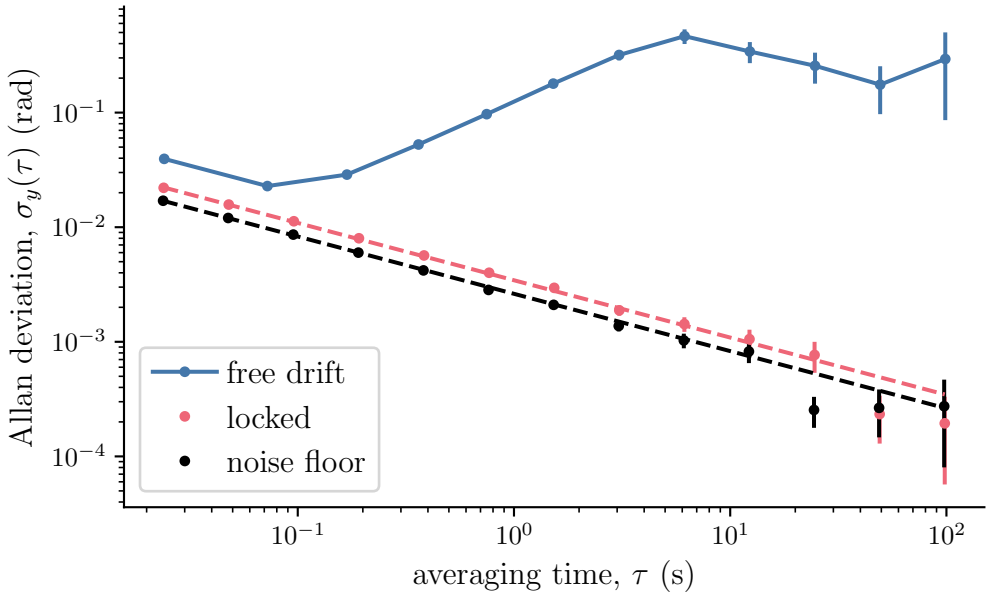

Figure 3.7: Interferometer stability evaluated using Allan deviation. Allan deviation computed for the free drifting (blue) and locked signal (pink) in Fig. 3.6(a.i) and the electronic noise floor (black). We fit the locked and noise floor data with a $1/\sqrt{\tau}$ model (dashed line). The standard deviation of the averages in the different clusters gives the error bars.

To further investigate the phase stability of the interferometer, we compute the Allan deviation of the time series measurements (see Fig. 3.6(a.i)). If we have N samples with sampling time τ_0, we can split the data into M clusters of duration

$\tau = m\tau_0$, where m is an integer. The Allan deviation is then defined as:

$$\sigma_y(\tau) = \sqrt{\frac{1}{2(M-1)} \sum_{i=1}^{M-1} (\bar{y}_{i+1} - \bar{y}_i)^2}, \tag{3.3}$$

where $\bar{y}_i$ is the average of the ith cluster [119]. We compare the locked data to the free drift and the electronic noise floor in the heterodyne configuration by calculating the Allan deviation, $\sigma_y(\tau)$, for different cluster sizes, m (see Fig. 3.7). The deviation for the free drifting signal starts increasing after 100 ms, indicating that the feedback loop should be applied at an interval shorter than this in order to combat the drifts in the system. We apply it every $\approx$ 20 ms.

The electronics noise floor nearly limits the locked signal. Using a $A/\sqrt{\tau}$ model to fit the locked and noise floor data, we find that the locked signal has approximately 1.3 times higher deviation than the noise floor. Approaching the noise floor more closely might be possible by using a low-pass filter with a lower cut-off frequency. The good agreement with the $1/\sqrt{\tau}$ model indicates that the main noise type is white noise, which justifies the Gaussian distribution observed in Fig. 3.6(a.ii). The electronic noise floor is measured by blocking the light at the PD and disabling the feedback loop.

3.4.2 The ion as a phase sensor

So far, we have only evaluated the quality of the phase stability measured at the photodiode. However, we are interested in controlling the relative phase between branches at the ion position. As shown in Fig. 3.3, the two branches co-propagate between the PW and the PD. Thus, the interference signal is insensitive to any vibrations or air drafts over this distance. We briefly verified this by having the interferometer locked and tapping the mirrors in that part of the setup with a metallic object; the interference signal remained unperturbed. This means that the difference in phase between the branches at the PW will be the same as the phase stabilised at the PD. From the PW to the ion position, the branches are counter-propagating and hence maximally sensitive to any changes in the optical path over a distance of $\approx$ 30 cm.

We can use the laser-ion interaction to infer the phase difference between the two branches at the ion position, $\phi_1 - \phi_2$. One method is through the direct standing-wave-ion interaction, discussed in Chapter 5, though it is not our main characterisation tool in this chapter. Instead, we consider applying a $\pi/2$-pulse with b1, $\hat{R}_{\mathrm{b1}}(\pi/2, 0) = \hat{R}_{\mathrm{b1}}(\pi/2)$ (see Eq. (2.20)), followed immediately by a $\pi/2$-pulse with b2, $\hat{R}_{\mathrm{b2}}(\pi/2)$, with the spin state initialised in $|\downarrow\rangle$. A complete transfer of population ($p_{|\downarrow\rangle} = 0$) occurs only if the phase difference between the two branches, $\phi_1 - \phi_2$, is zero. Ignoring that the two pulses use different fields, this setup is equivalent to a zero delay Ramsey experiment (see Sec. 4.1.1). Thus, the probability of finding the spin in $|\downarrow\rangle$ depends on $\phi_1 - \phi_2$ as follows:

$$p_{|\downarrow\rangle}(\phi_1 - \phi_2) = \sin^2\left(\frac{\phi_1 - \phi_2}{2}\right) = \frac{1 - \cos(\phi_1 - \phi_2)}{2}. \tag{3.4}$$

We use this method to characterise the stability of the relative phase between the branches at the ion position and also to implement a feedback mechanism with the ion.

3.4.3 Passive stability

While we achieved 0.04 rad phase stability at the photodiode, looking at the ion signal revealed that the passive stability needed to be improved (see Fig. 3.8(a)). For measuring this ion signal (pulse sequence shown in Fig. 3.5), we lock the interferometer at the PD and set $\hat{R}_{\mathrm{b1}}(\pi/2, \phi')$ and $\hat{R}_{\mathrm{b2}}(\pi/2, 0)$ (in 'exp.' in the pulse sequence) such that we start from $p_{|\downarrow\rangle} \approx 0.5$. Once this is set, we leave the system running and keep measuring while programming the same phase relationship between the branches. In Fig. 3.8(a.i), we measure the ion signal without any enclosure around the free space optical paths other than the shutters of the optical table. The signal shows abrupt random jumps, which can be translated into a phase drift rate. This is calculated by converting the population values to phase using Eq. (3.4) and then taking the difference of adjacent measurements and dividing it by the time step between them. The results are plotted in Fig. 3.8(a.ii). The normal distribution centred around zero indicates a random walk with an average

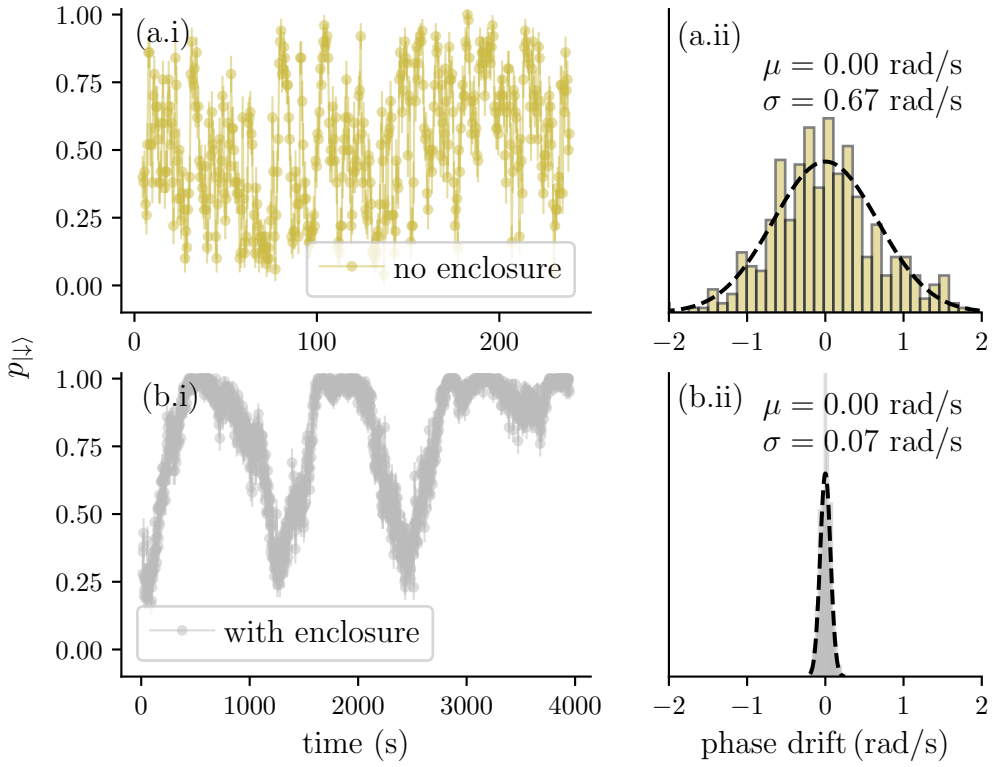

Figure 3.8: Passive stability of relative phase between the branches at the ion position with PD feedback enabled. We use the $\hat{R}_{b1}(\pi/2)$, $\hat{R}_{b2}(\pi/2)$ pulse sequence to infer the difference in phase between the two branches at the ion position. (a.i) The change in $p_{|\downarrow\rangle}$ as a consequence of the change in phase between the two branches at the ion position is shown in the case of no enclosure around the beam paths. (a.ii) Inferred phase drift rate based on (a.i). (b.i) Same as (a.i) but with an enclosure around the beam paths. (b.ii) Same as (a.ii), but for the data measured with the enclosure. In both cases, the PD feedback is enabled.

drift rate of 0.67 rad/s given by the standard deviation of the normal distribution. Adding a sturdy enclosure[18] over the 30 cm path from the pick-off to the vacuum chamber, together with an additional cardboard enclosure around the rest of the beam paths reduced the drifts to as low as 0.07 rad/s, as shown in Fig 3.8(b) with a much longer time axis. This is almost an order of magnitude improvement for the short-term changes. Removing the quick random jumps reveals a slow phase drift between the two branches, which we can correct for by using the ion feedback.

[18]We used Thorlabs TB4 black hardboard for building up the enclosure. This also provides enhanced acoustic absorption.

3.4.4 Ion feedback

For keeping the relative phase between branches constant at the ion position, which we call the ion feedback, we use the $\hat{R}_{b1}(\pi/2)$, $\hat{R}_{b2}(\pi/2)$ pulse sequence, discussed in Sec. 3.4.2. We interleave the experiments that depend on the relative phase between branches with the ion feedback, as shown in Fig. 3.9. The PD feedback is applied each shot during the ion feedback and the main experimental sequence.

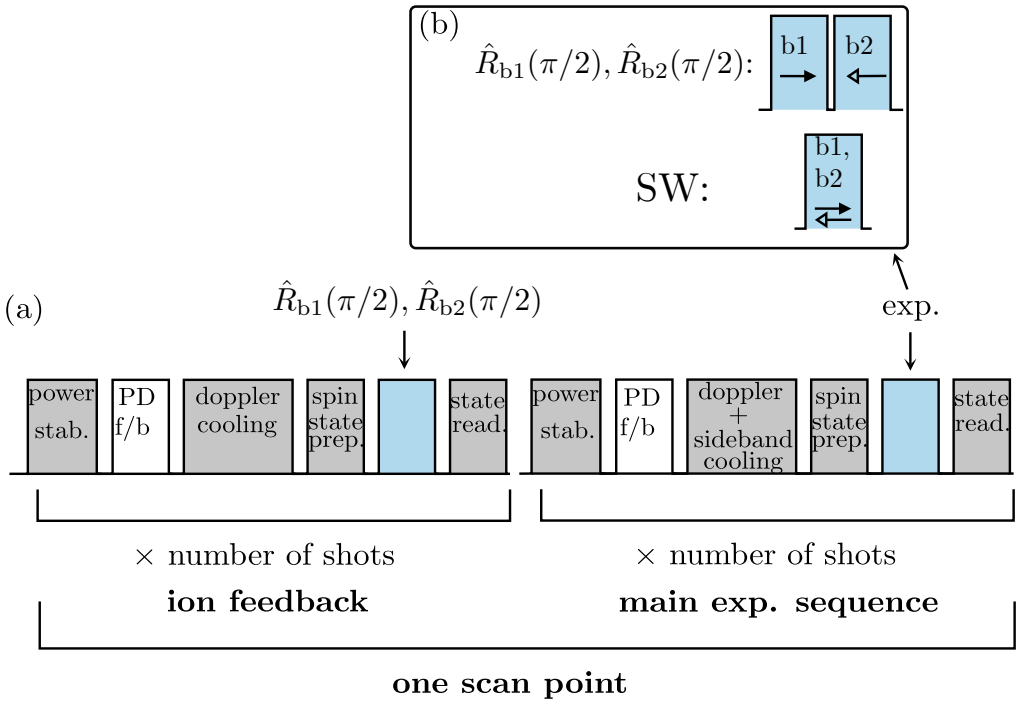

Figure 3.9: Experimental sequence with the ion feedback interleaved. (a) We use a similar experimental sequence to the one shown in Fig. 3.5 for implementing the ion feedback. For the zero delay Ramsey experiment $\hat{R}_{b1}(\pi/2)$, $\hat{R}_{b2}(\pi/2)$, the motion of the ion is not involved, hence, using only Doppler cooling for the ion feedback is sufficient. The PD feedback (white boxes) is applied every shot for both the ion feedback and the main experiment. (b) We show some examples of pulse sequences that can constitute the main experiment. The $\hat{R}_{b1}(\pi/2)$, $\hat{R}_{b2}(\pi/2)$ sequence is also used for the ion feedback.

We aim to lock at the maximum slope point of the sinusoid, i.e. at state transfer probability 0.5, which, when converted to phase using Eq. (3.4) yields $\pi/2$ rad, our phase setpoint, ϕ_{ST}. During the ion feedback, we estimate the current value of $p_{|\downarrow\rangle}$ using a certain number of shots, usually 100. This probability value is converted to phase, ϕ_{now} and it is used to infer the phase correction, ϵ_{ion} with:

$$\epsilon_{ion} = \epsilon_{ion,previous} + K(\phi_{ST} - \phi_{now}), \tag{3.5}$$

for maintaining the setpoint. K is the gain of the feedback loop.

In Fig. 3.10(a), we compare the difference in phase between the branches at the ion position when the PD-ion 30 cm path is left to free drift and when the ion feedback is interleaved. In the latter case, we can see how the difference in phase is maintained at the set point $\phi_{\mathrm{ST}} = \pi/2$ rad. Before starting an experiment where the ion feedback is interleaved, we run the ion feedback ten times on its own. These preliminary ion feedback rounds ensure that the phase is at $\phi_{\mathrm{ST}} = \pi/2$ rad by the time the main experimental sequence begins, avoiding any transitory effects, as shown in Fig. 3.10(b). For this measurement, in the main experimental sequence (see Fig. 3.9), we scan the relative phase between the branches, $\hat{R}_{\mathrm{b1}}(\pi/2, \phi')$ and $\hat{R}_{\mathrm{b2}}(\pi/2, 0)$, on top of the ion feedback setpoint.

The ion feedback is applied every ≈ 2.5 s. At this 'slow' rate, we found using the Allan variance to optimise the gain parameter K very useful (see Fig. 3.11). With both the PD and ion feedback enabled, we record traces as shown in Fig. 3.10 for different K values (free drift is equivalent to $K = 0$). The number of shots we use to measure the population to infer the phase corrections imposes a limit on the phase stability. In optimising K, we try to bring the locked data as close as possible to this shot noise limit. The shot noise trace shown in Fig. 3.10 is inferred from simulated data, where the population value is determined by sampling a binomial distribution with $n = 100$ and the success probability given by Eq. (3.4) with $\phi_1 - \phi_2 = \pi/2$. For the timestamps of the simulated values, we use the timestamps of the experimental data and then compute the Allan variance.

Once K is calibrated, we apply the sequence in Fig. 3.9 for ≈ 1.2 hours and look at the population used for calculating the phase corrections in the ion feedback. We convert these values to phase using Eq. (3.4), shown in Fig. 3.12. Similarly to the phase stability measured at the photodiode, we can evaluate the stability at the ion by calculating the standard deviation, σ. For the feedback data, we obtain $\sigma = 0.120(2)$ rad.

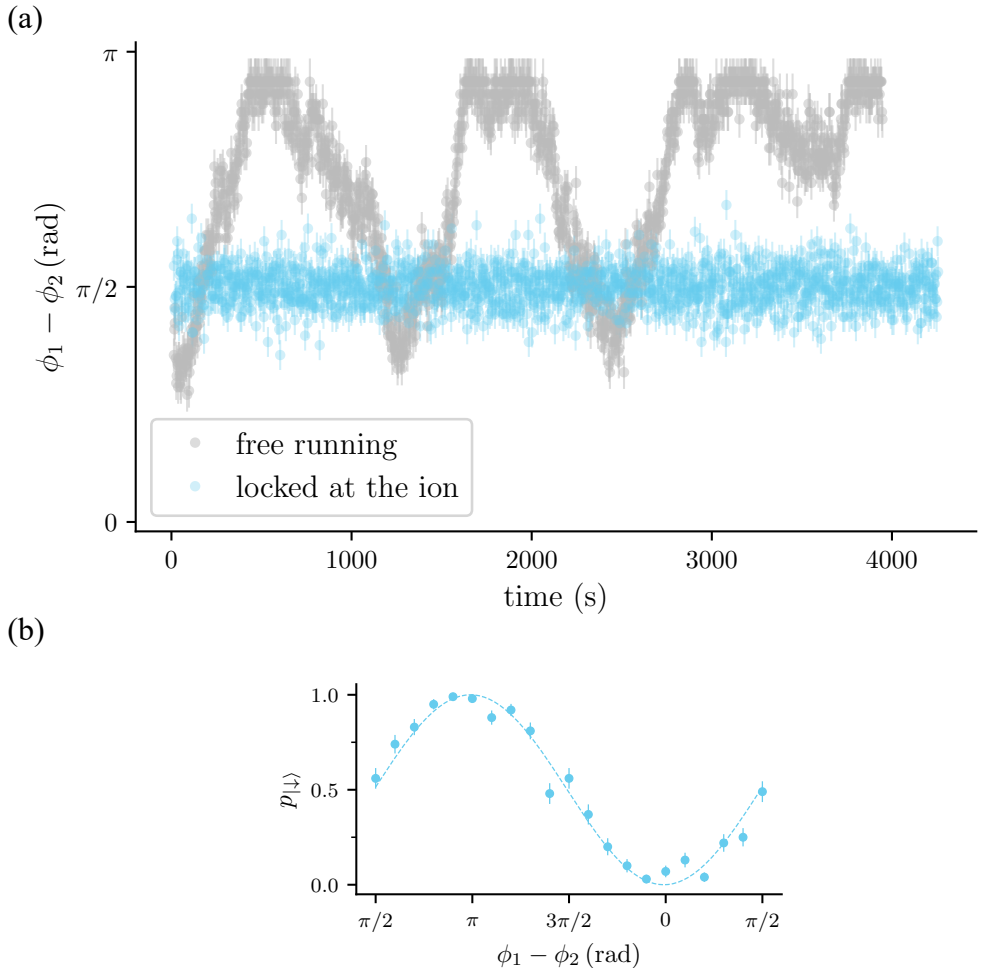

Figure 3.10: Phase difference between the branches at the ion position. (a) The population $p_{|\downarrow\rangle}$ when the PD-ion 30 cm path is allowed to free drift, shown in Fig. 3.8(b.i), is converted to phase (grey). This is compared to the case of having the ion feedback enabled (blue). In both cases, the PD feedback is enabled as well. (b) Scan of the relative phase between the branches with the ion feedback enabled; pulse sequence $\hat{R}_{\mathrm{b1}}(\pi/2, \phi')$, $\hat{R}_{\mathrm{b2}}(\pi/2, 0)$. The phase difference $\phi_1 - \phi_2 = \phi_{\mathrm{ST}} + \phi' = \pi/2 + \phi'$.

Depending on the number of shots, the precision of the measurement is limited by the shot noise error given by:

$$\sigma_p = \sqrt{\frac{p(1-p)}{n}}, \tag{3.6}$$

where n is the number of shots, and p is the measured state transfer probability value. The populations for correcting the phase in the ion feedback were taken with 100 shots and $p \approx 0.5$. Using Eq. (3.4), we can relate σ_p to $\sigma_{\Delta\phi}$, where $\Delta\phi$ small

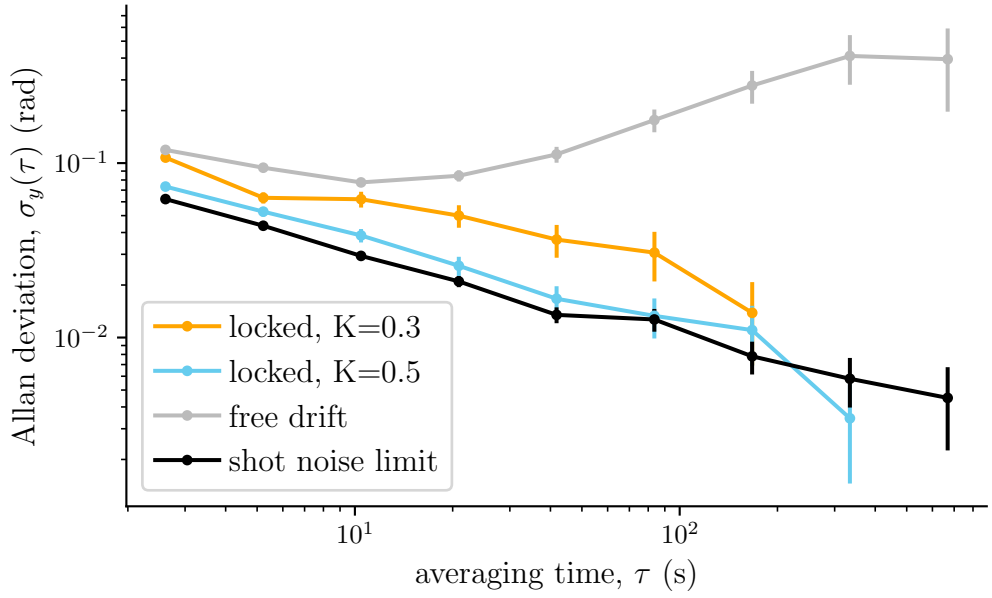

Figure 3.11: Allan variance for optimising the ion feedback performance. We show the Allan variance for the data without the ion feedback applied (grey), the locked signal for two different gain values, K (orange, blue) and simulated data (black) with shot noise due to 100 shots. The standard deviation of the averages in the different clusters gives the error bars.

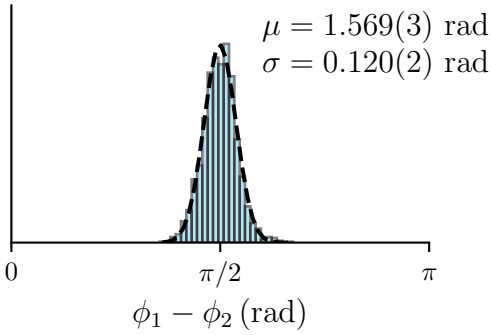

Figure 3.12: Phase stability at the ion position with ion feedback enabled. The population values $p_{|\downarrow\rangle}$ used for inferring the ion feedback ($\hat{R}_{\mathrm{b1}}(\pi/2), \hat{R}_{\mathrm{b2}}(\pi/2)$) corrections are converted to phase and plotted as a histogram. The black dashed line shows a Gaussian fit with μ, σ mentioned in the text box. Data were acquired over ≈ 1.2 hours.

phase fluctuations at the lock point $\pi/2$ such that $\phi_1 - \phi_2 = \pi/2 + \Delta\phi$ by

$$\sigma_p = \left| \frac{\mathrm{d}p_{|\downarrow\rangle}(\phi_1 - \phi_2)}{\mathrm{d}\Delta\phi} \right| \sigma_{\Delta\phi} = \frac{\sigma_{\Delta\phi}}{2} \tag{3.7}$$

which yields a $\sigma_{\Delta\phi} = 0.100\,\mathrm{rad}$[19] limit due to the shot noise, which needs to be

[19]This value is also verified through simulation by sampling a binomial distribution with $n = 100$

compared to the measured $\sigma = 0.120(2)$ rad. Hence, we think that the phase measurement with the ion is mainly limited by shot noise. The precision on the inferred phase could be further improved by increasing the number of shots or using an adaptive Bayesian phase estimation protocol [120]. Increasing the number of shots also reduces the repetition rate of the ion feedback loop, which should be high enough such that the phase accumulation due to the free drift rate is not significant.

3.4.5 Phase stability with two bichromatic fields

As a result of the two-stage feedback, there are two phase corrections that are applied to AOM in b1 using the rf ch1 in Fig. 3.4: ϕ_{PD} from the PD feedback and ϕ_{ion} from the ion feedback. The phase ϕ_{PD} is updated at every shot, while ϕ_{ion} is updated at every scan point. When using two bichromatic fields, the channels labelled ch1 and ch2 in Fig. 3.4 are used for implementing the blue-detuned tone in b1 and the blue-detuned tone in b2, respectively. Channels ch3 and ch4 are used to implement the red-detuned tone in b1 and the red-detuned tone in b2, respectively. We show this mapping in Table. 3.1.

tone phase	rf-channel
$(\phi_b)_{\mathrm{b1}}$	ch1
$(\phi_b)_{\mathrm{b2}}$	ch2
$(\phi_r)_{\mathrm{b1}}$	ch3
$(\phi_r)_{\mathrm{b2}}$	ch4

Table 3.1: Phases of the different tones in the two bichromatic fields b1 and b2 mapped to the respective rf channels. The phase of the blue-detuned tones is marked as ϕ_b, while the phase of the red-detuned tones is marked as ϕ_r.

Channels ch1 and ch3 are combined using an inverted splitter (see Sec. 3.3.2) and used to drive AOM in b1, while ch2 and ch4 are combined to drive the AOM in b2. In order to make sure that the red detuned tones are phase stable, we need to push the phase of ch3 by $\phi_{\mathrm{PD}} + \phi_{\mathrm{ion}}$.

trials and a success probability of $p = 0.5$. The sampled values are converted to phase using Eq. (3.4), and the standard deviation of the phase values is then computed.

In this section, we mainly described how we stabilise the relative phase between the branches at the position of the ion. The implications of this phase stabilisation on the SW-ion interaction are discussed in Chapter 5.

3.5 Phase stability in the co-propagating setup

The two bichromatic fields counter-propagating setup can be repurposed such that the two fields co-propagate, which we use for the experiments described in Chapter 6. The modified setup for combining the two bichromatic fields is shown in Fig. 3.13. In this case, the two branches are co-propagating for most of the optical path. Consequently, the primary source of phase fluctuations between the branches would be differential path length changes before the fibre beam splitter. Moreover, as discussed in Sec. 3.4.2, on the trap side, the phase difference between the branches should be highly insensitive to any changes in the optical path as the beams co-propagate. Therefore, the phase difference that is locked at the PD should be the same as the one at the ion. Hence, we only employ the PD feedback to maintain the difference in phase between the branches constant at the position of the ion. The PD feedback is applied every shot as shown in Fig. 3.5.

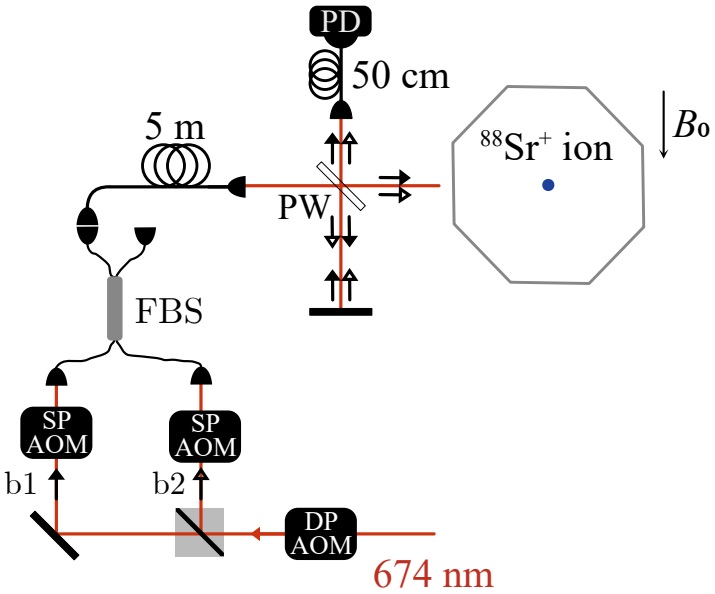

Figure 3.13: Two counter-propagating 674 nm beam setup. The two branches are combined using a fibre beam splitter (FBS) and sent to the trap. For more details, see Fig. 3.3(b) as well.

As before, to characterise the phase difference $\phi_1 - \phi_2$ at the position of the ion, we use the $\hat{R}_{\mathrm{b1}}(\pi/2)$, $\hat{R}_{\mathrm{b2}}(\pi/2)$ pulse sequence, which goes in the 'exp.' box in Fig. 3.5. We set the relative phase between $\hat{R}_{\mathrm{b1}}(\pi/2)$ and $\hat{R}_{\mathrm{b2}}(\pi/2)$ such that $p_{|\downarrow\rangle} \approx 0.5$, which is equivalent to $\phi_1 - \phi_2 \approx \pi/2$ rad. We obtain a histogram similar to the one shown in Fig. 3.12 to which we fit a Gaussian with $\mu = 1.65(1)$ rad and $\sigma = 0.108(10)$ rad. The Gaussian is slightly off-centred from $\pi/2$, probably due to a miscalibration of one of the $\pi/2$-pulse durations. Moreover, we repeat the same measurement and analysis while using the same branch $\hat{R}_{\mathrm{b1}}(\pi/2)$, $\hat{R}_{\mathrm{b1}}(\pi/2)$ and obtain $\mu = 1.55(1)$ rad and $\sigma = 0.097(8)$ rad. The two σ values are consistent with each other, suggesting that within the precision obtained from measuring 100 shots, we cannot distinguish between the quality of the phase stability for using the same branch for the Ramsey sequence and using different branches, which we accept as a positive result[20].

3.5.1 Relative phases between the channels

For the experiments presented in Chapter 6, we need specific phase relationships between the tones in the two bichromatic fields to be satisfied at the position of the ion. The various phase requirements are explained in Sec. 6.2.1. Here, we focus on the calibrations needed to fulfil them.

Before doing these calibrations, as highlighted in Sec. 3.4.5, we have to port the phase correction obtained through the PD feedback (ϕ_{PD}) also to the rf channels that drive the red-detuned tones; we push the phase of ch3, which is applied to AOM in b1, by ϕ_{PD}.

To establish all the phase relationships that we need (Sec. 6.2.1) it is enough to

[20] We expect a precision of 0.100 rad when using 100 shots (see Eq. (3.6) and (3.7)). Even though the measurement is slightly off from $\pi/2$, the offset is not significant enough to change the expected precision.

calibrate the following phase relationships at the position of the ion[21]:

$$(\phi_b)_{\mathrm{b1}} - (\phi_b)_{\mathrm{b2}} = 0 \tag{3.8a}$$

$$(\phi_r)_{\mathrm{b1}} - (\phi_r)_{\mathrm{b2}} = 0 \tag{3.8b}$$

$$(\phi_b)_{\mathrm{b1}} - (\phi_r)_{\mathrm{b2}} = 0 \tag{3.8c}$$

$$(\phi_r)_{\mathrm{b1}} - (\phi_b)_{\mathrm{b2}} = 0. \tag{3.8d}$$

Each one of these phases can be adjusted by the respective rf-channel, as shown in Table. 3.1.

Without calibration, the phase differences in Eq. (3.8) are actually not set to zero. We can measure the different offsets using the $\hat{R}_{\mathrm{b1}}(\pi/2, \phi')$, $\hat{R}_{\mathrm{b2}}(\pi/2, 0)$ pulse sequence, where we scan ϕ'. For example, in the case of measuring offset3 for the phase difference in Eq. (3.8c), the $\hat{R}_{\mathrm{b1}}(\pi/2)$ pulse is driven using ch1 and $\hat{R}_{\mathrm{b2}}(\pi/2)$ is driven using ch4. After all the offsets are measured, we can calculate using, for example,

$$\begin{pmatrix} 1 & 0 & 0 & 0 \\ 1 & -1 & 0 & 0 \\ 0 & 0 & 1 & -1 \\ 1 & 0 & 0 & -1 \\ 0 & -1 & 1 & 0 \end{pmatrix} \begin{pmatrix} (\phi_b)_{\mathrm{b1},0} \\ (\phi_b)_{\mathrm{b2},0} \\ (\phi_r)_{\mathrm{b1},0} \\ (\phi_r)_{\mathrm{b2},0} \end{pmatrix} = \begin{pmatrix} 0 \\ \mathrm{offset1} \\ \mathrm{offset2} \\ \mathrm{offset3} \\ \mathrm{offset4} \end{pmatrix} \tag{3.9}$$

the phase corrections that need to be added to the individual channels, $(\phi_b)_{\mathrm{b1},0}$, $(\phi_b)_{\mathrm{b2},0}$, $(\phi_r)_{b1,0}$, $(\phi_r)_{\mathrm{b2},0}$, in order to have Eq. (3.8) fulfilled. The rows circled in the dashed rectangle form a matrix that describes the phase relationships in Eq. (3.8). However, since it is a rank-3 matrix and we need to determine four values, we also include an additional row (which sets $(\phi_b)_{\mathrm{b1},0} = 0$) to ensure a unique solution.

We show an example calibration in Fig. 3.14. We find that the inferred correction values give us the desired relationships up to a phase π, which we subsequently add. We find that these values need to be re-calibrated only when we restart the FPGA.

[21] Sebastian came up with this idea on a typically warm British summer day when the best thing we could do was to be in the basement lab.

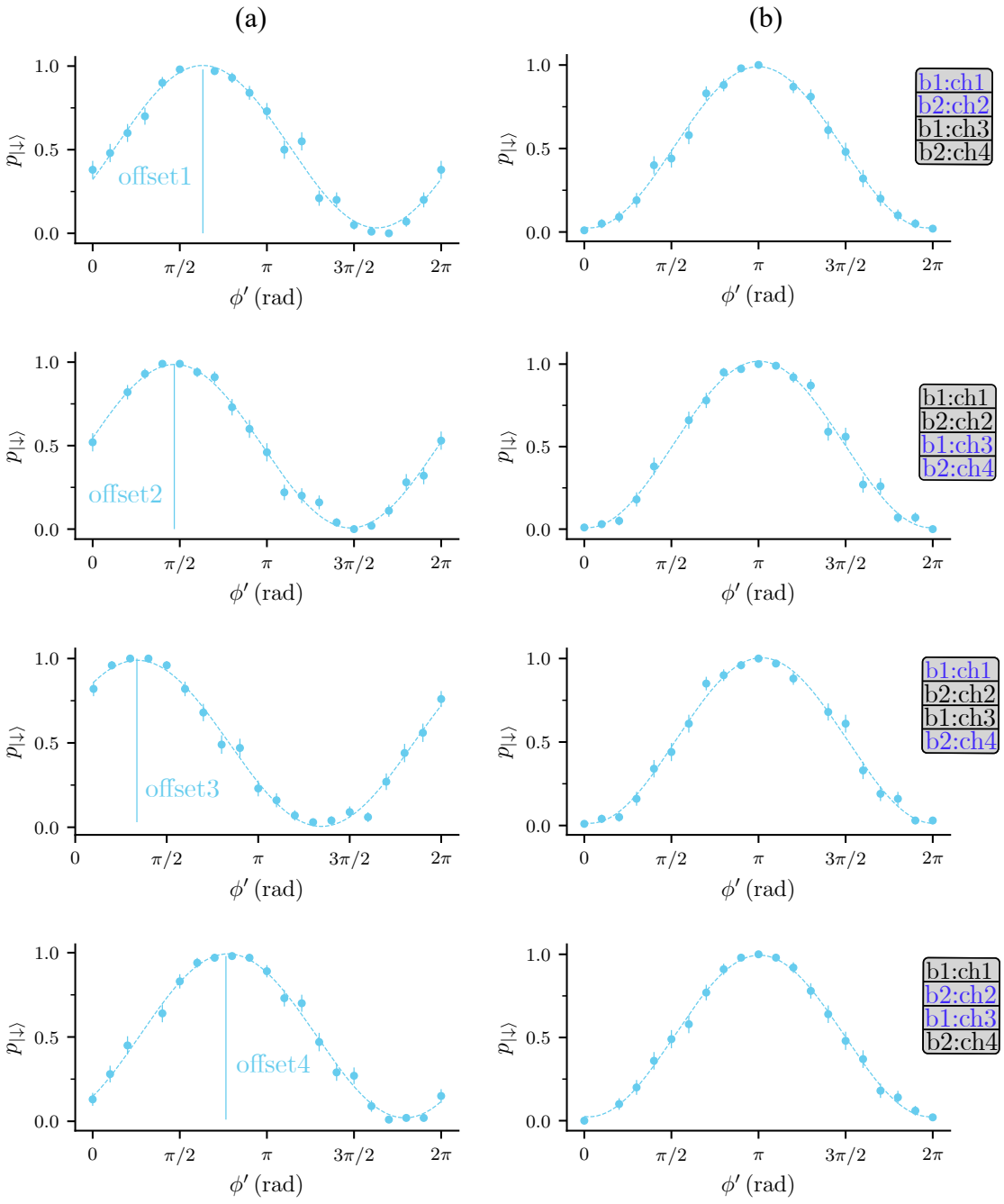

Figure 3.14: Example calibration of the relative phases between the different channels. To evaluate the relative phase between the channels, we use the $\hat{R}_{\mathrm{b1}}(\pi/2, \phi')$, $\hat{R}_{\mathrm{b2}}(\pi/2, 0)$ pulse sequence and we scan ϕ'. The channels involved in each measurement are highlighted in blue in the grey boxes. (a) Calibration scans used to infer the offsets. By fitting (dashed lines) the $p_{|\downarrow\rangle}$ dynamics, we infer (offset1, offset2, offset3, offset4) $= 2\pi \times (0.32, 0.23, 0.17, 0.38)$ rad, indicated by the vertical lines. The phase corrections are then determined using Eq. (3.9) as $((\phi_b)_{\mathrm{b1},0}, (\phi_b)_{\mathrm{b2},0}, (\phi_r)_{\mathrm{b1},0}, (\phi_r)_{\mathrm{b2},0}) = 2\pi \times (0., 0.68, 0.07, 0.83)$ rad. (b) Phase scans after the phase corrections $((\phi_b)_{\mathrm{b1},0}, (\phi_b)_{\mathrm{b2},0}, (\phi_r)_{\mathrm{b1},0}, (\phi_r)_{\mathrm{b2},0}) = 2\pi \times (0., 0.68 + 0.5, 0.07, 0.83 + 0.5)$ rad are applied.

4

Spin-oscillator system and spin-dependent forces characterisation

Contents

In this chapter, we start by briefly characterising the spin-oscillator system that we use in this work. Then, we prepare our most trustworthy tools that accompany us for the rest of the thesis, the spin-dependent forces (SDFs). We create SDFs using bichromatic fields. As described in Sec. 2.3.3, we generate SDFs conditioned on $\hat{\sigma}_\phi$, but also $\hat{\sigma}_z$, by taking advantage of the non-commuting off-resonant term that is also part of the interaction but often neglected. We then measure the strengths of these SDFs, which we compare to theory (Sec. 2.3.3). Moreover, we discuss the calibration steps that happen before the strength measurements. Some of the

results presented in this chapter are also published in Ref. [1, 64].

4.1 Spin-oscillator system characterisation

Although ions are levitated systems and relatively well isolated from external perturbations, several mechanisms still prevent them from serving as perfect qubits and perfect quantum harmonic oscillators. In this section, we characterise the coherence of each of these subsystems.

4.1.1 Spin

To measure the coherence times (T_2^*) of the qubits used in this work, we employ a Ramsey interferometry experiment with the pulse sequence shown in Fig. 4.1. This method allows us to examine the combined effect of the laser and qubit transition stability. With the spin initialised in $|\downarrow\rangle$, the first $\pi/2$ carrier pulse,

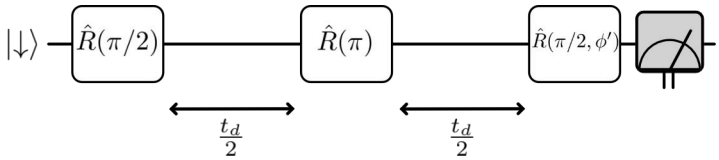

Figure 4.1: Ramsey sequence (by excluding the π-pulse) or spin-echo sequence for measuring the coherence time of a qubit. By scanning the relative phase between $\hat{R}(\pi/2) = \hat{R}(\pi/2, \phi' = 0)$ and $\hat{R}(\pi/2, \phi')$, $\phi' : 0 \rightarrow 2\pi$, we obtain a Ramsey fringe. The contrast $C(t_d)$ at different delay times t_d of the Ramsey fringe gives us information about the coherence of the spin superposition state.

$\hat{R}(\pi/2)$, creates the superposition

$$|\psi_s\rangle = \frac{1}{\sqrt{2}}(|\downarrow\rangle - ie^{i\phi_1}|\uparrow\rangle), \tag{4.1}$$

where ϕ_1 is the laser phase mapped to the spin state. The system then evolves freely for a duration t_d, accumulating phase ϕ_{ion,t_d}, resulting in the state

$$|\psi_s\rangle = \frac{1}{\sqrt{2}}(|\downarrow\rangle - ie^{i(\phi_1+\phi_{\text{ion},t_d})}|\uparrow\rangle), \tag{4.2}$$

up to a global phase. The phase ϕ_{ion,t_d} can be defined as $\int_{t_1}^{t_2}\delta(t)dt$, where $\delta(t)$ is the detuning from the qubit frequency, which varies non-trivially over time,

and $t_d = t_2 - t_1$. Similarly, the phase of the field changes over t_d, becoming ϕ_{laser,t_d}. When we apply the second $\pi/2$ carrier pulse with an additional controlled phase ϕ_2, the spin state becomes

$$|\psi_s\rangle = \frac{1}{2}((|\downarrow\rangle - ie^{i(\phi_{\text{laser},t_d}+\phi_2)}|\uparrow\rangle) - ie^{i(\phi_1+\phi_{\text{ion},t_d})}(-ie^{-i(\phi_{\text{laser},t_d}+\phi_2)}|\downarrow\rangle + |\uparrow\rangle)). \quad (4.3)$$

We can then compute the probability of finding the spin state in $|\downarrow\rangle$ as

$$p_{|\downarrow\rangle} = \sin^2\left(\frac{\phi_{\text{laser},t_d} - \phi_{\text{ion},t_d} + \phi_2 - \phi_1}{2}\right) = \frac{1}{2}(1 - \cos(\phi_{\text{laser},t_d} - \phi_{\text{ion},t_d} + \phi_2 - \phi_1)). \quad (4.4)$$

Scanning $\phi_2 - \phi_1$ ($\phi_2 - \phi_1 = \phi'$[1] in Fig. 4.1) produces Ramsey fringes. However, in Eq. (4.4) we did not account for fluctuations in $\phi_{\text{laser},t_d} - \phi_{\text{ion},t_d}$ that occur from shot to shot, leading to decoherence. Averaging over these different outcomes, a more accurate formula for $p_{|\downarrow\rangle}$ is

$$p_{|\downarrow\rangle} = C(t_d)\sin^2\left(\frac{\phi_2 - \phi_1}{2}\right) = \frac{C(t_d)}{2}(1 - \cos(\phi_2 - \phi_1)), \quad (4.5)$$

where the contrast of the Ramsey fringes, $C(t_d)$, is reduced due to decoherence, with $C(t_d)$ reflecting the sources of decoherence and their time scale. The spin coherence time can be estimated by measuring $C(t_d)$ for different delay durations t_d. Moreover, we can optionally introduce a spin-echo by introducing a carrier π-pulse as indicated in Fig. 4.1 in order to reduce the effects of slow varying offsets in the qubit frequency [88].

Since the experiment does not engage with the ion's motional state and the carrier interaction is sufficiently insensitive, we can perform it after the ions have only been Doppler-cooled.

Ground state qubit

We measure the coherence for the ground state qubit ($|\Downarrow\rangle = |5S_{1/2}, m_j = -\frac{1}{2}\rangle$ and $|\Uparrow\rangle = |5S_{1/2}, m_j = \frac{1}{2}\rangle$) using rf carrier pulses, see Fig. 4.2. By fitting a Gaussian model $Ae^{-(t_d/\tau)^2/2}$, where A is a constant accounting for contrast reduction due to

[1] In the experiment, we can't control ϕ_1 and ϕ_2 at the position of the ion, we can only control the relative phase between the pulses.

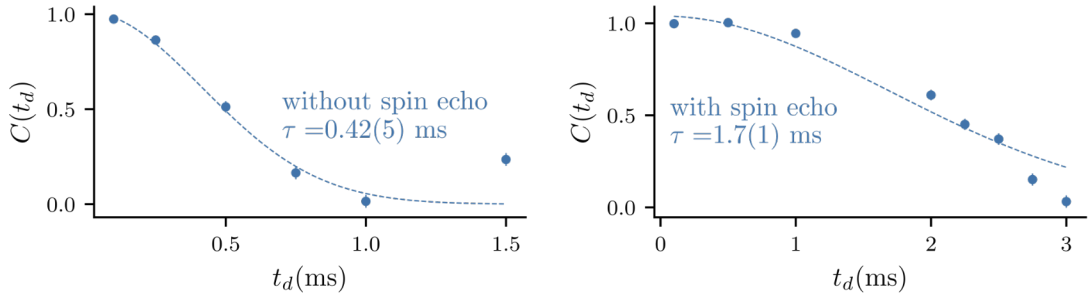

Figure 4.2: Spin coherence of the ground state qubit measured without the spin echo or including the spin echo. The model fitted to the data is a Gaussian $Ae^{-(t_d/\tau)^2/2}$, where A is a constant.

state preparation and measurement imperfections, we obtain the coherence time $\tau = 0.42(5)\,\text{ms}$. Using the spin-echo sequence increases the coherence time to $\tau = 1.7(1)\,\text{ms}$.

Optical qubit

We measure the coherence time for the optical qubit ($|\downarrow\rangle = |5S_{1/2},\, m_j = -\frac{1}{2}\rangle$ and

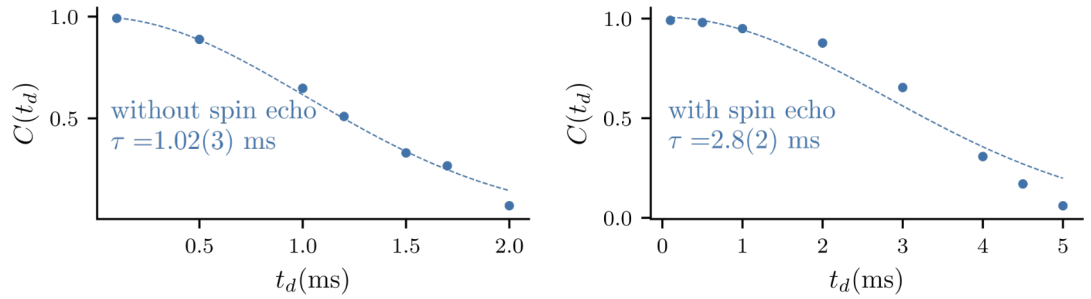

Figure 4.3: Spin coherence of the optical qubit measured without the spin echo or including the spin echo. The model fitted to the data is a Gaussian $ae^{-(t_d/\tau)^2/2}$, where a is a constant.

$|\uparrow\rangle = |4D_{5/2},\, m_j = -\frac{3}{2}\rangle$) using 674 nm laser carrier pulses, see Fig. 4.3. Also, in this case, the data agree well with a Gaussian model, yielding $\tau = 1.02(3)\,\text{ms}$ when using no spin echo and $\tau = 2.8(2)\,\text{ms}$ when introducing the spin-echo.

The good agreement to a Gaussian model for the contrast decay suggests that decoherence is dominated by low-frequency noise (compared to the time scale given by t_d).

4.1.2 Motional oscillator

Initialising the oscillator state

The main oscillator that we interact with in this work is the motional mode along the trap axis with angular frequency $\omega_z/2\pi = 1.17\,\text{MHz}$. The oscillator state is initialised before each experimental sequence close to the ground state. This is done by first applying the Doppler cooling sequence (2 ms), followed by continuous sideband cooling (1 ms) and pulsed sideband cooling (50 pulses); we achieve $\bar{n}_{\text{osc}} = 0.09(1)$ and we refer to this motional state[2] as $|\bar{n}_{\text{osc}}\rangle$. For a single ion, this is measured by looking at the relative excitation probabilities of the red (p_{rsb}) and blue (p_{bsb}) sidebands, where the mean thermal occupation $\bar{n}_{\text{osc}} = r/(1-r)$ with $r = p_{\text{rsb}}/p_{\text{bsb}}$ [121].

Decoherence

Decoherence in the oscillator state primarily arises from the ion interacting with the noisy environment provided by the trapping electrodes. The two dominant effects are heating and dephasing. Understanding the mechanisms that give rise to these effects is a challenging experimental task, with difficulties ranging from noise varying on different timescales to (very) specific details about trap fabrication and materials, which are still under active investigation in the ion trapping community [122, 123]. Heating and dephasing can be modelled by considering the harmonic oscillator being coupled to an environment [124]. Since these decoherence mechanisms lead to irreversible incoherent errors (unlike coherent errors, which can potentially be mitigated), it is important to quantify their effect.

Heating rate

Heating can be modelled by coupling the oscillator to an amplitude reservoir [124], where the average phonon occupation $\bar{n}_{\text{osc}}$ increases linearly (at short durations) with time as it thermalises with a bath. The heating rate $\dot{\bar{n}}_{\text{osc}}$ describes the rate of change of the average phonon occupation $\bar{n}_{\text{osc}}$.

[2] Using the ket notation for a thermal state is not ideal since thermal states are mixed states. However, we opted for this form for simplicity.

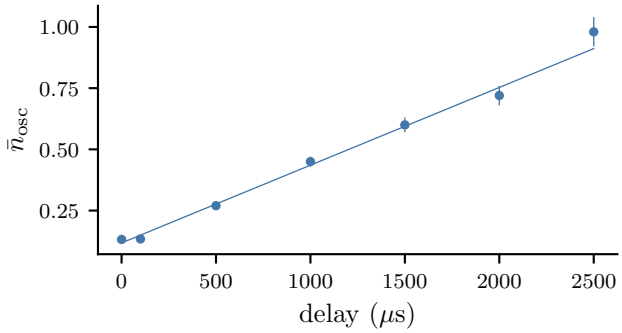

Figure 4.4: Heating rate measured on a single $^{88}\mathrm{Sr}^{+}$ ion. Measurement yields $\dot{\bar{n}}_{\mathrm{osc}} = 300(20)$ quanta/s at $\omega_z/2\pi = 1.17\,\mathrm{MHz}$.

We measure the heating rate of the axial motional mode by adding variable delays before measuring the $\bar{n}_{\mathrm{osc}}$ through sideband asymmetry, as explained above. As the average occupation number $\bar{n}_{\mathrm{osc}}$ increases linearly with time under the effect of heating, we determine $\dot{\bar{n}}_{\mathrm{osc}} = 300(20)$ quanta/s, as shown in Fig. 4.4.

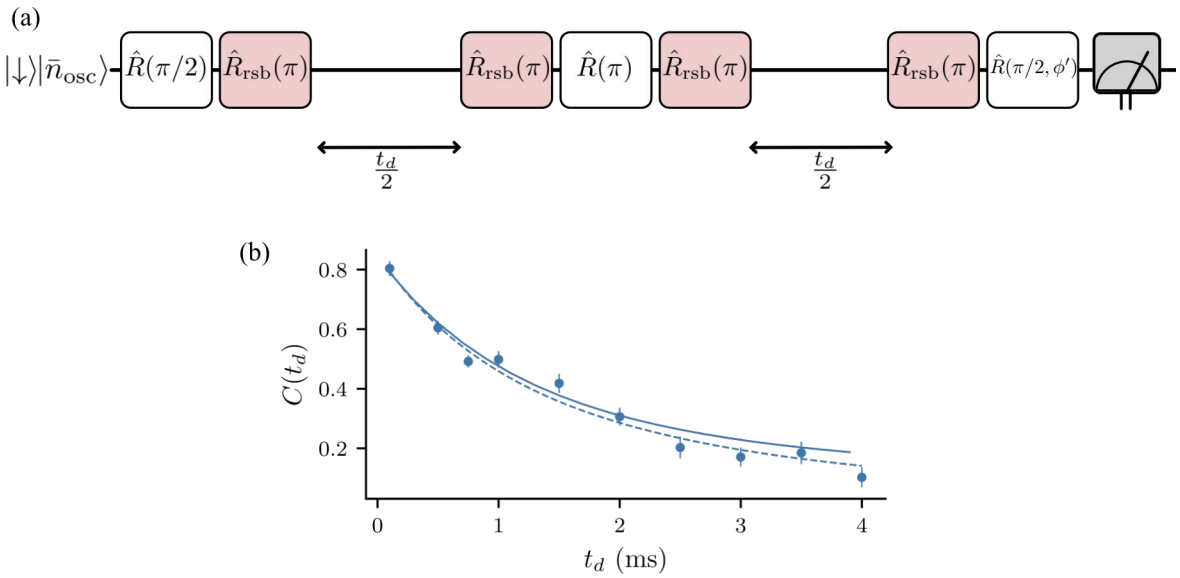

Figure 4.5: Motional coherence measured using a motional Ramsey experiment. (a) Pulse sequence including carrier rotations $\hat{R}(\theta', \phi')$ and red sideband rotations $\hat{R}_{\mathrm{rsb}}(\theta', 0) = \hat{R}_{\mathrm{rsb}}(\theta')$. (b) The dashed line is a fit to the experimental data using $A/(1 + \dot{\bar{n}}t)^2$. The continuous line shows the simulated decay model, including heating during the free evolution segments and red sideband pulses, initial thermal occupation and perfect carrier rotations.

To investigate the role of heating in the decoherence of the oscillator, we perform a Ramsey experiment between the Fock states $|0\rangle$ and $|1\rangle$, as shown in Fig. 4.5(a) [124].

To prepare the state $|\downarrow\rangle(|0\rangle + |1\rangle)/\sqrt{2}$, we use the fact that a spin superposition can be mapped to a motion superposition. First, we create a spin superposition using a carrier $\pi/2$-rotation. This spin superposition is then mapped to the motion using a π-pulse on the red sideband, leaving us with the desired state. We can add a spin-echo on the motion to cancel out small changes in the mode frequency. At the end of the sequence, the motional superposition is mapped back to the spin for readout. By scanning the phase of the final $\pi/2$-rotation on the spin, we can measure the remaining coherence of the Fock state superposition. An example of such a measurement, where we vary t_d is shown in Fig. 4.5(b).

Assuming that the decoherence we observe is only due to the heating of the ion (amplitude reservoir), then the contrast of the Ramsey fringes is given as

$$C = \hat{\rho}_{01}(t) + \hat{\rho}_{10}(t) = \frac{1}{(1+\dot{\bar{n}}t)^2}, \tag{4.6}$$

where we kept the same notation as in Ref. [124] with $\hat{\rho}$ the density matrix of the motional state[3] and $\hat{\rho}_{01}$ and $\hat{\rho}_{10}$, the two off-diagonal elements. By fitting the experimental data with $A/(1+\dot{\bar{n}}t)^2$, with A taking into consideration experimental imperfections such as the initial thermal distribution, we obtain

$$\dot{\bar{n}} = 360(30) \text{ quanta/s} \tag{4.7}$$

This value is consistent with what we measure using the sideband asymmetry method.

Moreover, we simulate the pulse sequence using the Lindblad master equation and QuantumOptics.jl package in Julia [125]:

$$\dot{\hat{\rho}} = -i\frac{i}{\hbar}[\hat{H}, \hat{\rho}] + \sum_i (\hat{J}_i \hat{\rho} \hat{J}_i^\dagger - \frac{1}{2}\hat{J}_i^\dagger \hat{J}_i \hat{\rho} - \frac{1}{2}\hat{\rho}\hat{J}_i^\dagger \hat{J}_i) \tag{4.8}$$

where $\hat{J}_i = \sqrt{\gamma_i}\hat{A}_i$ is a collapse operator. The heating effect is introduced in the simulation by setting the collapse operators [126] to $\sqrt{\dot{\bar{n}}_{\text{osc}}}\hat{a}^\dagger$ and $\sqrt{\dot{\bar{n}}_{\text{osc}}}\hat{a}$.

We consider the carrier pulses as perfect, take into consideration the initial thermal distribution with $\bar{n}_{\text{osc}} = 0.09$, and consider heating throughout the red sideband

[3] We truncate the motional state in the subspace of Fock states $|0\rangle$ and $|1\rangle$.

pulses (70 µs each) and free evolution time. The simulation and the experimental data show good agreement.

Based on these two considerations, we identify the heating as the dominant effect leading to decoherence in our oscillator and focus exclusively on this effect in our subsequent simulations.

4.2 Spin-dependent forces characterisation

4.2.1 Balancing the bichromatic tones

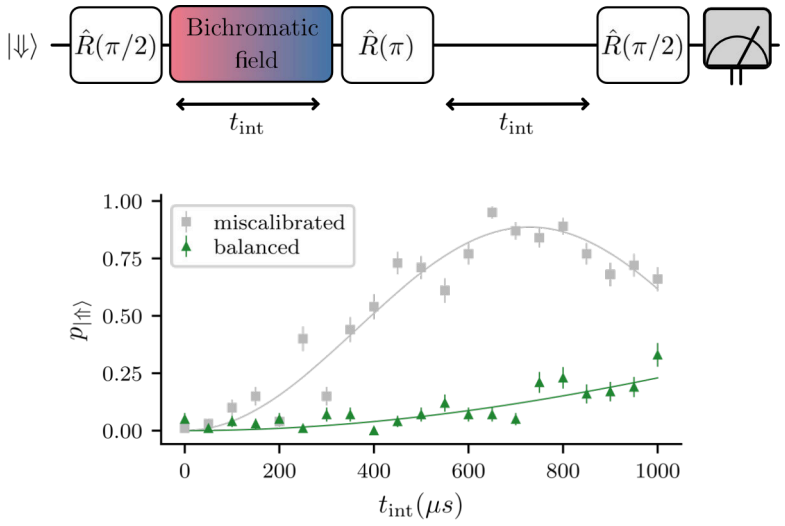

Figure 4.6: Example of balancing the strength of the tones in the bichromatic field. The bichromatic field is implemented using the 674 nm laser, while the rotations in the Ramsey sequence, $\hat{R}(\theta', 0) = \hat{R}(\theta')$, are implemented on the ground state qubit. If there is any differential light shift between $|\Downarrow\rangle$ and $|\Uparrow\rangle$, Ramsey fringes will be observed. The grey curve indicates a light shift of 340(10) Hz. By adjusting the power in each tone, we can suppress the Ramsey fringes (green line). The lift-off in $p_{|\Uparrow\rangle}$ in the "balanced" case is due to the limited coherence time of the ground state qubit.

An assumption made in deriving the Hamiltonian of the SDFs is that the strengths of the two tones are equal, i.e., $\Omega_b = \Omega_r = \Omega$ (see Sec. 2.3.2). In the experiment, we ensure that this is the case by using the ion as a sensor, as shown in Fig. 4.6. For this measurement, we use the ground state qubit, defined as $|\Downarrow\rangle \equiv |5S_{1/2},\, m_j = -\frac{1}{2}\rangle$ and $|\Uparrow\rangle \equiv |5S_{1/2},\, m_j = \frac{1}{2}\rangle$. We employ a spin-echo Ramsey experiment, where the bichromatic (674 nm transition) field is applied in the first arm for duration t_{int},

and a delay of the same duration is used in the second arm to compensate for other systematic frequency shifts. Given that the frequency splitting between the Zeeman levels in the ground state is 409 MHz, and the frequency spacing to other manifolds is much larger (the closest being ≈ 10 THz), we assume any off-resonant coupling to these manifolds will result in an identical light shift on both qubit states $|\Downarrow\rangle$ and $|\Uparrow\rangle$. Therefore, any differential light shift between the two ground state levels can only originate from the imbalance of the tones, leading to Ramsey fringes. When the tones are balanced, we expect a straight line at $p_{|\Uparrow\rangle} = 0$. An example of calibration is shown in Fig. 4.6. However, due to the limited coherence time of the ground state qubit (see Fig. 4.2(b)), there is still a deviation from 0 even when the tones are balanced.

For the bichromatic field configuration in this measurement, for a $\hat{\sigma}_\phi$ SDF, the detuning of the tones is set to $\delta = \pm(\omega_z + \Delta)$, and for a $\hat{\sigma}_z$ SDF, $\delta = \pm(\omega_z + \Delta)/2$. We set $\Delta/2\pi = 100$ kHz to suppress any off-resonant driving of the motion; what value one chooses for Δ depends on the amount of laser power used for the calibration experiment.

Using the ground state qubit instead of the optical qubit for this measurement allows us to separate light shifts induced by unbalanced tones (quadrupole light shifts) from those induced by off-resonant coupling to other levels (mainly dipole light shifts). The latter effect is discussed in the next section.

4.2.2 ac Stark shift

The tones in the bichromatic field are detuned from the qubit frequency ω_q, which is calibrated using a low power setting and a corresponding longer pulse. This means that the frequency measured is close to the bare qubit frequency. However, when we apply the bichromatic field, we use higher power values, which means that qubit frequency is light shifted by Δ_{LS} from the bare one due to the off-resonant coupling to the other levels becoming significant.

As shown in Sec. 2.2.4, this effect can be modeled as $\hat{\sigma}_z$ term, which can be added to the SDF bichromatic Hamiltonian, Eq. (2.44). A $\hat{\sigma}_z$ SDF commutes with such a

term, which means that we can mitigate its effect by sandwiching the interaction in a spin-echo Ramsey sequence, see Sec. 4.2.6. However, this is not true for the SDFs conditioned on $\hat{\sigma}_\phi$. In this case, we search to calibrate Δ_{LS} and then introduce it in the control software such that the tones are symmetrically detuned from the light-shifted qubit frequency.

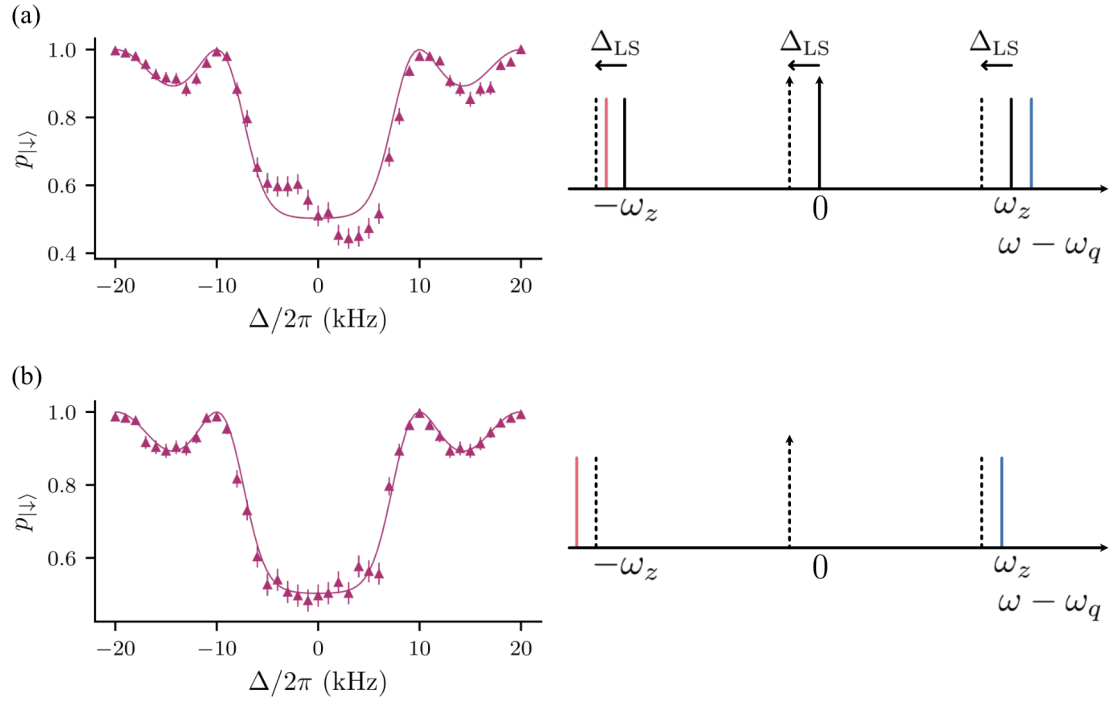

Figure 4.7: Example of calibrating the qubit light shift using SDF dynamics. The continuous lines represent the ideal dynamics inferred using Eq. (2.41) with $\bar{n}_{\mathrm{osc}} = 0.09$, $\Omega/2\pi = 95\,\mathrm{kHz}$ (0.5 mW), $\eta = 0.049$, determined through independent measurements, and $t_{\mathrm{probe}} = 100\,\mu\mathrm{s}$. (a) Dynamics without accounting for the ac Stark shifts Δ_{LS} introduced by off-resonant coupling of the bichromatic field. On the right-hand side, we show the frequency configuration of the tones in the bichromatic field. Solid lines represent the original carrier and sideband frequencies in the absence of the laser-ion interaction. Dashed lines show the shifted frequencies for the qubit and sideband transitions when the interaction with the laser light is switched on. (b) Dynamics after calibrating the ac Stark shifts to $\Delta_{\mathrm{LS}}/2\pi = 0.5\,\mathrm{kHz}$. From the light shift measurement that we use as guidance (see text), we expect a correction of $\Delta_{\mathrm{LS}}/2\pi = 0.625\,\mathrm{kHz}$. We consider the two measurements to be in good agreement. We illustrate how the frequencies of the bichromatic field tones need to be adjusted to be symmetrically detuned from the shifted frequency of the qubit and the sidebands.

We can infer the magnitude of Δ_{LS} by using a pulse sequence as shown in Fig. 4.6, where we use the optical qubit ($|\downarrow\rangle \leftrightarrow |\uparrow\rangle$) instead, the rotations are performed on

this qubit as well, and the bichromatic field pulse is replaced by a single beam far-detuned from qubit transition by δ_{probe}. The largest contribution to the light shift comes from being off-resonant with the qubit transition itself, $2\Omega^2/(4\delta_{\text{probe}})$. We can neglect the contribution of the other Zeeman transitions within the $S_{1/2} - D_{1/2}$ due to the significant Zeeman splitting $> 240\,\text{MHz}$ and given the transitions that we can couple within our geometry. The second largest contribution, Δ_{LS}, arises from the off-resonant dipole coupling of $S_{1/2}$ to $P_{1/2}, P_{3/2}$ and $D_{5/2}$ to $P_{3/2}$ [127]. Combining the two effects, the total light shift is $\Delta_{\text{LS,total}} = \Delta_{\text{LS}} + 2\Omega^2/(4\delta_{\text{probe}})$ and this gives the frequency of the Ramsey fringes. We measure $\Delta_{\text{LS,total}}$ as function of $\delta_{\text{probe}}/2\pi \in [-8\,\text{MHz}, -4\,\text{MHz}] \cup [4\,\text{MHz}, 8\,\text{MHz}]$ and infer $\Delta_{\text{LS}}/2\pi \approx 5\,\text{kHz}$ at $4\,\text{mW}$ laser power ($\Omega/2\pi = 375\,\text{kHz}$).

We use the inferred value as a guidance. However, in the experiment, we usually look at population dynamics. An example is shown in Fig. 4.7. We initialise in $|\downarrow\rangle$, apply the $\hat{\sigma}_\phi$ for a fixed pulse duration (t_{probe}) and vary Δ the detuning from the motional mode. If the tones are symmetrically detuned from the light-shifted qubit frequency, then we expect the population to stay at $p_{|\downarrow\rangle} = 0.5$ in the centre. We shift the frequency of the two tones in the same direction until the imbalance is suppressed.

4.2.3 Motional mode frequency calibration

To calibrate small offsets in the frequency of the oscillator, we apply a $\hat{\sigma}_\phi$ SDF to $|\downarrow\rangle\,|\bar{n}_{\text{osc}}\rangle$. We use two SDF pulses; for the first, the spin conditioning is set to $\hat{\sigma}_\phi$, while for the second, it is set to $-\hat{\sigma}_\phi$ (achieved by shifting the phase of both tones by π). This produces a sharp feature when scanning Δ; see Fig. 4.8. This feature occurs when the SDF is on resonance with the harmonic oscillator, as only then can we split the oscillator wavepacket in phase space and return perfectly to the initial motional state[4]. We can calibrate offsets in the motional mode frequency by fitting this feature using a Lorentzian.

We found that light shifts can slightly influence the calibration of the motional mode frequency. For example, in the simulated data in Fig. 4.8, a $\Delta_{\text{LS}}/2\pi = 1\,\text{kHz}$

[4]This is true only when assuming no motional decoherence effects, which only affects the contrast of the feature.

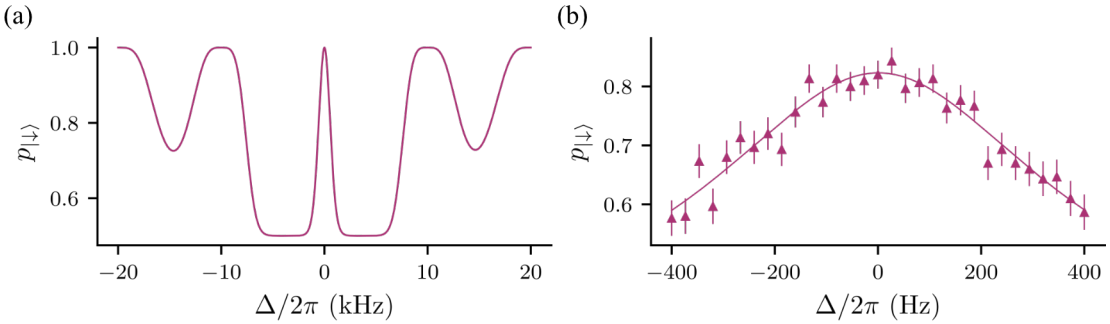

Figure 4.8: Motional mode frequency calibration using a spin-dependent force. The calibration method involves applying two consecutive SDF pulses of the same duration, t_{SDF}. The first pulse is conditioned on $\hat{\sigma}_\phi$, and the second pulse is conditioned on $-\hat{\sigma}_\phi$. When the SDF driving frequency matches the oscillator's frequency, the first pulse splits the wavefunction into two coherent states displaced in opposite directions, and the second pulse returns the superposition to the initial state. This creates a sharp feature in the SDF dynamics as a function of Δ. (a) Simulated dynamics of two consecutive SDF pulses, when resonant with the motional mode, with parameters $t_{\mathrm{SDF}} = 100\,\mu\mathrm{s}$, $\Omega/2\pi = 95\,\mathrm{kHz}$ ($0.5\,\mathrm{mW}$), and $\eta = 0.049$. (b) A scan over the sharp feature used to calibrate the motional mode frequency $\omega_z/2\pi = 1.173\,45(8)\,\mathrm{MHz}$ with $0.5\,\mathrm{mW}$ and $t_{\mathrm{SDF}} = 130\,\mu\mathrm{s}$. The power and probe duration can be adjusted to increase measurement accuracy.

translates to a frequency offset of the order $0.25\,\mathrm{kHz}$. Therefore, using lower intensities to drive the SDF as part of this calibration is advisable.

4.2.4 Measuring the strength of the SDF

Once all the calibrations are complete, we can measure the strength of the SDF. Our goal is to map the strength of the SDF as a function of $2\Omega/\delta$ for both $\hat{\sigma}_\phi$ and $\hat{\sigma}_z$ SDFs created using bichromatic fields (see Sec. 2.3.2). By initialising the spin state such that it is not an eigenstate of $\hat{\sigma}_\phi$ or $\hat{\sigma}_z$, respectively, and applying the SDF for variable durations, we can fit the dynamics using Eq. (2.41) and infer Ω_{SDF}.

For the $\hat{\sigma}_z$ SDF, a long ramp duration t_{ramp}, compared to $2\pi/(\omega_z/2)$, is required (see Sec. 4.2.6). When the SDF is on resonance we are unable to probe a significant part of the dynamics, as shown in Fig. 4.9, leading to inaccurate calibrations of the SDF strength. Therefore, we apply the SDF off-resonantly, i.e., with $\Delta \neq 0$. Although this is not necessary for the $\hat{\sigma}_\phi$ SDFs, to maintain consistency in comparing the strengths of different SDF types, we use detuned SDFs for all the measurements.

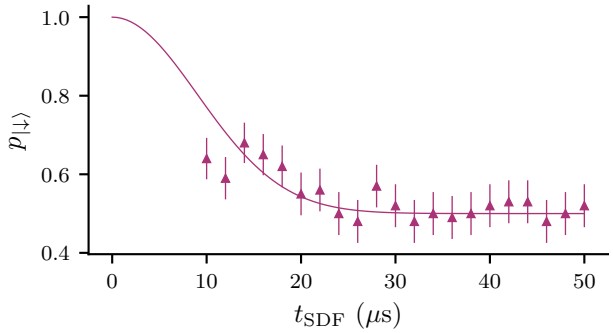

Figure 4.9: Example of SDF dynamics using amplitude-shaped pulses. The motional mode is driven resonantly with the SDF. As the overlap between the two coherent states decreases, $p_{|\downarrow\rangle} \to 0.5$. As a result of $t_{\mathrm{ramp}} = 10\,\mu\mathrm{s}$, we are unable to see the start of the dynamics as the first pulse has a full width at half maximum of $t_{\mathrm{SDF}} = 10\,\mu\mathrm{s}$.

One consideration when using detuned SDFs is that the denominator of $2\Omega/\delta$ changes: $\delta = \omega_z + \Delta$ for the $\hat{\sigma}_\phi$ SDF and $\delta = (\omega_z + \Delta)/2$ for the $\hat{\sigma}_z$ SDF. Moreover, as we increase the power to raise Ω, we also adjust Δ (increasing it as well) to keep $\Omega_{\mathrm{SDF}}/\Delta$ constant. This allows us to explore a similar region of phase space (see Fig. 2.4) for each measurement. Going further out in phase space makes the dynamics more sensitive to motional mode errors.

We compare the inferred values of the SDF strength to theory (Eq. (2.47) and Eq. (2.48)). The theory lines are inferred from calibrating ω_z (Sec. 4.2.3), η and Ω independently. By fitting carrier Rabi flops at different powers, we infer $\Omega/2\pi$ values in the range $0.095 - 0.8$ MHz[5] using a beam waist radius of $\approx 20\,\mu\mathrm{m}$ and $0.5 - 35$ mW laser powers. By cooling down the motion close to the ground state and concurrently fitting a carrier and blue sideband Rabi flops, we infer η.

4.2.5 $\hat{\sigma}_\phi$ SDF

For setting up the $\hat{\sigma}_\phi$ SDF, the bichromatic field is applied with the configuration shown in Fig. 4.10(a). The system is initialised in $|\downarrow\rangle\,|\bar{n}_{\mathrm{osc}}\rangle$ and we apply the SDF with various Ω and corresponding detunings from the motion Δ. The ramp for the SDF is $t_{\mathrm{ramp}} = 3.6\,\mu\mathrm{s}$ (≈ 4 times longer than the timescale given by $2\pi/\omega_z$).

[5]In this context, Ω represents the strength of a single tone of the bichromatic field. Since the bichromatic field in our system is implemented by combining two such tones (see Sec. 3.3.2), the value of Ω corresponds to that of a monochromatic field divided by $\sqrt{2}$.

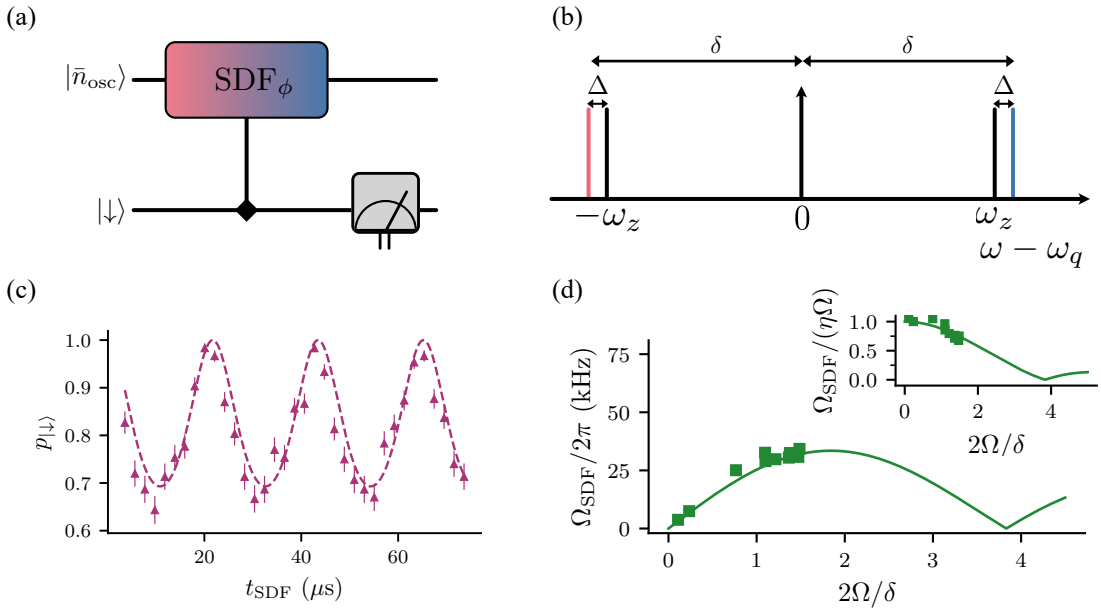

Figure 4.10: Evaluating the strength of $\hat{\sigma}_\phi$ SDFs generated using a bichromatic field. (a) Pulse sequence used to measure the SDF dynamics employed for determining the strength of the SDF, Ω_{SDF}. (b) Bichromatic field configuration for generating a detuned $\hat{\sigma}_\phi$ SDF. (c) Example dynamics of a detuned SDF applied for variable durations t_{SDF}, with $2\Omega/\delta = 1.1$ and $\Delta/2\pi = 45\,\mathrm{kHz}$, where Ω is the strength of a single tone in the bichromatic field, assuming that the tones are balanced. We fit (dashed line) the dynamics to infer Ω_{SDF}. (d) SDF magnitude Ω_{SDF} (normalised by $\eta\Omega$ in the inset) versus $2\Omega/\delta$. The solid lines show the analytical dependence; as predicted by the theory and shown explicitly in the inset, the coupling follows the Bessel functions ($|J_0 + J_2|$).

An example of dynamics for $2\Omega/\delta = 1.1$, with $\Delta/2\pi = 45\,\mathrm{kHz}$, is shown in Fig. 4.10(b). By fitting

$$\begin{aligned} p_{|\downarrow\rangle} &= \frac{1 + e^{-f(\alpha)}}{2}, \\ f(\alpha) &= |2\alpha(t_{\mathrm{SDF}})|^2 \left(\bar{n}_{\mathrm{osc}} + \frac{1}{2}\right) = \left(2\frac{\Omega_{\mathrm{SDF}}}{\Delta} \sin\left(\frac{\Delta t_{\mathrm{SDF}}}{2}\right)\right)^2 \left(\bar{n}_{\mathrm{osc}} + \frac{1}{2}\right), \end{aligned} \tag{4.9}$$

where we used Eq. (2.41) and (2.35), we determine Ω_{SDF}. We compare the inferred values to theory $\Omega_{\mathrm{SDF}} = \eta\Omega|J_0(2\Omega/\delta) + J_2(2\Omega/\delta)|$ as shown in Fig. 4.10(c). We observe good agreement between theory and experiment and confirm that the effect of the non-commuting carrier on the SDF is to suppress its magnitude.

4.2.6 $\hat{\sigma}_z$ SDF

For setting up the $\hat{\sigma}_z$ SDF, the bichromatic field is applied with the configuration shown in Fig. 4.13(a). Using $\delta = (\omega_z + \Delta)/2$ and applying the RWA with respect

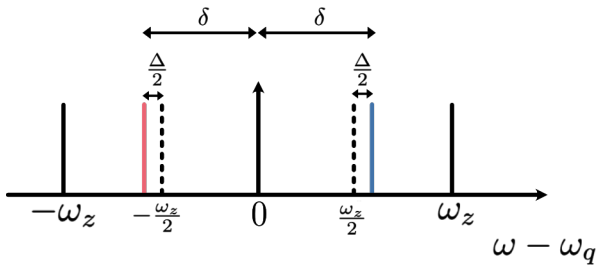

Figure 4.11: Bichromatic field configuration for generating a detuned $\hat{\sigma}_z$ SDF. The SDF off-resonantly drives the motional mode with ω_z (continuous black lines). The bichromatic field is, however, detuned from $\omega_z/2$ (dashed black lines).

to ω_z we rewrite Eq. (2.48) as

$$\hat{H}_z = -i\hbar\frac{\Omega_{\text{SDF}}}{2}\hat{\sigma}_z(\hat{a}e^{i(\Delta t-2\phi_d)} - \hat{a}^\dagger e^{-i(\Delta t-2\phi_d)}), \tag{4.10}$$

hence, by defining the detuning from $\omega_z/2$ as $\Delta/2$, we are able to recover Eq. (2.26) up to a phase and expect similar dynamics as described in Sec. 2.3.

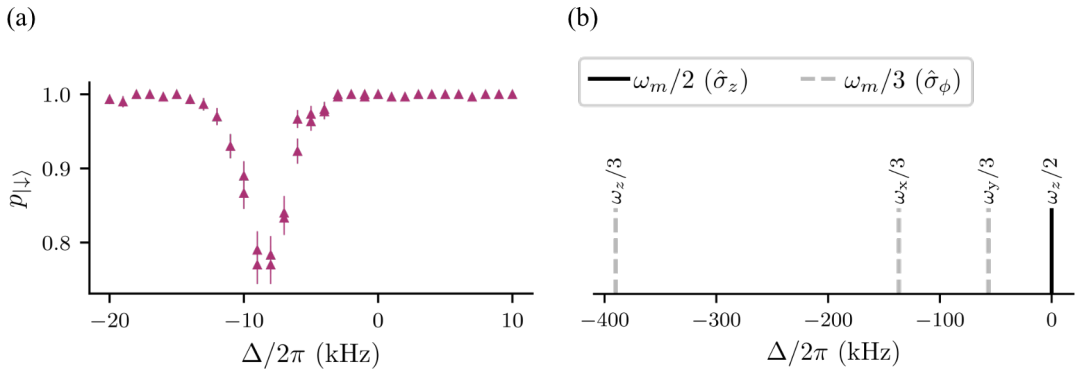

Figure 4.12: Dynamics of a $\hat{\sigma}_z$ conditioned SDF created using a bichromatic field. (a) Example dynamics of applying the bichromatic field with $\delta \approx \omega_z/2$ on the system initialised in $|\downarrow\rangle\,|\bar{n}_{\text{osc}}\rangle$. (b) Nearby spin-motion coupling resonances for a single ion with motional modes described by ω_z, ω_x and ω_y.

First, we want to check if the resulting effective spin-dependent force is conditioned on $\hat{\sigma}_z$. By initialising the system in $|\downarrow\rangle\,|\bar{n}_{\text{osc}}\rangle$ and applying the bichromatic field in this configuration, we expect that the spin state remains unchanged. In Fig. 4.12(a), we apply the bichromatic field with $t_{\text{ramp}} = 10\,\mu\text{s}$ ($\approx 6\times$ that the time scale given by $2\pi/(\omega_z/2)$; see Sec. 2.3.4 for details on the ramp duration requirements) while scanning the detuning Δ and measure $p_{|\downarrow\rangle}$. While the population remains

at $p_{|\downarrow\rangle} = 1$ for some detuning values, we observe a resonance. This is due to a $\hat{\sigma}_\phi$ SDF on one of the radial modes, which comes into resonance at $\omega_y/3$, see Eq. (2.46). By adjusting the strength of the trap rf drive providing the radial confinement, the frequency of the radial modes can be adjusted to reduce off-resonant driving of undesired terms. The motional mode configuration used for subsequent experiments is shown in Fig. 4.12(b).

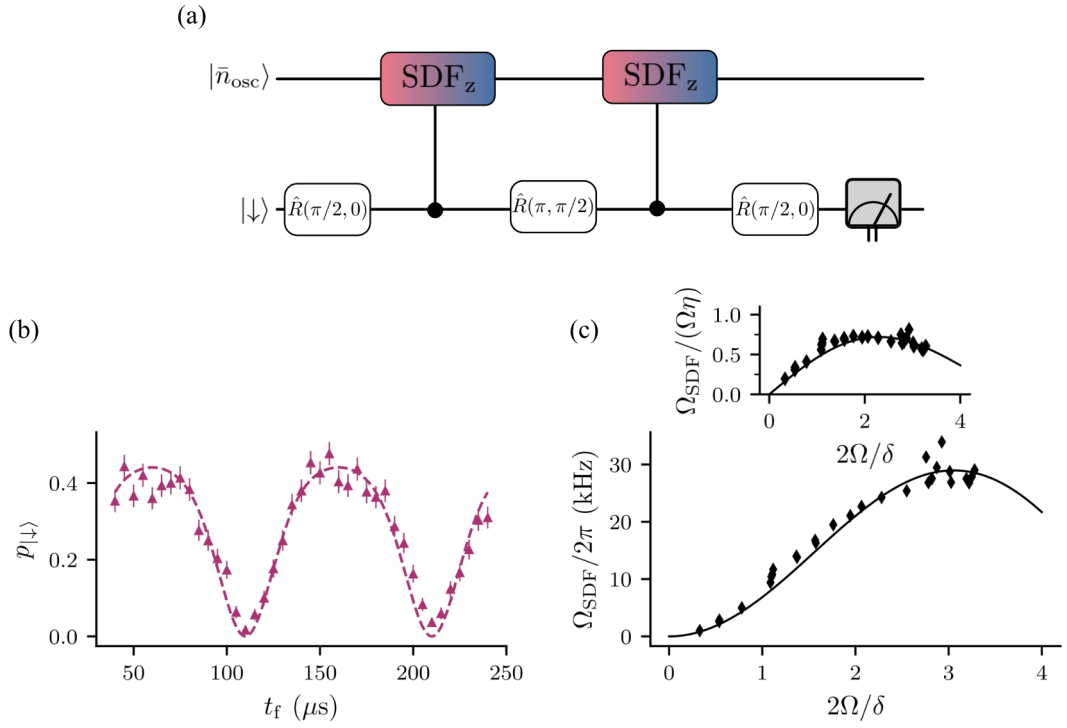

Figure 4.13: Evaluating the strength of $\hat{\sigma}_z$ SDFs generated using a bichromatic field. (a) Pulse sequence used to measure the SDF dynamics employed for determining the strength of the SDF, Ω_{SDF}. (b) Example dynamics of detuned SDF applied for variable durations t_f, full-width of the two SDF pulses ($t_{\mathrm{ramp}} = 5\,\mu\mathrm{s}$), with $2\Omega/\delta = 1.1$ and $\Delta/2\pi = 20\,\mathrm{kHz}$, where Ω is the strength of a single tone in the bichromatic field, assuming that the tones are balanced. We fit (dashed line) the dynamics to infer Ω_{SDF}. (c) SDF magnitude Ω_{SDF} (normalised by $\eta\Omega$ in the inset) versus $2\Omega/\delta$. The solid lines show the analytical dependence; as predicted by the theory and shown explicitly in the inset, the coupling follows the Bessel functions ($|J_1 + J_3|$).

Going back to measuring the magnitude of $\hat{\sigma}_z$ SDF, we want, as in the case of the $\hat{\sigma}_\phi$ SDF, to split the oscillator wavefunction. Hence, we apply $\hat{R}(\pi/2, 0)$ before the SDF pulse, as shown in Fig. 4.13(a), such that the spin state is not an eigenstate of $\hat{\sigma}_z$. By applying the last $\hat{R}(\pi/2, 0)$, we are able to evaluate the overlap between the two

displaced harmonic oscillator states when measuring the spin, with the dynamics being described by Eq. (2.41). Moreover, we can also introduce a spin-echo pulse $\hat{R}(\pi, \pi/2)$, as shown in Fig. 4.13(a), allowing to echo out any light shifts or slow magnetic field fluctuations during the SDF pulses, which would introduce systematic offsets in the Ω_{SDF} measurement. Alternating the phase ϕ' of the rotations, i.e., $0 - \pi/2 - 0$, makes the evolution more robust to miscalibrations in the $\pi/2$-pulses, which could cause under or over rotations [89].

The rotation $\hat{R}(\pi, \pi/2)$ flips the spin state, which means that if we are not careful, we can undo the displacement. To avoid this, we push the motional phase of the second SDF pulse by π. Moreover, while we are not applying the SDF, the oscillator continues evolving, which potentially changes the phase relationship between the oscillator and the SDF applied in the second pulse (in Eq. (4.10), given by $2\phi_d$). As our rf channels are in phase tracking mode (see Sec. 3.3.1), if the SDF is set on resonance with the oscillator frequency, there will be no catch-up to do. However, here, we drive the SDF off-resonantly, so we need to adjust the motional phase of the SDF ($2\phi_d$)) by a phase $\Delta\, t_{\mathrm{delay},1}$, where $t_{\mathrm{delay},1}$ is the time elapsed from the end of the first SDF pulse to the beginning of the second SDF pulse. Additionally, in the experiment, we push the motional phase of the second SDF pulse by an extra $\Delta\, t_{\mathrm{delay},2}$, where $t_{\mathrm{delay},2}$ is the time elapsed from the beginning to the end of the first SDF pulse, essentially making the motional phase at the beginning of two SDF pulses match. This is reminiscent of using first-order Walsh modulation[6] [128] in implementing two-qubit gates using this SDF [129]. Overall, we push the motional phase of the second SDF pulse by $2\phi_d \to 2\phi_d - \pi - \Delta(t_{\mathrm{delay},1} + t_{\mathrm{delay},2})$, which is done by adjusting the phase of the blue detuned tone by $-\pi - \Delta(t_{\mathrm{delay},1} + t_{\mathrm{delay},2})$, where it is useful to remember $\phi_d = (\phi_b - \phi_r)/2$). We show an example of dynamics where we scan the duration of the two SDF pulses in Fig. 4.13(b).

[6] In the case of the first-order Walsh modulation, we would omit to push the motional phase of the second SDF pulse by π. This would return any phase space trajectories back to the origin irrespective of the duration for which the SDF is applied, making the two-qubit gate robust against loop closure errors. However, in the case of measuring the SDF strength, we want to be displaced from the origin.

We infer Ω_{SDF} by fitting the dynamics using

$$\begin{aligned} p_{|\downarrow\rangle} &= \frac{1-e^{-f(\alpha)}}{2}, \\ f(\alpha) &= |2\alpha(t_f)|^2 \left(\bar{n}_{\mathrm{osc}} + \frac{1}{2}\right), \end{aligned} \tag{4.11}$$

where $\alpha(t_f)$ is inferred (up to a factor i) as

$$\begin{aligned} \alpha(t_f) &= \frac{\Omega_{\mathrm{SDF}}}{2}\int_0^{t_f} g(t)e^{i(\Delta\, t-2\phi_d)}dt = \Omega_{\mathrm{SDF}}\int_0^{t_f/2} g(t)e^{i(\Delta t-2\phi_d)}dt \\ &= \frac{ie^{-i(t_{\mathrm{ramp}}\Delta+2\phi_d)}\left(1+e^{it_{\mathrm{ramp}}\Delta}\right)\left(-e^{\frac{it_f\Delta}{2}}+e^{it_{\mathrm{ramp}}\Delta}\right)\pi^2}{2\Delta(\pi-t_{\mathrm{ramp}}\Delta)(\pi+t_{\mathrm{ramp}}\Delta)}, \end{aligned} \tag{4.12}$$

where we take into into consideration the two adiabatically switched on and off pulses and resetting the motional phase at the beginning of the second SDF pulse to the one at the beginning of the first SDF pulse

$$g(t) = g(t \mod (t_f/2)) = \begin{cases} \sin^2(\frac{\pi t}{2t_{\mathrm{ramp}}}),\ t < t_{\mathrm{ramp}} \\ 1,\ t_{\mathrm{ramp}} \le t \le t_f/2 - t_{\mathrm{ramp}} \\ \sin^2(\frac{\pi(t_f/2-t)}{2t_{\mathrm{ramp}}}),\ t_f/2 - t_{\mathrm{ramp}} < t < t_f/2. \end{cases} \tag{4.13}$$

We measure and fit SDF dynamics for various Ω and corresponding Δ values and compare the inferred Ω_{SDF} values to theory $\Omega_{\mathrm{SDF}} = \eta\Omega|J_1(2\Omega/\delta)+J_3(2\Omega/\delta)|$ as shown in Fig. 4.13(c). We observe good agreement between theory and experiment, confirming that we understand the interplay between the non-commuting carrier and spin-coupling terms in giving rise to an effective spin-dependent force conditioned on $\hat{\sigma}_z$.

5

Circumventing noncommutativity by using phase-stabilised standing-waves

Contents

The main aim of this chapter is to present experimental results demonstrating that using a bichromatic standing wave (SW) instead of a travelling wave (TW) can overcome the saturation in the spin-dependent force (SDF) magnitude caused by the non-commuting carrier off-resonant term. Achieving precise phase control of the SW

at the ion's position enabled us to explore the regime where the carrier contribution is strongly suppressed. The theoretical background is detailed in Sec. 2.4. In the laboratory, we create the SW using two counterpropagating 674 nm beams, b1 and b2, and phase stabilise it at the ion's position using both a fast feedback stage (with a photodiode, PD, as the sensor) and a slow feedback stage (using the ion as the sensor). The setup and the implementation of the phase stabilisation process are described in Sec. 3.4. Our investigation begins with coherent operations between a monochromatic SW and an ion, followed by generating an SDF using a bichromatic SW. Finally, we use the SDF to implement a two-qubit entangling gate. The results of this chapter are published in Ref. [64]. For further details on these experiments, consulting Sebastian Saner's thesis might also be beneficial, as we collaborated closely on this project.

As a reminder, the SW is used to drive coherent interactions on the optical qubit, $|\downarrow\rangle = |5S_{1/2},\, m_j = -\frac{1}{2}\rangle$ and $|\uparrow\rangle = |4D_{5/2},\, m_j = -\frac{3}{2}\rangle$, via a quadrupole transition.

5.1 Ion interacting with monochromatic standing wave

Coherent operations between a monochromatic SW and an ion have been studied previously in various setups involving trapped ions, such as using a cavity [96], reflecting from the trap chip [116], integrating optics [118], and employing free-space approaches [117]. Apart from the free-space method, which we also use, all other setups provide good passive stability for the phase of the SW relative to the ion. In terms of phase stabilisation, a difference between our method and that in Ref. [117] is that we adjust the SW's position relative to the ion using an AOM, while they shift the ion relative to the SW by modifying the DC potentials of the trap. Moreover, they rely solely on the ion as a sensor.

5.1.1 Ion at different points in the SW

To see the first signs of the SW interacting with the ion, we do what we call a SW phase scan. The spin is initialised in $|\downarrow\rangle$. For this, we apply both counterpropagating

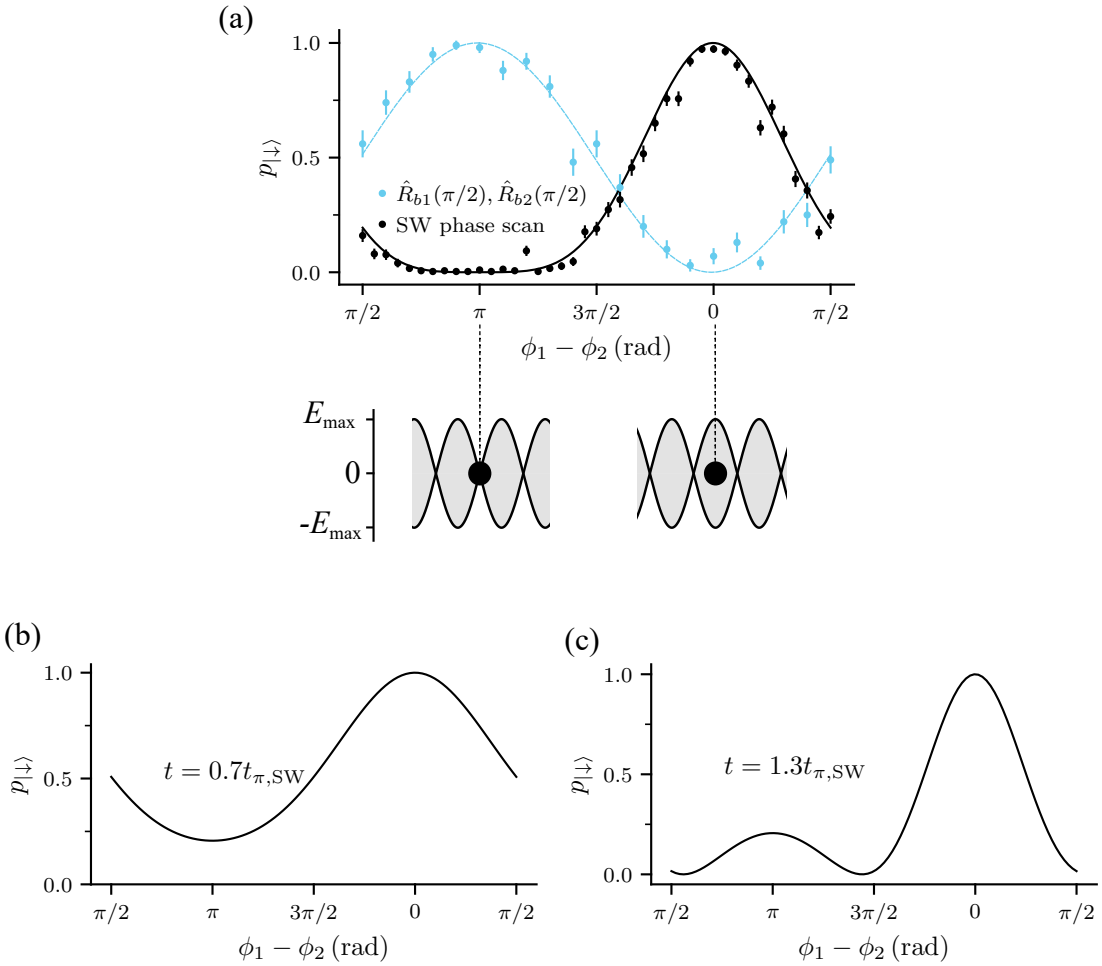

Figure 5.1: Monochromatic standing-wave phase scan on a single ion. (a) Spin dynamics as a function of the SW phase at the ion position while the SW is resonant with the carrier (black). We indicate the ion positions in the SW that maximise ($\phi_1 - \phi_2 = \pi$) or minimise ($\phi_1 - \phi_2 = 0$) the carrier coupling for a quadrupole transition. The SW pulse duration $t = t_{\pi,\mathrm{SW}}$ is set such that complete population transfer, i.e., $p_{|\downarrow\rangle} = 0$, is achieved at maximal carrier coupling. We also indicate the phase scan of a zero-delay Ramsey experiment executed with the two different branches (cyan). The continuous lines represent theory curves. (b), (c) Theory lines indicating how the dynamics of the SW phase scan would look like for probing times $t < t_{\pi,\mathrm{SW}}$ and $t > t_{\pi,\mathrm{SW}}$, respectively.

beams forming the SW simultaneously. We set the frequency of these laser beams such that we are in resonance with the carrier and aim to do a π-pulse with the standing wave while scanning the relative phase between the two counterpropagating beams $\phi_1 - \phi_2$. Doing a π-pulse with the SW means that $\Omega t/2 = \pi/4$[1] in

[1]This setting is equivalent to doing a $\pi/2$-pulse with an individual branch, see Eq. (2.20).

Eq. (2.62), which becomes

$$p_{|\downarrow\rangle} = \cos^2\left(\frac{\pi}{2}\sin\left(\frac{\phi_1-\phi_2}{2}\right)\right). \tag{5.1}$$

As we scan $\phi_1-\phi_2$, we move the SW with respect to the ion and, in doing so, modify the coupling strength of the carrier. The interaction duration $t_{\pi,\mathrm{SW}}$ is calibrated to give complete inversion, $p_{|\downarrow\rangle} = 0$ when the carrier coupling is maximised, i.e. $\phi_1 - \phi_2 = \pi/2$. We show a dynamics example in Fig. 5.1(a).

The SW scan is recorded with both feedback stages enabled, starting the phase scan from the ion feedback setpoint $\phi_1 - \phi_2 = \phi_{\mathrm{ST}} = \pi/2$. For comparison, we also include a phase scan from the zero-delay Ramsey experiment, $\hat{R}_{\mathrm{b1}}(\pi/2, \phi')$ and $\hat{R}_{\mathrm{b2}}(\pi/2, 0)$, as shown in Fig. 3.10(b). Both dynamics give information about the relative phase between the counterpropagating beams at the ion's position. The decision to use the zero-delay Ramsey for implementing ion feedback was motivated by $p_{|\downarrow\rangle}$ showing a slightly simpler dependence on $\phi_1 - \phi_2$ in this case.

To understand the dynamics of the SW phase scan, we Taylor expand Eq. (5.1) around $\phi_1-\phi_2 = 0$ and $\phi_1-\phi_2 = \pi$. Near $\phi_1-\phi_2 = 0$, the carrier coupling strength, represented by $\sin((\phi_1 - \phi_2)/2)$, is linear for small variations in $\phi_1 - \phi_2$, resulting in a quadratic dependence of $p_{|\downarrow\rangle}$ on $\phi_1 - \phi_2$ around this point. Near $\phi_1 - \phi_2 = \pi$, the carrier coupling strength becomes quadratic[2], leading to a quartic dependence of $p_{|\downarrow\rangle}$ on $\phi_1 - \phi_2$ around this point, as observed in Fig. 5.1(a).

At the bottom of Fig. 5.1(a), we also show where the ion is in the SW when $\phi_1 - \phi_2 = 0$ and $\phi_1 - \phi_2 = \pi$.

While not shown in Fig. 5.1, it is important to note that the coupling to the first-order sidebands (motion) is proportional to $\cos((\phi_1 - \phi_2)/2)$ (see Sec. 2.4.2), which results in reversed-phase dependencies and sensitivities. Around $\phi_1 - \phi_2 = 0$, the coupling strength ($p_{|\downarrow\rangle}$) is quadratic (quartic) in $\phi_1 - \phi_2$. While around $\phi_1 - \phi_2 = \pi$, the coupling strength ($p_{|\downarrow\rangle}$) is linear (quadratic) in $\phi_1 - \phi_2$.

In Fig. 5.1(b) and Fig. 5.1(c), we show examples of applying the SW interaction for $t > t_{\pi,\mathrm{SW}}$ and $t < t_{\pi,\mathrm{SW}}$, respectively.

[2] $\sin(\Delta(\phi_1 - \phi_2)/2 + \pi/2) = \sin(\Delta(\phi_1 - \phi_2)/2)\cos(\pi/2) + \cos(\Delta(\phi_1 - \phi_2)/2)\sin(\pi/2) \approx 1 - (\Delta(\phi_1 - \phi_2))^2/8$, where $\Delta(\phi_1 - \phi_2)$ represents small variations around π.

By controlling the phase of the SW at the position of the ion, we can realise any ratio between the carrier and the sideband coupling. We are particularly interested in configurations that either maximise the carrier coupling and minimise the sideband coupling or vice versa. This is achieved by setting $\phi_1 - \phi_2 = \pi$ (at the SW node) to enhance carrier coupling, or $\phi_1 - \phi_2 = 0$ (at the SW anti-node) to enhance sideband coupling. Fig. 5.2 displays detuning scans over the carrier and the first motional sideband at these two specific points within the SW. When probing the suppressed motional sideband, see Fig. 5.2 left, we observe only features that are due to the off-resonant (by $\approx 1.2\,\mathrm{MHz}$) carrier coupling.

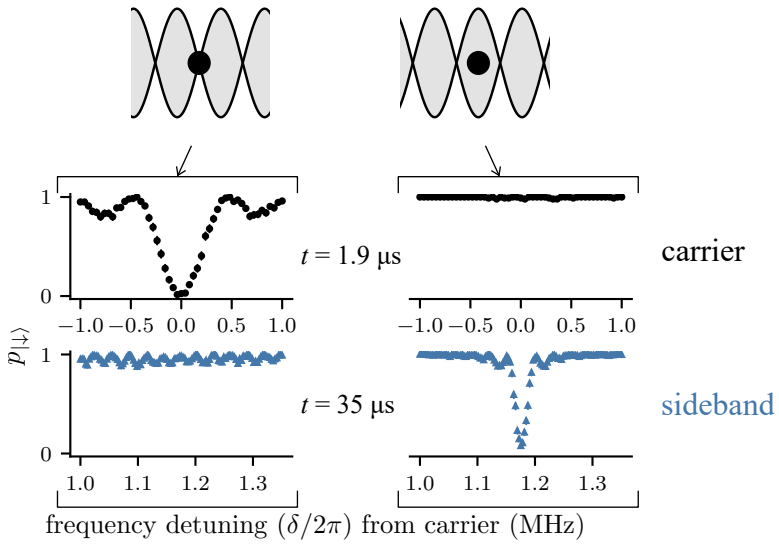

Figure 5.2: Detuning scans over the carrier (circles) and the first sideband (triangles) with the SW while placing the ion at a field node (left column) or field anti-node (right column). For each resonance, t is chosen such that full population transfer is reached in the case of maximal coupling to the SW. For the carrier resonance, $t = t_{\pi,\mathrm{SW}}$ (see Fig. 5.1).

5.1.2 How well can we null the carrier?

Returning to our original objective, we aim to implement a spin-dependent force using a bichromatic field without contributions due to the off-resonant carrier term. This requires positioning the ion at the anti-node of the bichromatic standing wave, which we will refer to as the carrier null. Before setting up the bichromatic standing wave, it is important to assess the precision with which we can position

the ion at the carrier null in a monochromatic wave This section presents such an assessment. The overall method involves using the standing wave to drive spin flips of the ion's internal state and inferring $p_{|\downarrow\rangle}$ from n experimental runs (typically $n = 100$). The observations are then compared with a numerical model that incorporates Gaussian noise in the SW phase, with the goal of understanding the standard deviation of that noise.

Similarly to how we investigated the phase stability at the ion's position with the ion feedback enabled and zero-delay Ramsey measurements (see Sec. 3.4.4), we apply the sequence in Fig. 3.9 for ≈ 1.2 hours (≈ 1730 sequence rounds). The ion feedback sets the lock setpoint to $\phi_1 - \phi_2 = \phi_{\mathrm{ST}} \approx \pi/2$. In the main experimental sequence, we place the SW such that the ion is at one of its anti-nodes ($\phi_1 - \phi_2 = \phi_{\mathrm{ST}} + 3\pi/2$, see Fig. 5.1), apply a π-pulse ($t_{\pi,\mathrm{SW}}$) with the SW, and measure $p_{|\downarrow\rangle}$. We then convert $p_{|\downarrow\rangle}$ into $\phi_1 - \phi_2$ values using Eq. (5.1) and plot them as a histogram in Fig. 5.3. We infer a standard deviation $\sigma = 0.14(5)\,\mathrm{rad}$.

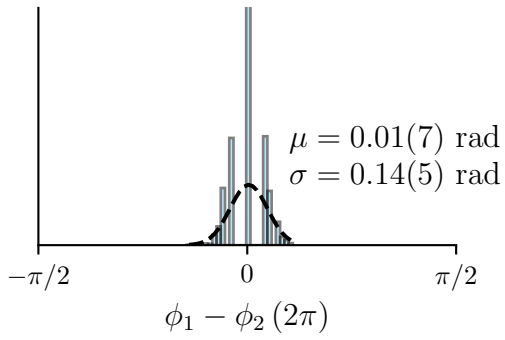

Figure 5.3: Phase stability with the ion positioned at the anti-node (carrier null). The SW is shifted by $3\pi/2$ from the lock setpoint, $\phi_1 - \phi_2 = \phi_{\mathrm{ST}} \approx \pi/2$. After applying the SW interaction for $t_{\pi,\mathrm{SW}}$, we measure $p_{|\downarrow\rangle}$ and convert it to $\phi_1 - \phi_2$ values for analysis.

To estimate the residual phase fluctuations due to shot noise, we simulate two binomial distributions to model statistical fluctuations in ion state detection (see also Sec. 3.4.4). Initially, we simulate phase fluctuations resulting from ion feedback. This is done by sampling a binomial distribution with $n = 100$ trials (the number of shots used for the readout of the ion feedback) and a success probability of $p = 0.5$. The population values inferred from these simulated outcomes, $p_{|\downarrow\rangle}$, are converted to phase values using Eq. (3.4). The deviation of each phase value

from $\pi/2$, denoted as $\phi_{\text{correction}}$, is then added to $\phi_1 - \phi_2 = 0 + \phi_{\text{correction}}$. The adjusted phase differences, $\phi_1 - \phi_2$, are used to compute a new success probability values p using Eq. (5.1). Subsequently, we sample from another set of binomial distributions based on these computed p values, each with $n = 100$ trials. The standard deviation of these sampled values, after converting to phase using Eq. (5.1), is calculated to be $\sigma = 0.100\,\text{rad}$. Comparing this with the experimentally measured value ($\sigma = 0.14(5)\,\text{rad}$), we conclude that the phase stabilisation process and its characterisation are close to the shot noise limit.

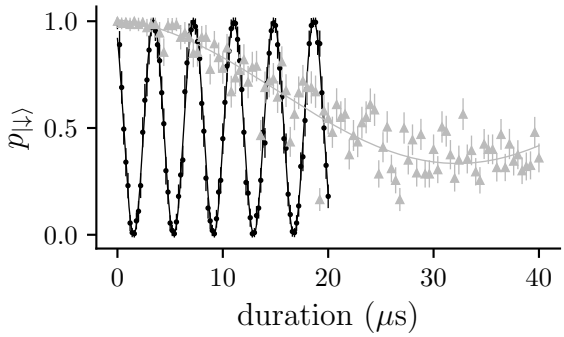

Figure 5.4: Carrier duration scans with the ion at different points in the SW. The ion is placed at a node, where the carrier coupling is maximised (black circles) or at an antinode, where the carrier coupling is minimised (grey triangles). By fitting the Rabi flops, we infer how the carrier coupling strength changes.

In the previous measurement, we set the probing duration to $t_{\pi,\text{SW}}$; we can also place the SW such that the ion is at the node or the anti-node and vary the probing duration. This allows us to measure Rabi flops as shown in Fig. 5.4 and infer the coupling strength of the carrier at the two positions in the SW. The ratio that we obtain between the two coupling strengths is 18, corresponding to a suppression of 25 dB between maximal and minimal carrier coupling[3].

Next we wish to verify if the observed carrier suppression matches our expectations. As discussed in Ref. [117] and [118], the jitter of the SW at the position of the ion, which changes for every shot, is associated with a decoherence effect. In the

[3]In Ref. [116, 130], this carrier suppression factor is discussed in the context of studying quantum field theory on an expanding spacetime using a trapped ion processor ('cosmology in an ion trap').

case of maximum carrier coupling, this leads to a decay in the amplitude of the Rabi oscillations, while for the carrier null configuration, it leads to the population slowly starting to transfer from $|\downarrow\rangle$ to a mixture of $|\downarrow\rangle$ and $|\uparrow\rangle$.
We conduct numerical simulations to understand how the measured phase stability influences the Rabi flops. As a reminder, the phase stabilisation is achieved through two feedback loops consisting of a fast and a slow loop. The fast loop is engaged every shot, while the slow loop is applied once per scan point. Hence, we believe that the decoherence effect results from averaging over the phase corrections applied by the fast loop (PD feedback). Moreover, during the ion feedback sequence, the fast loop is applied for every shot as well. Owing to this, we conduct the numerical simulation in the following way:

- ion feedback
  - we sample $n = 100$ (number of shots) phase values from a Gaussian distribution with $\mu = 0, \sigma$; we measure $\sigma = 0.04\,\text{rad}$ in the experiment for the corrections applied with the fast loop (see Sec. 3.4.1 and Fig. 3.6); these values are then added to the ion feedback setpoint $\phi_{\text{ST}} = \pi/2$.
  - each one of these values is used to calculate a success probability p using Eq. (3.4); we use these values to define n binomial distributions, each with a different p and with one trial; we average the sampled values and use this to infer the ion feedback correction
- main experimental sequence
  - we apply the ion feedback correction[4] to $\phi_1 - \phi_2$; $\phi_1 - \phi_2 = \pi$ at carrier coupling and $\phi_1 - \phi_2 = 0$ at carrier nulling.
  - in addition to this $\phi_1 - \phi_2$, we, once again, sample $n = 100$ (number of shots) phase values from a Gaussian distribution with $\mu = 0, \sigma$

[4] As in the experiment, we do this using Eq. (3.5), with $K = 0.5$

– each one of these values is used to calculate a success probability p using Eq. (5.1); we use these values to define n binomial distributions, each with a different p and with one trial; we average the sampled values to infer $p_{|\downarrow\rangle}$ shown in Fig. 5.5.

In Fig. 5.5, we evaluate various values for σ that characterise the phase stability resulting from the fast feedback. Changes in σ primarily affect the dynamics at carrier nulling ($\phi_1 - \phi_2 = 0$), a consequence of the quadratic dependence of $p_{|\downarrow\rangle}$ on $\phi_1 - \phi_2$, as previously discussed. This contrasts with the quartic dependence, which occurs at carrier coupling. Focusing on the behavior at carrier nulling ($\sigma = 0$ rad), we expect the population $p_{|\downarrow\rangle} = 1$. However, there are numerous noisy data points reaching up to $p_{|\downarrow\rangle} = 0$. The origin of this noise stems from the slow feedback loop setting the lock point based on a value inferred from a population measurement, which is constrained by shot noise (Sec. 3.4.4). As we increase σ, the noise initially caused by the slow feedback loop is overtaken by the decoherence effect due to $\phi_1 - \phi_2$ varying from shot to shot, resulting in $p_{|\downarrow\rangle} \to 0.5$. The value $\sigma = 0.04$ rad corresponds to our experimental measurements, as detailed in Sec. 3.4.1, with the corresponding data shown in Fig. 3.6(b). When comparing the simulated Rabi flops to those measured in Fig. 5.4, we observe similar noise levels; however, $p_{|\downarrow\rangle}$ approaches 0.5 more quickly in the experimental data. Furthermore, it even surpasses 0.5, which we believe is due to an imbalance in the Rabi frequencies of the two branches, estimated from an independent measurement to be around 5% on the day of the experiment.

5.1.3 Single qubit rotations with the SW

To evaluate the quality of the interaction with the SW further, we compare the quality of single qubit rotations using the SW against single qubit rotations with the TW using randomised benchmarking (RBM) [131], which allows us to verify the error behaviour over longer computational sequences which involve the randomly chosen single-qubit rotations. For the SW RBM, the SW is adjusted so that the ion is positioned at one of its nodes. As for the SW, we need to interleave the

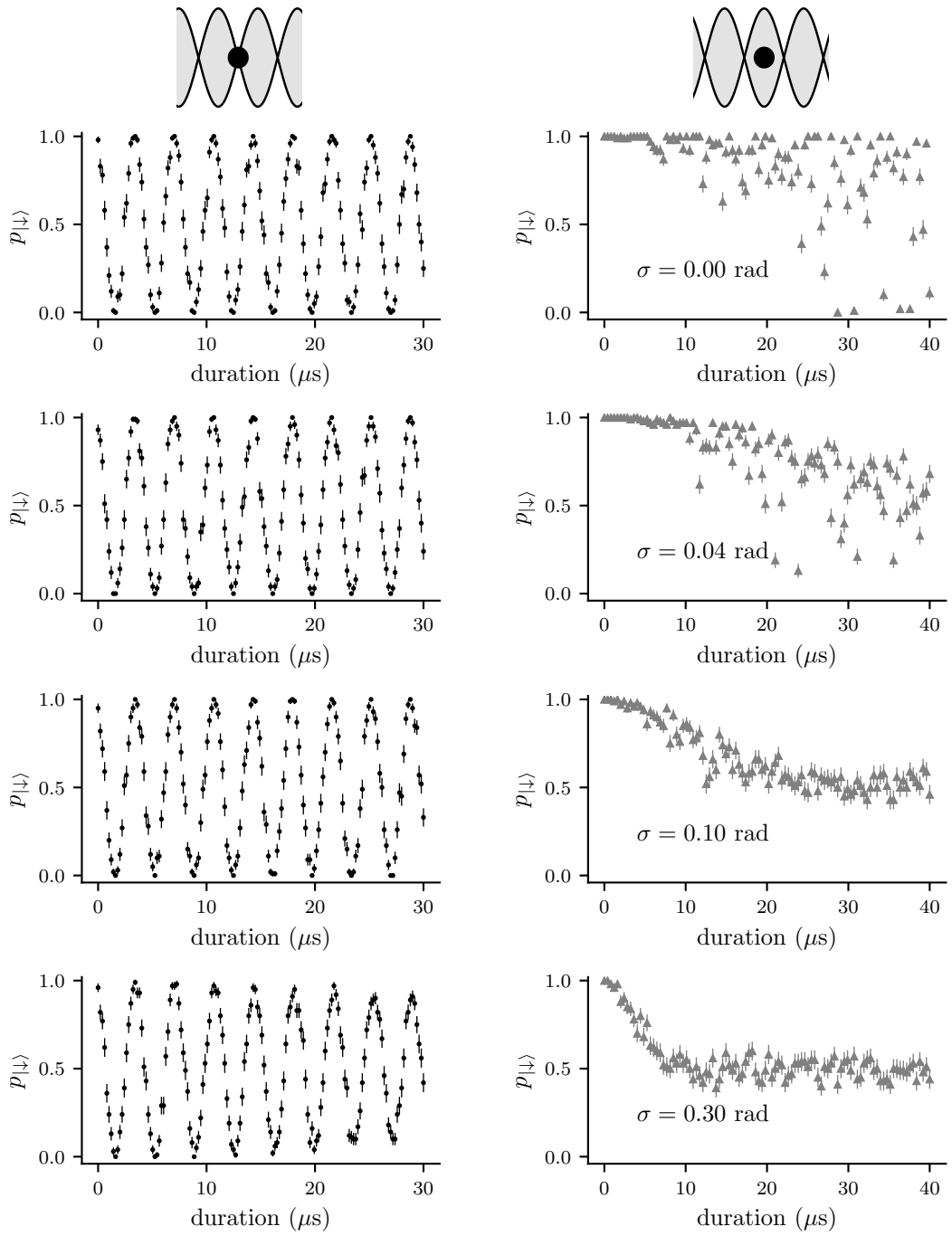

Figure 5.5: Simulations of Rabi flops accounting for phase stability at various points in the SW. For the column on the left, the ion is placed at a node where the carrier coupling is maximised (black circles). For the column on the right, the ion is placed at an antinode, where the carrier coupling is minimised (grey triangles). Each row corresponds to a different phase stability value σ for the fast feedback loop indicated in the text box.

main experimental sequence with the ion feedback; we did the same for the TW experiment in order to keep the same duty cycle. We obtain errors of $1.44(3) \times 10^{-3}$

and $1.73(3) \times 10^{-3}$ per Clifford gate[5], respectively. Thus, the use of the SW does not compromise single-qubit control. In fact, the SW demonstrates slightly better performance than the TW. While this has not been explored in detail, one possible explanation could be the reduced off-resonant coupling to the motional modes in the case of the SW, which is strongly suppressed compared to the TW.

5.2 Ion interacting with bichromatic standing wave

Now that we have explored the monochromatic SW-ion interaction, we are ready to study the interaction with a bichromatic SW that can be used to generate a spin-dependent force with a tunable contribution from the off-resonant carrier term. Details on how we set up the bichromatic SW in the experiment are described in Sec. 3.4.5.

5.2.1 Aligning blue and red detuned standing waves

We aim to position the ion at the anti-node of both the blue and red-detuned standing waves (SWs), i.e. $\phi_{1,b} - \phi_{2,b} = \phi_{1,r} - \phi_{2,r} = \phi_1 - \phi_2 = 0$ (see Sec. 2.4.3). When using ion feedback, the frequency of the two counterpropagating beams is such that we can drive the qubit resonantly. When doing the SW scan, as shown in Fig. 5.1, we find that the carrier nulling occurs at $3\pi/2$ rad away from the lock set point $\phi_{\mathrm{ST}} = \pi/2$ rad. However, when conducting a monochromatic SW scan off-resonant from the qubit transition by $\delta = \pm(\omega_z + \Delta)$—necessary for implementing the SDF—we find that the blue and red-detuned SWs are offset relative to each other, as depicted in Fig. 5.6. We use these scans to determine the relative offsets, allowing us to align the blue- and red-detuned SWs with the on-resonance SW scan by respectively adjusting the phases of the rf tones driving the SP AOM in b1, see Sec. 3.4. The observed offset between the two was inconsistent with the

[5]For the chosen decomposition of the single-qubit Clifford group, the area of a physical pulse averaged over all elements is 0.58π.

path difference expected from the electronic chain alone. Further investigations are needed to pinpoint the underlying reason.

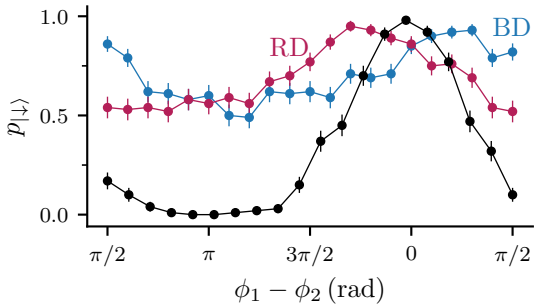

Figure 5.6: Aligning the blue and red-detuned SWs in the bichromatic field. SW phase scans with $\delta = 0$ (black), $\delta \approx -\omega_z$ (red, labeled RD), and $\delta \approx +\omega_z$ (blue, labeled BD). The SW phase scan on resonance is measured with 0.13 mW in each branch and $t_{\pi,\mathrm{SW}} = 1.9\,\mu\mathrm{s}$ and the detuned phase scans with 10 mW in each branch and $t_{\pi,\mathrm{SW}} = 0.4\,\mu\mathrm{s}$. This adjustment is needed as the SWs are far detuned ($\approx 1\,\mathrm{MHz}$). A sharper feature can be obtained by adjusting the power and $t_{\pi,\mathrm{SW}}$ further.

5.2.2 Standing wave spin-dependent force dynamics

Before delving into the dynamics of the SDF using a SW, we perform the following essential calibrations:

- balance the Rabi frequency of the monochromatic counterpropagating beams to maximise the carrier suppression.
- ensure that the strength of the tones in each of the counterpropagating bichromatic beams is balanced, as detailed in Sec. 4.2.1.
- calibrate the motional mode frequency using an SDF created with a single travelling wave bichromatic field, as described in Sec. 4.2.3.
- align the blue and red-detuned SWs as outlined in Sec. 5.2.1.
- with the ion positioned at the anti-node, apply the bichromatic SW with $\delta = \pm(\omega_z + \Delta)$ for a fixed duration. While varying Δ, we perform scans to calibrate any residual ac Stark shifts[6], as shown in Sec. 4.2.2.

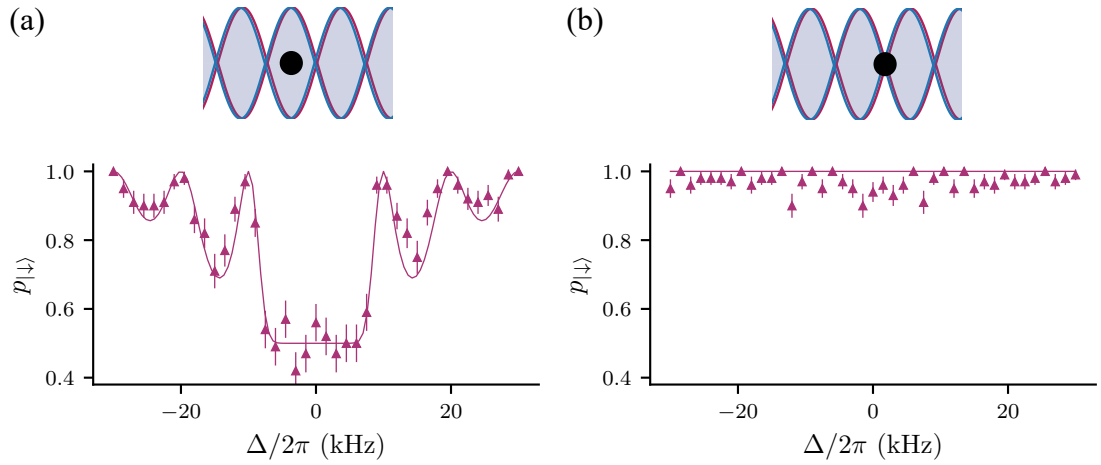

Figure 5.7: SDF dynamics - detuning scan at different points in the SW. We apply the bichromatic SW for a duration of 100 µs and scan detuning Δ from the motional mode frequency. (a) Ion is placed at the antinode, where the coupling to the first motional sideband is maximised. (b) Ion is placed at the node, where the motional coupling is minimised. In both cases, $t_{\text{ramp}} = 0.2\,\mu\text{s}$.

After completing the calibrations, if we conduct a detuning scan with the ion positioned at the anti-node of the SW as described in the last step of the calibration process, we observe dynamics as shown in Fig. 5.7(a). We can switch off the spin-dependent force interaction by placing the ion at the node of the SW ($\phi_1 - \phi_2 = \pi$). Here, the coupling to the motion is suppressed (first-order in the Lamb-Dicke expansion), as demonstrated in Fig. 5.7(b).

5.2.3 Spin-dependent force magnitude

Next, we confirm that the saturation effect caused by the non-commuting carrier term on the magnitude of the SDF is lifted when using the bichromatic SW. We infer the magnitude of the SDF created using the bichromatic field by applying the interaction for variable durations and fitting the dynamics, as detailed in Sec. 4.2.5. We repeat the measurement for different power settings[7] and show the results in Fig. 5.8. We compare the results to the measurements in Fig. 5.8 recorded using a bichromatic TW SDF with $\delta \approx \omega_z$. We observe that in the case of the SW, the

[6]When compensating for the ac Stark shifts, we adjust both bichromatic fields by the same frequency offset.

[7]Power settings for the SW measurement $0.25 - 14.5$ mW in each branch with Rabi frequency per tone $\Omega/2\pi = 0.048 - 0.33$ MHz and a beam waist radius of $\approx 20\,\mu\text{m}$

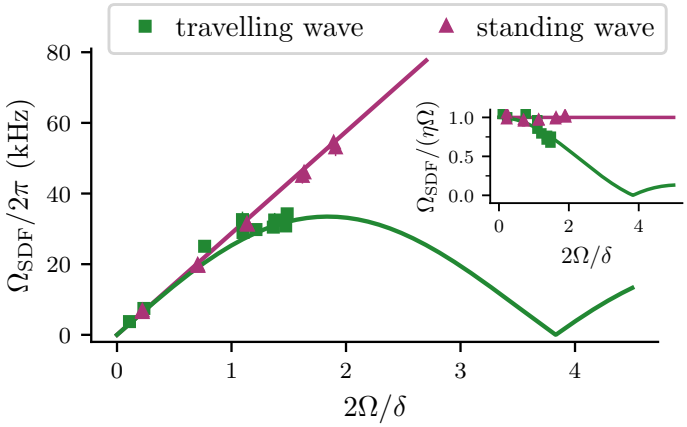

Figure 5.8: Spin-dependent force magnitude Ω_{SDF} (normalised by $\eta\Omega$ in the inset) versus $2\Omega/\delta$, measured with a bichromatic SW field (triangles) or a bichromatic TW field (squares). The solid lines show the analytical dependence; as predicted by the theory and shown explicitly in the inset, the TW coupling follows the Bessel functions ($|J_0 + J_2|$), while the SW coupling remains constant. In the case of the SW, the axis is scaled by a factor of 2 to account for this effect, i.e. we use the Rabi frequency of the 'SW' tone.

interaction magnitude increases linearly with Ω. Hence, there is no limit on the maximum achievable interaction strength. Moreover, we note that in the case of the SW, we reach higher values for the $2\Omega/\delta$ than in the case of the TW. This is a result of the constructive interference.

For both the SW and TW measurements, the pulses are amplitude-shaped with a ramp of $t_{\mathrm{ramp}} = 3.6\,\mu\mathrm{s}$. As discussed in Sec. 2.3.2, amplitude pulse shaping was introduced to counteract some effects of the off-resonant non-commuting carrier. While it is possible to reduce the ramp duration for the SW measurements, as done in the scans shown in Fig. 5.1, we continue to use the ramp in the SDF comparison measurements. This approach helps mitigate the effects of any residual carrier and the off-resonant coupling to other motional modes as power increases. Additionally, maintaining the same ramp shape across measurements simplifies the comparison of SDF strength by ensuring consistency in the pulse area.

5.3 Two-qubit entangling gates using a bichromatic standing wave

As mentioned in previous chapters, an important application of spin-dependent forces in trapped ions involves creating effective spin-spin interactions through the shared motion of the ions, commonly known as geometric phase gates [19, 80, 81, 83]. The necessity of using the motion as a quantum bus arises from the weak direct spin-spin interactions due to Coulomb repulsion, which leads to a large ion-ion spacing. The initial proposal by Cirac and Zoller, Ref. [18], for creating spin-spin interactions involved spin-motion coupling through first-order sideband interactions (see Sec. 2.2.2). This technique requires cooling the motion to the ground state, $n = 0$, a challenging task, and also individual addressing of the ions, which is more feasible in today's ion-trapping setups. Geometric phase gates, with their less stringent requirements for the initial state of motion and compatibility with global beam addressing, have proven more feasible for experimental implementation. Furthermore, these gates have facilitated the achievement of two-qubit gates with record-high fidelities [26–29] when compared to other quantum computing platforms [30]. We provide a brief overview of geometric phase gates and discuss the advantages of implementing a two-qubit gate using SWs instead of TWs.

5.3.1 Geometric phase gates

In Sec. 2.3, we extensively discussed how a spin-dependent force displaces the oscillator in phase space along spin-dependent trajectories for a single ion. Besides the displacement, there is also a geometric spin-dependent phase accumulated. To implement a gate, we consider applying the bichromatic field to an ion crystal with two ions only. To account for this, we modify the spin-operator in Eq. (2.26) as follows

$$\hat{H}_{\text{gate}} = -\frac{\hbar\Omega_{\text{SDF}}}{2}(\hat{\sigma}_{\alpha,1} \pm \hat{\sigma}_{\alpha,2})(\hat{a}e^{i(\Delta t-\phi)} + \hat{a}^\dagger e^{-i(\Delta t-\phi)}), \tag{5.2}$$

where $\hat{\sigma}_\alpha$ is a Hermitian operator and a linear combination of the Pauli operators $\hat{\sigma}_{x,y,z}$, as before, with the index specifying a respective ion, i.e., $\hat{\sigma}_{\alpha,1} = \hat{\sigma}_\alpha \otimes \hat{\mathbb{I}}_2$ and $\hat{\sigma}_{\alpha,2} = \hat{\mathbb{I}}_2 \otimes \hat{\sigma}_\alpha$. For two ions, there are two normal modes along each direction

of vibration, the centre-of-mass mode and the out-of-phase mode, each one of them having different Lamb-Dicke parameters which are hidden under the strength of the SDF, Ω_{SDF}. The spin-operator $(\hat{\sigma}_{\alpha,1} + \hat{\sigma}_{\alpha,2})$ corresponds to driving the centre-of-mass mode, while $(\hat{\sigma}_{\alpha,1} - \hat{\sigma}_{\alpha,2})$, corresponds to driving the out-of-phase mode [66]. The propagator derived in Eq. (2.34) still applies, with $\hat{\sigma}_\alpha \rightarrow (\hat{\sigma}_{\alpha,1} \pm \hat{\sigma}_{\alpha,2})$ and the adjusted strength.

To generate spin-spin entanglement, we require the spins to be disentangled from the motion, $\alpha = 0$, at the end of the sequence; α is the complex displacement variable (Eq. (2.35)). This is equivalent to returning to the initial motional state[8], which occurs for gate durations $t_g = 2K\pi/\Delta$, where K is an integer corresponding to the number of loops in the phase-space trajectory.

If we consider the case of $(\hat{\sigma}_{x,1}+\hat{\sigma}_{x,2})$, its eigenstates are $\{|{+}{+}\rangle, |{-}{-}\rangle, |{+}{-}\rangle, |{-}{+}\rangle\}$ with the respective eigenvalues $\{2, -2, 0, 0\}$. Using Eq. (2.36), only $|{+}{+}\rangle, |{-}{-}\rangle$ would accumulate a geometric phase $4\Phi(t)$ and be displaced in phase space. Hence, if we initialise the spin state in $|{\downarrow}{\downarrow}\rangle = (|{+}{+}\rangle + |{-}{-}\rangle - |{+}{-}\rangle - |{-}{+}\rangle)/2$ and apply the gate interaction (Eq. (5.2)) with the spin operator $(\hat{\sigma}_{x,1} + \hat{\sigma}_{x,2})$, the spin states acquire phases in the following way

$$\begin{aligned} |{+}{+}\rangle &\rightarrow e^{-4\Phi(t)} |{+}{+}\rangle \\ |{-}{-}\rangle &\rightarrow e^{-4\Phi(t)} |{-}{-}\rangle \\ |{+}{-}\rangle &\rightarrow |{+}{-}\rangle \\ |{-}{+}\rangle &\rightarrow |{-}{+}\rangle . \end{aligned} \tag{5.3}$$

To create the maximally entangled state[9]

$$|{\downarrow}{\downarrow}\rangle \rightarrow \frac{1}{\sqrt{2}}(|{\downarrow}{\downarrow}\rangle - i\,|{\uparrow}{\uparrow}\rangle), \tag{5.4}$$

we need to set $4\Phi(t) = \pi/2$, combined with the loop closing condition ($t_g = 2K\pi/\Delta$), yields the condition $\Delta = \pm 4\sqrt{K}\Omega_{\mathrm{SDF}}$.

[8] Unlike the Cirac-Zoller gate, this state does not need to be the motional ground state. Instead, the only requirement is that the motion is disentangled from the spin state at the end of the gate operation, which can occur even for nonzero mean phonon occupation $\bar{n}$. This condition remains valid in the Lamb-Dicke regime.

[9] We get the state in Eq. (5.4) up to a global phase $e^{-i\pi/4}$.

$\hat{\sigma}_\phi\hat{\sigma}_\phi$ or $\hat{\sigma}_z\hat{\sigma}_z$ gates?

There have been many experimental implementations of geometric phase gates using laser and laser-free schemes. A comprehensive overview is provided in Ref. [30]. I will briefly describe the categories of geometric phase gates that arise depending on the spin basis of the interaction using laser-based techniques. Previously, we considered the spin operator $(\hat{\sigma}_{x,1} \pm \hat{\sigma}_{x,2})$ to exemplify the mechanism behind a geometric phase gate. However, if we can create an SDF conditioned on an arbitrary $\hat{\sigma}_\alpha$ basis, the spin operator for the gate operation can be varied accordingly.

The Mølmer-Sørensen (MS) scheme uses bichromatic fields near-resonant with the qubit transition, and it is commonly associated with generating $\hat{\sigma}_\phi$-type $(\hat{\sigma}_x, \hat{\sigma}_y)$ interactions [27, 80, 87, 93, 132]. However, with some modifications, as discussed in Sec. 2.3.2 and Sec. 4.2.6, this scheme can also generate $\hat{\sigma}_z$-type interactions. Traditionally, $\hat{\sigma}_z$-type gate interactions would be implemented using a space-varying ac Stark shift, employing beams far-detuned from the qubit transition [26, 81, 133]. Each spin conditioning and field configuration offers certain advantages and drawbacks; selecting the appropriate interaction for a system thus involves carefully considering the desired application.

$\hat{\sigma}_z$-type gates, for instance, can be made insensitive to errors from qubit frequency offsets or dephasing which commute with the interaction, using spin-echo sequences [88, 89]. Implementations involving space-dependent ac Stark shifts that rely on dipole transitions are generally incompatible with magnetic-field insensitive 'clock' qubits [134], which are desirable for their long coherence times [135, 136]. However, recent experiments have adapted this approach for clock qubits using quadrupole transitions with ground state qubits [137, 138] or dipole transitions with optical qubits [28, 139].

Conversely, using a near-qubit-resonant bichromatic field in the MS scheme is compatible with implementing SDFs on clock qubits and allows the same fields to be used for single-qubit rotations. Yet, one drawback of $\hat{\sigma}_\phi$-type gate interactions in this scheme is their sensitivity to the phase of the driving fields, as the basis

of the interaction depends on the sum of the phases of the two tones at the ion's position, see Sec. 2.3.2.

Here, we considered the implementation of a gate using a modified MS scheme in which the two fields in the bichromatic field are SWs instead of TWs. We use the centre-of-mass mode along the axial direction of the trap with $\omega_z/2\pi = 1.17\,\mathrm{MHz}$ and set the detuning of the tones in the bichromatic field to $\delta = \omega_z + \Delta$, which yields the $\hat{\sigma}_{\phi,1} + \hat{\sigma}_{\phi,2}$ interaction basis (see Sec. 2.4.3 for the Hamiltonian formula of the SW SDF acting on a single ion.). Using the loop closure ($t_g = 2K\pi/\Delta$) and geometric phase ($\Delta = 4\sqrt{K}\Omega_{\mathrm{SDF}}$) conditions, we find that $t_g = \sqrt{K}\pi/(2\Omega_{\mathrm{SDF}})$. Therefore, when implementing an SDF using a bichromatic TW field, as the magnitude of the SDF experiences a global maximum due to the non-commuting carrier term, this inherently limits the speed at which we can execute a two-qubit entangling gate using the MS scheme. We can circumvent this speed limit by mitigating the carrier's effects with the standing wave. This is important as reducing the gate duration also means negligible errors due to incoherent processes such as motional heating and qubit dephasing [26, 32].

5.3.2 Two ions in a standing wave

To implement the gate interaction (Eq. (5.2)) using the SW, we need to ensure the two ions see the same phase of the SW. This is equivalent to saying both ions have the same coupling ratio between the carrier and the first-order sideband. In our apparatus, we globally address the two ions with a SW, which is angled at 45° relative to the trap axis (z); see Fig. 3.3. To ensure that the ions see the same phase of the SW, we adjust their spacing by changing the trapping potentials such that the distance between the ions, projected onto the $\mathbf{k_l}$-vector of the SW, is an integer multiple of the SW periodicity $\lambda/2 = 674\,\mathrm{nm}/2$.

This is calibrated by recording SW phase scans, as shown in Fig. 5.1(a), but on two ions. If the periodicity of the SW does not match the ion spacing, then the ions experience different carrier coupling strengths (equivalent to unequal illumination), which depend on the phase mismatch that they see $\phi_{\mathrm{sp}} = (\phi_1 - \phi_2)_1 - (\phi_1 - \phi_2)_2$,

where $\phi_1 - \phi_2$ the difference in phase between the two counterpropagating beams at the position of the respective ion, whose index is indicated as a subscript outside the bracket. With the spin state initialised in $|\downarrow\downarrow\rangle$, applying the SW, we find the following dynamics:

$$\begin{aligned} p_{|\downarrow\downarrow\rangle} &= p_{|\downarrow\rangle} p_{|\downarrow\rangle} = \cos^2\left(\frac{\pi}{2}\sin\left(\frac{\phi_{\text{scan}}+\phi_o}{2}\right)\right)\cos^2\left(\frac{\pi}{2}\sin\left(\frac{\phi_{\text{scan}}+\phi_o+\phi_{\text{sp}}}{2}\right)\right) \\ p_{|\uparrow\uparrow\rangle} &= p_{|\uparrow\rangle} p_{|\uparrow\rangle} = \sin^2\left(\frac{\pi}{2}\sin\left(\frac{\phi_{\text{scan}}+\phi_o}{2}\right)\right)\sin^2\left(\frac{\pi}{2}\sin\left(\frac{\phi_{\text{scan}}+\phi_o+\phi_{\text{sp}}}{2}\right)\right) \\ p_{|\downarrow\uparrow\rangle+|\uparrow\uparrow\rangle} &= 1 - p_{|\downarrow\downarrow\rangle} - p_{|\uparrow\uparrow\rangle}, \end{aligned} \tag{5.5}$$

where $p_{|\downarrow\downarrow\rangle}$ the probability that both ions are in $|\downarrow\rangle$, $p_{|\uparrow\uparrow\rangle}$ the probability that both ions are in $|\uparrow\rangle$, $p_{|\downarrow\uparrow\rangle+|\uparrow\uparrow\rangle}$ the probability that one ion is in $|\downarrow\rangle$, ϕ_{scan} is the relative phase difference between the counterpropagating beams that we program in as we record the scan, and ϕ_o is a phase offset that we need to account for if the ion feedback is not enabled. We used Eq. (5.1) in writing the equations above.

We record dynamics as we change the ion spacing and fit $p_{|\downarrow\downarrow\rangle}$ and $p_{|\uparrow\uparrow\rangle}$ simultaneously using Eq. (5.5) to infer ϕ_{sp}, examples shown in Fig. 5.9. We aim to achieve $\phi_{\text{sp}} = 0$, which corresponds to Fig. 5.9(a.iii) and (b). The dynamics in Fig. 5.9(a) were recorded with our initial version of the enclosure and no ion feedback, hence the observed offsets with respect to Fig. 5.9(b). We infer that the two ions are spaced (projected along the SW direction) by $\approx 3.8\,\mu\text{m} \cdot \cos(45°) = 4\lambda$, where $\lambda = 674\,\text{nm}$. When working with two ions, the ion feedback relies on the equivalent 'one-ion bright' population $p_{|\downarrow\downarrow\rangle} + p_{|\downarrow\uparrow\rangle+|\uparrow\downarrow\rangle}/2$. For the gate implementation, both ions are placed at the anti-nodes of the SW as we want to maximise the coupling to the motion and suppress the coupling to the carrier. Moreover, the red and the blue detuned SWs are aligned in the same manner as described in Sec. 5.2.1, but using the $p_{|\downarrow\downarrow\rangle}$ dynamics shown in Fig. 5.9(b).

5.3.3 Gate dynamics

Finally, we can examine the gate dynamics with the SW. As in the case of the SDF dynamics, we can implement durations or detuning scans; we show examples of

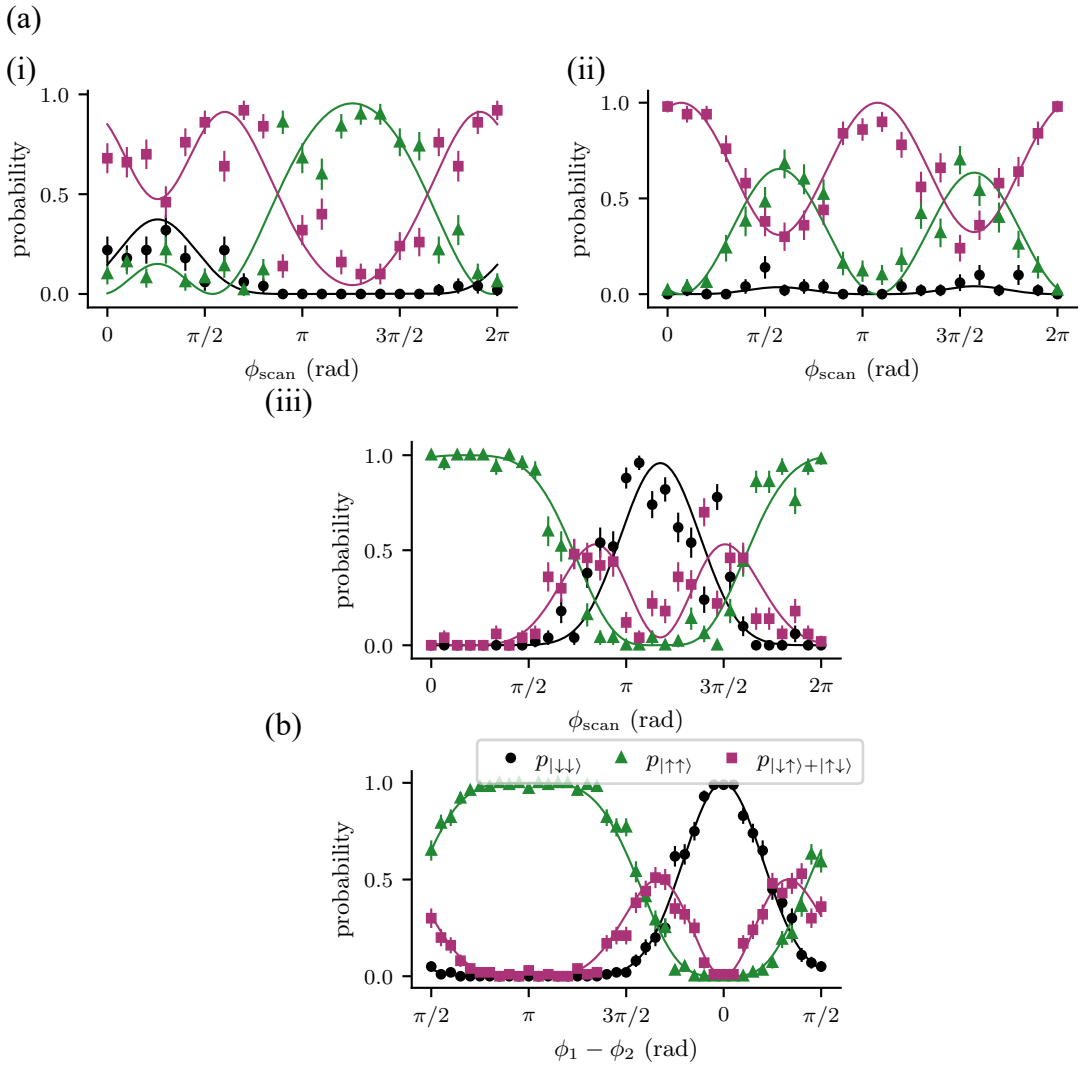

Figure 5.9: SW phase scans on two ions. (a) Each scan corresponds to a different spacing between the ions. By fitting the dynamics (see text), we infer the phase mismatch ϕ_{sp} between what phase of the SW each ion sees: (i) $\phi_{\text{sp}} \approx 0.6\pi$ rad, (ii) $\phi_{\text{sp}} \approx \pi$ rad and (iii) $\phi_{\text{sp}} \approx 0$ rad. These scans were recorded when the ion feedback was not enabled, and the final version of the enclosure was not set up (2021-07-28). (b) Scan with $\phi_{\text{sp}} \approx 0$ rad, ion feedback enabled, and the final version of the enclosure (2022-09-20). The legend applies to all plots.

both in Fig. 5.10. We found the detuning scans useful for calibrating ac stark shifts; one can look at the $p_{|\downarrow\uparrow\rangle+|\uparrow\downarrow\rangle}$ and follow the calibration steps described for a single ion in Sec. 5.2.2. For realising the maximally entangled state, the duration and the detuning parameters are, in principle, determined by the chosen SDF strength (Sec. 5.3.1). However, in the experiment, we fix the laser power and the detuning and optimise for the gate duration t_g, indicated in Fig. 5.10(a), bottom scan, that

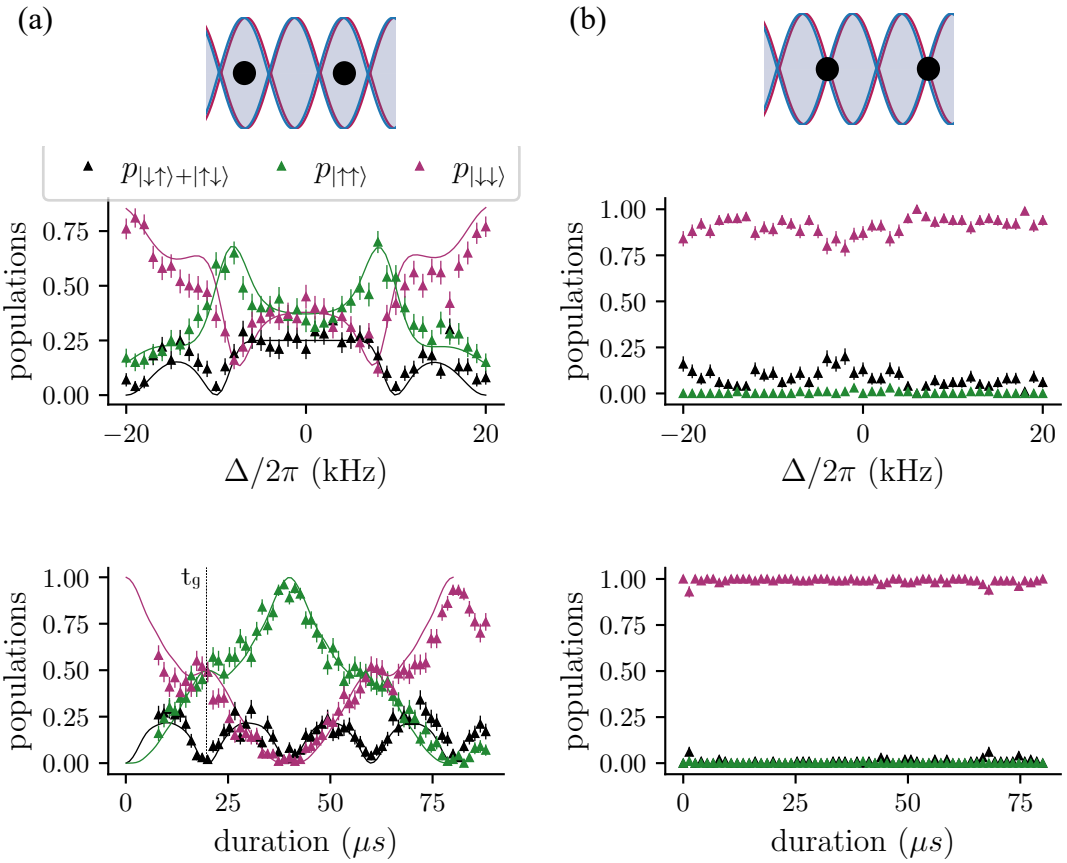

Figure 5.10: Detuning and duration scans of the gate interaction with the ions at different points in the SW: (a) both ions at antinodes and (b) both ions at nodes. Top row - detuning scans with 0.3 mW in each branch, $t_g = 100\,\mu s$ and $t_{\text{ramp}} = 0.2\,\mu s$. Bottom row - duration scans with with 6.8 mW in each branch, $\Delta/2\pi = -48\,\text{kHz}$ and $t_{\text{ramp}} = 10\,\mu s$.

gives us the best quality Bell state or fidelity. Moreover, we also try to match the dynamics to numerical simulations performed using Julia [125]. The simulations shown in Fig. 5.10 were obtained by initialising the state in $|\downarrow\downarrow\rangle\,|0\rangle$, i.e. Fock state $|0\rangle$, and numerically integrating Eq. (5.2)[10] with t_g and Δ found in the experiment and optimising Ω_{SDF} to achieve the best overlap (fidelity) to an ideal state.

[10]It is possible to use this Hamiltonian as the ions are placed at the anti-nodes of the SW, where the carrier coupling is suppressed.

5.3.4 Measuring fidelity

As a measure of the quality of the two-qubit gate, we evaluate the fidelity of producing a target Bell state[11]

$$|\psi_{\text{target}}\rangle = \frac{1}{\sqrt{2}}(|\downarrow\downarrow\rangle - e^{i\theta}|\uparrow\uparrow\rangle). \tag{5.6}$$

After initialising in $|\downarrow\downarrow\rangle$ and applying the gate interaction, we assume that the state created is described by the density matrix ρ. As $|\psi_{\text{target}}\rangle$ is a pure state, the fidelity, or the degree of overlap between the target and output state, is defined as

$$\begin{aligned} F(\rho, |\psi_{\text{target}}\rangle) &= \langle\psi_{\text{target}}|\,\rho\,|\psi_{\text{target}}\rangle \\ &= \frac{1}{2}(\langle\downarrow\downarrow|\,\rho\,|\downarrow\downarrow\rangle + \langle\uparrow\uparrow|\,\rho\,|\uparrow\uparrow\rangle) - \frac{1}{2}(e^{i\theta}\langle\downarrow\downarrow|\,\rho\,|\uparrow\uparrow\rangle + e^{-i\theta}\langle\uparrow\uparrow|\,\rho\,|\downarrow\downarrow\rangle) \\ &= \underbrace{\frac{1}{2}(\langle\downarrow\downarrow|\,\rho\,|\downarrow\downarrow\rangle + \langle\uparrow\uparrow|\,\rho\,|\uparrow\uparrow\rangle)}_{\text{populations}} - \underbrace{|\langle\downarrow\downarrow|\,\rho\,|\uparrow\uparrow\rangle|\cos(\theta - \arg(\langle\downarrow\downarrow|\,\rho\,|\uparrow\uparrow\rangle))}_{\text{coherences}} \end{aligned} \tag{5.7}$$

The first two terms in the last line of the equation correspond to the diagonal elements of the density matrix or populations, which can be measured directly by reading out the spin state of the ions right after the gate is applied ($p_{|\uparrow\uparrow\rangle}$, $p_{|\downarrow\downarrow\rangle}$). The last two terms are off-diagonal elements or coherences. We can't measure these directly. We instead apply a $\pi/2$ rotation globally with variable ϕ', $\hat{R}(\pi/2, \phi') \otimes \hat{R}(\pi/2, \phi')$, which maps the off-diagonal terms to populations [93]. After this global rotation is applied, we measure, using the fluorescence readout, the populations $p_{|\uparrow\uparrow\rangle}$, $p_{|\downarrow\downarrow\rangle}$ and $p_{|\downarrow\uparrow\rangle+|\uparrow\downarrow\rangle}$. Using this, we can reconstruct the parity operator, P

$$\begin{aligned} P &= p_{|\uparrow\uparrow\rangle} + p_{|\downarrow\downarrow\rangle} - p_{|\downarrow\uparrow\rangle+|\uparrow\downarrow\rangle} \\ &= \langle\uparrow\downarrow|\,\rho\,|\downarrow\uparrow\rangle + \langle\downarrow\uparrow|\,\rho\,|\uparrow\downarrow\rangle - 2|\langle\downarrow\downarrow|\,\rho\,|\uparrow\uparrow\rangle|\cos(2\phi' - \arg(\langle\downarrow\downarrow|\,\rho\,|\uparrow\uparrow\rangle)) \end{aligned} \tag{5.8}$$

which exhibits oscillations with periodicity $2\phi'$ and amplitude (contrast) C, which is related to the magnitude of the coherences $|\langle\downarrow\downarrow|\,\rho\,|\uparrow\uparrow\rangle| = C/2$. We then compute the fidelity as

$$F = \frac{p_{|\uparrow\uparrow\rangle} + p_{|\downarrow\downarrow\rangle}}{2} + \frac{C}{2}. \tag{5.9}$$

[11] For the Mølmer-Sørensen gate $\theta = \pm 2\phi$, where ϕ is the basis of the gate interaction spin-basis $\hat{\sigma}_{\phi,1} \pm \hat{\sigma}_{\phi,2}$ [134].

5.3.5 Two-qubit gates - SW vs TW

We evaluate the two-qubit gates implemented using the bichromatic SW by assessing the fidelity of the resulting Bell states, as previously described. Furthermore, we compare the SW scheme to entangling gates implemented using the conventional MS scheme - with a bichromatic TW field, focusing on fidelity changes as we reduce the gate duration. Both entangling gate schemes are performed on the axial centre-of-mass mode and using a ramp duration of $t_{\text{ramp}} = 10\,\mu\text{s}$ to minimise coupling to other motional modes, this is especially relevant for the shorter gate durations where more power is required.

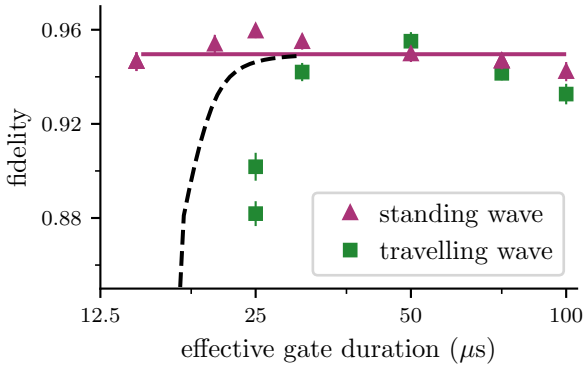

Figure 5.11: Characterisation of SW (triangles) and TW (squares) Mølmer-Sørensen gates as a function of the effective two-qubit gate duration ($2\pi/\Delta$). Using the SW, we achieve gate fidelities that are consistent with ≈ 0.95 (solid line) for all gate durations. Using the TW, the fidelity decreases rapidly for durations $\leq 25\,\mu\text{s}$. As a guide to the eye, we show TW MS gate simulations (dashed lines), with the maximum fidelity normalised to 0.95.

In Fig. 5.11, we present the two-qubit fidelities achieved with both schemes as a function of the effective gate duration ($2\pi/\Delta$)[12]. For slower gates, the fidelity of the SW gate is comparable to that of the TW gate. However, as the gate speed increases, the fidelity of the TW gate rapidly deteriorates. This degradation aligns with predictions from direct numerical integration of Eq. (2.44), where we made the substitution $\hat{\sigma}_{\phi_s} \rightarrow (\hat{\sigma}_{\phi_s,1} + \hat{\sigma}_{\phi_s,2})$ and we set all parameters to experimental

[12]The effective gate duration is approximately equal to the full-width half maximum (FWHM) of the pulse shape. The total pulse duration from start to end is $2\pi/\Delta + t_{\text{ramp}}$, where t_{ramp} is the ramp duration.

values except for the Rabi frequency Ω, which was optimised for maximum fidelity[13]. We observe that measured fidelities degrade earlier (by approximately 5 µs) than predicted, likely due to experimental imperfections (e.g., in ramp shape) not captured in the numerical model.

In contrast, the fidelity for the SW gate remains consistently around 0.95 across the entire available power range, indicating that the limitation from carrier coupling has been effectively eliminated. To achieve shorter gate durations, we increase Δ, which means that we also need to proportionally increase Ω_{SDF} such that we still achieve the right geometric phase $4\Phi = \pi/2$. However, this becomes impossible for the TW bichromatic gate as the non-commuting carrier term causes a saturation in the strength of the SDF, as discussed in Section 5.2.3, which is one way to explain the physics behind the decline in fidelity for the TW gates. The shortest SW gate duration is 15 µs, limited by the total available laser power of 29 mW.

We believe the main source of infidelity for entangling operations is phase noise from the 674-nm laser, which is common to both gate implementations.

5.4 Summary

In conclusion, we implemented single- and two-qubit operations for trapped-ion qubits using a phase-stabilised SW(s). The degree of control of the optical phase at the position of the ion(s) enables us to tune the ratio of the field intensity and gradient that the ions experience, which sets the relative strengths between the first sideband and carrier. Our experiments confirmed that using the SW helps us circumvent the effects of the non-commuting off-resonant carrier term. Firstly, we demonstrated that the strength of the SDF no longer saturates as we increase the power of the driving fields. Secondly, we explored two-qubit MS gates using a bichromatic TW in a regime where the non-commuting off-resonant carrier term typically induces significant errors that cannot be removed adiabatically through amplitude pulse shaping. However, the bichromatic SW allowed us to exceed this limitation without compromising the fidelity.

[13] Sebastian Saner conducted these simulations.

6

Non-commuting interactions for nonlinear bosonic interactions

Contents

This chapter reports on experimentally generating effective interactions that are nonlinear in the amplitude of the motional (bosonic) mode of a trapped $^{88}Sr^{+}$ ion, based on the theory developed in Ref. [140]. The method relies on the ion being a hybrid system comprising motional modes and an internal spin state. The main ingredients required for implementing this technique are two spin-dependent forces whose spin components are non-commuting. While spin-dependent forces (SDFs) have been extensively used before in trapped ions, this method proposes a shift in perspective, where the spin mediates the bosonic interaction, i.e., the spin is the quantum bus instead of the usual converse (see Sec. 1.3). We demonstrate effective nonlinear bosonic interactions, mediated by the spin, up to the fourth order; specifically, we focus on generalised squeezing [141] interactions and demonstrate squeezing (second order), trisqueezing (third order), and quadsqueezing (fourth order). We characterise this class of interactions, including their favourable magnitude scaling, spin dependence, and unitarity, and perform full-state tomography by reconstructing the Wigner function of the resulting states. Moreover, we discuss some limitations of this technique. The results discussed in this chapter are published in Ref. [129].

6.1 Nonlinear bosonic interactions in trapped ions

So far, we have mainly considered interactions linear in $\hat{a}$ and $\hat{a}^{\dagger}$, such as (first order) sideband interactions, Eq. (2.17) and (2.16), and spin-dependent forces, Eq. (2.25), the latter of which we have extensively investigated.

In trapped ions, nonlinear bosonic interactions have been implemented through a variety of experimental techniques. Driving higher orders in the Lamb-Dicke expansion facilitates implementations such as squeezing and beam-splitter interactions (both second order) [57, 60], and cross-Kerr nonlinearities (third order) [142]. Additionally, parametrically driving the trapping potential has enabled implementations of squeezing by driving at $2\omega_z$ [36, 143], two-mode squeezing by driving at $\omega_x + \omega_y$, and

beam-splitter interactions by driving at $\omega_x - \omega_y$ [144]. Squeezing through reservoir engineering has also been successfully implemented [79, 145].

6.1.1 Higher orders in the Lamb-Dicke expansion

As mentioned above, one way to create interactions that contain higher-order terms, $\hat{a}^n$ and $\hat{a}^{\dagger n}$, in a trapped-ion system is by driving higher-order terms in the Lamb-Dicke expansion. In Eq. (2.43), describing the interaction of a bichromatic field with an ion, the $\mathcal{O}(\eta^2)$ terms are neglected as they have diminishing strengths (η^n) and are off-resonant. However, we now consider driving some of these terms resonantly [57, 146]. Looking at the second order term, $(i\eta(\hat{a}+\hat{a}^\dagger))^2/2!$, there are two interactions that we can drive resonantly. If the detuning from the qubit is set to $\delta = 2\omega_z$ (second motional sideband), we drive:

$$\hat{H}_{\text{bi}} = \hbar\Omega\frac{(i\eta)^2}{2!}\hat{\sigma}_{\phi_s-\pi/2}\cos(\delta t-\phi_d)(\hat{a}^2e^{-i2\omega_z t}+\hat{a}^{\dagger 2}e^{i2\omega_z t}), \tag{6.1}$$

and if $\delta = 0$ (this is also the resonance condition for the carrier), we drive:

$$\hat{H}_{\text{bi}} = \hbar\Omega\frac{(i\eta)^2}{2!}\hat{\sigma}_{\phi_s-\pi/2}\cos(\delta t-\phi_d)(\hat{a}\hat{a}^\dagger+\hat{a}^\dagger\hat{a}), \tag{6.2}$$

where we moved into the interaction picture with respect to the oscillator Hamiltonian $\hat{H}_{\text{osc}}$, Eq. (2.4). Eq. (6.1) is a spin-conditioned squeezing Hamiltonian [147], while the action of the Hamiltonian in Eq. (6.2) describes a rotation in phase space[1] [149] conditioned on the spin. We can obtain higher-order squeezing or higher-order combinations of the creation and annihilation operators, e.g., $\hat{a}\hat{a}^\dagger\hat{a}+\text{h.c.}$, by further expanding Eq. (2.42). Here, we focus on generalised squeezing [141]. Going up to the fourth order and after applying the rotating wave approximation with respect to $\hat{H}_{\text{osc}}$, we write the generalised squeezing interaction of order n

$$\hat{H}^{\eta^n} = \frac{\hbar\Omega_{\eta^n}}{2}\hat{\sigma}_\alpha(\hat{a}^n e^{-i\phi_d}+\hat{a}^{\dagger n}e^{i\phi_d}), \tag{6.3}$$

[1] If the interaction is calibrated to introduce a $\pi/2$ rotation in phase space, then the propagator for this Hamiltonian is also referred to as a Fourier transform [148].

where the spin-conditioning alternates based on the order

$$\hat{\sigma}_\alpha = \begin{cases} \hat{\sigma}_{\phi_s - \frac{\pi}{2}} & \text{if } n \bmod 2 = 0 \\ \hat{\sigma}_{\phi_s} & \text{otherwise,} \end{cases} \tag{6.4}$$

and the magnitudes Ω_{η^n} are given by

$$\Omega_{\eta^2,\eta^3,\eta^4} = \left\{ -\frac{\Omega\eta^2}{2!}, \frac{\Omega\eta^3}{3!}, \frac{\Omega\eta^4}{4!} \right\}. \tag{6.5}$$

We can quickly notice that since $\eta \sim 0.05$, every subsequent order is weaker by more than an order of magnitude[2].

6.1.2 Spin-mediated nonlinear bosonic interactions

Our proposed method for circumventing this unfavourable scaling is by introducing an alternative method which combines two non-commuting SDFs instead. Together, they generate a plethora of nonlinear interactions with different resonance conditions, as proposed in Ref. [140] (see Fig. 6.1).

We start by considering two SDFs detuned from the motional mode with angular frequency ω_z, one by Δ and the other by $m\Delta$, where m is an integer different from zero, applied simultaneously

$$\begin{aligned} \hat{H} = &\frac{\hbar\Omega_\alpha}{2}\hat{\sigma}_\alpha(\hat{a}e^{i(\Delta t - \phi_\alpha)} + \hat{a}^\dagger e^{-i(\Delta t - \phi_\alpha)}) \\ &+ \frac{\hbar\Omega_{\alpha'}}{2}\hat{\sigma}_{\alpha'}(\hat{a}e^{i(m\Delta t - \phi_{\alpha'})} + \hat{a}^\dagger e^{-i(m\Delta t - \phi_{\alpha'})}), \end{aligned} \tag{6.6}$$

where the spin-bases of the two SDFs are $\hat{\sigma}_\alpha$ (SDF_α) and $\hat{\sigma}_{\alpha'}$ ($\text{SDF}_{\alpha'}$), respectively. From now on, we are going to refer to SDF_α and $\text{SDF}_{\alpha'}$ as the *interaction* SDFs. Without loss of generality, we set $\phi_\alpha = 0$.

To determine the dynamics of the two SDFs, we consider the resulting unitary propagator found via the Magnus expansion [4, 5, 140] introduced in Sec. 2.3.

[2]We note that in trapped ions, fourth-order sideband (bosonic) interactions have been driven using monochromatic fields [150, 151]. In these systems, the Lamb-Dicke parameters are at least five and ten times larger, respectively, than in our system and generally exceed the values commonly achieved in trapped ion processors.

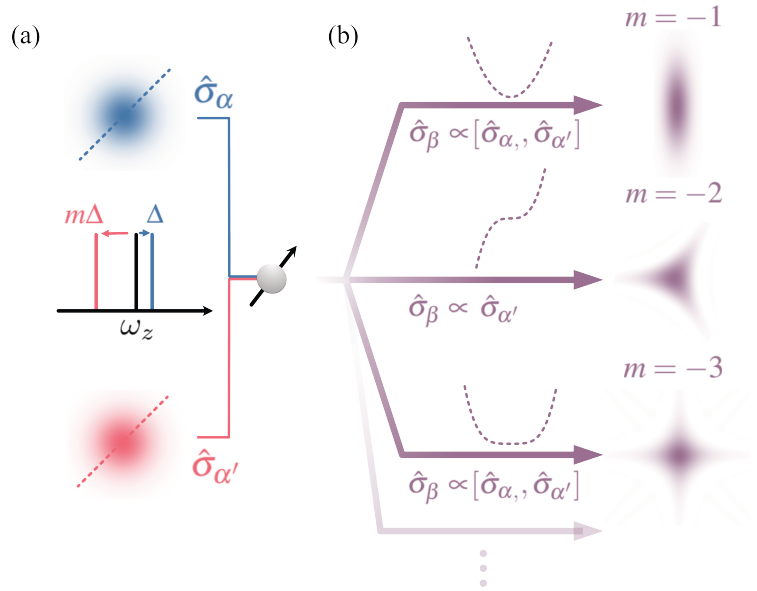

Figure 6.1: Conceptual illustration of spin-mediated nonlinear interactions. (a) We apply two spin-dependent forces detuned from the oscillator motion frequency ω_z by Δ and $m\Delta$, where m is an integer. These interactions are linear and cause a spin-dependent displacement. We set the spin components of these forces $\hat{\sigma}_\alpha$ and $\hat{\sigma}_{\alpha'}$ such that they do not commute, i.e. $[\hat{\sigma}_\alpha, \hat{\sigma}'_\alpha] \neq 0$. We show the Wigner functions of the coherent states (blue and red blobs) that would be generated by the effective potential of the linear interactions (blue and red dashed lines). (b) Generation of n^{th}-order nonlinear interactions. We can drive arbitrary nonlinear interactions by adjusting the relative detunings of the linear interactions, and hence m. Setting $m = -1$ gives rise to squeezing $\sim (\hat{a}^{\dagger 2} + \hat{a}^2)$ (second order), $m = -2$ trisqueezing $\sim (\hat{a}^{\dagger 3} + \hat{a}^3)$ (third order), and $m = -3$ quadsqueezing $\sim (\hat{a}^{\dagger 4} + \hat{a}^4)$ (fourth order). Purple dashed lines indicate the effective potential for the nonlinear interactions that are proportional to $(\hat{a}^\dagger + \hat{a})^n$; by setting $m = 1 - n$, we can select the terms in the expansion of this potential that correspond to generalised squeezing interactions. The Wigner functions corresponding to the respective generalised squeezed states are indicated in purple. The faint arrow indicates the method can be extended beyond the fourth order.

The first-order term in the Magnus expansion (Eq. (2.28)) leads to periodic displacements (i.e. loops) of the oscillator in phase space:

$$\begin{aligned} -\frac{i}{\hbar}\int_0^t dt_1 \hat{H}_1 &= -\frac{i}{2}\int_0^t dt_1 (\Omega_\alpha \hat{\sigma}_\alpha (\hat{a}e^{i\Delta t_1} + \text{h.c.}) + \Omega_{\alpha'}\hat{\sigma}_{\alpha'}(\hat{a}e^{i(m\Delta t_1 - \phi_{\alpha'})} + \text{h.c.})) \\ &= i\frac{\Omega_\alpha}{\Delta}\hat{\sigma}_\alpha \sin\left(\frac{\Delta t}{2}\right)(\hat{a}e^{i\Delta t/2} + \hat{a}^\dagger e^{-i\Delta t/2}) \\ &+ i\frac{\Omega_{\alpha'}}{m\Delta}\hat{\sigma}_{\alpha'} \sin\left(\frac{m\Delta t}{2}\right)(\hat{a}e^{i(m\Delta t/2 - \phi_{\alpha'})} + \hat{a}^\dagger e^{-i(m\Delta t/2 - \phi_{\alpha'})}). \end{aligned} \tag{6.7}$$

For integer multiples of $2\pi/\Delta$ durations, the oscillator state returns to its original position in the case of both displacements (see Sec. 2.3.1).

Looking at the second term in more detail

$$-\frac{1}{2\hbar^2}\int_0^t\int_0^{t_1} dt_1 dt_2[\hat{H}_1,\hat{H}_2] \tag{6.8}$$

$$=-\frac{1}{8}\int_0^t\int_0^{t_1} dt_1 dt_2[\Omega_\alpha\hat{\sigma}_\alpha(\hat{a}e^{i\Delta t_1}+\text{h.c.})+\Omega_{\alpha'}\hat{\sigma}_{\alpha'}(\hat{a}e^{i(m\Delta t_1-\phi_{\alpha'})}+\text{h.c.}),$$

$$\Omega_\alpha\hat{\sigma}_\alpha(\hat{a}e^{i\Delta t_2}+\text{h.c.})+\Omega_{\alpha'}\hat{\sigma}_{\alpha'}(\hat{a}e^{i(m\Delta t_2-\phi_{\alpha'})}+\text{h.c.})] \tag{6.9}$$

$$=-\frac{1}{8}\int_0^t\int_0^{t_1} dt_1 dt_2\Omega_\alpha^2[\hat{\sigma}_\alpha(\hat{a}e^{i\Delta t_1}+\text{h.c.}),\hat{\sigma}_\alpha(\hat{a}e^{i\Delta t_2}+\text{h.c.})] \tag{6.10}$$

$$+\Omega_\alpha\Omega_{\alpha'}[\hat{\sigma}_\alpha(\hat{a}e^{i\Delta t_1}+\text{h.c.}),\hat{\sigma}_{\alpha'}(\hat{a}e^{i(m\Delta t_2-\phi_{\alpha'})}+\text{h.c.})] \tag{6.11}$$

$$+\Omega_{\alpha'}\Omega_\alpha[\hat{\sigma}_{\alpha'}(\hat{a}e^{i(m\Delta t_1-\phi_{\alpha'})}+\text{h.c.}),\hat{\sigma}_\alpha(\hat{a}e^{i\Delta t_2}+\text{h.c.})] \tag{6.12}$$

$$+\Omega_{\alpha'}^2[\hat{\sigma}_{\alpha'}(\hat{a}e^{i(m\Delta t_1-\phi_{\alpha'})}+\text{h.c.}),\hat{\sigma}_{\alpha'}(\hat{a}e^{i(m\Delta t_2-\phi_{\alpha'})}+\text{h.c.})]. \tag{6.13}$$

Lines (6.10) and (6.13) give rise to geometric phases which are dependent on the spin state, as discussed in the case of a single SDF in Sec. 2.3. This combined with setting $\hat{\sigma}_\alpha,\hat{\sigma}_{\alpha'}$ to commute, i.e., $[\hat{\sigma}_\alpha,\hat{\sigma}_{\alpha'}]=0$, would cause all terms higher than the second order in the Magnus expansion to vanish, as well as lines (6.11) and (6.12). However, if the bases of the SDFs are chosen such that $[\hat{\sigma}_\alpha,\hat{\sigma}_{\alpha'}]\neq 0$, we obtain the sought-after nonlinear interactions. Lines (6.11) and (6.12), then lead to driving resonantly a squeezing interaction by setting $m=-1$:

$$\hat{H}_{\text{eff}}^2=\frac{i\hbar\Omega_2}{2}\hat{\sigma}_\beta(-\hat{a}^2e^{-i\theta}+\hat{a}^{\dagger 2}e^{i\theta}) \tag{6.14}$$

or the Hamiltonian that gives rise to a rotation in phase-space by setting $m=1$:

$$\hat{H}_{\text{eff}}^2=\frac{i\hbar\Omega_2}{2}\hat{\sigma}_\beta(\hat{a}^\dagger\hat{a}e^{-i\theta}-\hat{a}\hat{a}^\dagger e^{i\theta}+\cos\theta). \tag{6.15}$$

By choosing the correct integer m for the detuning setting, each term can be brought into resonance separately (i.e., have the leading contribution to the dynamics), while the other terms in the expansion can be neglected under certain conditions, as discussed later in this section, Sec. 6.1.2. Moreover, to clarify an important point: although the SDFs that comprise the interaction are driven off-resonantly, the resulting effective nonlinear interaction is driven on resonance.

While it is possible to drive terms such as shown in Eq. (6.15), we shall henceforward restrict ourselves to investigating generalised squeezing interactions. Trisqueezing

originates from the third order term ((2.30)) in the Magnus expansion and by setting $m = -2$

$$\hat{H}^3_{\text{eff}} = \frac{\hbar\Omega_3}{2}\hat{\sigma}_\beta(\hat{a}^3 e^{-i\theta} + \hat{a}^{\dagger 3} e^{i\theta}). \tag{6.16}$$

Quadsqueezing originates from the fourth order term ((2.31)) in the Magnus expansion and by setting $m = -3$

$$\hat{H}^4_{\text{eff}} = \frac{i\hbar\Omega_4}{2}\hat{\sigma}_\beta(-\hat{a}^4 e^{-i\theta} + \hat{a}^{\dagger 4} e^{i\theta}). \tag{6.17}$$

We note the $\pi/2$ phase difference in the motional phase between the odd and the even orders of the generalised squeezing. We can generate higher-order squeezing interactions by fulfilling the $m = 1 - n$ resonance condition; however, we stop at the fourth order here. The axis of the interactions is defined by $\theta = \phi_{\alpha'}$, indicating that we can fully control it by adjusting the motional phase of the $\text{SDF}_{\alpha'}$.

The spin dependence $\hat{\sigma}_\beta$ is given by the initial choice of $\hat{\sigma}_{\alpha,\alpha'}$ and the desired squeezing order n. The spin operator corresponding to the squeezing interaction is $[\hat{\sigma}_\alpha, \hat{\sigma}_{\alpha'}]$, trisqueezing $[\hat{\sigma}_\alpha, [\hat{\sigma}_\alpha, \hat{\sigma}_{\alpha'}]]$ and, quadsqueezing $[\hat{\sigma}_\alpha, [\hat{\sigma}_\alpha, [\hat{\sigma}_\alpha, \hat{\sigma}_{\alpha'}]]]$. Simplifying the nested commutator relationships, the spin-conditioning is given as

$$\hat{\sigma}_\beta \propto \begin{cases} [\hat{\sigma}_\alpha, \hat{\sigma}_{\alpha'}] & \text{if } n \bmod 2 = 0 \\ \hat{\sigma}_{\alpha'} & \text{otherwise,} \end{cases} \tag{6.18}$$

where the preference towards $\hat{\sigma}_{\alpha'}$ arises due to the relative detuning setting between the two SDFs[3], see Eq. (6.6). Hence, by being able to generate SDFs conditioned on any Pauli operator, the spin component of the nonlinear interaction can be arbitrarily chosen.

The magnitudes of these interactions are given by

$$\Omega_{2,3,4} = \left\{ \frac{\Omega_{\alpha'}\Omega_\alpha}{\Delta}, \frac{\Omega_{\alpha'}\Omega_\alpha^2}{2\Delta^2}, \frac{\Omega_{\alpha'}\Omega_\alpha^3}{8\Delta^3} \right\}. \tag{6.19}$$

By applying the generalised squeezing Hamiltonians in Eq. (6.14), (6.16) and (6.17)

[3]Let's try to understand this by taking the example of trisqueezing ($m = -2$). As we focus on selecting a resonant nonlinear bosonic term from the Magnus expansion, we are going to select terms for which the rotating terms cancel, i.e., $e^{i\Delta t}e^{i\Delta t}e^{-i2\Delta t}$. This means that the basis of SDF_α detuned by Δ contributes more significantly to the nested commutator $[\hat{\sigma}_\alpha, [\hat{\sigma}_\alpha, \hat{\sigma}_{\alpha'}]] \propto \hat{\sigma}_{\alpha'}$.

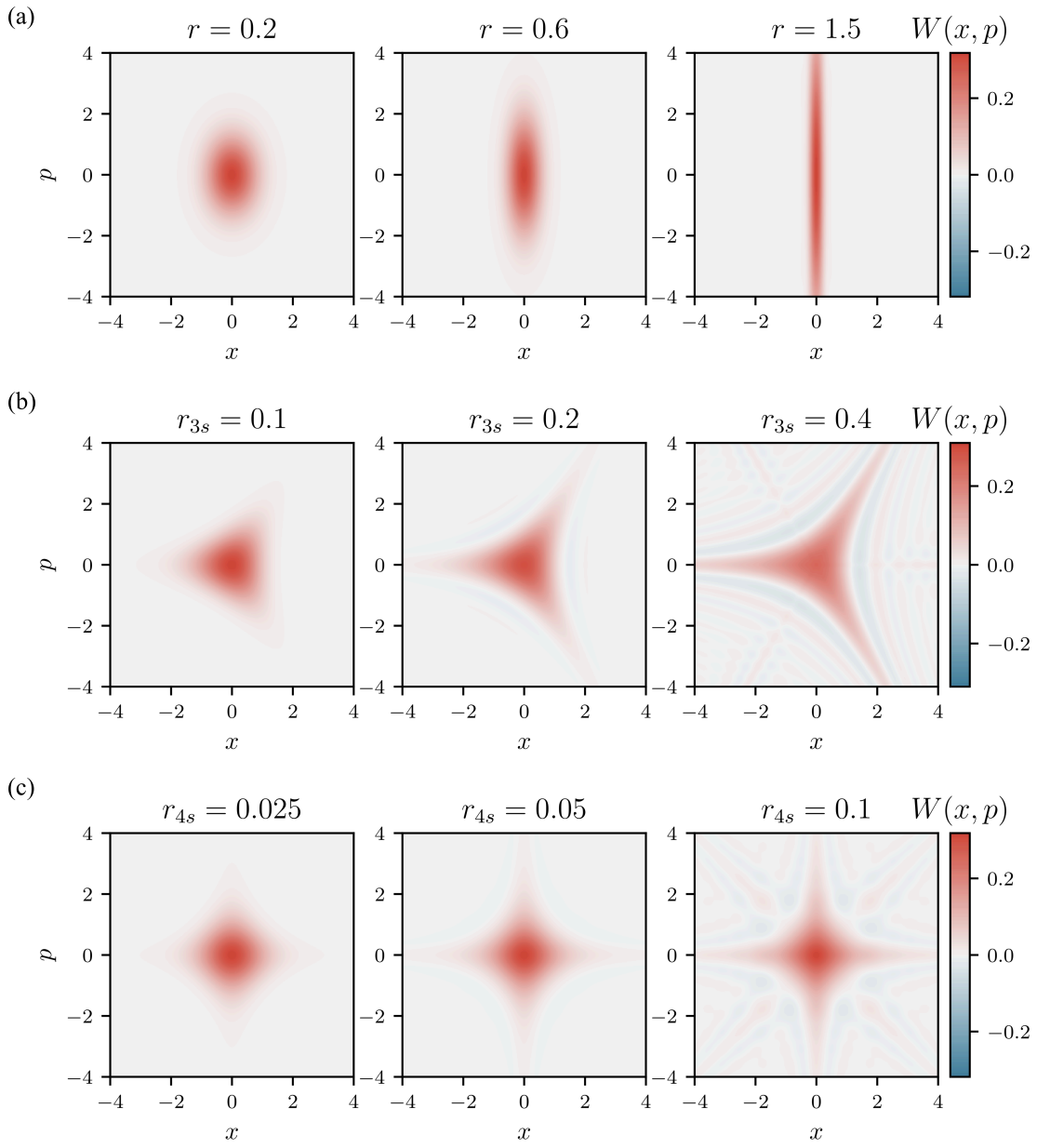

Figure 6.2: Simulation of (a) squeezed, (b) trisqueezed, and (c) quadsqueezed states using the ideal effective Hamiltonians. For each generalised squeezed state, we vary the squeezing parameter, which is r for squeezed states, r_{3s} for trisqueezed states, and r_{4s} for quadsqueezed states.

for a duration t_{sqz}, we can generate n^{th}-order squeezed states characterised by the squeezing parameter $r = \Omega_n t_{\text{sqz}}$. To differentiate between the squeezing parameters of squeezed, trisqueezed, and quadsqueezed states, we use the notations r, r_{3s}, and r_{4s}, respectively. In the following, we shall use the term 'effective Hamiltonian' for the Hamiltonians shown in Eq. (6.14), (6.16), and (6.17), as we temporarily

neglect the many off-resonant terms in the full Hamiltonian. We directly compute the time-evolution operators for squeezing, trisqueezing, and quadsqueezing using the effective Hamiltonians in Eq. (6.14), (6.16) and (6.17), respectively, using a Fock state cutoff of 200. These propagators are then applied to a system initialised in $|\downarrow\rangle|0\rangle$ to generate squeezed, trisqueezed and quadsqueezed states with various squeezing parameter values. We show the Wigner functions $W(x,p)$ of the resulting oscillator states in Fig. 6.2. In the case of the trisqueezed and quadsqueezed states, we observe that there are areas where $W(x,p) < 0$ hinting at their non-Gaussian nature [38, 39], which we briefly introduced in Sec. 1.1.

Ref. [140] discusses in detail how well the two non-commuting SDFs approach (Eq. (6.6)) approximates the ideal effective Hamiltonians, particularly for squeezing (Eq. (6.14)) and trisqueezing (Eq. (6.16)). We extend this discussion to more realistic experimental settings in the following sections.

To gain further insight into the two non-commuting SDFs method, we also numerically integrate the Hamiltonian in Eq. (6.6) for $m = -1$ (squeezing) and show the Wigner functions of the created states at different time instances, $t_{\mathrm{sqz}} = \{0, 10, 25\} \times 2\pi/\Delta$, as illustrated in Fig. 6.3. These time steps are chosen as integer multiples of $2\pi/\Delta$ to ensure that no residual displacement remains. The system is initialised in the state $|\downarrow\rangle|0\rangle$ and before computing the Wigner functions, we trace out the spin degree of freedom.

Additionally, we illustrate the phase space trajectories of the quantum harmonic oscillator due to the two non-commuting off-resonant SDFs. Without loss of generality, we set the basis of SDF_α to $\hat{\sigma}_x$ and the basis of $\mathrm{SDF}_{\alpha'}$ to $\hat{\sigma}_y$ basis. We reconstruct these trajectories by independently integrating the Hamiltonian for each SDF. We choose the separate treatment due to their non-commutativity, which complicates the choice of spin eigenstates for a joint representation (see Sec. 2.3.1 for further details). It is important to note the difference in scale between the trajectory plots and the Wigner function plots: while displacement-induced excursions are relatively small ($x \sim 0.14$), the maximum squeezing results in a much larger phase-space spread ($x \sim 4$). For this particular simulation, we use $\Delta/2\pi = 50\,\mathrm{kHz}$ and

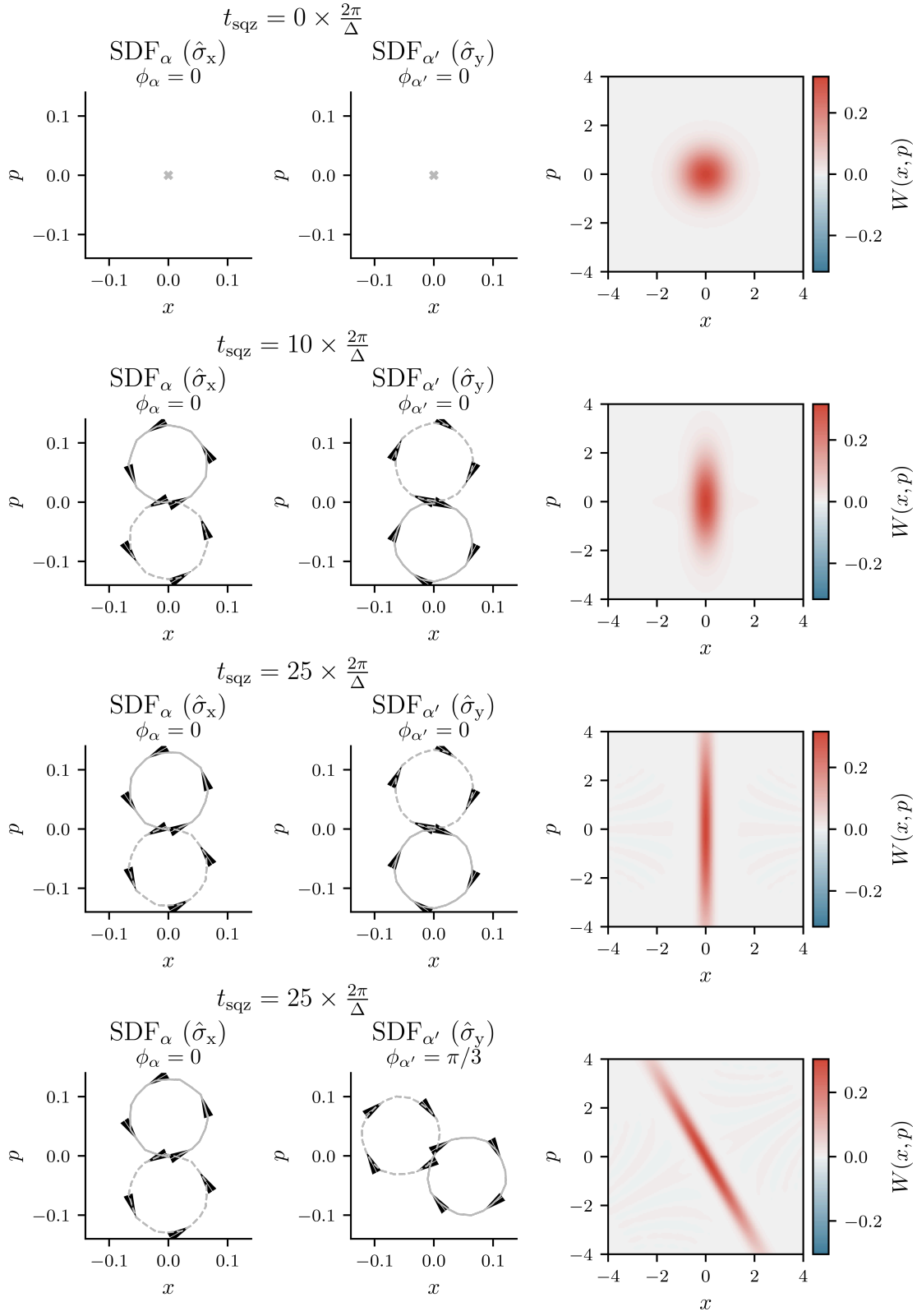

Figure 6.3: Squeezing via two non-commuting off-resonant spin-dependent forces, SDF_{α} and $\mathrm{SDF}_{\alpha'}$. The phase-space trajectories and Wigner functions are shown at different evolution times, $t_{\mathrm{sqz}} = \{0, 10, 25\} \times 2\pi/\Delta$. The first column shows the trajectory due to SDF_{α} only, applied in the $\hat{\sigma}_x$ basis and with motional phase ϕ_{α}. The second column shows the trajectory due to $\mathrm{SDF}_{\alpha'}$ only, applied in the $\hat{\sigma}_y$ basis and with motional phase $\phi_{\alpha'}$. The final column presents the corresponding squeezed state Wigner functions obtained by combining SDF_{α} and $\mathrm{SDF}_{\alpha'}$.

$\Omega_\alpha/2\pi = \Omega_{\alpha'}/2\pi = 4.6\,\mathrm{kHz}$, values that are experimentally accessible. We also explore the impact of different motional phases, ϕ_α and $\phi_{\alpha'}$, on the squeezing axis θ.

Effective interactions and the magnitude scaling of this method

If the spin components of the SDFs do not commute, the Magnus expansion in Eq. (2.27) contains an infinite number of terms. As discussed above, specific terms can be brought into resonance by satisfying the appropriate resonance conditions. The remaining terms in the Magnus expansion fall into two categories: (1) terms that are off-resonant by $\sim \Delta$ relative to the leading interaction, and (2) terms that are resonant with it and originate from higher orders of the expansion. Category (1) includes, for example, cases where a single-mode squeezing interaction is made resonant, while other terms, such as displacements, are detuned by $\sim \Delta$. Category (2) comprises higher-order terms that satisfy the same resonance condition as the desired interaction. For instance, when we are resonant with the single-mode squeezing interaction ($m = -1$), the term $\hat{a}^\dagger\hat{a}^\dagger\hat{a}\hat{a} + \mathrm{h.c.}$, originating from the fourth order in the Magnus expansion, also satisfies the same resonance condition[4].

Just as the off-resonant displacement terms are eliminated when the interaction duration is an integer multiple of $2\pi/\Delta$, the detuned terms in category (1) can likewise be suppressed by enforcing the same timing condition. As discussed in Sec. 6.5, this requirement can be relaxed by employing amplitude-shaped pulses over a period of more than $2\pi/\Delta$, which reduces the contributions of these off-resonant terms through temporal filtering.

In contrast, the spurious terms that are resonant with the leading interaction (category (2)) cannot be removed by adjusting the interaction time or by employing amplitude shaping. These contributions originate solely from higher-order terms in the Magnus expansion. For a target interaction of order n, they introduce an error

[4]An analogous situation arises in the Lamb–Dicke expansion. For example, when the carrier transition (a zeroth-order term) is driven by setting $\delta = 0$ in Eq. (2.43), it is resonant with the second-order, rotation-in-phase Hamiltonian given in Eq. (6.2).

ϵ in the unitary evolution that scales as $(\Omega_\alpha/\Delta)^{n+1}$, under the assumption of equal-strength SDFs (i.e. $\Omega_\alpha = \Omega_{\alpha'}$). This error decreases faster with Δ than the desired leading interaction. As such, the error can be minimised arbitrarily by increasing Δ. Thus, provided that the off-resonant terms (category (1)) are effectively suppressed through timing or amplitude shaping, the dynamics generated by the Hamiltonian in Eq. (6.6) faithfully implement the desired interaction, such as the generalised squeezing Hamiltonians in Eqs. (6.14), (6.16), and (6.17), up to an error $\epsilon = (\Omega_\alpha/\Delta)^{n+1}$ arising from higher-order on-resonant terms (category (2)), where n denotes the order of the target term.

Examining this error term more closely provides further insight into the scaling of the strength of the desired interactions. If we accept a fixed error $\epsilon = (\Omega_\alpha/\Delta)^{n+1} =$ const., we can express the interaction strength as $\Omega_\alpha = \Delta \sqrt[n+1]{\epsilon}$. Since Ω_α is linear in η, the Lamb-Dicke parameter, Δ, also effectively scales linearly with respect to η. Consequently, the strength of the desired interaction, $\propto \Omega_{\alpha'}\Omega_\alpha^{n-1}/\Delta^{n-1}$, can be made effectively linear in η irrespective of n. This tunable scaling is in contrast to driving higher-order spatial derivatives of the field, where the interaction strength scales as η^n (see Sec. 6.1.1).

We emphasise that although the formal expression for Ω_n involves higher powers of η, our scheme enables this dependence to be effectively reduced to linear in η by experimentally controlling Δ.

To investigate this scaling in more detail, we consider two error values: $\epsilon = 10^{-3}$ and $\epsilon = 10^{-2}$. Fixing $\Omega_\alpha/2\pi = 95\,\mathrm{kHz}$, a value that is accessible in our experimental setup, we vary η and adjust the detuning Δ to maintain a constant error in each case. As shown in Fig. 6.4, the resulting interaction strengths for squeezing, trisqueezing, and quadsqueezing, respectively, exhibit effective linear scaling with η. For comparison, we also plot the corresponding interaction strengths obtained by driving higher-order sidebands within the Lamb–Dicke expansion. We assume equal power is available for both approaches: if the two non-commuting SDF scheme employs 0.5 mW of laser power per SDF, then the higher-order sideband approach, requiring only a single bichromatic field, uses a total of $2 \times 0.5\,\mathrm{mW}$ laser power.

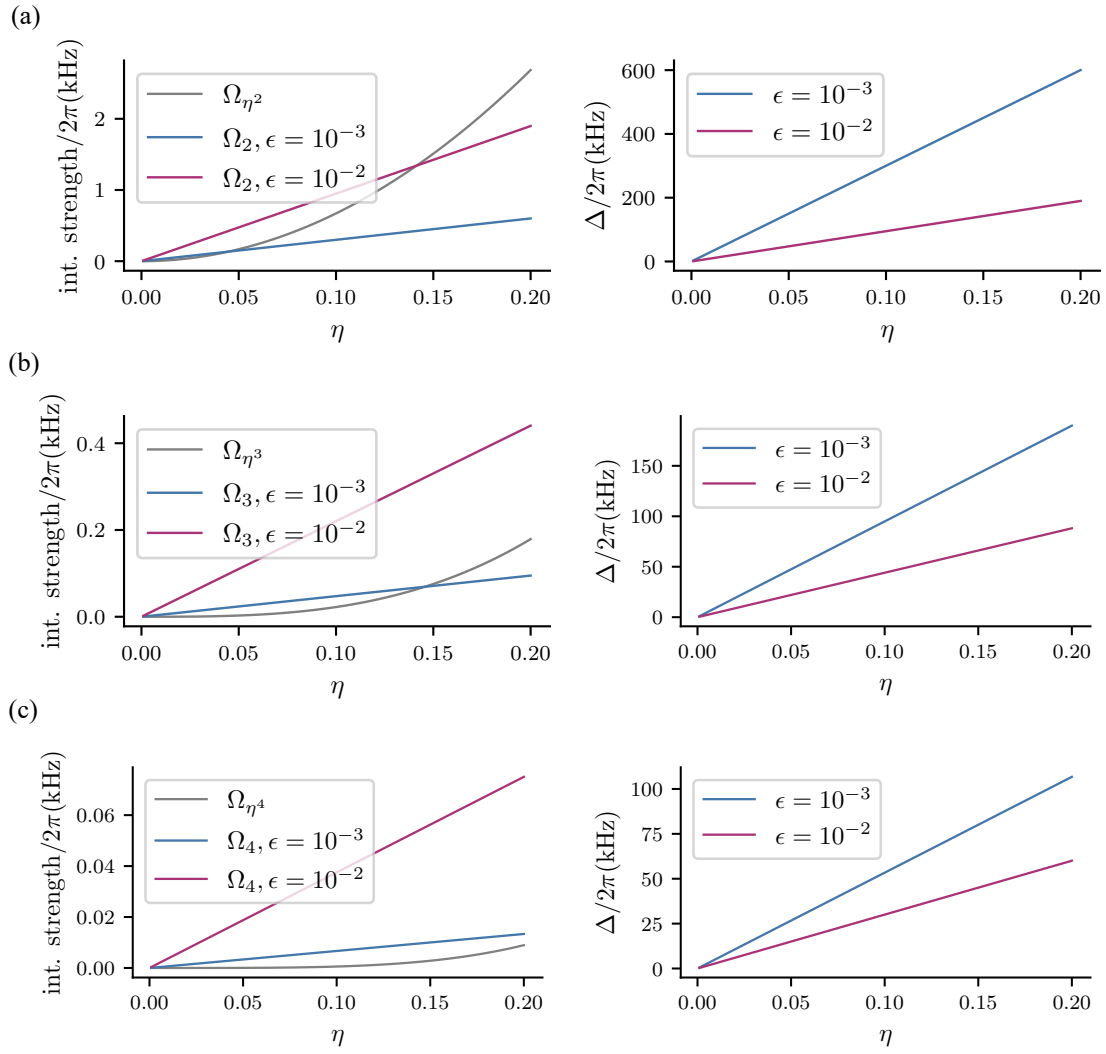

Figure 6.4: Nonlinear interaction strength scaling comparison. We compare the method demonstrated in this work, with magnitude Ω_n, to the method of driving higher-order terms in the Lamb-Dicke expansion, with magnitude Ω_{η^n} (left column). We vary the value of the Lamb-Dicke parameter in this process while keeping the intensity of the driving field constant. For the two non-commuting SDFs method, we keep $\epsilon = (\Omega_\alpha/\Delta)^{n+1}$ constant by varying the detuning Δ as a function of η (right column). We evaluate this for (a) squeezing, (b) trisqueezing, and (c) quadsqueezing interactions.

As the order of the interaction increases, the corresponding interaction strength decreases for both methods. However, for the approach based on two non-commuting SDFs, the effective linear scaling with η leads to more favourable behaviour, particularly at higher orders. The purpose of this analysis is to provide deeper insights into the scaling of the two non-commuting SDFs method. To isolate this aspect, we intentionally assume that driving higher-order terms in the Lamb–Dicke

expansion produces ideal, error-free nonlinear interactions. In doing so, we neglect effects such as off-resonant contributions and higher-order resonant terms, both of which become relevant as η grows. Furthermore, the parameter ϵ used here does not quantify the total error expected in generating a generalised squeezed state; a full assessment would require accounting for the interaction duration. In later sections (e.g. Sec. 6.7), we address this by evaluating the resulting infidelities $1 - F$ of specific target states.

6.2 Two non-commuting spin-dependent forces in the lab

Let us consider how to implement the two non-commuting interactions in the lab. Each SDF is generated by using a Mølmer-Sørensen scheme, i.e., each SDF is created using a laser bichromatic field composed of two tones that are symmetrically detuned from the qubit transition ω_q by $\pm\delta$ (see Sec. 2.3.2) and is described by the following Hamiltonian:

$$\begin{aligned}\hat{H}_{\mathrm{bi}} = &- \frac{\hbar\Omega_\alpha}{2}\hat{\sigma}_\phi(\hat{a}e^{i(\Delta\, t-\phi_\alpha)} + \hat{a}^\dagger e^{-i(\Delta\, t-\phi_\alpha)}) \\ &+ \hbar\Omega\hat{\sigma}_{\phi-\pi/2}\cos(\delta t - \phi_\alpha),\end{aligned} \tag{6.20}$$

where we modified the notation in Eq. (2.44) to be easier to parse in the context of this chapter, with $\Omega_\alpha = \eta\Omega$. The setup for introducing the two bichromatic fields is described in Sec. 3.5; the two bichromatic fields are co-propagating and concurrently driven.

6.2.1 Many, many phases

We note again that both the spin-basis $\hat{\sigma}_\phi$, where $\phi = \pi/2 - (\phi_\mathrm{r} + \phi_\mathrm{b})/2$, and the motional phase $\phi_\alpha = ((\phi_b - \phi_r)/2)_\alpha$ depend on the optical phases of the two tones in the bichromatic field at the position of the ion. While we cannot control the absolute phase of the tones at the position of the ion, we are interested in establishing certain phase relations between the four tones of the two interaction SDFs.

The mechanism of the nonlinear interaction relies on the commutator relationship between the spin components of the individual SDFs. This means that we need to maintain $((\phi_\mathrm{r}+\phi_\mathrm{b})/2)_\alpha - ((\phi_\mathrm{r}+\phi_\mathrm{b})/2)_{\alpha'}$ constant between different experiment repetitions. If all four tones travelled along the same path throughout the setup, this condition would be fulfilled at no additional cost, e.g., by creating all tones using the same AOM. However, in our configuration, each bichromatic field is generated by a separate AOM, and subsequently, the two fields are combined to travel along the same path. We opted for this geometry due to concerns regarding additional terms that might arise from mixing products caused by nonlinearities in the AOM or rf amplifier, potentially complicating the debugging and calibrating of the effective interactions. Hence, we actively stabilise the relative phase between the two bichromatic fields, as described in Sec. 3.5.

To implement the effective nonlinear interactions, we need two non-commuting SDFs. One approach is to set $\hat{\sigma}_\alpha = \hat{\sigma}_\phi$ and $\hat{\sigma}_{\alpha'} = \hat{\sigma}_{\phi+\pi/2}$. To achieve $\hat{\sigma}_{\alpha'} = \hat{\sigma}_{\phi+\pi/2}$, we push the phase of both rf signals driving the blue detuned and the red detuned tones of $\mathrm{SDF}_{\alpha'}$, respectively, by $\pi/2$. This assumes that $(\phi_\mathrm{r}+\phi_\mathrm{b})_\alpha = (\phi_\mathrm{r}+\phi_\mathrm{b})_{\alpha'}$ in the first place. Furthermore, as discussed Sec. 6.1.2, the axis of the nonlinear interaction θ is determined by the motional phase of the $\mathrm{SDF}_{\alpha'}$, $\phi_{\alpha'}$ with $\phi_\alpha = 0$ for SDF_α. Hence, additional phase relationships between the tones of the bichromatic fields need to be satisfied. We aim to establish the following relationships through calibrations:

$$\begin{aligned}(\phi_\mathrm{r}+\phi_\mathrm{b})_\alpha &= (\phi_\mathrm{r}+\phi_\mathrm{b})_{\alpha'}\\ (\phi_\mathrm{b}-\phi_\mathrm{r})_\alpha &= 0\\ (\phi_\mathrm{b}-\phi_\mathrm{r})_{\alpha'} &= 0,\end{aligned} \tag{6.21}$$

as it mildly alleviates the misery of phases. The first line results from establishing a relationship between the spin phases (spin bases) of the SDFs, while the last two lines correspond to the motional phases of the two SDFs (see Sec. 2.3.2). The calibration protocol[5] is detailed in Sec. 3.5. Once the phases are calibrated, implementing the nonlinear interactions becomes straightforward[6]. For instance,

[5]The labelling of the phases is different between the current chapter and Chapter 3, α corresponds to b1 and α' corresponds to b2.

[6]I am more serious than you might think.

we can easily incorporate a $\pi/2$ phase as an offset with respect to the calibrated values to ensure $\hat{\sigma}_{\alpha'} = \hat{\sigma}_{\phi+\pi/2}$, as described earlier.

6.2.2 Arbitrary SDF basis and the elephant (carrier) in the room

The capability to generate SDFs conditioned on various Pauli operators enables full control over the basis of the resulting effective nonlinear interaction (see Sec. 6.1.2). For the experiments presented in this chapter, we create forces in the $\hat{\sigma}_\phi$ basis by setting $\delta \approx \omega_z$ or $\hat{\sigma}_z$ basis $\delta \approx \omega_z/2$ (see Sec. 2.3). Characterisation and calibration of the individual SDFs are presented in Chapter 4.

We need to combine two of the non-commuting SDFs mentioned above to generate the nonlinear interactions; see Eq. (6.6). This introduces the question of how the carrier terms affect the dynamics. Drawing from our analysis in the case of creating an effective $\hat{\sigma}_z$ SDF (Sec. 2.3), as the carrier terms do not act on the oscillator, we might expect that they only alter the strength of the nonlinear interaction. We leave evaluating this further for future work. While we do not provide an analytic analysis of the effect of the carrier terms, we include them in the simulations to ensure their influence is appropriately accounted for (see Sec. 6.3).

Since we aim to measure and estimate the magnitude of the nonlinear interactions, which depends on the strength of the comprising SDFs, we make a naive assumption and check its validity as we advance. The assumption is that each carrier term solely affects the corresponding SDF, neglecting that they may also affect each other as they do not commute. Hence, for forces in the $\hat{\sigma}_\phi$ basis, we hypothesise that the strength is given by $\Omega_\alpha \to \Omega_\alpha |J_0(2\Omega/\delta) + J_2(2\Omega/\delta)|$. For the experiments presented here, we operate in a small Ω regime where $|J_0 + J_2| \approx 1$. This implies that, in this scenario, we can disregard the effect of the carrier. For forces in the $\hat{\sigma}_z$ basis, we hypothesise that the strength of the effective SDF is given by $\Omega_\alpha \to \Omega_\alpha |J_1(2\Omega/\delta) + J_3(2\Omega/\delta)|$. In the following sections, when we mention the strength of the comprising interaction SDFs, we will quote the laser power that we use for each of them. We find this less cumbersome, especially in the light of the $|J_1(2\Omega/\delta) + J_3(2\Omega/\delta)|$ modulation

term for the $\hat{\sigma}_z$. However, magnitudes of SDFs $\Omega_\alpha, \Omega'_\alpha$ are calibrated every day, with typical values shown in Table 6.1. In our setup, the beam waist radius is 20 µm, and the Lamb-Dicke parameter is $\eta = 0.049(1)$.

power (mW)	SDF basis	$\Omega_{\alpha,\alpha'}/2\pi$(kHz)
0.5	$\hat{\sigma}_\phi$	4.6
1	$\hat{\sigma}_\phi$	6.5
2	$\hat{\sigma}_\phi$	9.2
1	$\hat{\sigma}_z$	1.3
2	$\hat{\sigma}_z$	3

Table 6.1: Typical spin-dependent force strength depending on the power and the spin basis.

6.3 Numerical simulations

In the forthcoming sections, we present the results of the experimental implementation and characterisation of these nonlinear bosonic interactions. We compare the experimental results to simulations, which we compute through numerical integration of the Lindblad master equation under time-dependent Hamiltonians using the QuantumOptics.jl package in Julia [125]:

$$\dot{\hat{\rho}} = -i\frac{i}{\hbar}[\hat{H}, \hat{\rho}] + \sum_i (\hat{J}_i \hat{\rho} \hat{J}_i^\dagger - \frac{1}{2}\hat{J}_i^\dagger \hat{J}_i \hat{\rho} - \frac{1}{2}\hat{\rho}\hat{J}_i^\dagger \hat{J}_i) \tag{6.22}$$

where $\hat{J}_i = \sqrt{\gamma_i}\hat{A}_i$ is a collapse operator. The decoherence mechanism is governed by the operator $\hat{A}_i$ and the rate γ_i.

When investigating the generation of nonlinear interactions in simulation, the Hamiltonian $\hat{H}$ in Eq. (6.22) is specified by the sum of two non-commuting SDFs (Eq. (6.6)), where the Hamiltonian of the individual SDFs is given as Eq. (2.44), i.e., we do not apply the RWA with respect to ω_z and we include the carrier terms. The resulting states of this simulation are often compared in the following sections to states created using the respective ideal interactions. Specifically, in the case of simulating the ideal interaction, $\hat{H}$ in Eq. (6.22) is replaced by one of Eqs. (6.14), (6.16), or (6.17).

Moreover, in Sec. 6.5, we explain that smoothly ramping on and off the interaction SDFs is necessary. This is introduced in the simulation by modulating the interaction strength with $g(t)$ in Eq. (4.12). This is done for simulating both the effective interactions and the ideal Hamiltonians to ensure that the interactions are applied over the same durations when comparing states.

As outlined in Sec. 6.5.1, we use a probe SDF to characterise the nonlinear interactions, which is simulated by integrating Eq. (6.20), but without making the RWA with respect to ω_z. Another characterisation tool is applying a blue sideband interaction corresponding to the oscillator to extract the Fock state populations, which is simulated by integrating the anti-Jaynes-Cummings Hamiltonian in Eq. (2.17). The motional decoherence in our system is dominated by the heating rate $\dot{\bar{n}}_{\mathrm{osc}} = 300\,(20)$ quanta/s, see Sec. 4.1.2. The heating effect is introduced in the simulation by setting the collapse operators [126] to $\sqrt{\dot{\bar{n}}_{\mathrm{osc}}}\hat{a}^{\dagger}$ and $\sqrt{\dot{\bar{n}}_{\mathrm{osc}}}\hat{a}$.

The Hilbert space is truncated at phonon number 50 or 200. The higher phonon number is especially necessary when the effect of the probing SDF is simulated (see Sec. 6.5.1).

6.4 Setting up an interaction

Once the phases are calibrated as detailed in Sec. 6.2.1[7], we are almost ready to investigate some of the nonlinear interactions. Before that, we perform the following checks:

- Ensure that the strength of the tones in the two bichromatic fields is balanced for both interaction SDFs (and the probe SDF), as detailed in Sec. 4.2.1.
- Calibrate the motional mode frequency, as detailed in Sec. 4.2.3.
- Perform detuning scans for each of the individual SDFs to calibrate any residual ac Stark shifts, as detailed in Sec. 4.2.2. Assuming that each SDF

[7]These calibrations are only conducted when the control system is restarted. The offsets are related to how the DDS channels are initialized, which do not drift over time.

has an ac Stark shift offset of $\delta_{\mathrm{dp},1}$ and $\delta_{\mathrm{dp},2}$, then, when both bichromatic fields are on, we apply $\delta_{\mathrm{dp},1} + \delta_{\mathrm{dp},2}$ for the calibration.

After these steps, we decide which nonlinear interaction to create. This is set by changing the relative frequency of the driving fields as dictated by m.
We begin our investigation of this family of interactions, starting with squeezing Eq. (6.14).

6.5 Squeezing

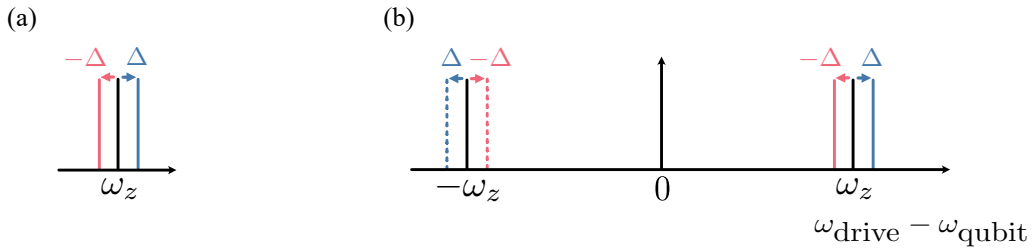

Figure 6.5: Spin-dependent forces configuration for generating the squeezing interaction. The two forces SDF_{α} and $\mathrm{SDF}_{\alpha'}$ are shown in blue and red, respectively. (a) Detuning of the spin-dependent forces relative to the motional mode frequency ω_z. (b) Frequency configuration of the laser (drive) tones in the bichromatic fields used to implement SDF_{α} and $\mathrm{SDF}_{\alpha'}$. Continuous lines represent the blue-detuned tones, while dashed lines represent the red-detuned tones.

For generating squeezing, we set the detunings of the interaction SDFs to be Δ and $-\Delta$, respectively, i.e., $m = -1$. The exact detunings of the bichromatic fields, from the qubit frequency, are the $\delta = \omega_z - \Delta$ for the $\mathrm{SDF}_{\alpha'}$ and $\delta = \omega_z + \Delta$ for the SDF_{α}, as shown in Fig. 6.5. This means we create SDFs in the $\hat{\sigma}_{\phi}$ basis, see Sec. 6.2.2. We set the relative phase between the bichromatic fields such that $\hat{\sigma}_{\alpha} = \hat{\sigma}_{\phi}$ and $\hat{\sigma}_{\alpha'} = \hat{\sigma}_{\phi+\pi/2}$, respectively. Thus, the expected spin basis of the squeezing is $[\hat{\sigma}_{\alpha}, \hat{\sigma}_{\alpha'}] \propto \hat{\sigma}_z$.
The ion is initialised in $|{\downarrow}\rangle\,|\bar{n}_{\mathrm{osc}}\rangle$, where the motional state is in a thermal state with $\bar{n}_{\mathrm{osc}} = 0.09(1)$. We apply the two non-commuting SDFs for variable durations t_{sqz} and read the spin state at the end, $p_{|{\downarrow}\rangle}$. As we expect the effective interaction to be conditioned on $\hat{\sigma}_z$ and we start in an eigenstate of it, $|{\downarrow}\rangle$, it follows that the $p_{|{\downarrow}\rangle}$ should ideally remain unchanged. In Fig. 6.6(a), we see that depending on the

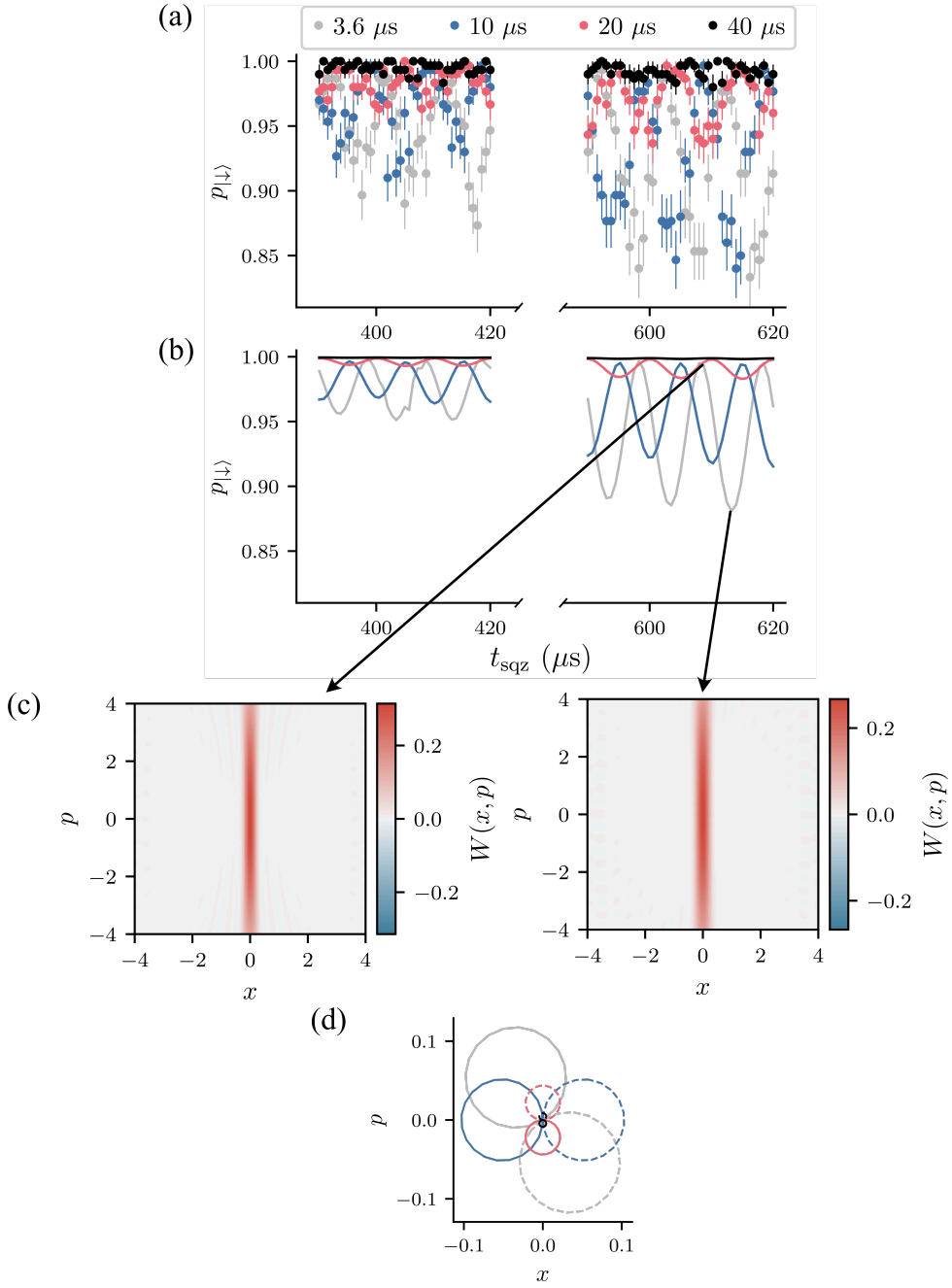

Figure 6.6: Example dynamics from applying the squeezing interaction generated by two non-commuting SDFs (Eq. (6.6)) with varying ramp durations. (a) Experimental data. While these dynamics are analysed for the effective squeezing interaction with spin-dependence in the $\hat{\sigma}_z$ basis, they will be similar to any other effective nonlinear bosonic interaction conditioned on $\hat{\sigma}_z$. (b) We compare the experiment to simulations. The spin state is initially prepared in $|\downarrow\rangle$ before we apply the SDFs for variable durations t_{sqz} and measure the probability of staying in the $|\downarrow\rangle$ state, $p_{|\downarrow\rangle}$. We repeat the measurement(simulation) for different ramp durations. The amount of residual displacement, indicated by the relatively large oscillations in $p_{|\downarrow\rangle}$, is suppressed as the ramp duration increases. The periodicity (10 µs) of the oscillations is given by the beating effect between the two SDFs with detunings $\pm\Delta/2\pi = \pm 50\,\mathrm{kHz}$ and it is predicted by the simulation. (c) Simulated Wigner functions of two squeezed states: one at a large excursion in phase space and one at the origin for $t_{\mathrm{ramp}} = 3.6\,\mu\mathrm{s}$. (d) Reconstructed phase-space trajectories of the oscillator due to SDF_α for different ramp durations.

duration over which the amplitude of the laser fields is smoothly ramped on and off, t_{ramp}, this is not the case (see Sec. 3.3.3 and 2.3.4 for details on the ramp). This effect is also observed in the numerical simulations, see Fig. 6.6(b).

As discussed in the context of the Mølmer-Sørensen Hamiltonian (Sec. 2.3.2), the amplitude shaping of the pulse reduces its bandwidth in the frequency domain and, hence, suppresses the driving of undesired off-resonant terms. In the present case, the undesired terms are off-resonant terms in the Magnus expansion, such as spin-dependent displacement, as well as the residual carrier term present for each interaction SDFs (see Eq. (6.20)). Returning to Fig. 6.6(a), (b), we observe periodic changes in population, indicating a residual displacement of the oscillator state in phase space. In Fig. 6.6(d), we reconstruct the motional mode phase-space trajectory due to SDF_α. Residual displacement occurs when the oscillator state is far from the origin. One way to obtain the squeezing interaction without any residual displacement is by precisely setting the interaction duration to integer multiples of $2\pi/\Delta$, where the motional state returns to the origin[8]. However, this duration might change due to offsets in qubit or motional mode frequency. A more robust approach is using a ramp duration t_{ramp} that is long compared to $2\pi/\Delta$, which dictates the periodicity (time constant) of the displacement. In Fig. 6.6(a), (b), (d), the detuning is set to $\Delta/2\pi = 50\,\text{kHz}$, and we can observe that for $t_{\text{ramp}} = 2\times 2\pi/\Delta$, the excursions in phase space are strongly suppressed. Furthermore, for $t_{\text{ramp}} = 3.6\,\mu\text{s}$, we also plot the simulated Wigner functions of two squeezed states: one at a large excursion in phase space and one at the origin, as shown in Fig. 6.6(c). The residual displacements are present but barely discernible in these plots, see Sec. 6.10.2 as well. The periodicity of the excursions is $10\,\mu\text{s}$, predicted by simulation and resulting from the interference of the two SDFs. Moreover, we observe that as we apply the two non-commuting SDFs for longer durations, $p_{|\downarrow\rangle}$ reaches lower and lower values. The SDFs split the oscillator wavefunction, and as the state becomes increasingly squeezed (less radially symmetric, in contrast to a thermal state), the overlap between the two parts of the wavefunction decreases, leading to lower $p_{|\downarrow\rangle}$ values.

[8]This same requirement applies to realising entangling gates.

6.5.1 Probe spin-dependent force for squeezed states

We use a spin-dependent force to characterise the squeezed states. To avoid any confusion, we refer to this as the *probe* SDF, while the two non-commuting SDFs that constitute the nonlinear interaction are referred to as the *interaction* SDFs. The probe SDF is implemented via an MS-type scheme; we use the same bichromatic field employed to generate SDF_α. Using an SDF to probe the squeezed state allows us to extract information about both its magnitude and orientation in phase space, defined by θ in Eq. (6.14), by generating a superposition in the oscillator wavepacket. This method is analog to the one described for measuring the magnitude of the SDF in Sec. 4.2.5, with the distinction that it leads to squeezed cat states [85, 152–154]. After applying the squeezing interaction, the ion is left in the $|{\downarrow}\rangle\,|\xi_{\mathrm{th}}\rangle$ state, where $|\xi_{\mathrm{th}}\rangle$ is a squeezed thermal state. We then apply the probe SDF on resonance to the motional mode ($\Delta = 0$ in Eq. (6.20)) for a duration t_{probe} and in the $\hat{\sigma}_x$ basis, for which $|{\downarrow}\rangle$ is not an eigenstate. The wavepacket is split into two squeezed states displaced in opposite directions based on the $|{\pm}\rangle$, eigenstates of $\hat{\sigma}_x$[9], as shown in the insets in Fig. 6.7 and described by

$$|\psi\rangle = \frac{1}{\sqrt{2}}(|+\rangle\,|\alpha,\xi_{\mathrm{th}}\rangle - |-\rangle\,|-\alpha,\xi_{\mathrm{th}}\rangle) \tag{6.23}$$

where $\alpha = i\Omega_{\mathrm{probe}}e^{i\phi_{\mathrm{probe}}}t_{\mathrm{probe}}/2$ quantifies the displacement, where $\Omega_{\mathrm{probe}} = \eta\Omega$. As before, as the spin is entangled with the oscillator state, measuring the spin allows us to gain information about the overlap between the two parts of the oscillator wavefunction. Eq. (2.41) describes the probability of finding the spin in $|{\downarrow}\rangle$ when splitting a thermal state. We can extend it to describe the splitting of a squeezed thermal state [152]:

$$\begin{aligned} p_{|\downarrow\rangle} &= \frac{1+f(\alpha,\xi_{\mathrm{th}})}{2}, \\ f(\alpha,\xi_{\mathrm{th}}) &= e^{-g(\alpha)h(\xi)}, \\ g(\alpha) &= |2\alpha(t_{\mathrm{probe}})|^2\left(\bar{n}_{\mathrm{osc}}+\frac{1}{2}\right), \\ h(\xi) &= e^{2r}\cos\left(\phi_{\mathrm{probe}}-\theta/2\right)^2 + e^{-2r}\sin\left(\phi_{\mathrm{probe}}-\theta/2\right)^2. \end{aligned} \tag{6.24}$$

[9] Generally speaking, we should have used $\hat{\sigma}_\phi$, but we are not losing any important aspect by assuming it is $\hat{\sigma}_x$.

The overlap $f(\alpha, \xi_{\text{th}})$ depends on the squeezing parameter r and the relative orientation between the motional phase of the probe SDF ϕ_{probe} and the squeezing axis θ. If the two are aligned ($\phi_{\text{probe}} - \theta/2 = 0$), the splitting corresponds to the inset in Fig. 6.7(b.i), referred to as splitting about the squeezed axis. Conversely, if $\phi_{\text{probe}} - \theta/2 = \pi/2$, the splitting corresponds to the inset in Fig. 6.7(b.iii), referred to as splitting about the anti-squeezed axis.

In the experiment, we calibrate the values for which ϕ_{probe} satisfies $\phi_{\text{probe}} - \theta/2 = \pi/2$ or $\phi_{\text{probe}} - \theta/2 = 0$. We apply the probe SDF for a fixed duration while scanning its motional phase ϕ_{probe}, as shown in Fig. 6.7(a). We perform a fine scan over one of the peaks, where the wavefunction is split about the anti-squeezed axis, and fit a parabola to it. We offset the calibrated ϕ_{probe} by $\pi/2$ to split about the squeezed axis. Given the intended calibration described in Sec. 6.2, we expect the peaks to occur for ϕ_{probe} at integer multiples of $\pi/2$, which is not the case.

The origin of the offset has not been investigated in detail[10]. However, similar to the standing-wave experiments (Sec. 5.2.1), we believe it might be caused by either the phase stabilisation or the channel phase calibration in Sec. 6.2 being conducted for the frequency $\omega_{\text{q}}/2\pi$ instead of $(\omega_{\text{q}} \pm \omega_z)/2\pi$, which is used for the experiments. Importantly, the offset value remains constant over time and does not change with the increase in the pulse duration for the nonlinear interaction or probe SDF, so it can be calibrated.

Once ϕ_{probe} is calibrated, we can investigate the dependence of $p_{|\downarrow\rangle}$ as a function of t_{probe} for splitting along the squeezed axis or orthogonal to it (anti-squeezed axis), see Fig. 6.7(b). We observe that applying the probe along the squeezing axis (b.i) reduces the overlap faster than splitting about the anti-squeezed (b.iii).

In the following sections, we investigate the characteristics of this family of nonlinear interactions, examining them through the lens of squeezing. Our analysis will focus on their magnitude, spin-dependence, and non-commutativity and how these properties relate back to the interaction SDFs that make the effective interaction. Moreover, we also evaluate the unitarity of the effective interaction.

[10]The Sword of Damocles/dying 674 M2 laser hanging over the heads of two students eager to finish their D.Phil.

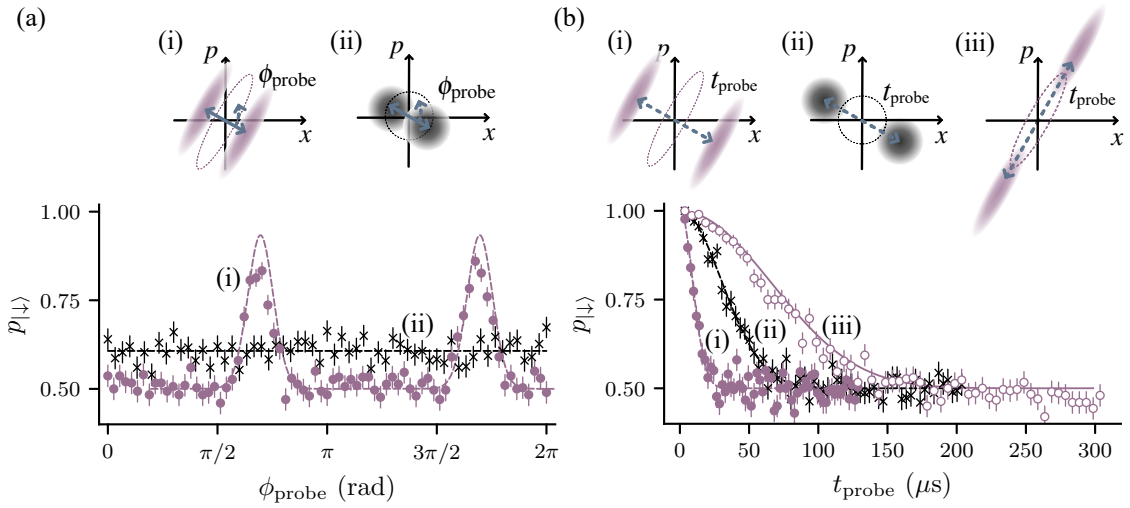

Figure 6.7: Characterising the motional state of an ion using an SDF. Once the desired motional state is created (squeezed (purple) or thermal close to the motional ground state (black)), we employ a probe spin-dependent force (SDF) to map the oscillator state to the spin state that we measure ($p_{|\downarrow\rangle}$). The insets show the effect of the probe SDF on the Wigner functions of the respective motional states in phase space. The dashed ellipses represent the state before the probe SDF is applied. (a) Varying the motional phase ϕ_{probe} of the SDF. We fix the duration for applying the SDF ($t_{\text{probe}} = 53.6\,\mu\text{s}$) and scan ϕ_{probe}. The dashed lines are fits to the data. (i) For the squeezed state, $p_{|\downarrow\rangle}$ varies as a function of the relationship between ϕ_{probe} and the squeezing axis; the peaks occur when the probe SDF is aligned with the anti-squeezed (long) axis. We use these peaks to calibrate the relative orientation of the squeezed state with respect to the probe SDF. (ii) Splitting the thermal state wavefunction has no dependence on ϕ_{probe}. (b) Varying the duration t_{probe} for which the probe SDF is applied for a fixed ϕ_{probe}. As t_{probe} increases, the spin-dependent displacement separates the oscillator wavefunction (insets). The probe SDF is applied along the two principal axes of a squeezed state ((i), (iii)) and, as a comparison, to a thermal state (ii). The dashed lines are fits to the data in (i) and (ii) and are used to infer the squeezing parameter r (see text). We plot the numerical simulation for the anti-squeezed axis (iii), which accounts for motional decoherence effects (see text).

6.5.2 Magnitude

From Sec. 6.1.2, the expected dependence of the squeezing interaction magnitude is $\Omega_2 = \Omega_\alpha \Omega_{\alpha'}/\Delta$, see Eq. (6.19), where $\Omega_\alpha, \Omega_{\alpha'}$ are the magnitudes of the constituent SDFs and Δ is the detuning from the oscillator frequency. We check that this relationship holds in the experiment. The squeezing parameter for a squeezed state is given as $r = \Omega_2 t_{\text{sqz}}$, where t_{sqz} is the duration for which the squeezing interaction is applied, and we can infer r by fitting dynamics shown in Fig 6.7(b.i, b.ii).

The model used to fit the experimental data is $p_{|\downarrow\rangle} = (1 + Cf(\alpha, \xi_{\text{th}}))/2$, where C accounts for experimental imperfections in the spin state preparation or readout.

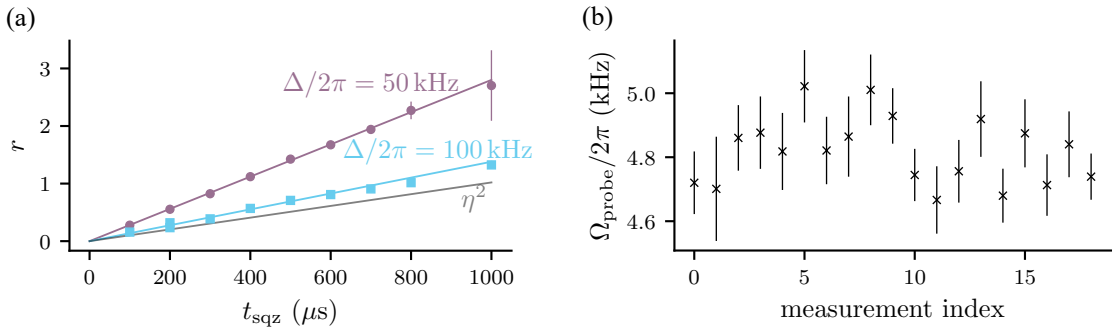

Figure 6.8: Analysis of the squeezing interaction strength. (a) We plot the squeezing parameter r against t_{sqz} for $\Delta/2\pi = 50\,\mathrm{kHz}$ and $\Delta/2\pi = 100\,\mathrm{kHz}$. The theory lines (continuous purple and cyan lines) are given by $r = \Omega_2 t_{\mathrm{sqz}}$. The grey continuous line illustrates the squeezing parameter that would be achieved by driving the second-order term in the Lamb-Dicke expansion with the same laser power. (b) Probe SDF strength calibrated independently for each of the points shown in (a).

We first fit the ground-state data (Fig 6.7(b.ii)) by setting $r = 0$ in Eq. (6.24) and having Ω and C as free parameters, which allows us to extract the strength of the probe SDF. We use this value to fit the splitting about the squeezed axis (Fig 6.7(b.i)) by setting $\phi_{\mathrm{probe}} - \theta/2 = 0$ and having r and C as free parameters. The squeezed state considered in Fig 6.7 is created by using 0.5 mW for driving each interaction SDF, setting $\Delta/2\pi = 50\,\mathrm{kHz}$ and applying the interaction for a pulse duration of $t_{\mathrm{sqz}} = 400\,\mu\mathrm{s}$ with a ramp duration of $t_{\mathrm{ramp}} = 40\,\mu\mathrm{s}$ [11]. This yields $r = 1.09(4)$, equivalent to 9.5(3) dB of squeezing[12].

We record dynamics for various t_{sqz} values and extract the respective r values, see Fig. 6.8. Moreover, we repeat the procedure for creating squeezed states using $\Delta/2\pi = 100\,\mathrm{kHz}$. The data agree well with the theory, calculated from independently measured values of $\Omega_\alpha, \Omega_{\alpha'}$, and we observe that the magnitude is inversely proportional to Δ.

We compare the squeezing strength generated by our method to driving the interaction directly, driving the second order in the Lamb-Dicke expansion (Eq. (6.1)) [57]. As shown in Eq. (6.1), this interaction strength scales with η^2. To calculate the values shown in Fig. 6.8(a), we assume the same total power is available for both

[11] All pulse durations quoted in this text are measured at full-width half-maximum of the pulse shape. The ramp shape is a $\sin(\pi t/2t_{\mathrm{ramp}})^2$ with a total rise time given by the ramp duration t_{ramp}.

[12] $\mathrm{dB}_{\mathrm{sqz}} = 20\log_{10}(e^r)$ [67].

methods, i.e., if the two non-commuting SDFs method uses 0.5 mW for each SDF, then the higher motional sideband method, which only requires one bichromatic field, uses $2 \times 0.5\,\text{mW} = 1\,\text{mW}$. This underscores that we can adjust the free parameter Δ in our method to achieve a higher coupling strength than driving the second-order interaction directly.

Note on data fitting: addressing the motional decoherence governed by the heating rate

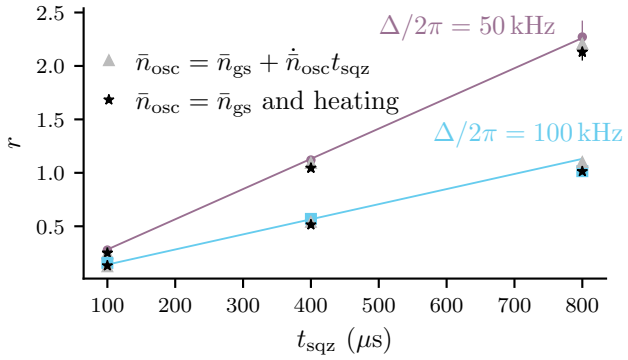

Figure 6.9: Verification of incorporating heating in the fitting model for extracting the squeezing parameter r. We compare the inferred r values for two cases: starting in the ground state with $\bar{n}_{\text{osc}} = \bar{n}_{\text{gs}}$ and applying the squeezing interaction together with heating (black stars), and starting in a thermal state with $\bar{n}_{\text{osc}} = \bar{n}_{\text{gs}} + \dot{\bar{n}}_{\text{osc}} t_{\text{sqz}}$ followed by applying only the squeezing interaction (grey triangles). The second simulated case is equivalent to assuming that the heating and the squeezing interaction are independent. The splitting dynamics for the two cases are simulated, and r is determined using the same fitting procedure as the experimental data. We overlay the simulated results to the experimental data and theory lines in Fig. 6.8(a).

Fitting the splitting about the anti-squeezed axis (see Fig. 6.7(b.iii)) by setting $\phi_{\text{probe}} - \theta/2 = \pi/2$ in the analytic model underestimates the value of r due to motional decoherence, whose effect is more apparent in this case as it takes longer to reduce the overlap completely. Simulating the dynamics while factoring in the heating rate (see Sec. 6.3) and the initial thermal state yields excellent agreement with the experimental data. Notably, no parameters were optimized to achieve this agreement; all parameters were set to independently measured values.

We have observed that heating during the squeezing interaction also affects the splitting dynamics of splitting about the squeezed axis. Particularly, for prolonged

squeezing durations ($t_{\mathrm{sqz}} > 400\,\mu\mathrm{s}$), we have noticed an overstimation of r. Consequently, we attempted to incorporate the heating into our fitting analysis by assuming that the heating and the squeezing interaction are independent processes. Instead of using an initial $\bar{n}_{\mathrm{osc}} = \bar{n}_{\mathrm{gs}} = 0.09(1)$, we consider that the state before applying the probe was a squeezed thermal state with $\bar{n}_{\mathrm{osc}} = \bar{n}_{\mathrm{gs}} + \dot{\bar{n}}_{\mathrm{osc}}\, t_{\mathrm{sqz}}$.
We verified the validity of this assumption in simulation. We simulated the squeezing interaction followed by applying the probe SDF (Sec. 6.3). The resulting splitting dynamics were fit in the same way as the experimental data. In Fig. 6.9, we compare the results for three squeezing durations, t_{sqz}, and two magnitudes parametrised by Δ. In one case, we start with a thermal state with $\bar{n}_{\mathrm{osc}} = \bar{n}_{\mathrm{gs}} + \dot{\bar{n}}_{\mathrm{osc}} t_{\mathrm{sqz}}$ and add no heating during the squeezing interaction. In the other case, we start in $\bar{n}_{\mathrm{osc}} = \bar{n}_{\mathrm{gs}}$ and apply heating during the squeezing interaction. As the squeezing interaction duration increases, a slight discrepancy between the two models becomes apparent. However, this discrepancy is within the uncertainty of the experimental measurements. We plot the simulation results onto the theory and experimental data, which show good agreement, in Fig. 6.9.
The fitting analysis did not include heating throughout the duration of applying the probe SDF. The splitting takes, on average, around 100 µs, and heating effects are negligible over this duration, which was checked in the simulation as well.

6.5.3 Spin-dependence

We next investigate the spin dependence of the interaction as shown in Fig. 6.10. The spin dependence of our interaction is in contrast to spin-independent squeezing achieved by modulating the confinement of the trapped ions [36, 143, 155].
We create squeezed states using the same parameters as in Fig. 6.7 by once starting in $|\downarrow\rangle$ and once in $|\uparrow\rangle$. We analyse the two resulting squeezed states by scanning the phase of the probe SDF in the same way as we did in Fig. 6.7(a). The peaks and the dips in the population correspond to splitting about the anti-squeezed axis and have π periodicity. There is a $\pi/2$ shift between the two curves due

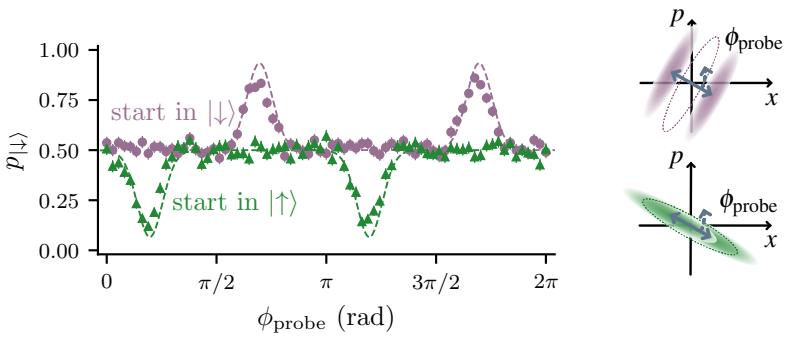

Figure 6.10: Spin dependence of the squeezing interaction. We apply the probe SDF for a fixed duration and vary its phase ϕ_{probe}. The dashed lines are fits to the data. Peaks and dips occur when the probe SDF is aligned with the anti-squeezed axis. Changing the initial spin state from $|\downarrow\rangle$ to $|\uparrow\rangle$ shifts the pattern by $\pi/2$, confirming the spin dependence of the interaction. The insets show the effect of the probe SDF on the Wigner functions of the respective motional states in phase space. The dashed ellipses represent the state before the probe SDF is applied.

to squeezing about orthogonal axes in phase space introduced by the different spin state settings (see insets).

6.5.4 Non-commutativity

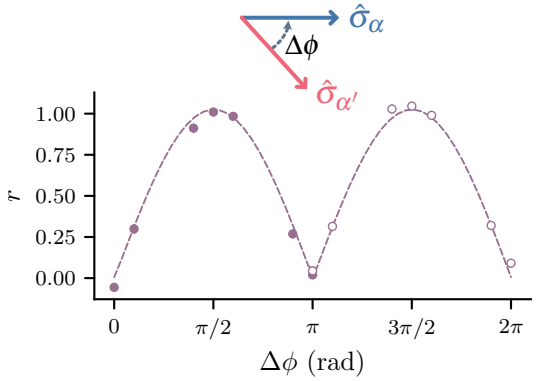

Figure 6.11: Non-commutativity of the interaction SDFs. We apply the two interaction SDFs with bases $\hat{\sigma}_\alpha = \hat{\sigma}_\phi$ and $\hat{\sigma}_{\alpha'} = \hat{\sigma}_{\phi+\Delta\phi}$ and measure the squeezing parameter r as a function of $\Delta\phi$. When the forces commute ($\Delta\phi = 0,\ \pi,$ and 2π) the initial state is not squeezed $r = 0$ and when the forces do not commute ($\Delta\phi = \pi/2$ and $3\pi/2$), the squeezing is maximised. The data is fit using $A|\sin\Delta\phi|$, where A is a constant (dashed lines). The change in marker (full to empty circles) reflects the change in the phase of the probe SDF (see text).

To generate this family of interactions, the spin components of the SDFs must be non-commuting. We explore this non-commutativity by varying the phase between

the spin components of the two SDFs, i.e., one of the forces is $\hat{\sigma}_\alpha = \hat{\sigma}_\phi$ and the other is $\hat{\sigma}_{\alpha'} = \hat{\sigma}_{\phi+\Delta\phi}$. We measure r as a function of $\Delta\phi$, keeping the phase of the probe SDF constant. The squeezing parameter r varies as $\sin(\Delta\phi)$ following the commutator relationship $[\hat{\sigma}_\phi, \hat{\sigma}_{\phi+\Delta\phi}] \propto \sin(\Delta\phi)\hat{\sigma}_z$, as shown in Fig. 6.11. If the spin components commute, i.e., $\Delta\phi = 0,\ \pi,$ and 2π, there is no squeezing, while for $\Delta\phi = \pi/2$ and $3\pi/2$, the commutator of the spin components, and hence the squeezing, is maximised. When $\sin(\Delta\phi)$ becomes negative, i.e., $\Delta\phi > \pi$, the axis of squeezing shifts by $\pi/2$; hence, we change the phase of the probe SDF to $\phi_{\text{probe}} + \pi/2$ such that we always split about the squeezed axis.

6.5.5 Unitarity

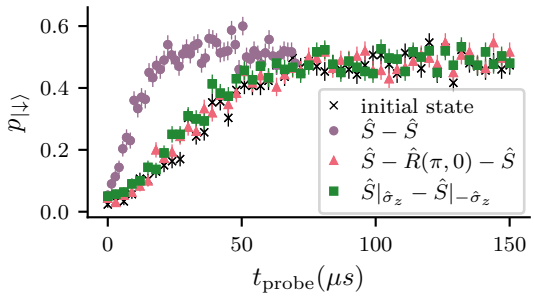

Figure 6.12: Verifying the unitarity of the squeezing interaction. To confirm its unitarity, we use its spin-conditioning property and our control over the basis of the squeezing. We apply a probe SDF for a variable duration and measure the probability of the $|\downarrow\rangle$ state $p_{|\downarrow\rangle}$. We insert a π-pulse on the spin, $\hat{R}(\theta' = \pi, \phi' = 0)$, between two squeezing interactions $\hat{S} - \hat{R}(\pi, 0) - \hat{S}$ (orange triangles) or add a π phase to the spin basis of the second squeezing pulse $\hat{S}|_{\hat{\sigma}_z} - \hat{S}|_{-\hat{\sigma}_z}$ (green squares) and confirm that the resulting splitting dynamics match that of the initial thermal state (black crosses). We also plot the data for two consecutive squeezing pulses (purple circles), resulting in a squeezed state.

An important aspect of our method is its unitarity, which distinguishes it from approaches that rely on dissipative processes to generate nonlinear interactions [79]. This unitary nature allows the interaction to be concatenated or arbitrarily placed within a single circuit.

In this section, we experimentally investigate and verify the unitarity of our interactions (Fig. 6.12). Specifically, we demonstrate that applying the spin-dependent squeezing interaction described by the time evolution operator $\hat{S}$ followed

by its adjoint $\hat{S}^\dagger$ to an initial state $|\uparrow\rangle|\bar{n}_{\text{osc}}\rangle$ leaves the state unchanged. The sequence, implemented as two consecutive pulses, is compared across three settings against the thermal state where no squeezing pulses are applied.

In the first sequence, we apply two identical squeezing pulses for 200 µs each, i.e. $\hat{S}-\hat{S}$, resulting in a squeezed state. In the second sequence, a π-pulse on the spin, $\hat{R}(\theta'=\pi,\phi'=0)$, is introduced between the two squeezing pulses, $\hat{S}-\hat{R}(\pi,0)-\hat{S}$. Due to the spin-conditioning of the interaction, the spin-flip induced by the π-pulse transforms the second squeezing interaction into its adjoint. This effectively reverses the effect of the first squeezing interaction and restores the state to the initial thermal state. Note, we initialise the second sequence in $|\downarrow\rangle|\bar{n}_{\text{osc}}\rangle$ to keep the readout consistent. In the third sequence, the spin basis of the second squeezing pulse is changed by π by changing the phase of one of the SDFs by π such that the sequence is $\hat{S}|_{\hat{\sigma}_z}-\hat{S}|_{-\hat{\sigma}_z}$. Once again, this transforms the second squeezing interaction into its adjoint, resulting in the final state returning to the initial thermal state. Each sequence is followed by the default analysis explained in Fig. 6.7(b).

6.5.6 Fock state analysis

An alternative approach to deduce the r value involves extracting Fock state populations by analysing the dynamics of a sideband interaction as shown in Fig. 6.13(a). Subsequently, a model (Eq. (2.2.5)) is used to fit the Fock state populations from the resulting dynamics and thus infer r, again using a model for the Fock state distribution for a given squeezed state. We did not use this method in our study due to heating which occurs during squeezing and complicates the resulting Fock state distribution. However, we do extract the Fock state populations and compare them to the simulation; see Fig. 6.13(b.i). We also show the Fock state population for the case in which the interaction is applied to Fock state $|0\rangle$, and there is no motional decoherence due to heating, see Fig. 6.13(b.ii). In the latter, one can observe the squeezing signature where only Fock states that are integer multiples of two get populated. There is also clear evidence of this signature in the experimental data, Fig. 6.13(b.i).

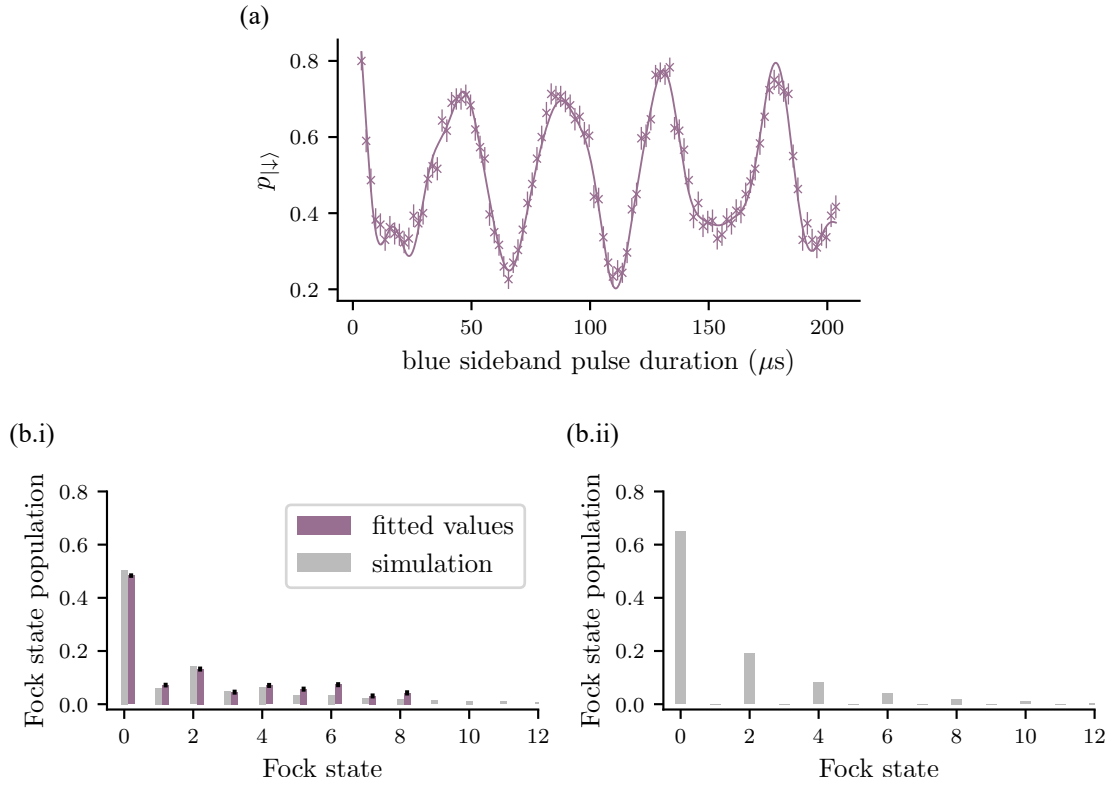

Figure 6.13: Fock state analysis of a squeezed state. (a), Blue sideband dynamics. We apply a blue sideband interaction for a variable duration for a squeezed state with $r = 1.09(4)$. Fock state populations are inferred by fitting an unconstrained model to dynamics. (b) Fock state population distribution. (i) We plot the histogram of the determined Fock state populations (purple vertical bars) and compare them to simulation (grey vertical bars). (ii) Using the same parameters, we simulate the Fock state distribution for a state created by applying the interaction to Fock state $|0\rangle$ without considering heating.

6.6 Going beyond squeezing

After using the effective squeezing interaction to debug our family of nonlinear interactions, we want to see if it is possible to create other interactions as well. As the representation of the states in phase space gets more and more non-trivial and beautiful, see Fig. 6.2, the 1D analysis used for squeezing, Fig. 6.7, does not suffice anymore. We implement the technique introduced in Ref. [71] to reconstruct the Wigner quasi-probability function of the resulting quantum states to obtain their full description.

6.6.1 Reconstructing the Wigner function for motional states

In Sec. 2.1, we introduced how the Wigner quasiprobability can be defined as the Fourier transform of the complex-valued characteristic function $\chi(\beta) = \langle\psi_{\text{osc}}| \hat{\mathcal{D}}(\beta) |\psi_{\text{osc}}\rangle$ with the displacement operator $\hat{\mathcal{D}}(\beta) = e^{\beta\hat{a}^\dagger - \beta^*\hat{a}}$. Writing the complex argument of the displacement operator as $\beta = \beta_r + i\beta_i$, we can rewrite Eq. (2.8)

$$W(x,p) = \frac{1}{2\pi^2}\int\int \chi(\beta_r,\beta_i) e^{-2i\frac{x\beta_i - p\beta_r}{\sqrt{2}}} d\beta_r d\beta_i, \tag{6.25}$$

where x, p are the position and momentum variables associated with the dimensionless position and momentum operators $\hat{x}, \hat{p}$.

As demonstrated in Ref. [71], the real and imaginary part of the characteristic function of a harmonic oscillator in a trapped ion system can be measured directly by applying a probe SDF, which creates the displacement $\hat{\mathcal{D}}(\beta/2)$. This measurement is an extension of the method discussed in Fig. 6.7, where we scan both t_{probe} and ϕ_{probe} to measure the characteristic function as a function of β_r and β_i with $\beta/2 = \alpha = i\Omega_{\text{probe}} e^{i\phi_{\text{probe}}} t_{\text{probe}}/2$.

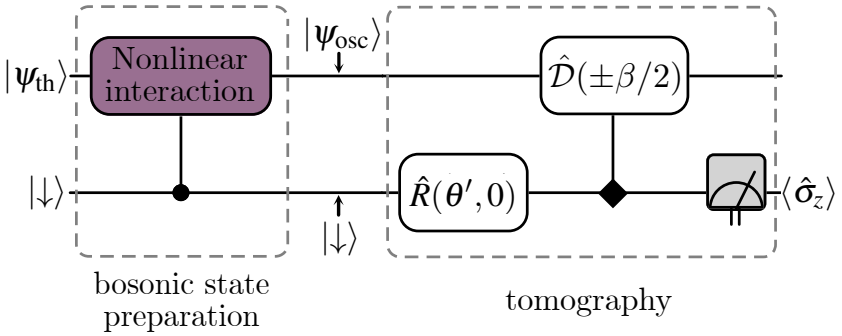

Figure 6.14: Circuit diagram for bosonic state preparation and tomography. The nonlinear interaction, conditioned on $\hat{\sigma}_z$ (filled circle), is applied to the system initialised in a thermal state and spin down $|\downarrow\rangle|\psi_{\text{th}}\rangle$. The characteristic function $\chi(\beta)$ of the resulting oscillator state $|\psi_{\text{osc}}\rangle$ is measured during the tomography step. The rotation $\hat{R}(\theta', \phi' = 0)$ that is applied to $|\downarrow\rangle$ determines if the real or the imaginary part of $\chi(\beta)$ is measured. The displacement is conditioned on $\hat{\sigma}_x$ (diamond), which influences its orientation ($\pm\beta/2$). Finally, the spin state is measured in the $\hat{\sigma}_z$ basis.

The sequence for measuring the characteristic function is shown in Fig. 6.14. After applying the spin-dependent nonlinear interaction, the system is left in the state

$|\downarrow\rangle |\psi_{\text{osc}}\rangle$. Applying the tomography part of the circuits yields:

$$\begin{aligned}\langle\hat{\sigma}_z\rangle = 1 - 2p_{|\downarrow\rangle} &= \frac{\langle\psi_{\text{osc}}| e^{i\theta'}\hat{\mathcal{D}}(-\beta) + e^{-i\theta'}\hat{\mathcal{D}}(\beta) |\psi_{\text{osc}}\rangle}{2} \\ &= \cos(\theta')\text{Re}[\langle\psi_{\text{osc}}|\hat{\mathcal{D}}(\beta)|\psi_{\text{osc}}\rangle] + \sin(\theta')\text{Im}[\langle\psi_{\text{osc}}|\hat{\mathcal{D}}(\beta)|\psi_{\text{osc}}\rangle] \\ &= \cos(\theta')\text{Re}[\chi(\beta)] + \sin(\theta')\text{Im}[\chi(\beta)].\end{aligned} \tag{6.26}$$

The real part of the characteristic function $\text{Re}[\chi(\beta)]$ is inferred by omitting the single-qubit rotation and directly applying the SDF conditioned on $\hat{\sigma}_x$, i.e. setting $\theta' = 0$ for the single-qubit rotation $\hat{R}(\theta' = 0, \phi' = 0)$ and then, measuring in the $\hat{\sigma}_z$ basis. For the imaginary part $\text{Im}[\chi(\beta)]$, we rotate the spin state in an eigenstate of $\hat{\sigma}_y$ with the rotation $\hat{R}(\theta' = \pi/2, \phi' = 0)$ and then apply the SDF followed by a measurement in $\hat{\sigma}_z$. We vary both t_{probe} and ϕ_{probe} to sample β in the complex plane. We measure a grid of 41×41 settings for $\text{Re}[\chi(\beta)]$ and $\text{Im}[\chi(\beta)]$, which are combined to calculate $\chi(\beta)$. For each setting, we use 300 shots, meaning a 41×41 grid requires approximately 45 minutes to record. To approximate the Fourier transform of $\chi(\beta)$, we zero-pad the measured data by 200 points on every side resulting in a grid size of 441×441 and perform a discrete Fourier transform. We do not account for the bias parameter that corresponds to state preparation and measurement errors in the spin state. We measure the entire extent of the characteristic function without making assumptions about its hermiticity, as opposed to only measuring half of the complex plane. Our reconstruction technique could also be improved by employing maximum-likelihood estimation directly on $\chi(\beta)$ or the Wigner function [156].

6.6.2 Wigner function reconstruction of squeezed states

We next return to squeezed states to reconstruct their Wigner functions. As in Sec. 6.5, we create the squeezing interaction conditioned on $\hat{\sigma}_z$ by setting the detunings of the interaction SDFs to be Δ and $-\Delta$ and their spin components to be $\hat{\sigma}_\alpha = \hat{\sigma}_\phi$ and $\hat{\sigma}_{\alpha'} = \hat{\sigma}_{\phi+\pi/2}$, respectively. We use 0.5 mW for driving each interaction SDF, set $\Delta/2\pi = 50$ kHz and apply the interaction for a pulse duration of $t_{\text{sqz}} = 400\,\mu\text{s}$ with a ramp duration of $t_{\text{ramp}} = 40\,\mu\text{s}$. We measure the real $\text{Re}[\chi(\beta)]$ and the imaginary part $\text{Im}[\chi(\beta)]$ of the characteristic function for a

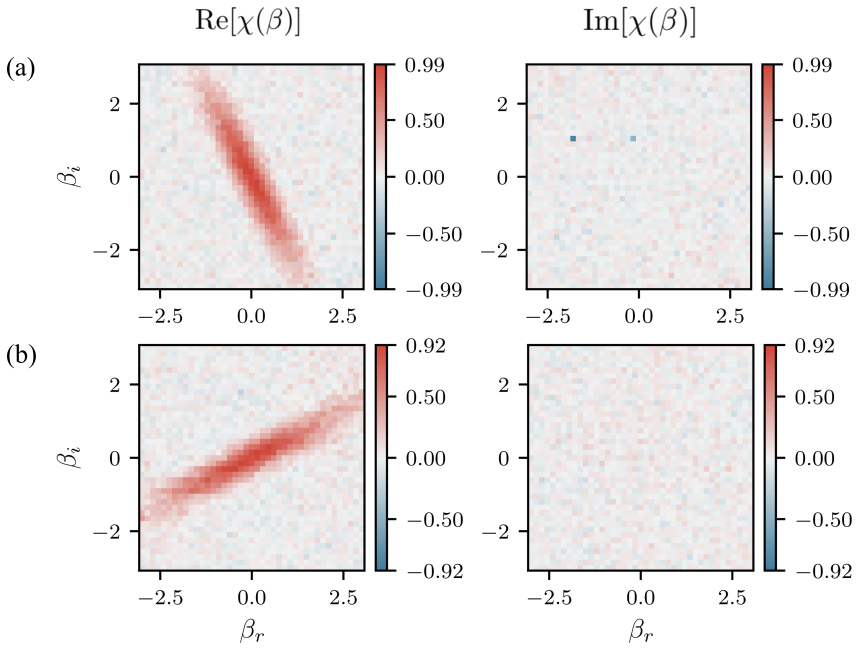

Figure 6.15: Measured characteristic functions for squeezed states. For each state, we measure the real $\mathrm{Re}[\chi(\beta)]$ and the imaginary part $\mathrm{Im}[\chi(\beta)]$. The observed imaginary part vanishes, as expected for a squeezed state. The parameters for the squeezing interaction are $\Delta/2\pi = 50\,\mathrm{kHz}$, $t_{\mathrm{sqz}} = 400\,\mu\mathrm{s}$ and $0.5\,\mathrm{mW}$ for each SDF for both (a) and (b). (a) The spin state is initialised in $|\downarrow\rangle$. (b) The spin state is initialised in $|\uparrow\rangle$. Hence, the states are squeezed about orthogonal axes. The max value of $|\mathrm{Re}[\chi(\beta)]|$ is diminished for (b) as a result of the error on the single-qubit rotation used to initialise the state in $|\uparrow\rangle$.

squeezed prepared by having the spin state initialised in $|\downarrow\rangle|\bar{n}_{\mathrm{osc}}\rangle$ (Fig. 6.15(a)) and in $|\uparrow\rangle|\bar{n}_{\mathrm{osc}}\rangle$ (Fig. 6.15(b)).

Using the characteristic function data, we reconstruct the Wigner functions shown in Fig. 6.16, column 'experiment'. We compare this reconstruction to simulations; see Sec. 6.3. In the 'simulation interaction + tomography' column, we simulate both the bosonic state preparation and the measurement of the characteristic function. The Wigner function is then computed by applying the same analysis protocol as in the case of the experimental data. When simulating the dynamics of the probe SDF (for measuring the characteristic function), we include the motional dephasing due to heating as well as the shot noise for each point. The shot noise is simulated by sampling a binomial distribution $P(n, q)$, with n the number of shots used in the experiment and q the success probability of being in state $|\downarrow\rangle$ obtained from performing the simulation of the bosonic state preparation and the probing SDF. We

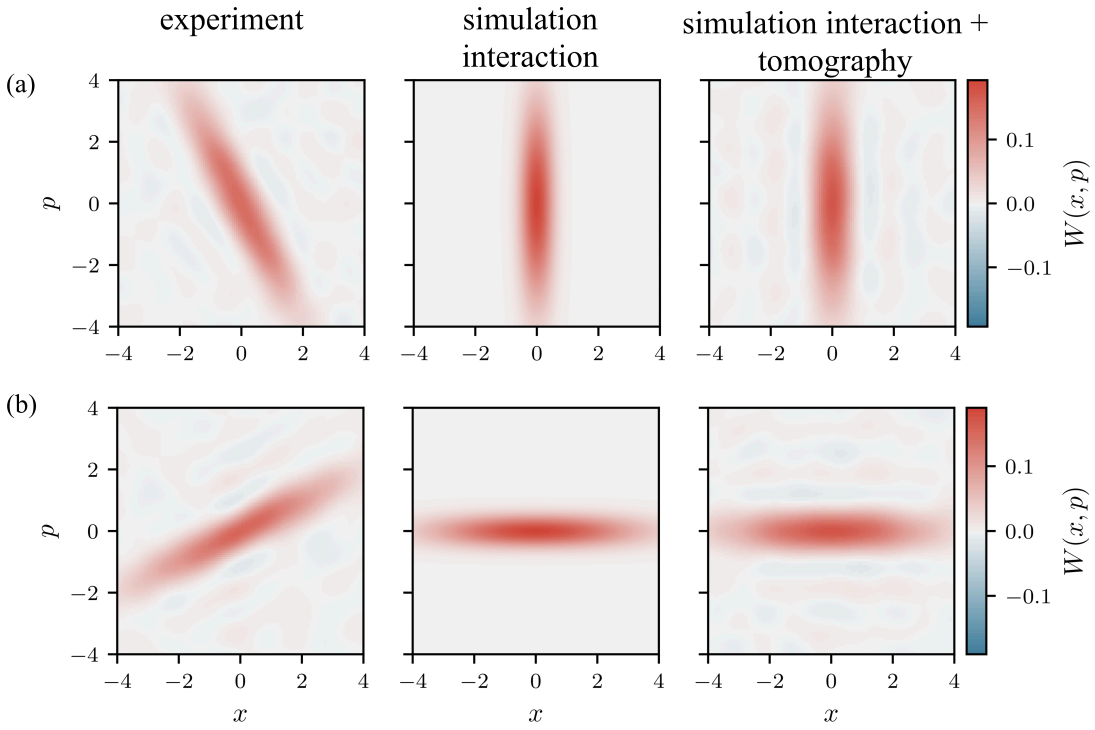

Figure 6.16: Wigner functions of squeezed states with $r = 1.09(4)$. The spin state is initialised in (a) $|\downarrow\rangle$ and (b)$|\uparrow\rangle$ before the squeezing interaction is applied. The first column shows Wigner functions $W(x, p)$ reconstructed from experimental data. The Wigner functions are inferred from the measured characteristic functions shown in Fig. 6.15. We compare these to Wigner functions of numerically simulated states with independently measured experimental parameters. For the 'simulation interaction + tomography simulation' column, we simulate both the generation of the squeezed states and the effect of the probing SDF. The rotation observed in comparison to the simulation is due to a constant offset between the squeezing axis θ and the phase of the probing SDF ϕ_{probe}. This offset can be calibrated out if desired.

observe that both the 'experiment' and the 'simulation interaction + tomography' columns show fluctuations with $W(x, p) < 0$, which we do not expect for a squeezed state. These are artifacts in our measurements that result from the reduced number of shots and not measuring the characteristic function for a large enough (β_r, β_i) range, which could have been avoided. This effectively sets an aperture on the squeezed state and leads to a diffraction-like effect in the resulting Wigner function.

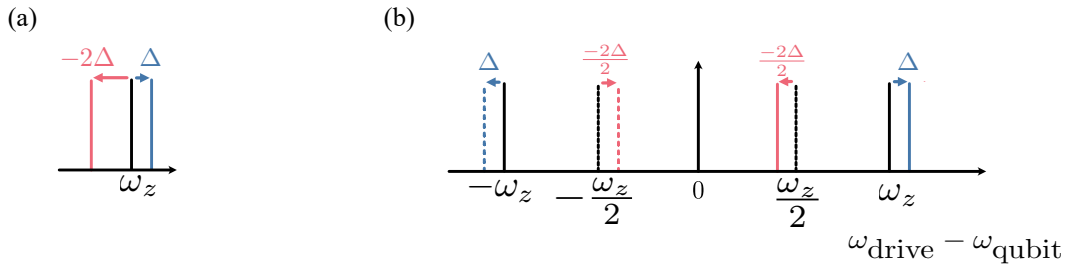

Figure 6.17: Spin-dependent forces configuration for generating the trisqueezing interaction. The two forces SDF_α and $\mathrm{SDF}_{\alpha'}$ are shown in blue and red, respectively. (a) Detuning of the spin-dependent forces relative to the motional mode frequency ω_z. (b) Frequency configuration of the laser bichromatic field used to implement SDF_α and $\mathrm{SDF}_{\alpha'}$. Continuous lines represent the blue-detuned tones, while dashed lines represent the red-detuned tones.

6.7 Trisqueezing

At last, going beyond conventional squeezing, to set up the trisqueezing interaction, we simply set its resonance condition by detuning one of the SDFs by Δ and the other by -2Δ. The spin-conditioning for the two SDFs was set initially to $\hat{\sigma}_\alpha = \hat{\sigma}_\phi$ and $\hat{\sigma}_{\alpha'} = \hat{\sigma}_{\phi+\pi/2}$, respectively. As the basis of the effective trisqueezing interaction is given by $[\hat{\sigma}_\alpha, [\hat{\sigma}_\alpha, \hat{\sigma}_{\alpha'}]]$, we expect it to be conditioned on $\hat{\sigma}_{\phi+\pi/2}$. As discussed in the case of the probe SDF in Sec. 6.5.1, if the spin is initialised in $|\downarrow\rangle$, i.e., not an eigenstate of $\hat{\sigma}_{\phi+\pi/2}$, applying the trisqueezing interaction leads to an entangled state between the spin and the motion of the form $(|+_{\phi+\pi/2}\rangle\,|+T\rangle + |-_{\phi+\pi/2}\rangle\,|-T\rangle)/\sqrt{2}$, where $|\pm_{\phi+\pi/2}\rangle$ the eigenstates of $\hat{\sigma}_{\phi+\pi/2}$ and $|\pm T\rangle$ the trisqueezed and anti-trisqueezed states respectively. This is interesting from the point of view of creating superpositions of trisqueezed states, which will be discussed in detail in Ref. [154]. However, here, we focus on generating trisqueezed states.

A first attempt is to sandwich the trisqueezing interaction in between two $R_\phi(\pi/2)$ rotations on the spin that take us into an eigenstate of $\hat{\sigma}_{\phi+\pi/2}$ and back to the $\hat{\sigma}_z$, ready for reading out the motional state. However, given the magnetic sensitivity of our qubit and the current magnetic field stability in our setup, maintaining a

consistent superposition state $(-i\left|\uparrow\right\rangle e^{-i\phi}+\left|\downarrow\right\rangle)/\sqrt{2}$ throughout the experiment has proven to be unfeasible.

The solution is to create the trisqueezing interaction conditioned on $\hat{\sigma}_z$. This is achieved by setting the spin-conditioning of the two interaction SDFs to $\hat{\sigma}_\alpha = \hat{\sigma}_\phi$ and $\hat{\sigma}_{\alpha'} = \hat{\sigma}_z$. The $\hat{\sigma}_z$ SDF is realised by setting the detuning of the bichromatic field to $\delta \approx \omega_z/2$. The exact detunings of the bichromatic fields, from the qubit frequency, in order to drive the trisqueezing interaction resonance are $\delta = (\omega_z - 2\Delta)/2$ for the $\text{SDF}_{\alpha'}$ and $\delta = \omega_z + \Delta$ for the SDF_α, see Fig. 6.17.

With this setup of the bichromatic fields, we intialise the ion in $\left|\downarrow\right\rangle\left|\bar{n}_{\text{osc}}\right\rangle$ and apply the two non-commuting interaction SDFs for variable durations t_{sqz} to check if the effective trisqueezing interaction is in the $\hat{\sigma}_z$ basis, as we did for the squeezing interaction in Fig. 6.6. We consider two sets of parameters $\Delta/2\pi = -25\,\text{kHz}$, 1 mW for each SDF in Fig. 6.18(a) and $\Delta/2\pi = 25\,\text{kHz}$, 2 mW in Fig. 6.18(b). We compare the experimental data to simulation. Any residual spin-motion entanglement from incomplete loop closures is strongly suppressed as we use a ramp duration $t_{\text{ramp}} = 80\,\mu\text{s}$, which is longer than the timescale given by $2\pi/\Delta$. We observe a decay in $p_{\left|\downarrow\right\rangle}$ with the increase in t_{sqz} for both the experimental data and simulation. We attribute this effect to the coherent error caused by the higher order terms in the Magnus expansion (see Sec. 6.1.2), as well as heating.

We will analyse two trisqueezed states, one created using the parameters in Fig. 6.18(a) and applying the interaction for $t_{\text{sqz}} = 600\,\mu\text{s}$ and one using the parameters in Fig. 6.18(b) and applying the interaction for $t_{\text{sqz}} = 400\,\mu\text{s}$. For the first state, $1 - p_{\left|\downarrow\right\rangle}$ is 5×10^{-3} in the simulation and 2×10^{-2} in the experiment. For the second state, $1 - p_{\left|\downarrow\right\rangle}$ is 9×10^{-3} in the simulation and 4×10^{-2} in the experiment. We believe that the discrepancy between the simulation and experiment comes from errors not considered in the simulation, such as spin coherence time.

In Fig. 6.19, we measure the real $\text{Re}[\chi(\beta)]$ and the imaginary part $\text{Im}[\chi(\beta)]$ of the characteristic functions for the two aforementioned trisqueezed states. Features of the trisqueezed states are also discernible in 1D scans, shown in Fig. 6.19(b.i)

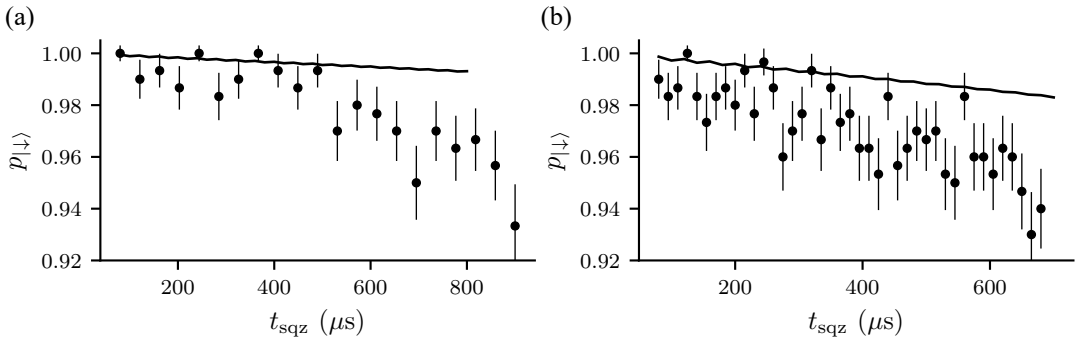

Figure 6.18: Dynamics resulting from applying the effective trisqueezing interaction conditioned on $\hat{\sigma}_z$. We compare experimental data to simulation (continuous lines). We consider two sets of parameters (a) $\Delta/2\pi = -25\,\mathrm{kHz}$, 1 mW for each SDF and (b) $\Delta/2\pi = 25\,\mathrm{kHz}$, 2 mW. As in Fig. 6.6, the spin state is initialised in $|\downarrow\rangle$ before the effective trisqueezing interaction is applied for variable durations t_{sqz} and we measure the probability of staying in the $|\downarrow\rangle$ state, $p_{|\downarrow\rangle}$.

and (b.ii), which served as useful diagnostics prior to undertaking the 2D-dimensional scans.

We use the characteristic functions to reconstruct the Wigner functions of the respective states in Fig. 6.20, which we compare to the simulation. The simulations in the columns 'simulation interaction' and 'simulation interaction + tomography' are conducted in the same way as described in Sec. 6.6.2, and they show good agreement with the experiment. For trisqueezing, the artifacts in the reconstruction for columns 'experiment' and 'simulation interaction + tomography' are mainly due to the limited number of shots.

To assess the strength of the interaction, we estimate the trisqueezing parameter for the trisqueezed states depicted in Fig. 6.20. From theory, the strength of the trisqueezing interaction is given as $\Omega_3 = \Omega_{\alpha'}\Omega_\alpha^2/(2\Delta^2)$, where $\Omega_\alpha = \eta\Omega$ and $\Omega_{\alpha'} = \eta\Omega|J_1(2\Omega/\delta)+J_3(2\Omega/\delta)|$, see Sec. 6.1.2. In the simulation, we compare an ideal trisqueezed state with strength Ω_3 to a trisqueezed state generated using the two non-commuting SDFs, both simulated following Sec. 6.3. Assuming that the two states are described by the density matrices ρ and σ, respectively, their overlap is given as

$$F(\rho,\sigma) = \left(\mathrm{tr}\sqrt{\sqrt{\rho}\sigma\sqrt{\rho}}\right)^2. \tag{6.27}$$

For a state created using the parameters in Fig. 6.20(a), we obtain $1 - F = 4 \times 10^{-4}$. The quoted value of $1 - F$ is obtained without any parameter optimisation. The

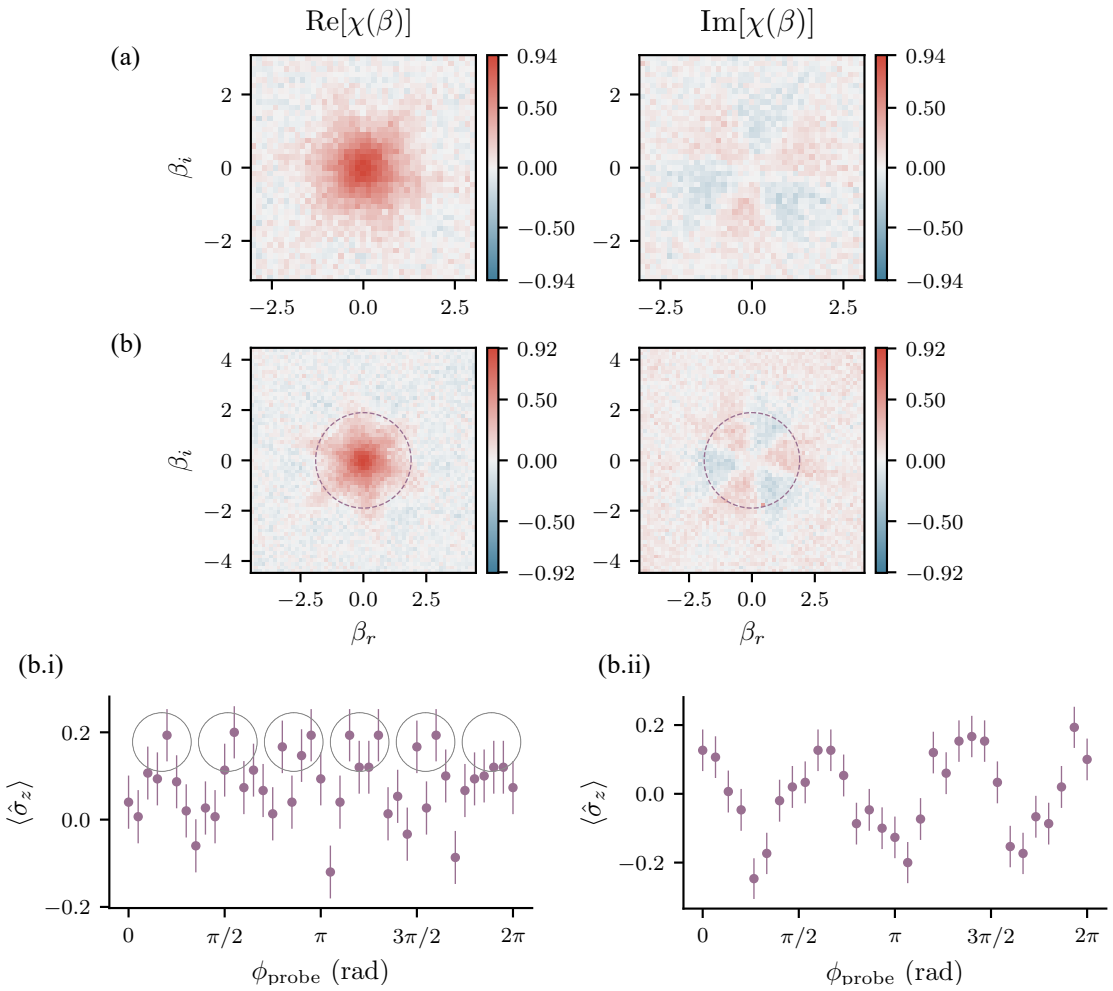

Figure 6.19: Measured characteristic functions for trisqueezed states. For each state, we measure the real $\mathrm{Re}[\chi(\beta)]$ and the imaginary part $\mathrm{Im}[\chi(\beta)]$. The real and imaginary parts have a star-shaped pattern with six features. The imaginary part oscillates between positive and negative values. The parameters used for implementing the trisqueezing interaction are (a) $\Delta/2\pi = -25\,\mathrm{kHz}$, $t_{\mathrm{sqz}} = 600\,\mu\mathrm{s}$ and 1 mW for each SDF and (b) $\Delta/2\pi = 25\,\mathrm{kHz}$, $t_{\mathrm{sqz}} = 400\,\mu\mathrm{s}$ and 2 mW for each SDF. (b.i) 1D cross-section through $\mathrm{Re}[\chi(\beta)]$ and (b.ii) 1D cross-section through $\mathrm{Re}[\chi(\beta)]$, measured by fixing t_{probe} and varying ϕ_{probe}. The dashed purple circles in (b) indicate how the 1D data was recorded. The grey dashed circles in (b.i) indicate the six peaks observed for the real part.

high degree of overlap ensures that we can use the analytic formula for Ω_3 to give an estimate for the trisqueezing parameter r_{3s}. Combining this with the good agreement between simulation and experimental data, we conclude $r_{3s} \approx 0.18(1)$ for the state in Fig. 6.20(a), utilising independently measured values for Ω, η, and δ.

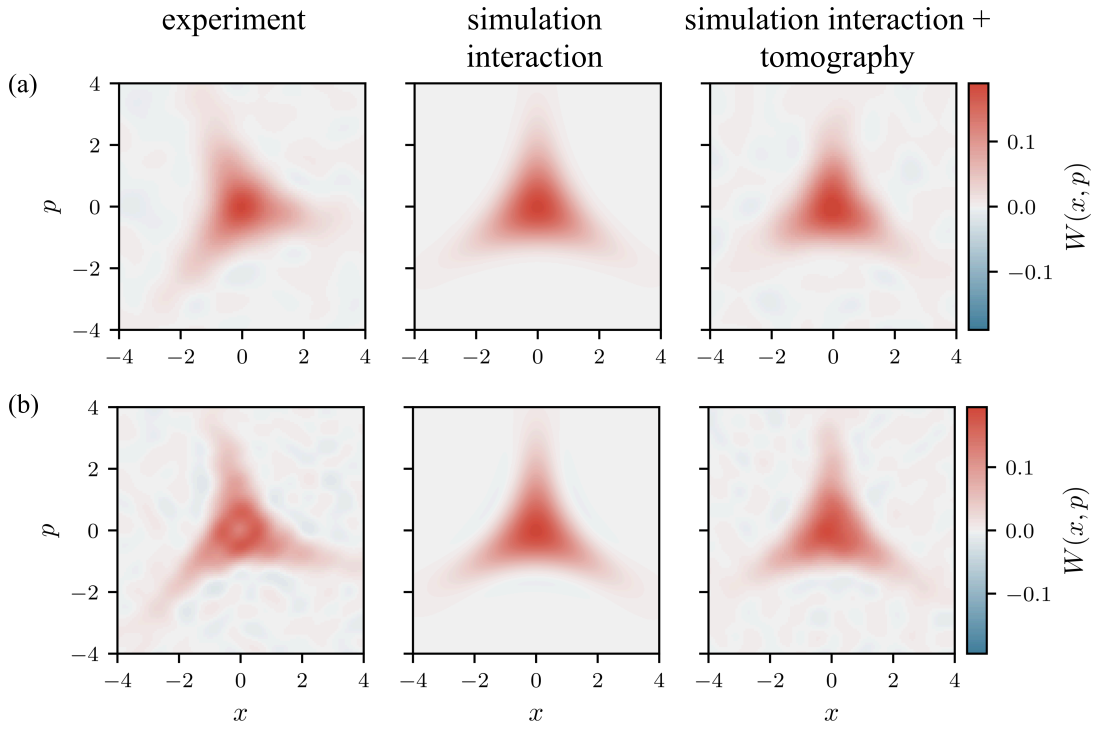

Figure 6.20: Wigner functions of trisqueezed states with (a) $r_{3s} \approx 0.18(1)$ and (b)$r_{3s} \approx 0.24$. The first column shows Wigner functions $W(x, p)$ reconstructed from experimental data. The Wigner functions are inferred from the measured characteristic functions shown in Fig. 6.19. We compare these to Wigner functions of numerically simulated states with independently measured experimental parameters. For the 'simulation interaction + tomography' column, we simulate both the generation of the trisqueezed states and the effect of the probing SDF. Compared to the simulation, the observed rotation is due to a constant offset between the squeezing axis θ and the phase of the probing SDF ϕ_{probe}. This offset can be calibrated out if desired.

A failed attempt at Wigner negativity

What about the state in Fig. 6.20(b)? Trisqueezed states exhibit Wigner negativity, which becomes more apparent with the increase in r_{3s}, see Fig. 6.2. We attempted to observe Wigner negativity by increasing the power in each SDF to 2 mW from 1 mW. However, we also changed the detuning $\Delta/2\pi$ from -25 kHz to 25 kHz, which, unexpectedly, strongly reduced the trisqueezing magnitude of Ω_3.

Changing the detuning Δ is motivated by reducing off-resonantly driving an interaction corresponding to another motional mode of the ion. When considering the $\omega_z/2$ resonance, the nearby terms that we can off-resonantly drive are the $\omega_{x,y}/3$ resonances, which are spin-motion couplings in the $\hat{\sigma}_\phi$ basis. More details

on this aspect can be found in Sec. 4.2.6. The data for the trisqueezed states shown in Fig. 6.20(a) and Fig. 6.20(b) were taken on different days. During this time, fluctuations in the frequencies of the radial modes occurred, which prompted the adjustment of the detuning Δ.

Investigating the unexpected reduction in Ω_3 further in simulation, we find that the strong change arises from the phase of the bichromatic fields being offset by $\pi/2$ with respect to each other. To clarify, considering Eq. (6.20), when the trisqueezed state in Fig. 6.20(b) was implemented, the bases of the terms involved were set as outlined in Table 6.2. However, one can use a different configuration where the

	spin-motion coupling basis	carrier basis	δ
SDF_{α}	$\hat{\sigma}_{\phi}$	$\hat{\sigma}_{\phi-\pi/2}$	$\approx \omega_z$
$\mathrm{SDF}_{\alpha'}$	$\hat{\sigma}_{\phi+\pi/2}$	$\hat{\sigma}_{\phi}$	$\approx \omega_z/2$

Table 6.2: Configuration of SDFs for driving trisqueezing interaction; bichromatic fields driving the SDFs are offset by $\pi/2$. This leads to the spin-motion and carrier terms being non-commuting, respectively.

bichromatic fields are not offset by $\pi/2$, see Table. 6.3.

	spin-motion coupling basis	carrier basis	δ
SDF_{α}	$\hat{\sigma}_{\phi}$	$\hat{\sigma}_{\phi-\pi/2}$	$\approx \omega_z$
$\mathrm{SDF}_{\alpha'}$	$\hat{\sigma}_{\phi}$	$\hat{\sigma}_{\phi-\pi/2}$	$\approx \omega_z/2$

Table 6.3: Configuration of SDFs for driving trisqueezing interaction; bichromatic fields driving the SDFs are in phase. This leads to the spin-motion and carrier terms commuting, respectively.

In Fig. 6.21, we show simulation results investigating the effect of the two configurations for the bichromatic fields. We use the same parameters as in Fig. 6.20(b). We observe that in the case in which the bichromatic fields are not offset by $\pi/2$, Fig. 6.21(a), the strength of the trisqueezing interaction is almost invariant under the sign change in Δ, which is predicted by our naive hypothesis of $\Omega_{\alpha} = \eta\Omega$ and $\Omega_{\alpha'} = \eta\Omega|J_1(2\Omega/\delta) + J_3(2\Omega/\delta)|$. Intuitively, this aligns with the hypothesis as we assume that the carrier terms of the two SDFs do not affect each other, which is the

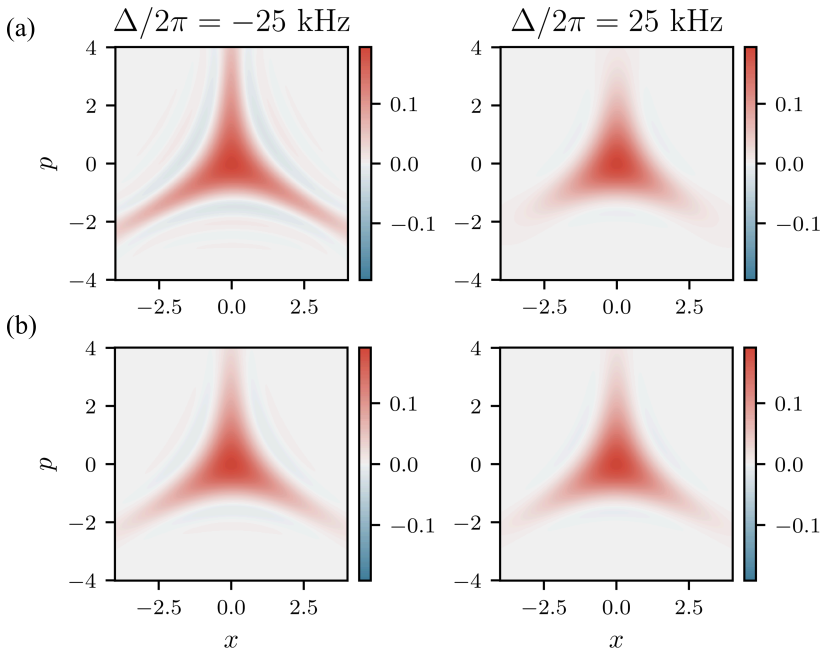

Figure 6.21: Generating trisqueezed states using different bichromatic field configurations for the comprising interaction SDFs. (a) The bichromatic fields are offset by $\pi/2$ with respect to each other. (b) The bichromatic fields are in phase. We consider two detuning values from the motion $\Delta/2\pi = \pm 25\,\text{kHz}$ The interaction is applied for $t_{\text{sqz}} = 400\,\mu\text{s}$ and we use 2 mW for each interaction SDF.

case when they commute. We do not observe this effect for the state in Fig. 6.20(a) because the strength of the comprising interactions was lower.

As mentioned in the theory section, Sec. 6.1.2, understanding the effects of the non-commuting carrier terms requires further exploration, particularly with the increase in power of the driving fields. In this case, we believe that the effect was mainly to reduce the strength of the interaction compared to what we expected, as we were able, in simulation, to find a low overlap error of $1 - F = 4 \times 10^{-3}$ to an ideal state with $r_{3s} \approx 0.24$ instead of the naive expectation of $r_{3s} \approx 0.53(1)$ resulting from the increase in power.

Fock state distribution

We do not extract the Fock state distribution from the blue sideband dynamics as shown in the case of a squeezed state; however, in Fig. 6.22(a), we plot the simulated Fock state distribution for the state in Fig. 6.20(b). We also show the Fock state

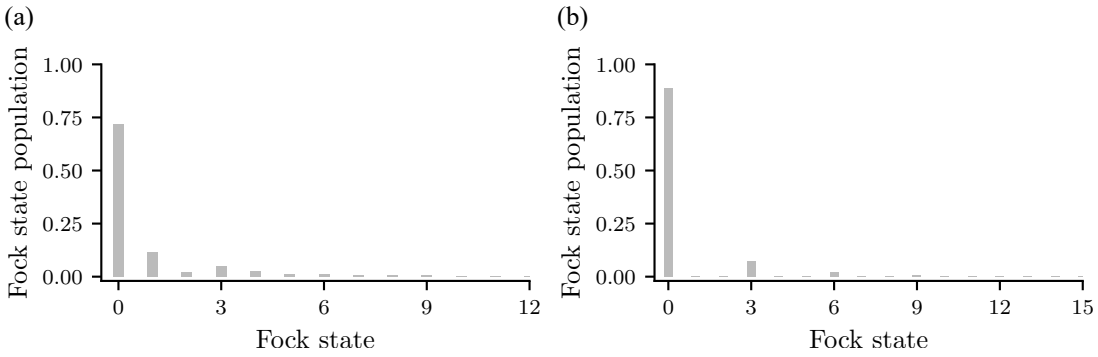

Figure 6.22: Simulated Fock state distribution of a trisqueezed state. (a) We plot the Fock state distribution of the state simulated in Fig. 6.20(b) with $r_{3s} = 0.24$. (b) We plot the simulated distribution using the same interaction parameters but by starting in Fock state $|0\rangle$ and considering no heating.

population for the case in which the interaction is applied to Fock state $|0\rangle$, and there is no motional decoherence due to heating. We can observe the trisqueezing signature where the only Fock states that get populated are integer multiples of three.

6.8 Quadsqueezing

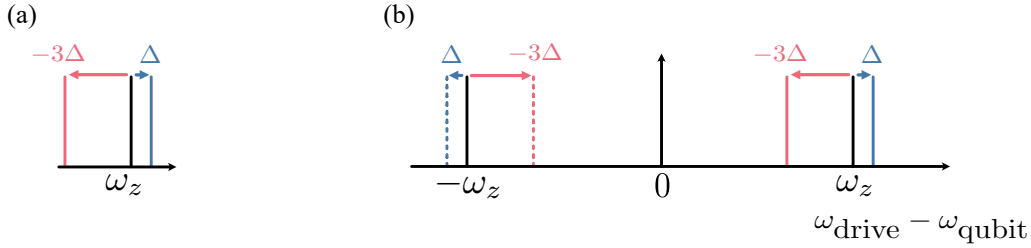

Figure 6.23: Spin-dependent forces configuration for generating the quadsqueezing interaction. The two forces SDF_{α} and $\mathrm{SDF}_{\alpha'}$ are shown in blue and red, respectively. (a) Detuning of the spin-dependent forces relative to the motional mode frequency ω_z. (b) Frequency configuration of the laser bichromatic field used to implement SDF_{α} and $\mathrm{SDF}_{\alpha'}$. Continuous lines represent the blue-detuned tones, while dashed lines represent the red-detuned tones.

Lastly, we investigate the quadsqueezing interaction. The resonance condition for this fourth-order interaction is achieved by setting the detunings of the interaction SDFs to be Δ and -3Δ. The exact detunings of the bichromatic fields, from the qubit frequency, are $\delta = \omega_z + \Delta$ for the SDF_{α} and $\delta = \omega_z - 3\Delta$ for the

$\mathrm{SDF}_{\alpha'}$, as shown in Fig. 6.23. The spin basis of the quadsqueezing is given by $[\hat{\sigma}_\alpha, [\hat{\sigma}_\alpha, [\hat{\sigma}_\alpha, \hat{\sigma}_{\alpha'}]]]$. Thus, choosing the basis of the comprising interaction SDFs to be $\hat{\sigma}_\alpha = \hat{\sigma}_\phi$ and $\hat{\sigma}_{\alpha'} = \hat{\sigma}_{\phi+\pi/2}$, we achieve a $\hat{\sigma}_z$ interaction, which is favorable given our magnetically-field sensitive qubit.

For the data presented in this section, we use $\Delta/2\pi = 25\,\mathrm{kHz}$ and $t_{\mathrm{ramp}} = 80\,\mu\mathrm{s}$. Moreover, we consider two power settings, 1 mW or 2 mW per interaction SDF.

As previously mentioned, we anticipate that the effective quadsqueezing interaction is conditioned on $\hat{\sigma}_z$, and we verify this using a similar approach as demonstrated for squeezing and trisqueezing in Fig. 6.6 and 6.18. We initialise the system in $|\downarrow\rangle$ and apply the two non-commuting SDFs for variable durations t_{sqz} and considering both power settings, as shown in Fig. 6.24. In Fig. 6.24(a), the discrepancy between the simulation and experiment appears consistent with our observations for squeezing and trisqueezing. For example, at $t_{\mathrm{sqz}} = 600\,\mu\mathrm{s}$, $1 - p_{|\downarrow\rangle}$ corresponds to 5×10^{-3} in the simulation and $4(1) \times 10^{-2}$ in the experiment. However, this is not the case for Fig. 6.24(b), where $1 - p_{|\downarrow\rangle}$ decreases significantly faster in the experiment compared to the simulation. For example, at $t_{\mathrm{sqz}} = 400\,\mu\mathrm{s}$, $1 - p_{|\downarrow\rangle}$ corresponds to 1×10^{-2} in the simulation and $11(2) \times 10^{-2}$ in the experiment. Further investigations are required to determine the reason for this discrepancy.

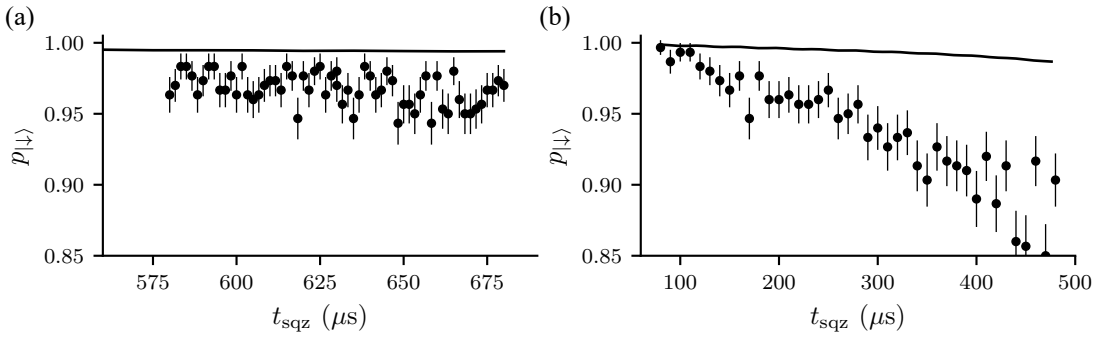

Figure 6.24: Dynamics resulting from applying the effective quadsqueezing interaction conditioned on $\hat{\sigma}_z$. We compare experimental data to simulation (continuous lines). We consider two sets of parameters (a) $\Delta/2\pi = 25\,\mathrm{kHz}$, 1 mW for each SDF and (b) $\Delta/2\pi = 25\,\mathrm{kHz}$, 2 mW. As in Fig. 6.6 and 6.18, the spin state is initialised in $|\downarrow\rangle$ before the effective quadsqueezing interaction is applied for variable durations t_{sqz} and we measure the probability of staying in the $|\downarrow\rangle$ state, $p_{|\downarrow\rangle}$. The loops are strongly suppressed as we use a ramp duration $t_{\mathrm{ramp}} = 80\,\mu\mathrm{s}$, which is longer than the timescale given by $2\pi/\Delta$.

In Fig. 6.25, we show the experimentally measured real Re[$\chi(\beta)$] and imaginary part Im[$\chi(\beta)$] of the characteristic functions for two quadsqueezed states. These states are generated by applying the interaction for 600 µs with 1 mW of power and for 400 µs with 2 mW of power. In Fig. 6.25(b.i), we show a 1D scan, which is equivalent to scanning the circle indicated in the real part of the characteristic function in (b). Similar to trisqueezing, we found such a scan to be a useful diagnostic tool before committing to the time costly 2D scans.

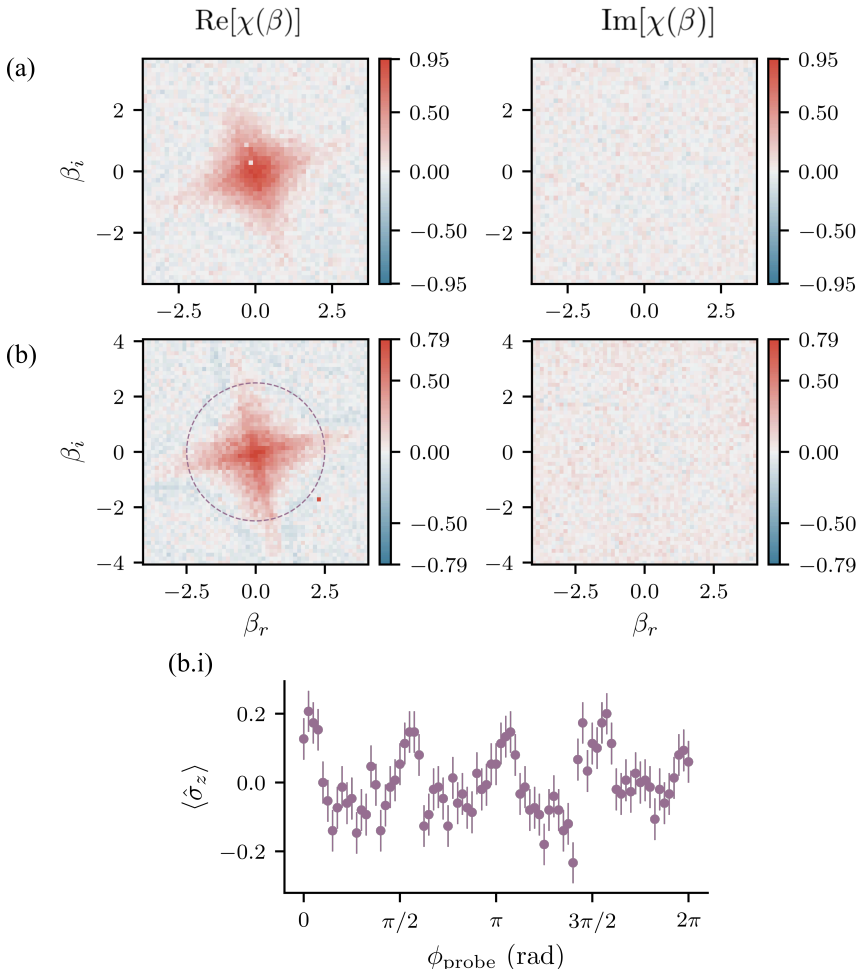

Figure 6.25: Measured characteristic functions for quadsqueezed states. For each state, we measure the real Re[$\chi(\beta)$] and the imaginary part Im[$\chi(\beta)$]. The imaginary part vanishes. The parameters used for implementing the quadsqueezing interaction are (a) $\Delta/2\pi = 25\,\text{kHz}$, $t_{\text{sqz}} = 600\,\mu\text{s}$ and 1 mW for each SDF and (b) $\Delta/2\pi = 25\,\text{kHz}$, $t_{\text{sqz}} = 400\,\mu\text{s}$ and 2 mW for each SDF. Features of the quadsqueezed states can also be observed in 1D scans, four peaks in (b.i), by fixing t_{probe} and varying ϕ_{probe}. The dashed purple circles in (b) indicate how the 1D data was recorded.

We use the characteristic functions to reconstruct the Wigner functions of the respective states in Fig. 6.26. The simulations in the columns 'simulation interaction' and 'simulation interaction + tomography' are conducted in the same way as described in Sec. 6.6.2, and they show good agreement with the experiment. For quadsqueezing, the artifacts in the reconstruction for columns 'experiment' and 'simulation interaction + tomography' are mainly due to the limited number of shots. We observe negative values for the Wigner quasiprobability for the 2 mW power setting in Fig. 6.26(b).

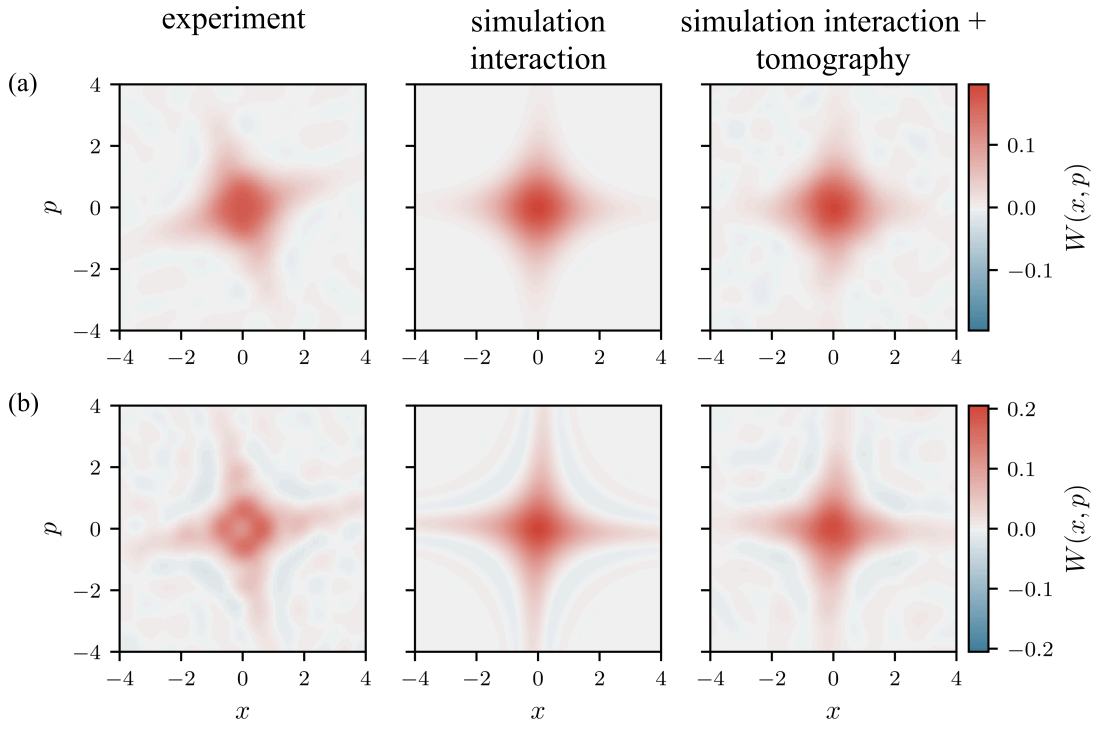

Figure 6.26: Wigner functions of quadsqueezed states with (a) $r_{4s} \approx 0.054(5)$ and (b) $r_{4s} \approx 0.15(1)$, showing Wigner negativity. The first column shows Wigner functions $W(x, p)$ reconstructed from experimental data. The Wigner functions are inferred from the measured characteristic functions shown in Fig. 6.25. We compare these to Wigner functions of numerically simulated states with independently measured experimental parameters. For the 'full tomography simulation', we simulate both the generation of the quadsqueezed states and the effect of the probing SDF. The rotation observed in comparison to the simulation is due to a constant offset between the squeezing axis θ and the phase of the probing SDF ϕ_{probe}. This offset can be calibrated out if desired.

The quadsqueezing parameters r_{4s} for the two states are inferred similarly as it was for the trisqueezed states; we validate that the Ω_4 magnitude formula holds by

comparing simulated states created using the ideal interaction versus states created by simulating the full Hamiltonian. For the state in Fig. 6.26(a), the inferred overlap is $1 - F = 1 \times 10^{-3}$ and the quadsqueezing parameter $r_{4s} \approx 0.054(5)$. For the state in Fig. 6.26(b), the inferred overlap is $1 - F = 8 \times 10^{-2}$ and the quadsqueezing parameter $r_{4s} \approx 0.15(1)$. This error in the overlap does not originate from the presence of the carrier terms, as removing them does not alter the error. Instead, it arises from the contribution of higher-order resonant terms in the Magnus expansion, which can be mitigated, as discussed in the next section.

Fock state distribution

As for trisqueezing, we show the simulated Fock state distribution of a quadsqueezed

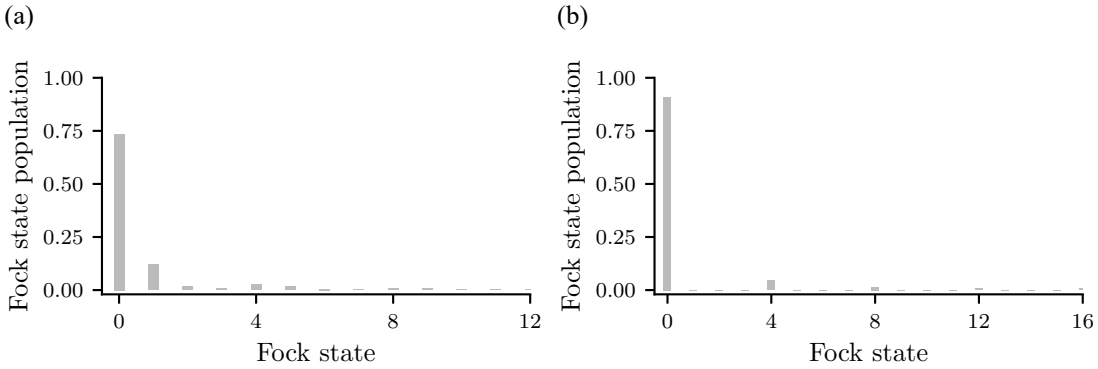

Figure 6.27: Simulated Fock state distribution of a quadsqueezed state. (a) We plot the Fock state distribution of the state simulated in Fig. 6.20(b) with $r_{4s} = 0.15$. (b) We plot the simulated distribution using the same interaction parameters by starting in Fock state $|0\rangle$ and considering no heating.

state. In Fig. 6.27(a), we plot the simulated Fock state distribution for the state in Fig. 6.26(b). We also show the Fock state population for the case in which the quadsqueezing interaction is applied to Fock state $|0\rangle$, and there is no motional decoherence due to heating. We can observe the quadsqueezing signature where the only Fock states that get populated are integer multiples of four.

6.9 Scaling of the nonlinear interaction strength

In Fig. 6.28, we compare the magnitude of our interactions Ω_n, Eq. (6.19) to that of the method of directly driving higher orders in the Lamb-Dicke expansion

Ω_{η^n}, Eq. (6.5). For our method, we consider the parameters used for creating the squeezed state in Fig. 6.16(a) ($1 - F = 1.6 \times 10^{-3}$), trisqueezed state in Fig. 6.20(a), and quadsqueezed state in Fig. 6.26(a), because they give rise to states with a high degree of overlap when compared to ideal states. Moreover, we assume the same power is available for both methods, i.e., if the two non-commuting SDFs method uses 0.5 mW for each SDF, then the higher motional sideband method, which only requires one bichromatic field, uses $2 \times 0.5\,\text{mW} = 1\,\text{mW}$.

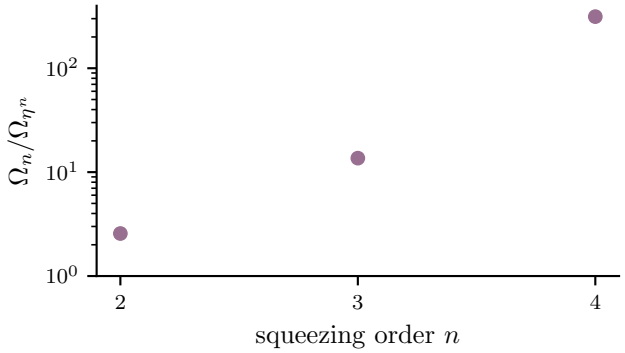

Figure 6.28: Comparison of the strength of generalised squeezing interactions. We compare the method demonstrated in this work, with magnitude Ω_n, to the method of driving higher-order terms in the Lamb-Dicke expansion, magnitude Ω_{η^n}. We assume the same total amount of laser power is used in both cases.

We observe that our trisqueezing and quadsqueezing interactions are more than 10 and a 100 times stronger, respectively, than interactions using the higher-order terms in the Lamb-Dicke expansion. Without this increase in strength, these interactions would have been unfeasible[13] in our system due to the decoherence effects.

6.10 Some experimental considerations

In this section, we present a few notes on some experimental considerations and limitations we observed while working on the presented results; it is not

[13]This work focuses on synthesising specific interactions, which are essential for applications such as simulating nonlinear bosonic interactions in analog quantum simulations, for example, in molecular dynamics [14]. Alternatively, to create specific states like a trisqueezed state, linear bosonic interactions (e.g., blue and red sidebands) and numerically optimised pulses, as shown in Ref. [156], can be employed. Although such methods are effective for achieving target states from a given initial state, they are not well-suited for studying the evolution of a system under a specific Hamiltonian.

an exhaustive list.

6.10.1 Higher order terms

In Fig. 6.8(a), we observe that for $\Delta/2\pi = 50\,\text{kHz}$, $t_{\text{sqz}} = 1000\,\mu\text{s}$, the inferred r of above 2 has an error bar larger than the other experimental points. Here, the fitting model does not properly describe the splitting dynamics. In Fig. 6.29, we show the recorded experimental data for $t_{\text{sqz}} = 1000\,\mu\text{s}$ including the fitting and simulation. The oscillations are predicted by the simulation, and they are due to the higher-order resonant terms in the Magnus expansion becoming significant. Their effect can be mitigated by increasing Δ, which would reduce the overall strength of the squeezing interaction if $\Omega_\alpha, \Omega_{\alpha'}$ are not adjusted accordingly.

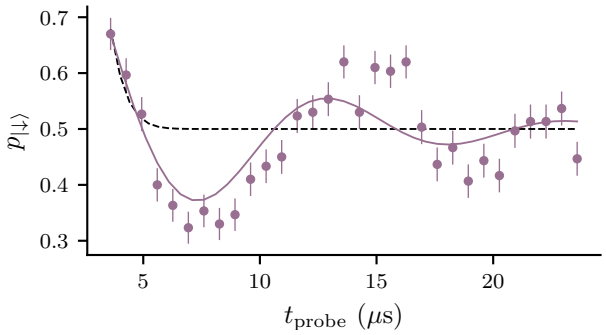

Figure 6.29: Splitting dynamics for applying the squeezing Hamiltonian for $t_{\text{sqz}} = 1000\,\mu\text{s}$ with $\Delta/2\pi = 50\,\text{kHz}$ and 0.5 mW for each SDF. We show the fit to the data using the model described above (dashed black line) and the free parameter simulation (continuous purple line), where all parameters are fixed by independent experimental measurements.

We evaluate, in simulation, how the effects of the higher-order resonant terms in the Magnus expansion can be mitigated by adjusting the interaction parameters. We choose to create a squeezed state with $r = 1.56$ and maintain the ramp duration constant $t_{\text{ramp}} = 80\,\mu\text{s}$. By varying Δ, t_{sqz} and the power of the interaction SDFs, we can maintain the squeezing parameter constant for different error values $1 - F$. As before, F is the overlap between a state created using the ideal interaction with $\Omega_2 = \Omega_\alpha \Omega_{\alpha'}/\Delta$ and a state created by integrating the full Hamiltonian of the two non-commuting SDFs. For these simulations, we don't introduce any decoherence effects. The results are shown in In Table 6.4.

$\Delta/2\pi$(kHz)	t_{sqz}(µs)	$\mathrm{SDF}_{\alpha,\alpha'}$ power (mW)	$1-F$
50	600	0.5	9×10^{-3}
12.5	150	0.5	0.24
12.5	600	0.125	0.05
25	300	0.5	0.06
25	600	0.25	0.02
100	300	2	0.02
100	600	1	6×10^{-3}
100	1200	0.5	1×10^{-3}

Table 6.4: Assessing errors arising from other terms in the Magnus expansion for a squeezed state with $r = 1.56$ for different interaction parameters. We compute, in simulation, the overlap (F) between a squeezed state created using the ideal interaction and one using the full simulation.

The key insight here is that unquestioningly enhancing the interaction strength by reducing Δ and increasing the power in the interaction SDFs rapidly leads to an interaction that differs from the ideal one, with effects going beyond changes in interaction magnitude. While very low errors can be achieved, this often comes at the expense of slower interactions. It becomes a balancing act between tolerable error levels due to terms in the Magnus expansion and the duration of the interaction, particularly considering other sources of error such as spin and motional decoherence.

6.10.2 Ramp

We nonchalantly amplitude-shaped our pulses over durations of $t_{\mathrm{ramp}} = 80\,\mu\mathrm{s}$ without acknowledging that this significant duration could lead to certain inconveniences, such as difficulties in trotterising the synthesised interactions for quantum simulation applications or generating others that are not readily available through the Magnus expansion. In this section, we briefly investigate some consequences of using a shorter ramp than $2\pi/\Delta$. We apply the squeezing interaction, with $\Delta/2\pi = 50\,\mathrm{kHz}$ and 0.5 mW in each interaction SDF for a range of durations, corresponding to different time steps in the evolution around one loop in phase space. Fig. 6.30 shows the outcome for two choices of t_{ramp}, 10 µs and 40 µs.

We infer r for each of the interaction durations t_{sqz} by splitting the oscillator wavefunction about the squeezed axis as described in Sec. 6.5.2, see Fig. 6.30(a).

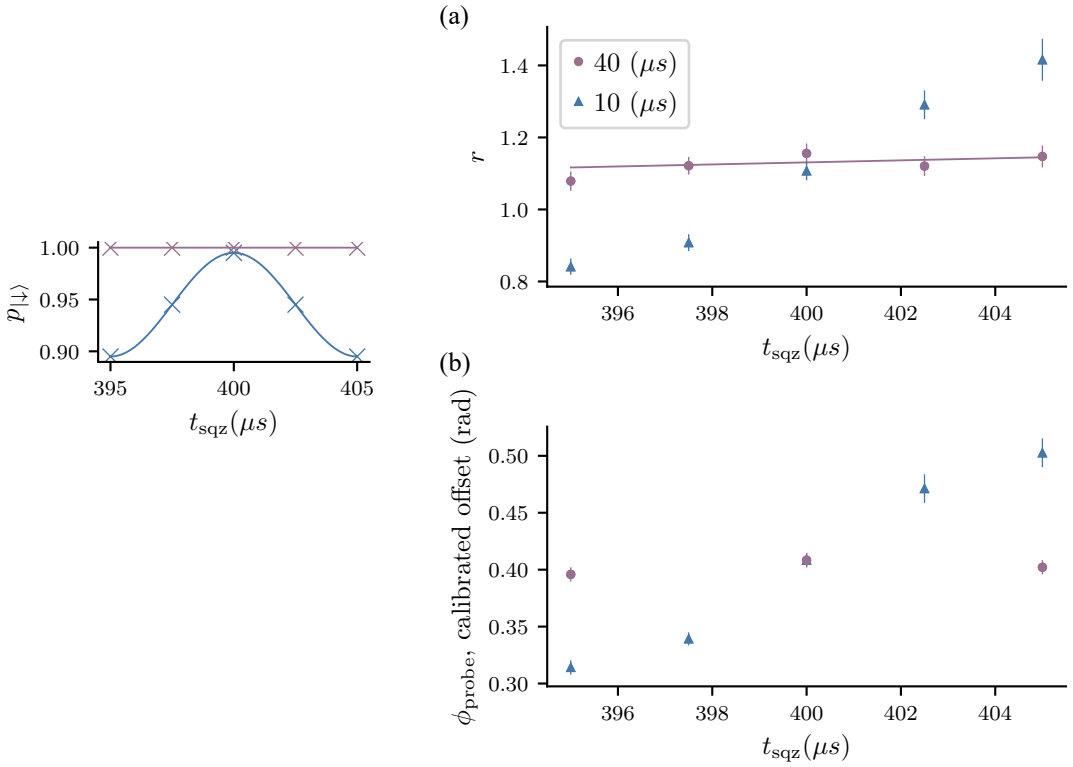

Figure 6.30: Investigating the effects of a shorter ramp than $2\pi/\Delta$. We create a squeezed state using $\Delta/2\pi = 50\,\mathrm{kHz}$ and 0.5 mW in each interaction SDF. In the inset, we show a diagram of dynamics occurring for $t_{\mathrm{ramp}} = 10\,\mu\mathrm{s}$ (purple) and $t_{\mathrm{ramp}} = 40\,\mu\mathrm{s}$ (blue) as well, as the squeezing durations t_{sqz} (crosses) for which the resulting state was analysed. (a) The inferred squeezing parameter values r for the durations indicated in the inset. (b) The offset between the squeezing axis and the phase of the probe SDF, which was calibrated before recording the data used to infer r.

Before each measurement, we calibrate the offset between the probing SDF and the squeezing axis. In the case of $t_{\mathrm{ramp}} = 10\,\mu\mathrm{s}$, we observe that both the offset and the r values change significantly as we sample around the loop. This is because, due to the residual displacement, we split a squeezed cat state instead of a squeezed state when applying the probe SDF. As the interaction SDFs are detuned, the oscillator wavepacket is displaced in circles in phase space, which causes the change in the offset between the probing SDF and the axis of the probed state. Moreover, even though we can find a point where the residual displacement effect is suppressed, this occurs at a maximum slope point, making us very sensitive to experimental changes, such as miscalibrations in the motional mode frequency, which would alter the loop closure periodicity.

Thinking further about this aspect, one of the beautiful things about this method is that it relies on spin-dependent forces to generate the nonlinear interaction. This means that methods used to make two-qubit gates more robust to specific errors could, in principle, be employed here. For example, we could use Walsh modulation, which involves changing the motional phase of the SDF throughout the interaction to end up closer to the origin in phase space. This has been shown to improve robustness to loop closure timing errors and resilience to errors due to heating in two-qubit gates [128].

6.10.3 Carrier terms

We have seen that keeping track of the carrier terms is cumbersome. For generating interactions in the $\hat{\sigma}_\phi$ basis, given the same Ω range, their effect is significantly reduced when using motional modes with higher frequencies, such as the radial modes $\omega_{x,y}$ in our system. This is because the argument of the Bessel functions (J_0, J_2) is inversely proportional to $\delta \approx \omega_{x,y}$, the detuning from the qubit frequency. The strength of the $\hat{\sigma}_z$-conditioned SDF generated using the method described in this work would also be significantly reduced for such a mode.

6.11 Summary

This work introduces a novel method for generating nonlinear bosonic interactions by utilising the ion's additional degree of freedom, the spin, to mediate effective interactions instead of creating them directly. We employ two non-commuting spin-dependent forces; these are linear interactions in the bosonic mode. Spin-dependent forces have been extensively used to develop boson-mediated spin-spin entanglement that overcomes weak direct spin-spin interactions. In contrast, this work reverses the typical roles, employing the spin as a tool to mediate boson-boson (self-boson) interactions. This shift in approach enabled us to demonstrate up to fourth-order generalised squeezing, which would otherwise be unattainable in our system with conventional techniques due to their limited strength.

Our method has no fundamental limit on the interaction order n and is applicable to platforms that support spin-dependent linear interactions. Notably, we use the same two linear interactions to achieve squeezing, trisqueezing, and quadsqueezing by simply adjusting the interaction frequency. Furthermore, our method is not limited to generalised squeezing interactions; it can also be used to create any nonlinear bosonic interaction involving various combinations of creation and annihilation operators, as detailed in [140].

7
Outlook

We explored how the presence of non-commuting terms in the interactions we studied can lead to both detrimental and advantageous outcomes. In the case of spin-dependent forces created using a bichromatic travelling field (Mølmer-Sørensen scheme), the presence of the off-resonant non-commuting carrier term sets a global maximum on the achievable interaction strength. Using a bichromatic phase-stabilised standing-wave field, instead, allowed us to circumvent the non-commuting term and use the spin-dependent force to demonstrate two-qubit entangling gates which are not limited by this effect.

Conversely, the presence of the non-commuting carrier term also enables us to generate spin-dependent forces conditioned on the $\hat{\sigma}_z$, emerging from the commutator of the spin conditioning of the carrier and spin-motional coupling term, i.e. $[\hat{\sigma}_x, \hat{\sigma}_y]$. Being able to generate SDFs conditioned on $\hat{\sigma}_x, \hat{\sigma}_y,$ and $\hat{\sigma}_z$, we demonstrated a new technique for generating nonlinear interactions in the motion of the ion with more favourable scaling than conventional techniques. We focused on generalised squeezing and experimentally implemented squeezing, trisqueezing, and quadsqueezing. To our knowledge, this is the first implementation of trisqueezing in an atomic system and the first demonstration of quadsqueezing in any platform.

How do we proceed from here?

7.1 Towards fast geometric phase gates with optical phase control

The proof of principle demonstrated in Chapter 5 shows that using standing waves allows for shorter gate durations without compromising the fidelity when compared to the traditional Mølmer-Sørensen (MS) scheme that employs travelling waves. However, there is potential for further speed improvements. The fastest gate[1] demonstration that employs the geometric phase gate mechanism and achieves fidelities comparable to state-of-the-art values was realised by Schaefer et al., achieving a 1.6 µs gate with 99.8% fidelity [157]. This implementation relied on spin-dependent forces generated by beams far-detuned from the qubit transition—a light-shift gate $\hat{\sigma}_z\hat{\sigma}_z$ [81, 133]—in combination with amplitude-shaped pulses [159]. As we push towards shorter gate durations, effectively increasing Δ, we encounter errors due to coherent couplings, such as the participation of additional motional modes. The complex amplitude-shaped pulses described in Ref. [159] and implemented by Schaefer et al. [157] introduce additional degrees of freedom that can be leveraged to mitigate the unwanted contributions of multiple motional modes to the interaction, thereby enhancing gate fidelity and robustness.

The application of amplitude-shaped pulses, as introduced in Ref. [159], is possible only when the terms in the Hamiltonian commute. Since the standing-wave MS implementation results in an interaction where all terms commute (see Eq. (2.64)), we can integrate this gate method with amplitude-shaped pulse techniques, enabling fast, non-adiabatic $\hat{\sigma}_\phi\hat{\sigma}_\phi$ gates. Notably, this provides a unified approach to implementing fast gates for both $\hat{\sigma}_z\hat{\sigma}_z$ and $\hat{\sigma}_\phi\hat{\sigma}_\phi$ interactions in trapped ions. Furthermore, employing a standing wave (SW) helps suppress undesired squeezing terms of order $\mathcal{O}(\eta^2)$, which constituted a significant source of error in previous implementations-referred to as out-of-Lamb-Dicke effects [157].

[1] Excluding Ref. [157], our gate durations compare favourably with other implementations based on the MS scheme [30], though interpreting reported gate durations can be challenging, as definitions vary. We specify the gate duration at full width at half maximum as 15 µs, equivalent to a pulse with a full width of 25 µs. Ref. [27] reports a gate duration of 30 µs for a Raman-based MS scheme on beryllium ions, which yields a Lamb-Dicke parameter of $\eta \approx 0.25$. For setups with η values closer to ours, gate durations of ≈ 100 µs are reported [158].

Conversely, the phase control techniques developed in this thesis could be applied to enhance the previous Raman-based scheme [157]. This approach would stabilise the optical phase between the two Raman beams used to implement the gate interaction [97], facilitating the discovery of pulse shape solutions that could counteract the effects of the squeezing term, thus enabling faster operations and improved gate fidelities [160].

However, before introducing such a shaped-pulse technique [159], we need to increase the laser intensity at the ions' positions to access these fast gate regimes. This adjustment can be achieved by singly addressing the ions with SWs, which introduces its own set of stability challenges.

Implementing these fast MS scheme gates also creates opportunities for using laser wavelengths that are better suited for large-scale chip integration and standard integrated optics, such as 674 nm and 729 nm laser light. These wavelengths experience lower losses in photonic waveguides compared to blue light, making them more compatible with integrated photonic platforms [161–163]. Furthermore, integrated optics offer inherent passive stability, reducing the need for active phase stabilisation [118]. Moreover, being able to access longer wavelengths provides a pathway for implementing fast entangling gates while circumventing the technical challenges associated with high-power blue Raman beams [157], pulsed lasers [164, 165], and Rydberg schemes [166].

7.2 Exploring the nonlinear interactions further

We focused on demonstrating generalised squeezing interactions in this work. However, the technique introduced can be employed to generate any nonlinear bosonic interaction comprising other combinations of the creation and annihilation operators and even extending to using multiple motional modes as described in Ref. [91]. Some examples of these interactions are shown in Table 7.1, adapted from Ref. [91]. Multi-mode interactions (e.g., beam splitters), together with single-mode Gaussian (e.g., squeezing) and non-Gaussian (e.g., trisqueezing) operations

demonstrated in this work, provide a universal gate set for scalable continuous-variable quantum computing [45, 46].

effective Hamiltonian	interaction name	m	same mode
$\hat{\sigma}_\beta(\hat{a}^\dagger\hat{a} - \hat{a}\hat{a}^\dagger + 1)$	parity, phase space rotation	1	yes
$\hat{\sigma}_\beta(\hat{a}^\dagger\hat{b}^\dagger - \hat{a}\hat{b})$	two-mode squeezing [144]	-1	no
$\hat{\sigma}_\beta(\hat{a}\hat{b}^\dagger - \hat{a}^\dagger\hat{b})$	beamsplitter [59–61]	1	no
$\hat{\sigma}_\beta(\hat{a}^2\hat{b}^\dagger - \hat{a}^{\dagger 2}\hat{b})$	cross-Kerr nonlinearity [142]	2	no

Table 7.1: Some examples of other nonlinear interactions that can be created by combining two non-commuting SDFs. For simplicity, we omitted the interaction strength and other constant factors and set $\theta = 0$ (see Sec. 6.1.2). For the interactions that require two motional modes with ω_a and ω_b, respectively, we simply set one SDF with $\delta = \omega_a + \Delta$ and the other with $\delta = \omega_b + m\Delta$. We also added references for experimental implementations of these interactions in trapped ions.

Furthermore, the spin dependence of these bosonic interactions can be further explored. This dependence enables mid-circuit measurements on the spin, allowing the creation of resourceful superposition quantum states for metrology or error correction [44, 79, 154, 167].

Finally, our technique extends to hybrid spin-boson encodings [40], which enable more efficient simulation of various physical models, including quantum field theories [10, 11] and chemical dynamics [12, 14], compared to using spin-only systems. For simulating quantum field theories, specifically lattice gauge theories, we developed a proposal [10] with collaborators, where the internal states of the ion serve as the gauge field and its motional modes host the charged matter. Using a spin-dependent beamsplitter operation created via the two noncommuting SDFs method, we can engineer real-time dynamics between the gauge field and the charged matter. Moreover, these hybrid encodings enable computational protocols that are inherently more robust to errors [17] while also reducing the computational requirements for representing a boson in a collection of qubits. This reduction is particularly beneficial for practical applications involving near-term devices with limited circuit depths.

List of Figures

List of Abbreviations

SDF . . . . . Spin-Dependent Force.

SW . . . . . Standing Wave.

TW . . . . . Travelling Wave.

QHO . . . . . Quantum Harmonic Oscillator.

MS . . . . . Mølmer-Sørensen.

b1 . . . . . branch 1.

b2 . . . . . branch 2.

rf . . . . . radio frequency.

ch . . . . . channel.

PD . . . . . photodiode.

AOM . . . . . Acousto-Optical Modulator.

DP . . . . . Double Pass.

SP . . . . . Single Pass.

CW . . . . . Continuous Wave.

FNC . . . . . Fibre Noise Cancellation.

NPL . . . . . National Physical Laboratory.

STFT . . . . . Short time Fourier transform.

PW . . . . . pick-off window.

DIO . . . . . digital input/output

PMT . . . . . photomultiplier tube

DDS . . . . . direct digital synthesis

AWG . . . . . arbitrary wave generator

ADC . . . . . analogue to digital converter

FPGA . . . . . field-programmable gate array

ARTIQ . . . . Advanced Real-Time Infrastructure for Quantum Physics

RPC . . . . . remote procedure call

LO . . . . . local oscillator

References

[1] O. Băzăvan, S. Saner, M. Minder, A. C. Hughes, R. T. Sutherland, D. M. Lucas, R. Srinivas, and C. J. Ballance, *Synthesizing a $\hat{\sigma}_z$ spin-dependent force for optical, metastable, and ground-state trapped-ion qubits*, *Phys. Rev. A* **107**, 022617 (2023).

[2] H. Ribeiro, A. Baksic, and A. A. Clerk, *Systematic Magnus-Based Approach for Suppressing Leakage and Nonadiabatic Errors in Quantum Dynamics*, *Phys. Rev. X* **7**, 011021 (2017).

[3] S. Blanes, F. Casas, J. A. Oteo, and J. Ros, *A pedagogical approach to the Magnus expansion*, *Eur. J. Phys.* **31**, 907 (2010).

[4] W. Magnus, *On the exponential solution of differential equations for a linear operator*, *Commun. Pure Appl. Math.* **7**, 649–673 (1954).

[5] S. Blanes, F. Casas, J. A. Oteo, and J. Ros, *The Magnus expansion and some of its applications*, *Phys. Rep.* **470**, 151–238 (2009).

[6] C. Monroe, D. M. Meekhof, B. E. King, and D. J. Wineland, *A "Schrödinger Cat" Superposition State of an Atom*, *Science* **272**, 1131–1136 (1996).

[7] S. Haroche, *Nobel Lecture: Controlling photons in a box and exploring the quantum to classical boundary*, *Rev. Mod. Phys.* **85**, 1083–1102 (2013).

[8] A. Blais, R.-S. Huang, A. Wallraff, S. M. Girvin, and R. J. Schoelkopf, *Cavity quantum electrodynamics for superconducting electrical circuits: An architecture for quantum computation*, *Phys. Rev. A* **69**, 062320 (2004).

[9] R. E. Evans, M. K. Bhaskar, D. D. Sukachev, C. T. Nguyen, A. Sipahigil, M. J. Burek, B. Machielse, G. H. Zhang, A. S. Zibrov, E. Bielejec, H. Park, M. Lončar, and M. D. Lukin, *Photon-mediated interactions between quantum emitters in a diamond nanocavity*, *Science* **362**, 662–665 (2018).

[10] A. Bermudez, G. Aarts, and M. Müller, *Quantum Sensors for the Generating Functional of Interacting Quantum Field Theories*, *Phys. Rev. X* **7**, 041012 (2017).

[11] O. Băzăvan, S. Saner, E. Tirrito, G. Araneda, R. Srinivas, and A. Bermudez, *Synthetic $\mathbb{Z}_2$ gauge theories based on parametric excitations of trapped ions*, *Commun. Phys.* **7**, 229 (2024).

[12] C. H. Valahu, V. C. Olaya-Agudelo, R. J. MacDonell, T. Navickas, A. D. Rao, M. J. Millican, J. B. Pérez-Sánchez, J. Yuen-Zhou, M. J. Biercuk, C. Hempel, T. R. Tan, and I. Kassal, *Direct observation of geometric-phase interference in dynamics around a conical intersection*, *Nat. Chem.* **15**, 1503–1508 (2023).

[13] J. Whitlow, Z. Jia, Y. Wang, C. Fang, J. Kim, and K. R. Brown, *Quantum simulation of conical intersections using trapped ions*, *Nat. Chem.* **15**, 1509–1514 (2023).

[14] M. Kang, H. Nuomin, S. N. Chowdhury, J. L. Yuly, K. Sun, J. Whitlow, J. Valdiviezo, Z. Zhang, P. Zhang, D. N. Beratan, et al., *Seeking a quantum advantage with trapped-ion quantum simulations of condensed-phase chemical dynamics*, *Nat. Rev. Chem.*, 1–19 (2024).

[15] R. Dutta, D. G. Cabral, N. Lyu, N. P. Vu, Y. Wang, B. Allen, X. Dan, R. G. Cortiñas, P. Khazaei, S. E. Smart, et al., *Simulating Chemistry on Bosonic Quantum Devices*, *arXiv preprint arXiv:2404.10214*, (2024).

[16] V. Olaya-Agudelo, B. Stewart, C. Valahu, R. MacDonell, M. Millican, V. Matsos, F. Scuccimarra, T. Tan, and I. Kassal, *Simulating open-system molecular dynamics on analog quantum computers*, *arXiv preprint arXiv:2407.17819*, (2024).

[17] J. Lee, N. Kang, S.-H. Lee, H. Jeong, L. Jiang, and S.-W. Lee, *Fault-tolerant quantum computation by hybrid qubits with bosonic cat-code and single photons*, *arXiv:2401.00450*, (2023).

[18] J. I. Cirac and P. Zoller, *Quantum Computations with Cold Trapped Ions*, *Phys. Rev. Lett.* **74**, 4091 (1995).

[19] K. Mølmer and A. Sørensen, *Multiparticle Entanglement of Hot Trapped Ions*, *Phys. Rev. Lett.* **82**, 1835–1838 (1999).

[20] R. Blatt and D. Wineland, *Entangled states of trapped atomic ions*, *Nature* **453**, 1008–1015 (2008).

[21] M. A. Rowe, D. Kielpinski, V. Meyer, C. A. Sackett, W. M. Itano, C. Monroe, and D. J. Wineland, *Experimental violation of a Bell's inequality with efficient detection*, *Nature* **409**, 791–794 (2001).

[22] D. Leibfried, M. D. Barrett, T. Schaetz, J. Britton, J. Chiaverini, W. M. Itano, J. D. Jost, C. Langer, and D. J. Wineland, *Toward Heisenberg-Limited Spectroscopy with Multiparticle Entangled States*, *Science* **304**, 1476–1478 (2004).

[23] D. Deutsch, *Quantum theory, the Church–Turing principle and the universal quantum computer*, *Proc. R. Soc. Lond. A* **400**, 97–117 (1985).

[24] S. Lloyd, *Universal Quantum Simulators*, *Science* **273**, 1073–1078 (1996).

[25] D. P. DiVincenzo and P. W. Shor, *Fault-Tolerant Error Correction with Efficient Quantum Codes*, *Phys. Rev. Lett.* **77**, 3260–3263 (1996).

[26] C. J. Ballance, T. P. Harty, N. M. Linke, M. A. Sepiol, and D. M. Lucas, *High-Fidelity Quantum Logic Gates Using Trapped-Ion Hyperfine Qubits*, *Phys. Rev. Lett.* **117**, 060504 (2016).

[27] J. P. Gaebler, T. R. Tan, Y. Lin, Y. Wan, R. Bowler, A. C. Keith, S. Glancy, K. Coakley, E. Knill, D. Leibfried, and D. J. Wineland, *High-Fidelity Universal Gate Set for $^{9}Be^{+}$ Ion Qubits*, *Phys. Rev. Lett.* **117**, 060505 (2016).

[28] C. R. Clark, H. N. Tinkey, B. C. Sawyer, A. M. Meier, K. A. Burkhardt, C. M. Seck, C. M. Shappert, N. D. Guise, C. E. Volin, S. D. Fallek, H. T. Hayden, W. G. Rellergert, and K. R. Brown, *High-Fidelity Bell-State Preparation with $^{40}Ca^{+}$ Optical Qubits*, *Phys. Rev. Lett.* **127**, 130505 (2021).

[29] C. Löschnauer, J. M. Toba, A. Hughes, S. King, M. Weber, R. Srinivas, R. Matt, R. Nourshargh, D. Allcock, C. Ballance, et al., *Scalable, high-fidelity all-electronic control of trapped-ion qubits*, *arXiv preprint arXiv:2407.07694*, (2024).

[30] Z. Cai, C.-Y. Luan, L. Ou, H. Tu, Z. Yin, J.-N. Zhang, and K. Kim, *Entangling gates for trapped-ion quantum computation and quantum simulation*, *J. Korean Phys. Soc.* **82**, 882–900 (2023).

[31] D. J. Wineland, C. Monroe, W. M. Itano, D. Leibfried, B. E. King, and D. M. Meekhof, *Experimental Issues in Coherent Quantum-State Manipulation of Trapped Atomic Ions*, *J. Res. Natl. Inst. Stand. Technol.* **103**, 259–328 (1998).

[32] C. J. Ballance. *High-fidelity quantum logic in Ca+*. Springer, 2017. URL: https://ora.ox.ac.uk/objects/uuid:1beb7f67-4d92-4d57-8754-50f92f9d27f4/.

[33] C. M. Caves, *Quantum-mechanical noise in an interferometer*, *Phys. Rev. D* **23**, 1693–1708 (1981).

[34] The LIGO Scientific Collaboration, *Enhanced sensitivity of the LIGO gravitational wave detector by using squeezed states of light*, *Nat. Photonics* **7**, 613–619 (2013).

[35] C. A. Casacio, L. S. Madsen, A. Terrasson, M. Waleed, K. Barnscheidt, B. Hage, M. A. Taylor, and W. P. Bowen, *Quantum-enhanced nonlinear microscopy*, *Nature* **594**, 201–206 (2021).

[36] S. C. Burd, R. Srinivas, J. J. Bollinger, A. C. Wilson, D. J. Wineland, D. Leibfried, D. H. Slichter, and D. T. C. Allcock, *Quantum amplification of mechanical oscillator motion*, *Science* **364**, 1163–1165 (2019).

[37] K. Banaszek and P. L. Knight, *Quantum interference in three-photon down-conversion*, *Phys. Rev. A* **55**, 2368–2375 (1997).

[38] F. Albarelli, M. G. Genoni, M. G. A. Paris, and A. Ferraro, *Resource theory of quantum non-Gaussianity and Wigner negativity*, *Phys. Rev. A* **98**, 052350 (2018).

[39] R. Takagi and Q. Zhuang, *Convex resource theory of non-Gaussianity*, *Phys. Rev. A* **97**, 062337 (2018).

[40] Y. Liu, S. Singh, K. C. Smith, E. Crane, J. M. Martyn, A. Eickbusch, A. Schuckert, R. D. Li, J. Sinanan-Singh, M. B. Soley, et al., *Hybrid Oscillator-Qubit Quantum Processors: Instruction Set Architectures, Abstract Machine Models, and Applications*, *arXiv preprint arXiv:2407.10381*, (2024).

[41] X. Gao, P. Appel, N. Friis, M. Ringbauer, and M. Huber, *On the role of entanglement in qudit-based circuit compression*, *Quantum* **7**, 1141 (2023).

[42] M. Ringbauer, M. Meth, L. Postler, R. Stricker, R. Blatt, P. Schindler, and T. Monz, *A universal qudit quantum processor with trapped ions*, *Nat. Phys.* **18**, 1053–1057 (2022).

[43] D. Gottesman, A. Kitaev, and J. Preskill, *Encoding a qubit in an oscillator*, *Phys. Rev. A* **64**, 012310 (2001).

[44] C. Flühmann, T. L. Nguyen, M. Marinelli, V. Negnevitsky, K. Mehta, and J. P. Home, *Encoding a qubit in a trapped-ion mechanical oscillator*, *Nature* **566**, 513–517 (2019).

[45] S. Lloyd and S. L. Braunstein, *Quantum computation over continuous variables*, *Phys. Rev. Lett.* **82**, 1784 (1999).

[46] S. L. Braunstein and P. van Loock, *Quantum information with continuous variables*, *Rev. Mod. Phys.* **77**, 513–577 (2005).

[47] Y. Zheng, O. Hahn, P. Stadler, P. Holmvall, F. Quijandría, A. Ferraro, and G. Ferrini, *Gaussian Conversion Protocols for Cubic Phase State Generation*, *PRX Quantum* **2**, 010327 (2021).

[48] A. Mari and J. Eisert, *Positive Wigner Functions Render Classical Simulation of Quantum Computation Efficient*, *Phys. Rev. Lett.* **109**, 230503 (2012).

[49] O. Hahn, R. Takagi, G. Ferrini, and H. Yamasaki, *Classical simulation and quantum resource theory of non-Gaussian optics*, *arXiv preprint arXiv:2404.07115*, (2024).

[50] E. Crane, K. C. Smith, T. Tomesh, A. Eickbusch, J. M. Martyn, S. Kühn, L. Funcke, M. A. DeMarco, I. L. Chuang, N. Wiebe, A. Schuckert, and S. M. Girvin, *Hybrid Oscillator-Qubit Quantum Processors: Simulating Fermions, Bosons, and Gauge Fields*, *arXiv preprint arXiv:2409.03747*, (2024).

[51] S. Varona, S. Saner, O. Băzăvan, G. Araneda, G. Aarts, and A. Bermudez, *Towards quantum computing Feynman diagrams in hybrid qubit-oscillator devices*, *arXiv preprint arXiv:2411.05092*, (2024).

[52] L. J. Bond, B. Gerritsen, J. Minář, J. T. Young, J. Schachenmayer, and A. Safavi-Naini, *Open quantum dynamics with variational non-Gaussian states and the truncated Wigner approximation*, *The Journal of Chemical Physics* **161**, 184113 (2024).

[53] M. Mielenz, H. Kalis, M. Wittemer, F. Hakelberg, U. Warring, R. Schmied, M. Blain, P. Maunz, D. L. Moehring, D. Leibfried, and T. Schaetz, *Arrays of individually controlled ions suitable for two-dimensional quantum simulations*, *Nat. Commun.* **7**, 11839 (2016).

[54] T. Hillmann, F. Quijandría, G. Johansson, A. Ferraro, S. Gasparinetti, and G. Ferrini, *Universal Gate Set for Continuous-Variable Quantum Computation with Microwave Circuits*, *Phys. Rev. Lett.* **125**, 160501 (2020).

[55] N. E. Frattini, U. Vool, S. Shankar, A. Narla, K. M. Sliwa, and M. H. Devoret, *3-wave mixing Josephson dipole element*, *Appl. Phys. Lett.* **110**, 222603 (2017).

[56] R. E. Slusher, L. W. Hollberg, B. Yurke, J. C. Mertz, and J. F. Valley, *Observation of Squeezed States Generated by Four-Wave Mixing in an Optical Cavity*, *Phys. Rev. Lett.* **55**, 2409–2412 (1985).

[57] D. M. Meekhof, C. Monroe, B. E. King, W. M. Itano, and D. J. Wineland, *Generation of Nonclassical Motional States of a Trapped Atom*, *Phys. Rev. Lett.* **76**, 1796–1799 (1996).

[58] E. E. Wollman, C. U. Lei, A. J. Weinstein, J. Suh, A. Kronwald, F. Marquardt, A. A. Clerk, and K. C. Schwab, *Quantum squeezing of motion in a mechanical resonator*, *Science* **349**, 952–955 (2015).

[59] K. R. Brown, C. Ospelkaus, Y. Colombe, A. C. Wilson, D. Leibfried, and D. J. Wineland, *Coupled quantized mechanical oscillators*, *Nature* **471**, 196–199 (2011).

[60] H. C. J. Gan, G. Maslennikov, K.-W. Tseng, C. Nguyen, and D. Matsukevich, *Hybrid Quantum Computing with Conditional Beam Splitter Gate in Trapped Ion System*, *Phys. Rev. Lett.* **124**, 170502 (2020).

[61] P.-Y. Hou, J. J. Wu, S. D. Erickson, D. C. Cole, G. Zarantonello, A. D. Brandt, A. C. Wilson, D. H. Slichter, and D. Leibfried, *Coherently coupled mechanical oscillators in the quantum regime*, *arXiv:2205.14841*, (2022).

[62] C. W. S. Chang, C. Sabín, P. Forn-Díaz, F. Quijandría, A. M. Vadiraj, I. Nsanzineza, G. Johansson, and C. M. Wilson, *Observation of Three-Photon Spontaneous Parametric Down-Conversion in a Superconducting Parametric Cavity*, *Phys. Rev. X* **10**, 011011 (2020).

[63] A. M. Eriksson, T. Sépulcre, M. Kervinen, T. Hillmann, M. Kudra, S. Dupouy, Y. Lu, M. Khanahmadi, J. Yang, C. C. Moreno, P. Deslsing, and S. Gasparinetti, *Universal control of a bosonic mode via drive-activated native cubic interactions*, *arXiv:2308.15320*, (2023).

[64] S. Saner, O. Băzăvan, M. Minder, P. Drmota, D. J. Webb, G. Araneda, R. Srinivas, D. M. Lucas, and C. J. Ballance, *Breaking the Entangling Gate Speed Limit for Trapped-Ion Qubits Using a Phase-Stable Standing Wave*, *Phys. Rev. Lett.* **131**, 220601 (2023).

[65] S. Haroche and J.-M. Raimond. *Exploring the quantum: atoms, cavities, and photons*. Oxford University Press, 2006.

[66] D. James, *Quantum dynamics of cold trapped ions with application to quantum computation*, *Appl. Phys. B*, (1998).

[67] A. I. Lvovsky. "Squeezed Light". *Photonics*. John Wiley & Sons, Ltd, 2015. Chap. 5, pp. 121–163. DOI: https://doi.org/10.1002/9781119009719.ch5. URL: https://onlinelibrary.wiley.com/doi/abs/10.1002/9781119009719.ch5.

[68] E. Wigner, *On the Quantum Correction For Thermodynamic Equilibrium*, *Phys. Rev.* **40**, 749–759 (1932).

[69] U. Leonhardt and H. Paul, *Measuring the quantum state of light*, *Progress in Quantum Electronics* **19**, 89–130 (1995).

[70] W. P. Schleich. "Wigner Function". *Quantum Optics in Phase Space*. John Wiley & Sons, Ltd, 2001. Chap. 3, pp. 67–98. DOI: https://doi.org/10.1002/3527602976.ch3. URL: https://onlinelibrary.wiley.com/doi/abs/10.1002/3527602976.ch3.

[71] C. Flühmann and J. P. Home, *Direct Characteristic-Function Tomography of Quantum States of the Trapped-Ion Motional Oscillator*, *Phys. Rev. Lett.* **125**, 043602 (2020).

[72] S. M. Barnett and P. M. Radmore. *Methods in Theoretical Quantum Optics*. Oxford University Press, Nov. 2002. DOI: 10.1093/acprof:oso/9780198563617.001.0001.

[73] S. T. Gulde. "Experimental realization of quantum gates and the Deutsch-Jozsa algorithm with trapped calcium ions". PhD thesis. University of Innsbruck, 2003. URL: https://www.osti.gov/etdeweb/biblio/20642744.

[74] C. J. Foot. *Atomic physics*. Vol. 7. Oxford University Press, 2004.

[75] D. Sakellariou, C. A. Meriles, A. Moulé, and A. Pines, *Variable rotation composite pulses for high resolution nuclear magnetic resonance using inhomogeneous magnetic and radiofrequency fields*, *Chem. Phys. Lett.* **363**, 25–33 (2002).

[76] J. A. Sherman, M. J. Curtis, D. J. Szwer, D. T. C. Allcock, G. Imreh, D. M. Lucas, and A. M. Steane, *Experimental Recovery of a Qubit from Partial Collapse*, *Phys. Rev. Lett.* **111**, 180501 (2013).

[77] K. DeBry, J. Sinanan-Singh, C. D. Bruzewicz, D. Reens, M. E. Kim, M. P. Roychowdhury, R. McConnell, I. L. Chuang, and J. Chiaverini, *Experimental Quantum Channel Discrimination Using Metastable States of a Trapped Ion*, *Phys. Rev. Lett.* **131**, 170602 (2023).

[78] P. Jurcevic, B. P. Lanyon, P. Hauke, C. Hempel, P. Zoller, R. Blatt, and C. F. Roos, *Quasiparticle engineering and entanglement propagation in a quantum many-body system*, *Nature* **511**, 202–205 (2014).

[79] D. Kienzler, H.-Y. Lo, B. Keitch, L. de Clercq, F. Leupold, F. Lindenfelser, M. Marinelli, V. Negnevitsky, and J. P. Home, *Quantum harmonic oscillator state synthesis by reservoir engineering*, *Science* **347**, 53–56 (2015).

[80] A. Sørensen and K. Mølmer, *Quantum Computation with Ions in Thermal Motion*, *Phys. Rev. Lett.* **82**, 1971–1974 (1999).

[81] G. Milburn, S. Schneider, and D. James, *Ion trap quantum computing with warm ions*, *Fortschritte der Physik: Progress of Physics* **48**, 801–810 (2000).

[82] S. Kotler, N. Akerman, N. Navon, Y. Glickman, and R. Ozeri, *Measurement of the magnetic interaction between two bound electrons of two separate ions*, *Nature* **510**, 376–380 (2014).

[83] R. Ozeri, *The trapped-ion qubit tool box*, *Contemp. Phys.* **52**, 531–550 (2011).

[84] P. C. Haljan, K.-A. Brickman, L. Deslauriers, P. J. Lee, and C. Monroe, *Spin-dependent forces on trapped ions for phase-stable quantum gates and entangled states of spin and motion*, *Phys. Rev. Lett.* **94**, 153602 (2005).

[85] M. J. McDonnell, J. P. Home, D. M. Lucas, G. Imreh, B. C. Keitch, D. J. Szwer, N. R. Thomas, S. C. Webster, D. N. Stacey, and A. M. Steane, *Long-Lived Mesoscopic Entanglement outside the Lamb-Dicke Regime*, *Phys. Rev. Lett.* **98**, 063603 (2007).

[86] D. J. Wineland, *Nobel Lecture: Superposition, entanglement, and raising Schrödinger's cat*, *Rev. Mod. Phys.* **85**, 1103–1114 (2013).

[87] A. Sørensen and K. Mølmer, *Entanglement and quantum computation with ions in thermal motion*, *Phys. Rev. A* **62**, 022311 (2000).

[88] E. L. Hahn, *Spin Echoes*, *Phys. Rev.* **80**, 580–594 (1950).

[89] M. H. Levitt, *Composite pulses*, *Prog. Nucl. Magn. Reson. Spectrosc.* **18**, 61–122 (1986).

[90] C. F. Roos, *Ion trap quantum gates with amplitude-modulated laser beams*, *New J. Phys.* **10**, 013002 (2008).

[91] R. Sutherland, R. Srinivas, S. C. Burd, D. Leibfried, A. C. Wilson, D. J. Wineland, D. Allcock, D. Slichter, and S. Libby, *Versatile laser-free trapped-ion entangling gates*, *New J. Phys.* **21**, 033033 (2019).

[92] R. Srinivas. "Laser-free trapped-ion quantum logic with a radiofrequency magnetic field gradient". PhD thesis. University of Colorado at Boulder, 2020. URL: https://www.proquest.com/docview/2447590165?pq-origsite=gscholar&fromopenview=true&sourcetype=Dissertations%20&%20Theses.

[93] C. A. Sackett, D. Kielpinski, B. E. King, C. Langer, V. Meyer, C. J. Myatt, M. Rowe, Q. Turchette, W. M. Itano, D. J. Wineland, et al., *Experimental entanglement of four particles*, *Nature* **404**, 256–259 (2000).

[94] K. Kim, C. F. Roos, L. Aolita, H. Häffner, V. Nebendahl, and R. Blatt, *Geometric phase gate on an optical transition for ion trap quantum computation*, *Phys. Rev. A* **77**, 050303 (2008).

[95] T. Monz, K. Kim, A. S. Villar, P. Schindler, M. Chwalla, M. Riebe, C. F. Roos, H. Häffner, W. Hänsel, M. Hennrich, and R. Blatt, *Realization of Universal Ion-Trap Quantum Computation with Decoherence-Free Qubits*, *Phys. Rev. Lett.* **103**, 200503 (2009).

[96] A. B. Mundt, A. Kreuter, C. Becher, D. Leibfried, J. Eschner, F. Schmidt-Kaler, and R. Blatt, *Coupling a Single Atomic Quantum Bit to a High Finesse Optical Cavity*, *Phys. Rev. Lett.* **89**, 103001 (2002).

[97] V. Schäfer. "Fast gates and mixed-species entanglement with trapped ions". PhD thesis. University of Oxford, 2018. URL: https://ora.ox.ac.uk/objects/uuid:65fddd29-ff17-49aa-85f1-13347839d73d.

[98] K. Thirumalai. "High-fidelity mixed species entanglement of trapped ions". PhD thesis. University of Oxford, 2019. URL: https://ora.ox.ac.uk/objects/uuid:74631d0e-2873-43c4-8f9a-d7ec470e2170.

[99] A. C. Hughes. "Benchmarking memory and logic gates for trapped-ion quantum computing". PhD thesis. University of Oxford, 2021. URL: https://ora.ox.ac.uk/objects/uuid:3fdb0b98-3c50-483c-b66e-132495ce71af/files/dwm117p323.

[100] W. Paul, *Electromagnetic traps for charged and neutral particles*, *Rev. Mod. Phys.* **62**, 531–540 (1990).

[101] S. Woodrow. "Linear Paul trap design for high-fidelity, scalable quantum information processing". PhD thesis. University of Oxford, 2016. URL: https://ora.ox.ac.uk/objects/uuid:27c4a222-e907-401c-8b3f-0c8ae618d6cb.

[102] D. Kielpinski, B. E. King, C. J. Myatt, C. A. Sackett, Q. A. Turchette, W. M. Itano, C. Monroe, D. J. Wineland, and W. H. Zurek, *Sympathetic cooling of trapped ions for quantum logic*, *Phys. Rev. A* **61**, 032310 (2000).

[103] J. P. Home, D. Hanneke, J. D. Jost, J. M. Amini, D. Leibfried, and D. J. Wineland, *Complete Methods Set for Scalable Ion Trap Quantum Information Processing*, *Science* **325**, 1227–1230 (2009).

[104] D. B. Hume, T. Rosenband, and D. J. Wineland, *High-Fidelity Adaptive Qubit Detection through Repetitive Quantum Nondemolition Measurements*, *Phys. Rev. Lett.* **99**, 120502 (2007).

[105] P. Drmota, D. Main, D. P. Nadlinger, B. C. Nichol, M. A. Weber, E. M. Ainley, A. Agrawal, R. Srinivas, G. Araneda, C. J. Ballance, and D. M. Lucas, *Robust Quantum Memory in a Trapped-Ion Quantum Network Node*, *Phys. Rev. Lett.* **130**, 090803 (2023).

[106] T. P. Harty, D. T. C. Allcock, C. J. Ballance, L. Guidoni, H. A. Janacek, N. M. Linke, D. N. Stacey, and D. M. Lucas, *High-Fidelity Preparation, Gates, Memory, and Readout of a Trapped-Ion Quantum Bit*, *Phys. Rev. Lett.* **113**, 220501 (2014).

[107] E. H. Pinnington, R. W. Berends, and M. Lumsden, *Studies of laser-induced fluorescence in fast beams of Sr+ and Ba+ ions*, *J. Phys. B* **28**, 2095 (1995).

[108] S. Mannervik, J. Lidberg, L.-O. Norlin, P. Royen, A. Schmitt, W. Shi, and X. Tordoir, *Lifetime Measurement of the Metastable* $4d^2D_{3/2}$ *Level in* Sr^+ *by Optical Pumping of a Stored Ion Beam*, *Phys. Rev. Lett.* **83**, 698–701 (1999).

[109] V. Letchumanan, M. A. Wilson, P. Gill, and A. G. Sinclair, *Lifetime measurement of the metastable* $4d\,^2D_{52}$ *state in* $^{88}Sr^+$ *using a single trapped ion*, *Phys. Rev. A* **72**, 012509 (2005).

[110] J. E. Sansonetti, *Wavelengths, Transition Probabilities, and Energy Levels for the Spectra of Strontium Ions (Sr II through Sr XXXVIII)*, *J. Phys. Chem. Ref. Data* **41**, 013102-013102–119 (2012).

[111] D. M. Lucas, A. Ramos, J. P. Home, M. J. McDonnell, S. Nakayama, J.-P. Stacey, S. C. Webster, D. N. Stacey, and A. M. Steane, *Isotope-selective photoionization for calcium ion trapping*, *Phys. Rev. A* **69**, 012711 (2004).

[112] G. Kasprowicz, P. Kulik, M. Gaska, T. Przywozki, K. Pozniak, J. Jarosinski, J. W. Britton, T. Harty, C. Balance, W. Zhang, D. Nadlinger, D. Slichter, D. Allcock, S. Bourdeauducq, R. Jördens, and K. Pozniak. "ARTIQ and Sinara: Open Software and Hardware Stacks for Quantum Physics". *OSA Quantum 2.0 Conference*. Optica Publishing Group, 2020, QTu8B.14. DOI: 10.1364/QUANTUM.2020.QTu8B.14.

[113] N. Krackow. "Short Time Fourier Transform Pulse Generator for Trapped Ion Quantum Gates". PhD thesis. Technische Universität Berlin, 2020. URL: https://m-labs.hk/experiment-control/publications/.

[114] D. Gallego, S. Hofferberth, T. Schumm, P. Krüger, and J. Schmiedmayer, *Optical lattice on an atom chip*, *Opt. Lett.* **34**, 3463–3465 (2009).

[115] K. Shibata, R. Yamamoto, and Y. Takahashi, *High-Sensitivity In situ Fluorescence Imaging of Ytterbium Atoms in a Two-Dimensional Optical Lattice with Dual Optical Molasses*, *J. Phys. Soc. Jpn.* **83**, 014301 (2014).

[116] T. E. DeLaubenfels, K. A. Burkhardt, G. Vittorini, J. T. Merrill, K. R. Brown, and J. M. Amini, *Modulating carrier and sideband coupling strengths in a standing-wave gate beam*, *Phys. Rev. A* **92**, 61402 (2015).

[117] C. T. Schmiegelow, H. Kaufmann, T. Ruster, J. Schulz, V. Kaushal, M. Hettrich, F. Schmidt-Kaler, and U. G. Poschinger, *Phase-Stable Free-Space Optical Lattices for Trapped Ions*, *Phys. Rev. Lett.* **116**, 33002 (2016).

[118] A. R. Vasquez, C. Mordini, C. Vernière, M. Stadler, M. Malinowski, C. Zhang, D. Kienzler, K. K. Mehta, and J. P. Home, *Control of an Atomic Quadrupole Transition in a Phase-Stable Standing Wave*, *Phys. Rev. Lett.* **130**, 133201 (2023).

[119] W. J. Riley, *Handbook of frequency stability analysis*, 2008.

[120] D. W. Berry, B. L. Higgins, S. D. Bartlett, M. W. Mitchell, G. J. Pryde, and H. M. Wiseman, *How to perform the most accurate possible phase measurements*, *Phys. Rev. A* **80**, 052114 (2009).

[121] D. Leibfried, R. Blatt, C. Monroe, and D. Wineland, *Quantum dynamics of single trapped ions*, *Rev. Mod. Phys.* **75**, 281–324 (2003).

[122] M. Brownnutt, M. Kumph, P. Rabl, and R. Blatt, *Ion-trap measurements of electric-field noise near surfaces*, *Rev. Mod. Phys.* **87**, 1419–1482 (2015).

[123] J. A. Sedlacek, J. Stuart, W. Loh, R. McConnell, C. D. Bruzewicz, J. M. Sage, and J. Chiaverini, *Method for determination of technical noise contributions to ion motional heating*, *J. Appl. Phys.* **124**, 214904 (2018).

[124] Q. A. Turchette, C. J. Myatt, B. E. King, C. A. Sackett, D. Kielpinski, W. M. Itano, C. Monroe, and D. J. Wineland, *Decoherence and decay of motional quantum states of a trapped atom coupled to engineered reservoirs*, *Phys. Rev. A* **62**, 053807 (2000).

[125] S. Krämer, D. Plankensteiner, L. Ostermann, and H. Ritsch, *QuantumOptics. jl: A Julia framework for simulating open quantum systems*, *Comput. Phys. Commun.* **227**, 109–116 (2018).

[126] T. P. Harty. "High-fidelity microwave-driven quantum logic in intermediate-field 43Ca+". PhD thesis. Oxford University, UK, 2013. URL: https://ora.ox.ac.uk/objects/uuid:55264c2d-bb42-4439-bf49-731b9f66de74.

[127] H. Häffner, S. Gulde, M. Riebe, G. Lancaster, C. Becher, J. Eschner, F. Schmidt-Kaler, and R. Blatt, *Precision Measurement and Compensation of Optical Stark Shifts for an Ion-Trap Quantum Processor*, *Phys. Rev. Lett.* **90**, 143602 (2003).

[128] D. Hayes, S. M. Clark, S. Debnath, D. Hucul, I. V. Inlek, K. W. Lee, Q. Quraishi, and C. Monroe, *Coherent Error Suppression in Multiqubit Entangling Gates*, *Phys. Rev. Lett.* **109**, 020503 (2012).

[129] O. Băzăvan, S. Saner, D. J. Webb, E. M. Ainley, P. Drmota, D. P. Nadlinger, G. Araneda, D. M. Lucas, C. J. Ballance, and R. Srinivas, *Squeezing, trisqueezing, and quadsqueezing in a spin-oscillator system*, *arXiv preprint arXiv:2403.05471*, (2024).

[130] N. C. Menicucci, S. Jay Olson, and G. J. Milburn, *Simulating quantum effects of cosmological expansion using a static ion trap*, *New J. Phys.* **12**, 095019 (2010).

[131] E. Knill, D. Leibfried, R. Reichle, J. Britton, R. B. Blakestad, J. D. Jost, C. Langer, R. Ozeri, S. Seidelin, and D. J. Wineland, *Randomized benchmarking of quantum gates*, *Phys. Rev. A* **77**, 012307 (2008).

[132] A. Erhard, J. J. Wallman, L. Postler, M. Meth, R. Stricker, E. A. Martinez, P. Schindler, T. Monz, J. Emerson, and R. Blatt, *Characterizing large-scale quantum computers via cycle benchmarking*, *Nat. Commun.* **10**, 5347 (2019).

[133] D. Leibfried, B. DeMarco, V. Meyer, D. Lucas, M. Barrett, J. Britton, W. M. Itano, B. Jelenković, C. Langer, T. Rosenband, et al., *Experimental demonstration of a robust, high-fidelity geometric two ion-qubit phase gate*, *Nature* **422**, 412–415 (2003).

[134] P. J. Lee, K.-A. Brickman, L. Deslauriers, P. C. Haljan, L.-M. Duan, and C. Monroe, *Phase control of trapped ion quantum gates*, *J. Opt. B* **7**, S371 (2005).

[135] C. Langer, R. Ozeri, J. D. Jost, J. Chiaverini, B. DeMarco, A. Ben-Kish, R. B. Blakestad, J. Britton, D. B. Hume, W. M. Itano, D. Leibfried, R. Reichle, T. Rosenband, T. Schaetz, P. O. Schmidt, and D. J. Wineland, *Long-Lived Qubit Memory Using Atomic Ions*, *Phys. Rev. Lett.* **95**, 060502 (2005).

[136] P. Wang, C.-Y. Luan, M. Qiao, M. Um, J. Zhang, Y. Wang, X. Yuan, M. Gu, J. Zhang, and K. Kim, *Single ion qubit with estimated coherence time exceeding one hour*, *Nat. Commun.* **12**, 233 (2021).

[137] L. Aolita, K. Kim, J. Benhelm, C. F. Roos, and H. Häffner, *High-fidelity ion-trap quantum computing with hyperfine clock states*, *Phys. Rev. A* **76**, 040303 (2007).

[138] C. H. Baldwin, B. J. Bjork, M. Foss-Feig, J. P. Gaebler, D. Hayes, M. G. Kokish, C. Langer, J. A. Sedlacek, D. Stack, and G. Vittorini, *High-fidelity light-shift gate for clock-state qubits*, *Phys. Rev. A* **103**, 012603 (2021).

[139] B. C. Sawyer and K. R. Brown, *Wavelength-insensitive, multispecies entangling gate for group-2 atomic ions*, *Phys. Rev. A* **103**, 022427 (2021).

[140] R. Sutherland and R. Srinivas, *Universal hybrid quantum computing in trapped ions*, *Phys. Rev. A* **104**, 032609 (2021).

[141] S. L. Braunstein and R. I. McLachlan, *Generalized squeezing*, *Phys. Rev. A* **35**, 1659–1667 (1987).

[142] S. Ding, G. Maslennikov, R. Hablützel, and D. Matsukevich, *Cross-Kerr Nonlinearity for Phonon Counting*, *Phys. Rev. Lett.* **119**, 193602 (2017).

[143] D. J. Heinzen and D. J. Wineland, *Quantum-limited cooling and detection of radio-frequency oscillations by laser-cooled ions*, *Phys. Rev. A* **42**, 2977–2994 (1990).

[144] J. Metzner, A. Quinn, S. Brudney, I. Moore, S. Burd, D. Wineland, and D. Allcock, *Two-mode squeezing and SU (1, 1) interferometry with trapped ions*, *arXiv:2312.10847*, (2023).

[145] J. I. Cirac, R. Blatt, A. S. Parkins, and P. Zoller, *Preparation of Fock states by observation of quantum jumps in an ion trap*, *Phys. Rev. Lett.* **70**, 762–765 (1993).

[146] O. Katz and C. Monroe, *Programmable Quantum Simulations of Bosonic Systems with Trapped Ions*, *Phys. Rev. Lett.* **131**, 033604 (2023).

[147] D. F. Walls, *Squeezed states of light*, *Nature* **306**, 141–146 (1983).

[148] A. F. Kockum, A. Soro, L. García-Álvarez, P. Vikstål, T. Douce, G. Johansson, and G. Ferrini, *Lecture notes on quantum computing*, *arXiv preprint arXiv:2311.08445*, (2023).

[149] S. D. Bartlett and B. C. Sanders, *Efficient Classical Simulation of Optical Quantum Information Circuits*, *Phys. Rev. Lett.* **89**, 207903 (2002).

[150] K. C. McCormick, J. Keller, S. C. Burd, D. J. Wineland, A. C. Wilson, and D. Leibfried, *Quantum-enhanced sensing of a single-ion mechanical oscillator*, *Nature* **572**, 86–90 (2019).

[151] N. Schwegler, D. Holzapfel, M. Stadler, A. Mitjans, I. Sergachev, J. P. Home, and D. Kienzler, *Trapping and Ground-State Cooling of a Single* H_2^+, *Phys. Rev. Lett.* **131**, 133003 (2023).

[152] H.-Y. Lo, D. Kienzler, L. de Clercq, M. Marinelli, V. Negnevitsky, B. C. Keitch, and J. P. Home, *Spin-motion entanglement and state diagnosis with squeezed oscillator wavepackets*, *Nature* **521**, 336–339 (2015).

[153] S. C. Burd. "Squeezing and amplification of trapped-ion motion". PhD thesis. University of Colorado at Boulder, 2020. URL: https://www.proquest.com/dissertations-theses/squeezing-amplification-trapped-ion-motion/docview/2447588778/se-2.

[154] S. Saner, O. Băzăvan, D. Webb, G. Araneda, D. Lucas, C. Ballance, and R. Srinivas, *Generating arbitrary superpositions of nonclassical quantum harmonic oscillator states*, *arXiv preprint arXiv:2409.03482*, (2024).

[155] M. Wittemer, F. Hakelberg, P. Kiefer, J.-P. Schröder, C. Fey, R. Schützhold, U. Warring, and T. Schaetz, *Phonon Pair Creation by Inflating Quantum Fluctuations in an Ion Trap*, *Phys. Rev. Lett.* **123**, 180502 (2019).

[156] V. G. Matsos, C. H. Valahu, T. Navickas, A. D. Rao, M. J. Millican, M. J. Biercuk, and T. R. Tan, *Robust and Deterministic Preparation of Bosonic Logical States in a Trapped Ion*, *arXiv:2310.15546*, (2023).

[157] V. M. Schäfer, C. J. Ballance, K. Thirumalai, L. J. Stephenson, T. G. Ballance, A. M. Steane, and D. M. Lucas, *Fast quantum logic gates with trapped-ion qubits*, *Nature* **555**, 75–78 (2018).

[158] I. Pogorelov, T. Feldker, C. D. Marciniak, L. Postler, G. Jacob, O. Krieglsteiner, V. Podlesnic, M. Meth, V. Negnevitsky, M. Stadler, B. Höfer, C. Wächter, K. Lakhmanskiy, R. Blatt, P. Schindler, and T. Monz, *Compact Ion-Trap Quantum Computing Demonstrator*, *PRX Quantum* **2**, 020343 (2021).

[159] A. M. Steane, G. Imreh, J. P. Home, and D. Leibfried, *New J. Phys.* **16**, 53049 (2014).

[160] M. Palmero, S. Martínez-Garaot, D. Leibfried, D. J. Wineland, and J. G. Muga, *Fast phase gates with trapped ions*, *Phys. Rev. A* **95**, 22328 (2017).

[161] S. X. Wang, G. Hao Low, N. S. Lachenmyer, Y. Ge, P. F. Herskind, and I. L. Chuang, *Laser-induced charging of microfabricated ion traps*, *J. Appl. Phys.* **110**, 104901 (2011).

[162] R. J. Niffenegger, J. Stuart, C. Sorace-Agaskar, D. Kharas, S. Bramhavar, C. D. Bruzewicz, W. Loh, R. T. Maxson, R. McConnell, D. Reens, G. N. West, J. M. Sage, and J. Chiaverini, *Integrated multi-wavelength control of an ion qubit*, *Nature* **586**, 538–542 (2020).

[163] K. K. Mehta, C. Zhang, M. Malinowski, T.-L. Nguyen, M. Stadler, and J. P. Home, *Integrated optical multi-ion quantum logic*, *Nature* **586**, 533–537 (2020).

[164] J. J. García-Ripoll, P. Zoller, and J. I. Cirac, *Speed Optimized Two-Qubit Gates with Laser Coherent Control Techniques for Ion Trap Quantum Computing*, *Phys. Rev. Lett.* **91**, 157901 (2003).

[165] J. D. Wong-Campos, S. A. Moses, K. G. Johnson, and C. Monroe, *Demonstration of Two-Atom Entanglement with Ultrafast Optical Pulses*, *Phys. Rev. Lett.* **119**, 230501 (2017).

[166] C. Zhang, F. Pokorny, W. Li, G. Higgins, A. Pöschl, I. Lesanovsky, and M. Hennrich, *Submicrosecond entangling gate between trapped ions via Rydberg interaction*, *Nature* **580**, 345–349 (2020).

[167] M. Drechsler, M. Belén Farías, N. Freitas, C. T. Schmiegelow, and J. P. Paz, *State-dependent motional squeezing of a trapped ion: Proposed method and applications*, *Phys. Rev. A* **101**, 052331 (2020).